
NLO QCD Corrections to Vector Boson Production in Association with Multiple Heavy and Light Jets

Dissertation

zur Erlangung des Doktorgrades
der Fakultät für Mathematik und Physik der

**Albert-Ludwigs-Universität
Freiburg**

vorgelegt von

Felix Richard Anger

Februar 2018

Dekan: Prof. Dr. Gregor Herten
Referent: JProf. Dr. Harald Ita
Koreferent: Prof. Dr. Stefan Dittmaier
Tag der mündlichen Prüfung: 23.04.2018

NLO QCD Corrections to Vector Boson Production in Association with Multiple Heavy and Light Jets

Dissertation

zur Erlangung des Doktorgrades
der Fakultät für Mathematik und Physik der

**Albert-Ludwigs-Universität
Freiburg**

vorgelegt von

Felix Richard Anger

Februar 2018

List of Publications

Partial results of the presented work have been published/submitted prior to submission of this thesis. The results presented in Chapter 5 are based on the following manuscript:

- **F.R. Anger** and V. Sotnikov, “*On the Dimensional Regularization of QCD Helicity Amplitudes With Quarks*”, [arXiv:1803.11127 \[hep-ph\]](https://arxiv.org/abs/1803.11127).

Chapters 7-9 on NLO QCD predictions for $Wb\bar{b} + n$ -jet ($n = 0, 1, 2, 3$) production are based on the following publication:

- **F.R. Anger**, F. Febres Cordero, H. Ita and V. Sotnikov, “*NLO QCD Predictions for $Wb\bar{b}$ Production in Association with up to Three Light Jets at the LHC*”, *Phys. Rev.* **D97**, 036018 (2018), [arXiv:1712.05721 \[hep-ph\]](https://arxiv.org/abs/1712.05721).

The results on weak vector boson production with light jets presented in Chapters 10 and 11 are based on the following publication:

- **F.R. Anger**, F. Febres Cordero, S. Höche and D. Maître, “*Weak Vector Boson Production with Many Jets at the LHC $\sqrt{s} = 13$ TeV*”, [arXiv:1712.08621 \[hep-ph\]](https://arxiv.org/abs/1712.08621). To appear in *Phys. Rev. D*.

Other Publications

- C. Gneiting, **F.R. Anger** and A. Buchleitner, “*Incoherent ensemble dynamics in disordered systems*”, *Phys. Rev.* **A93**, 032139 (2016), [arXiv:1508.07187 \[quant-ph\]](https://arxiv.org/abs/1508.07187).

Contents

Abstract	ix
1. Introduction	1
1.1. Structure of this Thesis	6
2. From the Standard Model to Hadronic Collisions	7
2.1. The Standard Model of Particle Physics	7
2.1.1. Gauge Invariance and the Yang-Mills Lagrangian	8
2.1.2. Electroweak Symmetry Breaking and GSW Theory	11
2.1.3. Matter Content of the Standard Model	17
2.1.4. QCD Quantization and Gauge Fixing	20
2.1.5. The S -Matrix in Perturbation Theory	21
2.2. Hadronic Collisions - The Realm of Perturbative QCD	21
2.2.1. Running coupling	22
2.2.2. Factorization and Partonic Cross Sections	23
2.2.3. Collimated Collection of Hadronic Particles - a Jet	24
Part 1: Methods and Tools	26
3. Color Decomposition	27
3.1. Partial Amplitudes	27
3.2. Primitive Amplitudes	29
3.3. Assembly of Virtual Matrix Elements	30
4. Numerical Unitarity With Massive Quarks	31
4.1. Preliminaries	31
4.1.1. A Generic One-Loop Amplitude in D -Dimensions	31
4.1.2. Dimensional Regularization	32
4.1.3. Exploiting Unitarity as a Computational Method	33
4.1.4. Master Integrals	34
4.2. The Loop Integrand	35
4.3. Generalized Unitarity Method	39
4.4. Massive Bubble and Tadpole Cuts	41
4.4.1. Massive One-Leg Bubble Cuts	41
4.4.2. Massive Tadpole Cuts	43
4.5. Tree Amplitude Generation with Berends-Giele Recursions	45
5. Dimensional Dependence of One-Loop Helicity Amplitudes	51
5.1. Helicity Amplitudes in Integer D_s	52
5.1.1. Regularization Schemes	52
5.1.2. Dirac Algebra and Spinor Representations in Integer D_s	54
5.1.3. One-loop Matrix Elements	58
5.1.4. Gluon Propagator in Axial Gauge	60
5.2. Establishing the Dimensional Dependence	61

5.3. Remarks on the FDF Scheme	65
5.4. Implementation Details	66
6. Renormalization	71
6.1. Multiplicative Renormalization	71
6.2. Coupling and Wave-Function Renormalization	72
6.2.1. Renormalization Shifts Proportional to Tree Amplitudes	72
6.2.2. Renormalization Constants	74
6.3. Mass Renormalization	76
6.4. Summary of Renormalization	77
6.5. Scheme Shift From FDH to 't Hooft-Veltman	78
6.6. Scale Variation Using N -tuple Data	78
Part 2: $Wb\bar{b} + n$ Jet Production ($n = 0, 1, 2, 3$)	81
7. Introduction to $Wb\bar{b} + n$ Jet Production	83
7.1. Calculational Setup	84
7.2. Monte Carlo Integration	85
7.3. Input Parameters: Partons Distributions, Couplings and Masses	86
7.4. Kinematics, Observables and Exclusive Sums	87
7.5. Dynamical Scale Choice	88
8. Validation of the New Matrix Elements	89
8.1. Numerical Stability of Virtual Matrix Elements	89
8.2. Phase-Space Point Comparison Against Automated Tools	92
8.3. Validation of Integrated Total Cross Sections	93
9. Results for the LHC with $\sqrt{s} = 13$ TeV	95
9.1. Effects of a Finite Bottom-Quark Mass	95
9.2. Results for $Wb\bar{b}$ Production in Association with Light Jets	99
9.2.1. Total Cross Sections	99
9.2.2. Scale Dependence	101
9.2.3. Differential Cross Sections	102
9.3. Backgrounds to HW Production	105
Part 3: $V + n$ Light Jet Production at the LHC $\sqrt{s} = 13$ TeV	111
10. Introduction to $V +$ Jets Production	113
10.1. Basic Setup	114
10.2. Kinematical Cuts	114
10.3. Dynamical Scale Choices	115
10.3.1. Fixed-Order Scales	115
10.3.2. The MiNLO' Procedure	116
10.3.3. Nomenclature for Dynamical Scales Explored	117
11. Results for $V +$ Jets Production	119
11.1. Total Cross Sections	119
11.2. Scale Dependence	122

11.3. Differential Cross Sections	124
11.4. Cross Section Ratios	128
11.4.1. Jet Ratios	129
11.4.2. Vector-Boson Ratios	130
12. Summary and Outlook	133
Appendices	135
A. The Van Nerven-Vermaseren Basis	137
B. Color-Ordered Feynman Rules	139
C. Results for Selected Scalar Integrals	141
D. Tadpole Coefficients From UV matching	142
Bibliography	143
Acknowledgments	159

Abstract

Precise theory predictions for scattering processes are an important input for the physics program at the Large Hadron Collider at CERN, Geneva. Notably the complex collider signatures of an electroweak vector boson and many jets that originate in either light partons (light jets) or bottom quarks (b jets) are relevant for both measurements of Standard Model processes as well as searches for new physics. In this thesis, we present new next-to-leading order QCD predictions for two related high-multiplicity processes at the LHC $\sqrt{s} = 13$ TeV. We show predictions for $W b \bar{b}$ production in association with two and three light jets that we computed for the first time. In order to obtain the required one-loop amplitudes, we implement the numerical unitarity approach for massive particles in a new version of the `BlackHat` library. To this end, we devise and apply a new algorithm for the evaluation of D -dimensional unitarity cuts. It builds on a consistent embedding of external fermions states in dimensional regularization and reduces the computational complexity of our calculations. Furthermore, we present next-to-leading order QCD predictions for $V + n$ -jet production in association with up to $n = 5$ light jets for $V = W^\pm$ and with up to $n = 4$ light jets for $V = Z$, which we extend to the higher center-of-mass energy of the Large Hadron Collider Run-II. For these processes we compare results obtained with fixed-order scales such as $\hat{H}'_T/2$ with the `MiNLO` reweighting procedure.

CHAPTER 1

Introduction

ΓΝΩΘΙ ΣΕΑΤΤΟΝ - Gnothi Seauton - know thyself

Inscription at the temple of Apollo in Delphi, Greece (1st millennium B.C.)

The most successful theory to describe fundamental particles and their interactions is the Standard Model of particle physics (SM). The SM is widely considered a low-energy approximation to some underlying and more fundamental description of nature. In particular due to its shortcoming of not to include both the gravitational force and the indirect evidence of new types of matter referred to as dark matter in its unified description of particle interactions. Currently, the SM undergoes stringent testing at the Large Hadron Collider (LHC) at CERN. With its current center-of-mass energy of 13 TeV, both measurements of properties of known particles as well as searches for yet to discover new physics are conducted at an unprecedented energy regime.

As of today, no apparent statistically significant deviations from SM predictions - and thus no physics beyond the SM (BSM) - have been detected at the LHC. Additionally many properties of the newly discovered Higgs boson have been established. These early results narrow the future exploration for new particle phenomena. An important input for the understanding of expected phenomena as well as searches for new physics are reliable theory predictions. In particular, since new phenomena will reveal themselves through subtle effects and small deviations from SM predictions for complex processes. This necessitates ever more precise predictions for multi-particle observables within the SM in order to probe it at a deeper level.

At the heart of theoretical predictions for particle collisions at the LHC are fixed-order calculations in perturbative quantum field theory. Currently required theory predictions include quantum corrections in quantum chromodynamics (QCD) and electroweak theory (EW). State-of-the-art are higher-order corrections at next-to-next-to-leading order (NNLO) accuracy in QCD for processes with up to two particles or objects in the final state, EW next-to-leading order (NLO) corrections as well as NLO QCD corrections for complex final states with many particles. In this dissertation we focus on the problem of computing NLO QCD corrections to processes with massive quarks in the loop and with many particles in the final state. Notably, we consider weak-gauge-boson production in association with many heavy and light jet. This process class is abundantly produced at the LHC and thus constitutes a suitable testing ground for theory predictions and measurements. Furthermore it is an irreducible background to many important signatures and needs to be understood precisely.

Calculations in perturbation theory at a fixed-order of the respective coupling are valuable from a theoretical point of view: Firstly, they are based on first principles and thus

directly link measurements to quantum field theory. Furthermore, a categorization of predictions by the included order is possible with an assumed order-by-order improvement of the accuracy. And finally, they are amenable to automation, which allows for the computation of higher-order correction to increasingly complex processes. In general, fixed-order predictions have a parametric dependence on the input of physical quantities such as couplings, parton-distribution functions (PDFs) and masses of the involved particles. The theoretical uncertainty associated to fixed-order predictions is then an accumulation of the uncertainties associated to the input parameters listed above as well as the uncertainties associated to missing higher-order effects due to the truncation of the perturbative expansion. Since the latter are not known in general and often constitute the leading source of uncertainty, the estimation of theoretical uncertainties of fixed-order calculations is a difficult problem.

The truncation of the perturbative series at a finite order leads to a dependence of fixed-order predictions on the unphysical renormalization and factorization scale μ . This residual dependence would not be present in a full prediction and is compensated in a complete perturbation series by higher-order terms. As a consequence, the dependence on μ can be used as an estimate of the magnitude of missing higher-order effects. The renormalization scale, which is introduced in dimensional regularization to retain the correct mass dimension of the appearing integral functions, is also used as the scale at which the input parameters are specified. In the computation of fixed-order cross-sections, the question of which scale to use is important and there exist different proposals how to deal with it.¹ One widely used approach for dynamical scale setting is to take an accelerated convergence of the perturbative expansion for particular observables as the guiding principle [1] of whether or not a scale choice is sensible. Typically, a functional form that reflects the hardness of the process under consideration is chosen. For example, the dynamical scale choice $\mu_0 = \hat{H}'_{\mathrm{T}}/2$ (defined in Sec. 7.4), the total partonic energy in the transverse plane, has proven to be a sensible choice for the process class of weak-vector-boson production in association with many light jets at the LHC. It tends to reduce the shape changes and global size of quantum corrections when going from leading order (LO) to NLO (see for example [2–4]). The above approach has been successfully applied to many NLO QCD predictions and is convenient from a practical point of view. However, it suffers from a missing underlying physical explanation and its coarse-grained approach uses no detailed information about kinematics and parton content of each event to determine the corresponding scale μ . The more intuitive MiNLO method [5] accommodates kinematical information of the underlying Born process by building the most likely branching history with a jet clustering algorithm, as in the CKKW procedure [6]. The strong couplings are then evaluated at the corresponding transverse momentum at each branching and no-branching probabilities in the form of Sudakov form factors are assigned. The MiNLO method ensures NLO accuracy of the procedure. Other approaches are based on the idea of restoring the conformal or scale-invariance symmetry in observables directly, like the Principle of Maximum Conformality [7, 8]. In this work we make for the first time an in depth study of the MiNLO procedure for processes with more than four jets in the final state and compare to results obtained with $\hat{H}'_{\mathrm{T}}/2$ for validation.

¹See for example the contributions to the recent workshop “Taming Unphysical Scales for Physical Predictions”, 30.-31.03.2017, Cambridge.

The current physics runs at the LHC explore a wide range of scales, from tens of GeVs to the multi-TeV regime. In particular this large hierarchy of scales makes LO QCD predictions unreliable, as they tend to be very sensitive to the unphysical renormalization and factorization scales. Furthermore, LO predictions often miss important initial-state partonic configurations. The inclusion of consecutive orders in perturbation theory reduces the dependence on unphysical scales and NLO QCD predictions allow for a first reliable extrapolation into tails of distributions.² The NLO QCD corrections to $W + \text{jets}$ production have a long history [10] and correction to $W + 2$ jets [11], $W + 3$ jets [12], $W + 4$ jets [13] and $W + 5$ jets [2] are known. Also predictions for W production in association with heavy quarks are known with NLO QCD results for $W b\bar{b}$ production [14] and $W b\bar{b} + 1$ -jet production [15] being available. Likewise the NLO QCD corrections to $Z + 1$ jet [10], $Z + 2$ jets [16], $Z + 3$ jets [17] and $Z + 4$ jets [3] production have been computed. We show in this work the first NLO QCD calculation of a process with a W boson, two heavy jets as well as two and three light jets in the final state and demonstrate how the quantum corrections considerably stabilize the theoretical predictions. Furthermore, we perform a dedicated study of W^\pm production in association with five light jets and Z in association with four light jets. Currently, there is also remarkable progress on NNLO calculations, with phenomenological prediction for $2 \rightarrow 2$ processes such as vector-boson production with a single jet [18–20] being available.

In the following, we elaborate in more detail on the difficulty of computing NLO QCD corrections to high-multiplicity processes with massive quarks in the loop and outline the approach that we have used and developed in this work. Furthermore, we highlight the two phenomenological studies on weak-gauge-boson production in association with heavy and light jets that we have performed.

The Challenge of Computing NLO QCD Corrections to High-Multiplicity Processes with Massive Quarks

We provide for the first time NLO QCD predictions for the production of $W b\bar{b}$ in association with two and three light jets, as presented in [21]. The high-multiplicity of these processes with up to eight particles in the loop as well as the additional scale introduced by the bottom quark mass makes the computation of NLO QCD predictions for these processes a challenging task.

We use the unitarity method [22–24] and its extension to massive particles [25] which has been applied by a number of groups for analytic as well as numerical computations of massive amplitudes [26–28]. To this end, we implement the numerical unitarity approach [29–32] and its extension to massive quarks [33] for the computation of our NLO QCD predictions. Unitarity methods obtain the integrands of one-loop amplitudes directly from on-shell tree amplitudes, thus avoiding an explicit reduction of tensor and higher-rank integrals. Our approach shares common features with the Ossola, Papadopoulos and Pittau (OPP) reduction method [29]. Using suitable loop-momentum parameterizations allows to set n loop propagators on-shell, and the amplitude factorizes into a prod-

²Processes with missing partonic channels and large accessible phase space at NLO are an exception to this and require NNLO calculations, as pointed out for example in [9].

uct of n tree amplitudes. We use Berends-Giele (BG) off-shell recurrence relations [34] to compute the required tree amplitudes numerically, which allows for an efficient and flexible tree generation for both complex and D -dimensional momenta.

The computation of single cuts for the extraction of tadpole coefficients and double cuts for the extraction of coefficients of bubbles with a single on-shell leg require a special treatment, since explicit divergences associated to both tadpole Feynman diagrams and self-energy insertions on external legs are encountered in their computation. We follow the prescription for the treatment of double cuts of Ref. [33] which also applies to single cuts, that is we remove the divergent contributions by adjusting the tree-diagram generation. This procedure is connected to mass renormalization in order to produce gauge-invariant results. Alternative approaches have been presented in Ref. [35] and, recently, in Ref. [36].

We use the four-dimensional helicity (FDH) [37, 38] variant of dimensional regularization in our calculation of D -dimensional unitarity [31]. We developed a prescription to map the higher-dimensional Dirac algebra into four-dimensional objects [39] to numerically evaluate the required cuts efficiently. More precisely, whenever possible we reduce the D_s -dimensional algebra and states to four dimensions. The known decomposition of the $D_s = 6$ dimensional gluon amplitude to a $D_s = 5$ amplitude plus a scalar contribution [23] is in close analogy to our approach. Our prescription allows to avoid an overhead of numerical computations in higher-dimensional representations of the Dirac algebra, and can be equivalently derived from the four-dimensional (re-)formulation (FDF) of FDH [40] with some adaptions. This is done with a crucial modification based on imposing higher-dimensional Dirac traces for the computation of the loop amplitudes. The latter proved fundamental for generic application which can include multiple massive fermion lines. We have implemented the described methods into an upgraded version of the `BlackHat` library [32], which can now compute one-loop matrix elements with multiple massive quarks. A future extension of the presented methods could come by an application in the recently developed numerical unitarity method for two-loop calculations [41, 42], which was applied for the computation of four- [43] and five-gluon amplitudes [44].

Phenomenology of Weak-Vector-Boson Production in Association with Heavy and Light Jets

The experimental signatures of vector-boson production in association with many heavy and light jets contain charged leptons, missing transverse energy from undetected neutrinos and multiple heavy and light jets. The possibility of identifying leptons and thereby distinguishing the events from QCD multijet background is important from the experimental point of view. The above mentioned processes appear as irreducible backgrounds to many searches for new physics ongoing at the LHC Run-II. The decay of $Z \rightarrow \nu\bar{\nu}$ in association with jets for example has a signature that appears at the end of a decay cascade of typical new-physics scenarios. For example, it is an irreducible background to searches for the hypothetical production of supersymmetric pairs of squarks and gluinos that decay into jets and undetected lightest supersymmetric particles [45–50]. Also the signature of $W b\bar{b}$ production often appears in the decay chains of heavy massive particles predicted in BSM theories, e.g. those for the superpartners of the third generation quarks, sbottom

and stop [51–53]. During the 7 and 8 TeV runs of the LHC, the ATLAS [54–61] and CMS [62–68] experiments have scrutinized vector-boson production in association with light jets. The first measurements at an energy of 13 TeV by both collaborations [69, 70] continue to illustrate to which extend theoretical predictions, by both calculations specific to the process class as well as general Monte Carlo event generators, describe the experimental data. The recent experimental analysis for $Z/\gamma^* + \text{jets}$ production [69] compares, amongst others, to our predictions [71] presented in Chapter 11.

The inclusion of b jets in the experimental signature is important to study since key processes of the SM and of BSM physics involve heavy quarks. Hence, this process is irreducible background to important measurements and searches such as the associated Higgs production in the HW channel, with the consequent decay of the Higgs boson into a $b\bar{b}$ pair. The HW production channel signal strength is well in accordance with the SM expectation [72] but only recently evidence for the decay of the Higgs boson to a b -quark pair was found [73]. Processes with heavy flavor content are harder to measure and to predict theoretically. Among the experimental challenges is the correct identification and modeling of bottom quarks [74]. Experimental measurements of $Wb\bar{b}$ production have been performed by both ATLAS [75] and CMS [76, 77], providing a variety of results, both with and without additional light jets.

In this dissertation, we present two phenomenological studies for the above process class, namely for $Wb\bar{b}$ production in association with light jets and for V ($V = W^\pm, Z$) production in association with light jets.

We present NLO QCD predictions for $Wb\bar{b}$ production in association with up to three light jets at the LHC [21]. In order to do so, we use our new version of the **BlackHat** library in combination with the **SHERPA** Monte Carlo program [78]. We compute in the four-flavor number scheme (4FNS), that is we consistently treat bottom quarks as massive particles and consider all mass effects in closed-fermion-loop contributions. Previously, NLO QCD predictions that retain the full mass dependence were computed for $Wb\bar{b}$ production [14, 79] and recently for $Wb\bar{b} + 1\text{-jet}$ production [15]. The NLO QCD correction to $Wb\bar{b}$ production are large [14, 79, 80] due to the opening of a gluon-initiated channel in real contributions and the release of a LO kinematical constraint which fixes the p_T of the W boson to that of the $b\bar{b}$ system. In order to get reliable theoretical predictions for this process in spite of giant K -factors [9], we employ our set of light-jet high-multiplicity NLO QCD results to compute observables based on exclusive sums [81]. Comparison to LHC data for $W + 1\text{-jet}$ production [59, 61] shows that exclusive-sum observables improve perturbative predictions, since they can contain large contributions that first appear at NNLO. Since $Wb\bar{b}$ production is an irreducible background to $H(\rightarrow b\bar{b})W$ production, we focus on observables associated to it and study the $p_T^{b\bar{b}}$, p_T^W , and $M_{b\bar{b}}$ exclusive-sum distributions.

We have made a dedicated study of weak-vector-boson production in association with light jets at the $\sqrt{13}$ TeV LHC [71]. We provide predictions for $W + n\text{-jet}$ and $Z + m\text{-jet}$ production in association with $n \leq 5$ and $m \leq 4$ light jets for which we use the **BlackHat** library [32] in combination with **SHERPA** [78], and extract a set of n -tuple files [82] for future usage. We study in detail the comparison of fixed-order scales based on the total partonic transverse energy and different variants of the more physically motivated **MiNLO**

method [5]. We thereby estimate the theoretical uncertainties associated to our predictions that are related to scale sensitivity. In addition, we perform conventional scale variations by constant factors around the central scales as a proxy for missing higher-order terms. With our analysis we extend the comparison of fixed-order scales with the `MiNLO` method to NLO QCD results with four or five light jets in the final state. Furthermore, we explore uncertainties of our high-multiplicity results associated to the choice of PDFs.

1.1. Structure of this Thesis

In Chapter 2, we introduce the SM and briefly describe hadronic collisions. The first part of the thesis consists of Chapters 3–6 and is devoted to a description of the methods and tools that we used and developed in order to obtain the required matrix elements for $Wb\bar{b} + n\text{-jet}$ ($n = 0, 1, 2, 3$) production, as implemented in the new version of the `BlackHat` library. In Chapter 3 we describe the handling of the color degrees of freedom and in Chapter 4 we present the method of numerical unitarity for massive quarks. Chapter 5 is devoted to the study of the dimensional dependence of one-loop helicity amplitudes, from which we derive an efficient prescription to compute higher-dimensional unitarity cuts. In Chapter 6, we give details for the required renormalization procedure of our matrix-elements.

In the second part of this thesis, we present a phenomenological study of $Wb\bar{b} + n\text{-jet}$ ($n = 0, 1, 2, 3$) production. In Chapter 7, we give an introduction and describe our basic setup. Chapter 8 is devoted to a thorough validation of the new matrix elements and we provide checks of the numerical stability as well as comparisons with other automated codes. In Chapter 9, we make use of the new matrix elements and provide NLO QCD predictions for $Wb\bar{b} + n\text{-jet}$ ($n = 0, 1, 2, 3$) production. We study both total rates and differential distributions as well as observables based on exclusive sums of relevance for $H(\rightarrow b\bar{b})W$ studies at the LHC.

The final part of the thesis, consisting of Chapters 10 and Chapter 11, is devoted to a phenomenological study of electroweak gauge boson ($V = Z, W^\pm$) production in association with up to four (Z) or five (W^\pm) light jets. We thereby extend existing predictions to the higher energy of 13 TeV attained during Run-II of the LHC. We provide predictions using two different functional forms of dynamical scales. In particular, we study for the first time the application of the `MiNLO` procedure to high-multiplicity processes and find that predictions obtained with both the `MiNLO` method and $\hat{H}'_T/2$ agree reasonably well.

We conclude and give an outlook in Chapter 12.

CHAPTER 2

From the Standard Model to Hadronic Collisions: A Short Survey

In the first part of this chapter, we give a brief introduction to the Standard Model of particle physics (SM), which forms the theoretical basis of the work described in this thesis. The second half gives a short introduction into the phenomenology of hadron colliders.

2.1. The Standard Model of Particle Physics

The SM is a unified description of the strong force, the weak force and electromagnetism in terms of a relativistic quantum field theory (QFT)¹. Of particular elegance is how the underlying principles, such as local gauge invariance, and their stringent application combined with experimental input leads to a well tested description of elementary particles and their interactions. In Fig. 2.1, we show the timeline of major discoveries of elementary particles. In the course of this chapter, we will see how these particles and their interactions are described in the common framework of the SM.

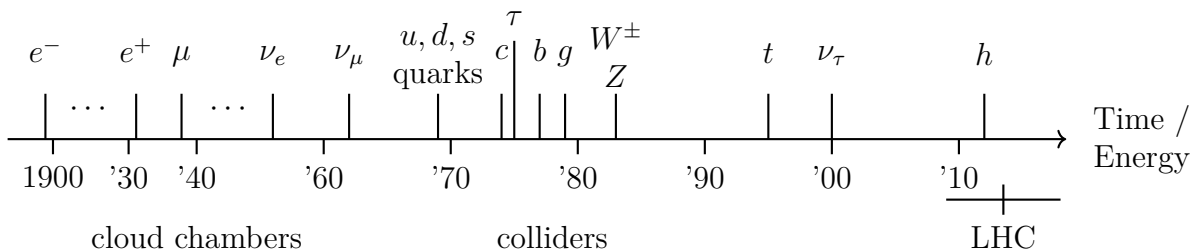


Figure 2.1.: Timeline of major particle physics discoveries.

The SM respects the space-time symmetries of special relativity, known as Poincaré symmetry² and is specified by a set of particles and further constrained by its internal symmetries. An internal symmetry does not interfere with space-time symmetry, hence it transforms fields that are in the same Poincaré or Lorentz group representation into each other. Precisely, the SM is a spontaneously broken, non-abelian gauge theory with the gauge group

$$SU(3)_C \times SU(2)_W \times U(1)_Y, \quad (2.1)$$

¹Including the fourth known force, gravity, remains an outstanding problem of physics.

²Translations in space and time (P), rotations (J) as well as boost (K) make up the Poincaré group.

where the subscripts correspond to the associated charges, that is color (C) for the strong force, weak isospin (W) and weak hypercharge (Y) for the electroweak sector.

In the following, we describe several aspects of the theory background of the SM. In particular, we aim at illustrating the concepts of gauge invariance and spontaneous symmetry breaking. There are many excellent books on the subject, we partly follow the description in [83, 84].

2.1.1. Gauge Invariance and the Yang-Mills Lagrangian

The concept of local gauge symmetry is fundamental to the construction of the SM Lagrangian. It is based on the assumption, that certain (continuous) symmetries hold for the physical systems we describe. Taking the viewpoint that symmetry is fundamental, one can *derive* the SM Lagrangian³. In the following, we will illustrate the concept of local gauge invariance for the gauge group $U(1)$ and see how replacing the standard derivative with a gauge-covariant derivative assures gauge invariance of kinetic terms in the Lagrangian. The additional fields introduced in this *minimal replacement* are called gauge fields. We will furthermore apply the argument to non-abelian gauge groups.

$U(1)$ gauge invariance and the QED Lagrangian

The case of Quantum Electrodynamics (QED) will serve as a pedagogical illustration of the concept, since it constitutes a simple, yet non-trivial application of local gauge invariance. We consider a relativistic QFT with an internal, local $U(1)$ symmetry and the Lagrangian for free massive fermions, i.e. for a complex valued Dirac field ψ , that is given by

$$\mathcal{L}_{\text{Dirac}} = \bar{\psi}(i\not{\partial} - m)\psi. \quad (2.2)$$

Transformations under the internal $U(1)$ group are complex phase rotations, with a position dependent phase $\alpha(x)$.⁴ That is the symmetry transformations can be different on different points in space-time:

$$\psi(x) \rightarrow e^{i\alpha(x)}\psi(x), \quad \bar{\psi}(x) \rightarrow e^{-i\alpha(x)}\bar{\psi}(x). \quad (2.3)$$

Obviously, the mass term $m\bar{\psi}\psi$ in the Lagrangian is invariant under this transformation, since the conjugation leads to the cancellation of the α dependence.

However, as soon as we have terms with derivatives, we cannot naively apply this transformation and preserve the invariance of \mathcal{L} . The directional derivative with respect

³Historically, the correct gauge group for theories only developed over time, with the careful analysis of experimental data.

⁴If the function α is constant, one speaks of a global symmetry.

to a vector n^μ is defined as

$$n^\mu \partial_\mu \psi = \lim_{\epsilon \rightarrow 0} \frac{1}{\epsilon} [\psi(x + \epsilon n) - \psi(x)]. \quad (2.4)$$

It therefore relates the field at points x and $x + \epsilon n$, each of which has a different associated phase $\alpha(x)$ and $\alpha(x + \epsilon n)$ respectively, which in general breaks the invariance of \mathcal{L} under the gauge transformation. In the principle of *minimal replacement*, we replace ordinary derivatives with the covariant derivative

$$D_\mu \psi(x) = \partial_\mu \psi(x) + ieA_\mu \psi(x), \quad (2.5)$$

where the gauge field A^μ transforms as

$$A_\mu(x) \rightarrow A_\mu(x) - \frac{1}{e}\partial_\mu \alpha(x). \quad (2.6)$$

Using the transformation properties of A_μ and the field $\psi(x)$, we can now check that the covariant derivative indeed yields the desired transformation property

$$\begin{aligned} D_\mu \psi(x) &\rightarrow \left[\partial_\mu + ie \left(A_\mu - \frac{1}{e}\partial_\mu(\alpha) \right) \right] e^{i\alpha(x)} \psi(x) \\ &= e^{i\alpha(x)} (\partial_\mu + ieA_\mu) \psi(x) = e^{i\alpha(x)} D_\mu \psi(x). \end{aligned} \quad (2.7)$$

Promoting the partial derivative in Eq. (2.2) to a covariant derivative, we obtain a kinematic term $\bar{\psi} \not{D} \psi$ that is invariant under local $U(1)$ gauge transformations. The existence of the photon field A_μ is thus a consequence of the principle of local gauge invariance, if one considers the latter to be fundamental. To complete the construction, we also need a kinematical term for the photon field A_μ . Instead of deriving it, we check that the known form of the field-strength tensor is indeed gauge invariant under $U(1)$ transformations

$$F_{\mu\nu} = \partial_\mu A_\nu - \partial_\nu A_\mu \rightarrow \partial_\mu (A_\nu - \frac{1}{e}\partial_\nu \alpha) - \partial_\nu (A_\mu - \frac{1}{e}\partial_\mu \alpha) = F_{\mu\nu}. \quad (2.8)$$

As an aside, we can observe that $U(1)$ gauge invariance forbids a photon mass, since the combination $m^2 A^\mu A_\mu$ is not gauge invariant. This problem will resurface later, when the problem of assigning a mass to gauge bosons of other symmetry groups will motivate the concept of electroweak symmetry breaking and the introduction of the Higgs field.

Imposing the principle of local gauge invariance and the internal symmetry group $U(1)$ thus leads to the additional vector field A_μ , which through its coupling to fermions leads to the correct transformation properties of the Lagrangian. We will now extend this concept to more general gauge groups, in particular that of $SU(N)$ transformations, which will allow us to construct the Lagrangian of QCD and later the full SM.

Yang-Mills theory and the QCD Lagrangian

We now aim at generalizing the principle of local gauge invariance to other continuous internal symmetry groups, in particular to the special unitary group $SU(N)$ of degree N ,

the group of unitary $N \times N$ matrices with determinant 1. We arrange N fermions into an N -component object

$$\Psi(x) \equiv (\psi_1, \dots, \psi_N). \quad (2.9)$$

The field transformation is thus given by

$$\Psi(x) \rightarrow V(x)\Psi(x), \quad (2.10)$$

with $V(x)$ being a unitary $N \times N$ dimensional matrix. The elements $V(x)$ of a Lie group G can be written as $V(x) = \exp(i\alpha^a T^a)$, where T^a is a hermitian matrix in the case of $SU(N)$ and we sum over repeated indices a . Expanding this relation for infinitesimal transformations, we get

$$V(x) = 1 + i\alpha^a(x)T^a + \mathcal{O}(\alpha^2). \quad (2.11)$$

The hermitian matrices T^a are the generators of the Lie group. The associated simple Lie algebra is defined by the vector space spanned by the generators as well as the commutator relation between them

$$[T^a, T^b] = i\sqrt{2}f^{abc}T^c, \quad (2.12)$$

for $\text{Tr}(T^a T^b) = 1$. The completely anti-symmetric structure constants f^{abc} are a set of numbers. Symmetries with non-commuting transformations $V(x)$ ($f^{abc} \neq 0$) are called non-abelian whereas those with commuting transformations are called abelian ($f^{abc} = 0$). We now generalize the covariant derivative, cf. Eq. 2.5, to $SU(N)$ transformations. Lagrangians that are invariant under $SU(N)$ symmetry transformations can then be constructed by writing down all possible terms formed by fields and covariant derivatives thereof. The covariant derivative associated to the general transformation (2.10) is a generalization of Eq. (2.5)

$$D_\mu = \partial_\mu - igA_\mu^a T^a. \quad (2.13)$$

Each independent generator of the local symmetry thus implies one additional vector field. The infinitesimal transformation laws for the fields $\Psi(x)$ and A_μ^a are then analogously given by

$$\Psi(x) \rightarrow (1 + i\alpha^a(x)T^a + \mathcal{O}(\alpha^2))\Psi(x), \quad A_\mu^a \rightarrow A_\mu^a + \frac{1}{g}\partial_\mu\alpha^a + f^{abc}A_\mu^b\alpha^c, \quad (2.14)$$

where the last term in the transformation of the gauge field A_μ^a reflects the non-abelian properties of $SU(N)$ and reduces for $f^{abc} = 0$ to the abelian case. From these infinitesimal transformations, we can deduce the finite transformations of the gauge field

$$A_\mu^a(x)T^a \rightarrow V(x) \left[A_\mu^a T^a + \frac{i}{g}\partial_\mu \right] V^\dagger(x). \quad (2.15)$$

As for the $U(1)$ symmetry, the transformation properties of A_μ^a give the desired transformation properties of the covariant derivative, i.e. the covariant derivative has the same

transformation properties as the field Ψ itself. The field strength tensor for this group is

$$F_{\mu\nu}^a = \partial_\mu A_\nu^a - \partial_\nu A_\mu^a + g f^{abc} A_\mu^b A_\nu^c, \quad (2.16)$$

where the last term is related to the non-abelian nature of the gauge group. Note that the field-strength tensor for a non-abelian theory is no longer a gauge invariant quantity. Expressions containing the field-strength tensor with contracted indices however are gauge and Lorentz invariant and we can construct a so called Yang-Mills Lagrangian by

$$\mathcal{L}_{\text{YM}} = -\frac{1}{4} F_{\mu\nu}^a F^{a\mu\nu}, \quad (2.17)$$

with self-interacting gauge fields that form cubic and quartic terms in the field. Another important observation is that explicit mass terms are prohibited as they would violate $SU(N)$ gauge invariance, i.e. the pure gauge bosons are massless.

The theory based on the $SU(3)_C$ part of the SM gauge group is called Quantum Chromodynamics (QCD). It describes the strong force that is responsible for the binding of quarks into hadronic particles. For the purpose of this subsection, we treat QCD interaction independent from electroweak interactions. One can combine electroweak theory and QCD by adding up the non-overlapping Lagrangian terms. Quarks transform under $SU(3)$ in the three-dimensional fundamental representation **(3)** and are thus represented as color triplets

$$q = \begin{pmatrix} q_r \\ q_g \\ q_b \end{pmatrix}, \quad (2.18)$$

with the customary assignment of the colors red (r), green (g) and blue (b). The QCD Lagrangian is build from Eq. (2.2) for the quark field as well as Eq. (2.17) and reads

$$\mathcal{L}_{\text{QCD}} = -\frac{1}{4} F_{\mu\nu}^a F^{a,\mu\nu} + \sum_f \bar{q}_f (i \not{D} - m_f) q_f, \quad (2.19)$$

where the summation runs over all quark flavors f (see Sec. 2.1.3), the covariant derivative for $SU(3)$ is given in Eq. (2.13) and contractions with the four-dimensional Dirac matrices are denoted as $\not{D} \equiv D_\mu \gamma^\mu$. The eight generators of the fundamental representation of $SU(3)$ can be written in terms of the Gell-Mann matrices $T^a = \frac{\lambda^a}{\sqrt{2}}$ (explicit expressions can e.g. be found in [84]) and the associated self-interacting gauge fields are called gluons.

2.1.2. Electroweak Symmetry Breaking and GSW Theory

The unified description of weak interactions and electromagnetism in terms of a gauge theory is more subtle. It is known from experiment that the electroweak force is mediated by the massive W^\pm and Z vector bosons as well as the massless photon. In a theoretical description, both the problems of assigning a mass to the gauge fields as well as respecting perturbative unitarity bounds in gauge boson scattering were resolved by the postulation

of the Higgs mechanism⁵ in 1964 [87–90]. It is based on spontaneous symmetry breaking of the combination $SU(2)_W \times U(1)_Y$ of the SM gauge group and introduces an additional scalar field, the Higgs field. In 2012, both the ATLAS and CMS collaborations at the LHC succeeded in detecting this last missing and long-predicted ingredient of the SM, the Higgs boson [91, 92]. The gauge theory of the combined gauge group $SU(2)_W \times U(1)_Y$ is also referred to as the electroweak sector of the SM. In this subsection, we will briefly illustrate spontaneous symmetry breaking of a local symmetry and introduce the Higgs mechanism. We partly follow the description in Ref. [93].

Spontaneous symmetry breaking of a local continuous symmetry - an illustrative example

We will briefly present the Abelian Higgs model, where a local $U(1)$ gauge symmetry is spontaneously broken. The starting point is a given Lagrangian invariant under (local) gauge transformations of some group G . Two inequivalent situations exist regarding the ground state of a system governed by this Lagrangian. Either a unique state of lowest energy exists and is therefore invariant under group transformation. Or a set of degenerate, physically equivalent ground states exists, which transform into themselves under group transformation of G . If one of the states from this set is chosen as the ground state of the theory, the symmetry G is said to be spontaneously broken.

In the Abelian Higgs model, the Lagrangian of a complex scalar field is coupled to both an electromagnetic (gauge) field and itself

$$\mathcal{L} = -\frac{1}{4}(F_{\mu\nu})^2 + |D_\mu\phi|^2 - V(\phi), \quad (2.20)$$

with the covariant derivative $D_\mu = \partial_\mu + ieA_\mu$ and the square of the modulus denoted by $|\cdot|$. The Lagrangian is invariant under the transformations $\phi(x) \rightarrow e^{i\alpha(x)}\phi(x)$ for the scalar field and (2.6) (for the gauge field A_μ), i.e. under local $U(1)$ gauge transformations. We choose a potential of the form

$$V(\phi) = -\mu^2\phi^*\phi + \frac{\lambda}{2}(\phi^*\phi)^2, \quad (2.21)$$

with $\lambda > 0$, which can develop a local maximum. The lowest energy configuration of the field ϕ depends on the sign of the parameter μ^2 . If $\mu^2 < 0$, the state of lowest energy is $\phi_0 = 0$ and the symmetries of the Lagrangian are preserved by the ground state. If $\mu^2 > 0$, the field ϕ_0 whose value minimizes the potential is non-zero and fixed by the condition

$$\phi_{0,\alpha} = \sqrt{\frac{\mu^2}{\lambda}}e^{i\alpha}, \quad (2.22)$$

⁵Sometimes referred to as the *Englert-Brout-Higgs-Guralnik-Hagen-Kibble* [85, 86] mechanism of spontaneous symmetry breaking.

with a phase α . The field therefore acquires a non-zero vacuum-expectation value (vev) given by

$$\langle \phi \rangle \equiv \langle 0 | \phi | 0 \rangle = \phi_{0,\alpha} = \sqrt{\frac{\mu^2}{\lambda}} e^{i\alpha}. \quad (2.23)$$

The possible ground states are related by $U(1)$ symmetry transformations. Conversely, choosing one of the states in Eq. (2.23) as the vacuum state, the $U(1)$ symmetry is not obeyed anymore, it is said to be spontaneously broken. If we want to formulate a perturbation theory for $\mu^2 > 0$, we have to expand the scalar field around one of the ground states (2.23)⁶

$$\phi(x) = v + \frac{1}{\sqrt{2}} (h(x) + i\chi(x)), \quad (2.24)$$

and the scalar potential Eq. (2.21) then takes the form

$$V(\phi) = -\frac{1}{2\lambda}\mu^4 + \frac{1}{2}2\mu^2 h^2 + (\text{cubic and quartic terms}). \quad (2.25)$$

The real field h is referred to as the Higgs boson and acquires a mass $m = \sqrt{2}\mu$ and the massless real field χ is referred to as would-be Goldstone boson [94, 95], since the field would correspond to a Goldstone boson in an ungauged theory. We use the above expansion around the vev and obtain for the kinematic term of ϕ in Eq. (2.20)

$$|D_\mu \phi|^2 = \sum_{i=1}^2 \frac{1}{2} (\partial_\mu \phi_i)^2 + \sqrt{2}ev A_\mu \partial^\mu \chi + e^2 v^2 A_\mu A^\mu + (\text{cubic and quartic terms}). \quad (2.26)$$

Interestingly, the gauge field A_μ now has acquired a mass term

$$\mathcal{L} = \frac{1}{2}m_A^2 A^\mu A_\mu, \quad (2.27)$$

with a mass $m_A^2 = 2e^2v^2$ related to the vev of the scalar field. The interaction between A^μ and χ can be removed by a gauge transformation

$$A_\mu(x) \rightarrow A'_\mu = A_\mu - \frac{1}{\sqrt{2}ev} \partial_\mu \chi, \quad (2.28)$$

and the degree of freedom (d.o.f.) of the would-be Goldstone boson delivers the longitudinal polarization of the now massive gauge field. It becomes clear that such a transformation can always be found when considering the d.o.f. before and after spontaneous symmetry breaking. We started out with four d.o.f., since the massless gauge boson and complex scalar field contribute two d.o.f. each. After spontaneous symmetry breaking, the massive gauge boson has three d.o.f. and the real scalar field h one, adding up to four d.o.f..

⁶The fields corresponding to particles are linear in creation and annihilation operators and thus have a vanishing vev. Therefore only the combination $\psi = \phi - v$ allows for a particle interpretation.

The gauge field A_μ thus acquires its mass through the interaction with the vacuum expectation value v after spontaneous symmetry breaking. The scalar would-be Goldstone boson associated to the spontaneous symmetry breaking of a local gauge symmetry delivers the d.o.f. of the longitudinal polarization of the massive gauge boson. This mechanism is referred to as Higgs mechanism [87–90]. We will now move away from the illustrative example of the Abelian Higgs model and additionally require that the spectrum of gauge boson masses matches the one realized in nature.

The Gauge Part of Glashow-Weinberg-Salam Theory

In order to reproduce the known spectrum of gauge bosons masses one requires the spontaneous breaking of a non-abelian gauge symmetry. In fact it was the insight of Glashow, Weinberg and Salam [96–99] to break the combined symmetry of $SU(2)_W \times U(1)_Y$, which then leads to three massive gauge bosons (W^\pm, Z) compatible with the nowadays known mass spectrum and a residual $U(1)_{em}$ symmetry. The latter naturally describes electrodynamics with its massless gauge boson, the photon. We first describe the gauge part of the unified electroweak gauge theory, this is in analogy to Sec. 2.1.1.

The covariant derivative is given by

$$D_\mu = \partial_\mu + ig_2 I_W^a W_\mu^a + ig_1 \frac{Y_W}{2} B_\mu, \quad (2.29)$$

where we have introduced two independent couplings g_1 and g_2 , since we have two independent gauge groups $SU(2)_W$ and $U(1)_Y$. The generators of $SU(2)_W$ describing weak isospin are called I_W^a and can be represented in 2-dimensions by the Pauli matrices $I_W^a = \sigma^a/2$, the $U(1)_Y$ generator $\frac{Y_W}{2}$ is a real number called weak hypercharge. There are three massless gauge fields W_μ^a associated to the isospin generators and one massless gauge field B_μ associated to the hypercharge generator. The gauge part of the Lagrangian then obtains kinematic terms for all four gauge fields and is given by

$$\mathcal{L}_{\text{gauge}} = -\frac{1}{4} W_{\mu\nu}^a W^{a,\mu\nu} - \frac{1}{4} B_{\mu\nu} B^{\mu\nu}, \quad (2.30)$$

where the index a runs over the associated three generators I_W^a .

The Higgs Mechanism and W - and Z -boson masses

We now describe how the Higgs mechanism reconciles the experimental fact of non-vanishing W - and Z -boson masses with the massless gauge fields obtained from the unbroken gauge theory. We take the structure from above, i.e a $SU(2)_W \times U(1)_Y$ gauge group and the associated gauge fields, together with a scalar field Φ transforming as an $SU(2)$ doublet

$$\Phi = \begin{pmatrix} \phi^+ \\ \phi^0 \end{pmatrix}, \quad (2.31)$$

with weak hypercharge $Y_W = +1$. In total, the scalar field Φ has four d.o.f.. The gauge transformation of Φ then becomes

$$\Phi \rightarrow e^{i\alpha(x)^a I_W^a} e^{i\beta(x)/2} \Phi. \quad (2.32)$$

The Higgs Lagrangian is given by

$$\mathcal{L}_{\text{Higgs}} = (D_\mu \Phi)^\dagger (D^\mu \Phi) - V(\Phi), \quad V(\Phi) = -\mu^2 (\Phi^\dagger \Phi) + \frac{\lambda}{4} (\Phi^\dagger \Phi)^2, \quad (2.33)$$

such that the field Φ can acquire a non-vanishing vacuum expectation value for positive λ if $\mu^2 > 0$, determined by the condition

$$(\Phi_0^\dagger \Phi_0) = \frac{2\mu^2}{\lambda} \equiv \frac{v^2}{2}, \quad v = 2\sqrt{\frac{\mu^2}{\lambda}}. \quad (2.34)$$

The vacuum state is fixed up to a $U(2)$ rotation and conventionally the state

$$\langle \Phi \rangle \equiv \langle 0 | \Phi | 0 \rangle = \Phi_0 = \begin{pmatrix} 0 \\ \frac{v}{\sqrt{2}} \end{pmatrix}, \quad (2.35)$$

is chosen from the degenerate set of vacuum states. Only gauge transformations of Φ with $\alpha^1 = \alpha^2 = 0$ and $\alpha_3 = \beta$ leave the vacuum state invariant, since the only combination of generators that annihilates the vacuum is given by

$$\left(I_W^3 + \frac{Y_W}{2} \right) \langle \Phi \rangle = \left(\frac{\sigma^3}{2} + \frac{1}{2} \right) \begin{pmatrix} 0 \\ \frac{v}{\sqrt{2}} \end{pmatrix} = 0. \quad (2.36)$$

The Gell-Mann-Nishijima formula identifies this combination with the electric charge operator

$$Q \equiv I_W^3 + \frac{Y_W}{2}, \quad (2.37)$$

and it becomes clear that ϕ^+ carries charge $+e$ and ϕ^0 is neutral. Gauge transformations with the charge operator Q leave the vacuum state invariant

$$e^{iQ} \langle \Phi \rangle = (1 + Q + \dots) \langle \Phi \rangle = \langle \Phi \rangle, \quad (2.38)$$

where we used Eq. (2.36). The gauge group $SU(2)_W \times U(1)_Y$ is thus broken in such a way, that it still contains one unbroken $U(1)_{\text{em}}$ symmetry with the associated massless gauge field corresponding to the photon.

As in the abelian Higgs model, we expand the scalar field Φ around the vacuum expectation value, such that we get fields with vanishing vev

$$\Phi = \begin{pmatrix} \phi^+ \\ \frac{1}{\sqrt{2}} (v + H(x) + i\chi(x)) \end{pmatrix}, \quad (2.39)$$

where the real field $H(x)$ corresponds to the massive physical Higgs boson and the fields $\phi^+(x)$ and $\chi(x)$, which are complex and real fields respectively, correspond to would-be

Goldstone bosons. The three d.o.f. of the would-be Goldstone bosons are unphysical and can be transformed away in an appropriate gauge, c.f. discussion in the previous section on the Abelian Higgs model. To identify the physical gauge boson masses, we apply a transformation of the fields into mass and electric charge eigenstates, called W^\pm , Z and A , which are related to W^a and B through

$$\begin{pmatrix} Z_\mu \\ A_\mu \end{pmatrix} = \begin{pmatrix} c_W & -s_W \\ s_W & c_W \end{pmatrix} \begin{pmatrix} W_\mu^3 \\ B_\mu \end{pmatrix}, \quad W_\mu^\pm = \frac{1}{\sqrt{2}}(W_\mu^1 \mp iW_\mu^2), \quad (2.40)$$

with the weak mixing angle θ_W defined by

$$\cos \theta_W \equiv c_W = \frac{g_2}{\sqrt{g_1^2 + g_2^2}}, \quad \sin \theta_W = \sqrt{1 - c_W^2} = \frac{g_1}{\sqrt{g_1^2 + g_2^2}}. \quad (2.41)$$

Both linear combination W^\pm are mass degenerate eigenstates of $U(1)_{\text{em}}$, i.e. $QW_\mu^\pm = I_W^3 W_\mu^\pm = \pm W_\mu^\pm$. We then use Eq. (2.39) in the gauge where the would-be Goldstone bosons are transformed away and insert it into the Higgs Lagrangian Eq. (2.33). We can identify mass and charge eigenstates of Eq. (2.40) and get the following Higgs Lagrangian

$$\mathcal{L}_{\text{Higgs}} = \frac{1}{2}(\partial_\mu H)^2 + \left(\frac{g_2^2}{4} W_\mu^+ W^{-\mu} + \frac{g_2^2}{8c_W^2} Z_\mu Z^\mu + \frac{\mu^2}{2} - \frac{\lambda}{16}(v + H)^2 \right) (v + H)^2. \quad (2.42)$$

The terms bilinear in the fields W^\pm , Z and H correspond to mass terms of the corresponding bosons with masses M_W , M_Z and M_H , which we can identify in Eq. (2.42) as

$$M_W = \frac{vg_2}{2}, \quad M_Z = \frac{vg_2}{2c_W} = \frac{M_W}{c_W}, \quad M_H = \sqrt{2\mu^2}, \quad M_A = 0. \quad (2.43)$$

Thus, as in the previous example of the abelian Higgs model, the gauge fields acquire their mass through an interaction with the scalar field Φ after symmetry breaking. The field H corresponds to a neutral spin-0 particle of mass M_H . The Lagrangian in Eq. (2.42) allows for both three- and four-point interactions of the Higgs boson with a massive weak gauge boson $V = W, Z$. The HVV^\dagger interactions are proportional to M_V^2/v and $HHVV^\dagger$ interactions are proportional to M_V^2/v^2 , as can be seen from the factor $v^2(1 + H/v)^2$ multiplying the gauge boson mass terms. Furthermore, the Higgs fields is self-interacting with three- and four-point interactions proportional to M_H^2 . Before spontaneous symmetry breaking, we had four massless gauge bosons (8 d.o.f.) and a complex scalar doublet field Φ (4 d.o.f.), thus in total twelve d.o.f.. After spontaneous symmetry breaking, we are left with three massive gauge boson (9 d.o.f.), one massless gauge boson (2 d.o.f.), and the real Higgs field (1 d.o.f.), which adds up to twelve d.o.f. as it should.

In summary, we have seen how the spontaneous breaking of the unified gauge group $SU(2)_W \times U(1)_Y$ for the electroweak sector of the SM generated a vector boson spectrum that matches the observed one. Note, that this does not imply a prediction about the size of the mass, since it is given in terms of *a priori* unconstrained coupling parameters. To spontaneously break the symmetry, we had to introduce an additional scalar field. Expanding this field around its non-vanishing vacuum expectation value, we obtained the massive scalar Higgs field.

2.1.3. Matter Content of the Standard Model

We now discuss how the electroweak gauge bosons couple to fermions and how the latter acquire their mass in the SM. The fermionic part or matter content of the SM consists of leptons ($e, \nu_e, \mu, \nu_\mu, \tau, \nu_\tau$) and quarks (d, u, s, c, b, t). The leptons are subject to electromagnetic and weak interactions and the quarks additionally interact strongly⁷. Each fermion type comes in three generations. The gauge transformation properties inside a generation are identical but both mass and flavor differ in generations. The weak force is of chiral nature, i.e. it couples differently to particles depending on their chirality. With no compelling explanation of why this is the case, we proceed by describing how the SM accounts for it⁸.

Left- and right-handed spin- $\frac{1}{2}$ particles are defined via the chirality projector

$$P_{L/R} = (1 \mp \gamma_5)/2, \quad \Psi^{L/R} \equiv P_{L/R}\Psi, \quad (2.44)$$

with the matrix $\gamma_5 = i\gamma^0\gamma^1\gamma^2\gamma^3$. Left-handed fermions (leptons L and quarks Q) are grouped into pairs, weak isospin doublets, that transform under $SU(2)_W$ in the fundamental representation

$$\Psi_{lepton,i}^L \equiv L_i^L \equiv \begin{pmatrix} \nu_{i,L} \\ l_{i,L} \end{pmatrix}, \quad \Psi_{quark,i}^L \equiv Q_i^L \equiv \begin{pmatrix} u_{i,L} \\ d_{i,L} \end{pmatrix}, \quad (2.45)$$

where the index i is running over the three generations and the particles (ν, l) represent neutrinos and charged leptons respectively and (u, d) represent up- and down-type quarks. The residual symmetry generators of $SU(2)_W \times U(1)_Y$ are given by $Q = I_W^3 + \frac{Y_W}{2}$, see Eq. (2.37). Given the associated charge $I_W^3 = +\frac{1}{2}$ for $\nu_{i,L}, u_{i,L}$ and $I_W^3 = -\frac{1}{2}$ for $l_{i,L}, d_{i,L}$ respectively, the weak hypercharge Y_W is fixed such that the known electric charge values are recovered. Table 2.1 gives an overview of the SM matter fields and their charge assignments. Right-handed particles are uncharged under the weak interaction, i.e. are $SU(2)_W$ singlets. We thus have isospin singlets

$$\Psi_{l,i}^R \equiv l_{i,R}, \quad \Psi_{u,i}^R \equiv u_{i,R}, \quad \Psi_{d,i}^R \equiv d_{i,R}, \quad (2.46)$$

where the index i is again running over generations. Right-handed neutrinos are not charged under the SM gauge group and therefore do not interact with the SM gauge interactions. We stick to the original formulation of the SM in which right-handed neutrinos are omitted.

With the gauge transformation properties of the fermions established, we can now build the kinetic terms of the fermions in the Lagrangian. We promote the normal derivative in the free Dirac theory of massless fermions to the covariant derivative Eq. (2.29) and

⁷We will suppress the color charge index from $SU(3)_C$ in this section for clarity.

⁸Why the weak force is chiral in nature and why there are three generations of fermions remain outstanding problems in physics, an argument for the latter is presented in Ref. [100].

	generation			rep.	charges		
	1 st	2 nd	3 rd		I_W^3	Y_W	Q
quarks	L	$\begin{pmatrix} u \\ d \end{pmatrix}_L$	$\begin{pmatrix} c \\ s \end{pmatrix}_L$	$\begin{pmatrix} t \\ b \end{pmatrix}_L$	(3,2)	$\frac{1}{2}$	$\frac{1}{3}$
	R	u_R	c_R	t_R	(3,1)	$-\frac{1}{2}$	$\frac{1}{3}$
	R	d_R	s_R	b_R	(3,1)	0	$\frac{4}{3}$
	R					$-\frac{2}{3}$	$-\frac{1}{3}$
leptons	L	$\begin{pmatrix} \nu_e \\ e \end{pmatrix}_L$	$\begin{pmatrix} \nu_\mu \\ \mu \end{pmatrix}_L$	$\begin{pmatrix} \nu_\tau \\ \tau \end{pmatrix}_L$	(1,2)	$\frac{1}{2}$	-1
	R	e_R	μ_R	τ_R	(1,1)	$-\frac{1}{2}$	-1
	R					0	-2
	R						-1

Table 2.1.: Overview of the fermionic matter content of the SM. We show the three generations of quarks and leptons of different chirality (L, R). The representation in which the corresponding fields transform under the SM gauge group is shown in the format $(SU(3)_C, SU(2)_W)$. All fields transform as singlets under $U(1)_Y$. The electroweak charges I_W^3, Y_W and Q are specified in the last four columns. Table is adapted from [101].

obtain

$$\mathcal{L}_{\text{Fermion}} = \sum_{i=1}^3 (\bar{L}_i^L \not{D} L_i^L + \bar{Q}_i^L \not{D} Q_i^L + \bar{l}_i^R \not{D} l_i^R + \bar{u}_i^R \not{D} u_i^R + \bar{d}_i^R \not{D} d_i^R), \quad (2.47)$$

where we again suppress the color indices.

Fermion Masses

Direct and indirect observations show that all fermions are massive.⁹ However, an explicit formulation of mass terms such as Dirac mass terms $m(\bar{\Psi}^R \Psi^L + \bar{\Psi}^L \Psi^R)$ in the Lagrangian violates $SU(2)$ gauge invariance. They would mix the two chiralities of the fermion field which transform in different representations of $SU(2)$. Fermion masses can be consistently introduced through an indirect mechanism as in the case of electroweak gauge boson. Mass terms are generated by an interaction with the Higgs field, i.e. they are dynamically created and appear only after symmetry breaking. We mention that we work with the approximation of three massless neutrinos.

With the Higgs field introduced above, the most general gauge invariant Lagrangian contains a Yukawa coupling¹⁰ between the Higgs doublet and the chiral fermion fields for

⁹We work with the approximation of three massless neutrinos. However, the existence of three light neutrinos with distinct masses smaller 1 eV is implied by the experimentally well established mixing of three neutrino states.

¹⁰A Yukawa coupling is an interaction between a scalar field and a Dirac field of the type $g\bar{\Psi}\phi\Psi$.

leptons and quarks, that is

$$\mathcal{L}_{\text{Yukawa}} = - \sum_{i,j=1}^3 \left(\bar{L}_i^L G_{ij}^l l_j^R \Phi + \bar{Q}_i^L G_{ij}^u u_j^R \tilde{\Phi} + \bar{Q}_i^L G_{ij}^d d_j^R \Phi + \text{h.c.} \right), \quad (2.48)$$

where the field $\tilde{\Phi} = (\phi^{0*}, -\phi^-)^T$ is the charge conjugate of the scalar field Φ , with $\phi^- = (\phi^+)^*$. The field $\tilde{\Phi}$ transforms under the fundamental representation of $SU(2)$ with hypercharge $Y_W = -1$. Note that all terms in $\mathcal{L}_{\text{Yukawa}}$ are invariant under transformations of the SM gauge group Eq. (2.1). The Yukawa interaction matrices G_{ij}^f ($f = l, u, d$) are 3×3 matrices in generation space. The fields written above are in the flavor basis of left- and right-handed fields, therefore the Yukawa matrices do not have to be diagonal. The non-diagonal elements of G_{ij}^f mix fermions of type f from different generations. Since the fields Φ and $\tilde{\Phi}$ contain a constant piece proportional to the vev v , $\mathcal{L}_{\text{Yukawa}}$ contains mass terms for the fermion fields. A diagonalization of the matrices G_{ij}^f is achieved by the unitary transformations

$$\hat{f}_i^L = \sum_{j=1}^3 U_{ij}^{f,L} f_j^L, \quad \hat{f}_i^R = \sum_{j=1}^3 U_{ij}^{f,R} f_j^R, \quad (2.49)$$

where f denotes the fermion type $f = l, u, d$. The mass terms of the fermion fields in the new mass basis (denoted by a hat) become transparent and are related to the Higgs vev

$$U^{f,L} G^f (U^{f,R})^\dagger = \frac{\sqrt{2}}{v} \begin{pmatrix} m_{f',1} & 0 & 0 \\ 0 & m_{f',2} & 0 \\ 0 & 0 & m_{f',3} \end{pmatrix}, \quad (2.50)$$

with fermion masses $m_{f,i}$. The Yukawa part of the Lagrangian thus takes on the simple form

$$\mathcal{L}_{\text{Yukawa}} = - \sum_{f,i} m_{f,i} (\bar{f}_i^L f_i^R + \bar{f}_i^R f_i^L) \left(1 + \frac{H}{v} \right), \quad (2.51)$$

with the summation running over the three generations i and fermion types $f = l, u, d$ and the gauge in which the would-be Goldstone bosons are absent is used. The Yukawa coupling between fermions and the Higgs field is thus proportional to $m_{f,i}/v$. The field redefinitions of Eq. (2.49) have several effects on the SM Lagrangian. Fermion fields are replaced by those in the mass basis (and the hat notation is conventionally dropped), the Yukawa coupling matrices are replaced with their diagonal form Eq. (2.50) and charged-current interactions receive a modification from the matrices U , whereas neutral current interactions remain unchanged since they do not mix up- and down-type quarks. The interaction of W^1 and W^2 with quarks via the covariant derivative Eq. (2.29) was given in (2.47). Since σ^1 and σ^2 are off-diagonal, W^1 and W^2 do connect u - and d -type quarks of one generation. The transformations in Eq. (2.49) now imprint a non-diagonal mixing across generations in the W -coupling matrix. The matrix parameterizing this mixing is

called the Cabibbo-Kobayashi-Maskawa [102, 103] (CKM) matrix¹¹ and connected to the mass eigenstate transformation by

$$V_{\text{CKM}} \equiv U^{u,L} (U^{d,L})^\dagger. \quad (2.52)$$

In summary, we have seen some of the underlying concepts of the SM. In particular, we saw how Lagrangians are constructed out of the SM gauge group and how masses for both electroweak gauge bosons as well as fermions are generated via the Higgs interactions and spontaneous symmetry breaking. We can now collect all the pieces that make up the SM Lagrangian¹² and obtain by using Eqs. (2.19),(2.30),(2.33),(2.47) and (2.48)

$$\begin{aligned} \mathcal{L}_{\text{SM}} &= \mathcal{L}_{\text{QCD}} + \mathcal{L}_{\text{EW}} \\ &= \mathcal{L}_{\text{QCD}} + \mathcal{L}_{\text{gauge}} + \mathcal{L}_{\text{Higgs}} + \mathcal{L}_{\text{Fermion,EW}} + \mathcal{L}_{\text{Yukawa}}. \end{aligned} \quad (2.53)$$

2.1.4. QCD Quantization and Gauge Fixing

We briefly illustrate the concept of quantization and the associated gauge fixing in the case of QCD. For the more involved case of electroweak theory, we refer to the literature e.g. [104]. If we perform the quantization by following the path-integral formulation, all gauge field configurations are considered

$$\int \mathcal{D}A_\mu^a \exp \left\{ i \int d^4x \mathcal{L}_{\text{YM}} \right\}, \quad (2.54)$$

including those related by gauge transformations. In order to avoid the overcounting of physically identical configurations that are gauge-equivalent, we pick out a specific one which is achieved by adding a gauge fixing term to the Lagrangian

$$\mathcal{L}_{\text{fix}} = \frac{1}{2\xi} (\partial^\mu A_\mu^a)(\partial^\nu A_\nu^a), \quad (2.55)$$

as well as the Faddeev-Popov term

$$\mathcal{L}_{\text{ghost}} = -\bar{c}^\alpha \partial^\mu D_\mu^{\alpha\beta} c^\beta, \quad (2.56)$$

with the covariant derivative in the adjoint representation $D_\mu^{\alpha\beta}$, $\alpha, \beta = 1, \dots, 8$. The ghosts from the Faddeev-Popov Lagrangian contribute to loop amplitudes. In an application of the unitarity method, where at least one loop momentum is forced on the physical mass-shell, unphysical degrees of freedom directly cancel against the ghosts and explicit gauge fixing can be omitted when working with physical polarization states in the loop. Therefore, we omit ghost fields for the rest of this thesis.

¹¹In the approximation of three massless neutrinos, the left-handed neutrino fields are transformed by the same unitary matrix as their charged counterparts and the analogous neutrino mixing matrix, called Pontecorvo-Maki-Nakagawa-Sakata (PMNS) matrix, can be transformed away by field redefinitions.

¹²We suppress CP violating terms of gauge fields such as the θ_{FF} term.

2.1.5. The S -Matrix in Perturbation Theory

S -matrix elements are transition amplitudes between asymptotic initial and final states. The states are approximate momentum eigenstates $|i\rangle$ at some early time before or after interaction $t = \pm\infty$ when the particles were freely moving. One can decompose S -matrix elements and isolate the non-trivial part due to interactions \mathcal{M}_{fi} by

$$\langle f|S|i\rangle = \langle f|i\rangle + (2\pi)^4 \delta^{(4)}(p_i - p_f) \cdot i\mathcal{M}_{fi}, \quad (2.57)$$

where four-momentum conservation between initial and final states is ensured by the corresponding delta function. The interpretation of the absolute square of S -matrix elements corresponds to the probability of scattering between initial and final state. The reduction formula due to Lehmann-Symanzik-Zimmermann (LSZ) [105] relates the S -matrix elements to the Fourier transformed correlation functions $\tilde{G}(p_1, \dots, p_n)$ of the theory. For scalar fields, we get the following relation for the computation of S -matrix elements

$$\langle f|S|i\rangle \simeq \left(\prod_{k=1}^n \sqrt{Z_{\phi_k}} \right) \tilde{G}(p_1, \dots, p_n)|_{\text{truncated}} \quad (2.58)$$

where we used the definition of the field-strength renormalization constants Z_ϕ to obtain the truncated correlation or Green function. For particles with spin, the corresponding wave functions have to be included in the above expression. In the context of the renormalization procedure described in Chapter 6 the field-strength renormalization constants are accounted for. In general, the Green function in an interacting theory is only accessible in a perturbative expansion, which can be organized diagrammatically in terms of Feynman diagrams. Feynman diagrams consist of propagators, vertices and external wave functions. Only connected and amputated Feynman diagrams contribute, that is no corrections to external lines are computed. The color-ordered Feynman rules of QCD are listed in Appendix B. More details on the LSZ formula and perturbation theory as well as the Feynman rules of the full SM can be found for example in [84, 104].

2.2. Hadronic Collisions - The Realm of Perturbative QCD

Below a certain energy scale, the strongly interacting quarks and gluons form bound states, so called *hadrons*. This property of QCD is known as *confinement*. It is associated to the fact that the strength of the coupling between colored objects increases if the energy scale μ of the interaction decreases, the so called running of the strong coupling $\alpha_s(\mu)$. Quarks and gluons can thus not be directly detected in scattering experiments, which are performed with hadrons in the initial and final state configuration. The theoretical description of hadron collisions is elaborate, since composite and not fundamental objects are colliding¹³. At high energy scales μ attained at hadron colliders such as the LHC, the strong coupling $\alpha_s(\mu)$ becomes small and the elementary constituents of hadrons, quarks

¹³Compare this to an e^+e^- -collider, where elementary objects are colliding.

and gluons, can be seen as *asymptotically free*. We are in particular interested in studying the interaction of these elementary objects as described by the SM.

A full description of high-energetic hadron collisions therefore requires a prescription to embed the interaction of the elementary constituents into the scattering reaction of the external hadrons. The parton model [106] does so and decomposes hadrons into point-like constituents, the partons. For protons these elementary constituents are quarks (q), anti-quarks (\bar{q}) and gluons (g). *Hard scattering* processes with more than a few GeV typically probe distances below the proton radius and therefore can be understood as collisions between partons. They can be described in terms of perturbation theory and thereby allow for quantitative theoretical predictions. In this section, we will give a brief overview of hadron-hadron collisions and show how the treatment of the partonic cross section in perturbative QCD (pQCD) is embedded in the description of hadron collisions.

2.2.1. Running coupling

The QCD $\beta(\alpha_s)$ -function captures the dynamical behavior of the strong coupling α_S as a function of the energy scale μ . It is given in one-loop approximation obtained in the $\overline{\text{MS}}$ renormalization scheme by

$$\beta(\alpha_S^{\overline{\text{MS}}}) = \mu^2 \frac{d}{d\mu^2} \frac{\alpha_S^{\overline{\text{MS}}}(\mu)}{\pi} = -\frac{1}{4} \left[\frac{11N_C - 2n_f}{3} \right] \left(\frac{\alpha_S^{\overline{\text{MS}}}(\mu)}{\pi^2} \right)^2, \quad (2.59)$$

where N_C denotes the number of colors and n_f the number of massless quark flavors. For the SM values of $N_C = 3$ and $n_f = 5$ ¹⁴ the beta function is negative and the strong coupling decreases with increasing energy. Knowing the coupling at some scale $\alpha_s^{\overline{\text{MS}}}(\mu_0)$, the β -function allows to deduce the coupling at another scale by

$$\alpha_s^{\overline{\text{MS}}}(\mu_1) = \frac{\alpha_s^{\overline{\text{MS}}}(\mu_0)}{1 + \frac{\alpha_s^{\overline{\text{MS}}}(\mu_0)}{\pi} \beta_0 \ln\left(\frac{\mu_1}{\mu_0}\right)}, \quad (2.60)$$

where $\beta_0 = \frac{11N_C - 2n_f}{3}$. The consequences of this running of the QCD coupling are profound. At high energies μ QCD becomes an almost free theory and perturbative calculations of hard scattering cross sections are possible. However, if the coupling approaches unity perturbative calculations are not possible anymore. The parameter Λ_{QCD} is the scale below which one is surely in the non-perturbative regime¹⁵ and is defined as the scale at which the coupling formally diverges. The modeling of LHC collisions thus has to account for confined initial and final hadronic matter detected in the experiment as well as the quasi free gluons and quarks at high scales appearing at high momentum transfer collisions. There is no first-principle understanding of the transition between confined and free regime. Quantitative calculations require a prescription to identify the partonic hard scattering cross-section in hadron collisions, which is the topic of the next subsection.

¹⁴Or $n_f = 6$ at very high energies

¹⁵ $\Lambda_{QCD} \approx 210$ MeV assuming $n_f = 5$ quark flavors [107].

2.2.2. Factorization and Partonic Cross Sections

At a hadron-hadron collider, such as the LHC, the cross section for a hard scattering process $H_1 + H_2 \rightarrow X$ factorizes in the high-energy limit as

$$\begin{aligned} \sigma_{H_1 H_2}(P_1, P_2) &= \sum_{i,j} \int_0^1 dx_1 \int_0^1 dx_2 f_{i/H_1}(x_1, \mu_F^2) f_{j/H_2}(x_2, \mu_F^2) \hat{\sigma}_{ij \rightarrow X}(x_1 P_1, x_2 P_2, \mu_R^2, \mu_F^2) \\ &\quad + \mathcal{O}\left(\frac{s}{\Lambda_{QCD}}\right), \end{aligned} \quad (2.61)$$

where the two initial hadrons (protons in the case of the LHC) have momenta P_1 and P_2 respectively. The sum runs over all contributing initial state partons q , \bar{q} and g , i.e. partonic sub-processes. The initial state partons involved in the hard scattering cross section $\hat{\sigma}_{ij \rightarrow X}$ carry momentum fractions $p_1 = x_1 P_1$ and $p_2 = x_2 P_2$, with partonic quantities such as $\hat{\sigma}$ denoted by a hat. The PDF $f_{i/H_1}(x_1, \mu_F)$ gives the probability of parton i to carry the momentum fraction x_1 of initial hadron H_1 's momentum P_1 . The total partonic energy is thus given by $\hat{s} = x_1 x_2 s$, i.e. a fraction of the total squared hadronic center-of-mass energy $s = (P_1 + P_2)^2$ for near light-like hadron momenta P_i . Truncating the series expansion of the partonic cross section in the strong coupling leads to the explicit dependence on renormalization and factorization scales μ_R^2 and μ_F^2 in the above expression.

For the scope of this thesis, we assume that the scale μ associated to the hard process is much larger than Λ_{QCD} . Roughly speaking, factorization means that for energies larger than Λ_{QCD} , the internal binding structure of the hadron can be neglected and the partonic sub-channels factorize, i.e. can be treated independently. The factorization scale μ_F then describes the scale below which interactions between partons are absorbed into the PDFs. The factorization ansatz of Eq. (2.61) is fundamental in order to obtain quantitative pQCD prediction that can be compared to experimental scattering data from LHC. It allows to use a power series expansion of the partonic cross-section in the coupling α_S , denoting the coefficients as leading-order (LO), next-to-leading order (NLO), next-to-next-to-leading order (NNLO) and so on. The cross-section to NLO accuracy in the strong coupling α_S is thus given by

$$\begin{aligned} \sigma_{H_1 H_2}^{\text{NLO}}(P_1, P_2) &= \sum_{i,j} \int_0^1 dx_1 \int_0^1 dx_2 f_{i/H_1}^{\text{NLO}}(x_1, \mu_F^2) f_{j/H_2}^{\text{NLO}}(x_2, \mu_F^2) \\ &\quad \times [\hat{\sigma}_{ij \rightarrow X}^0(p_1, p_2, \mu_R^2) + \hat{\sigma}_{ij \rightarrow X}^{\text{NLO}}(p_1, p_2, \mu_R^2, \mu_F^2)], \end{aligned} \quad (2.62)$$

with the momenta p_1 and p_2 defined as above. The partonic cross-section to NLO accuracy in the strong coupling α_S contains both virtual loop corrections $d\sigma_V$ and real-emission corrections $d\sigma_R$, from the radiation of an additional parton. For a process involving n final state partons, it can be written as

$$\hat{\sigma}^{\text{NLO}} = \int_n d\sigma_V + \int_{n+1} d\sigma_R, \quad (2.63)$$

where real-emission corrections are integrated over the correspondingly larger phase-space. The virtual corrections are defined to be renormalized, all appearing parameters are con-

nected to physical quantities and the appearing ultraviolet (UV) divergencies are canceled by the inclusion of appropriate counter-terms. In Chapter 6, more details on this are provided. Furthermore, both virtual and real-emission corrections contain infrared (IR) divergencies. There are two sources for IR divergencies: soft and collinear divergencies. In virtual contributions, they occur in the loop integration for situations where the loop-momentum is either softer than the external momenta or becomes collinear with one of the external momenta. They can be studied systematically with the Landau equations [108] that give the necessary condition for IR divergencies in loop integrations. In real-emission corrections $d\sigma_R$, collinear splitting configurations and soft emissions of another parton lead to IR divergencies in the phase-space integration. The IR divergencies of virtual and real corrections are closely related. For inclusive enough observables, the IR divergencies cancel in the sum of the two contributions according to the Kinoshita-Lee-Nauenberg (KLN) theorem [109, 110]. In the hadronic cross-section defined in Eq. (2.62), collinear divergencies from initial-state splittings are absorbed into the PDF definition which gives rise to the factorization scale μ_F . Only after these parts attributed to long-distance physics are removed does the quantity in Eq. (2.62) become an IR-safe observable. Comparable to the discussion in the previous subsection 2.2.1, the requirement that any dependence on μ_F must drop out when considering results to all orders in perturbation theory leads to the Dokshitzer-Gribov-Lipatov-Altarelli-Parisi [111–113] (DGLAP) PDF evolution equation.

2.2.3. Collimated Collection of Hadronic Particles - a Jet

We have not yet discussed the final state X of Eq. (2.61), in particular the transition from partons to measurable particles and their detection¹⁶. We employ the concept of hadronic jets to get a well-defined but yet manageable description of this transition. In particular, we require that it captures the key properties of the hard scattering, and thereby allows inference about the fundamental building blocks of nature.

A hadronic jet is a collimated bundle of hadronic particles, whose energy and momentum can be measured in a detector. The crucial point is that low-energetic non-perturbative effects in QCD mostly decouple from the hard scattering. On a perturbative level, the reason for this decoupling lies in a spectrum of bremsstrahlung that is logarithmically enhanced for low-angle radiation. Also the running strong coupling α_S increases at lower energies and thereby enhances low-angle and low-energy radiation. The subsequent hadronization does not change this picture strongly, since the transverse momentum transfer is limited by the hadronization scale of about $\Lambda_{QCD} \sim 200$ MeV. The partonic modeling of decreasing energy scales, in particular the multiple emission of partons in soft and collinear regions, is done by parton showers, for a detailed explanation see [114]. As a consequence, high-energetic partons first fragment into a collimated jet of partons and after hadronization, into a jet of particles, carrying energy and momentum of the initial parton. Therefore, instead of looking at the detailed production of particles, it mostly suffices to measure the properties of jets to infer information about the perturbatively defined hard-scattering and in particular the partonic cross-section.

¹⁶As we have seen in Sec. 2.2.1, the running of the strong coupling α_S leads to a breakdown of the perturbative description below a certain energy.

In order to compare experimental data and theoretical predictions, an unambiguous definition of what constitutes a jet is required. Several jet-algorithms exist [115–120] and the LHC collaborations most widely use the infrared and collinear safe¹⁷ anti- k_T algorithm [120]. It is based on a sequential recombination procedure of the final state objects, that is an iterative combination of the closest pairs of objects, with a given jet size parameter ΔR . For the phenomenological work done in this theses, we will use the anti- k_T algorithm.

Jets With Flavor

The predictions for $Wb\bar{b}$ production presented later in this thesis require a b -jet algorithm, i.e. the possibility to distinguish jets according to the flavor of the parton they were originating from. Experimental b -jet tagging algorithms are lifetime-based, i.e. they exploit the fact that b hadrons typically decay inside the detector whilst their relatively long lifetime allows to identify a secondary vertex displaced from the point of the hard scattering in the corresponding jet. A technical description of b -jet tagging algorithms and their implementation in the ATLAS experiment can be found in [74]. Throughout this thesis, we distinguish b -jets and jets, where the latter stem from light partons.

¹⁷A measured jet variable is infrared safe if it does not change under the emission of a soft $E_T \rightarrow 0$ parton or when the parton splits into collinear partons.

Part 1:

Methods and Tools

CHAPTER 3

Color Decomposition

NLO QCD predictions require the computation of virtual one-loop corrections. They appear as interference terms of n -parton loop amplitudes $\mathcal{A}_n^{1\text{-loop}}$ with n -parton tree level contributions $\mathcal{A}_n^{\text{tree}}$

$$\sum_{c,h} 2 \operatorname{Re} \{ \mathcal{A}_n^{\text{tree}*} \mathcal{A}_n^{1\text{-loop}} \}, \quad (3.1)$$

summed over color (c) and helicity (h) of the involved partons. We handle the dynamical degrees of freedom of color and kinematics separately, which has several advantages. A fixed cyclic ordering of external particles results in less kinematical invariants for each color-ordered amplitude and thereby makes the analytic structure more transparent, which was in particular relevant for the development of unitarity methods. In numerical approaches, the smaller building blocks allow for a fine-grained numerical precision monitoring and control. Furthermore, using a color decomposition allows for an expansion of the virtual cross-section in powers of $1/N_C$, which gives a significant speedup for the numerical phase space integration. The typically smaller subleading-color contributions have to be evaluated on fewer phase space points in order to reach the same overall integration error.

In order to disentangle kinematical and color degrees of freedom of QCD one-loop amplitudes, we apply a trace-based color decomposition [121]. As a result, we can express one-loop amplitudes as the product of color factors and purely kinematic functions, so called partial amplitudes. At one-loop, partial amplitudes are further decomposed into the basic building blocks of gauge-invariant primitive amplitudes [11, 122] with a fixed cyclic ordering of external particles. The handling of color is independent of whether the involved quarks are massless or massive, which is of particular relevance for our application. It allows us to use an existing algorithm to obtain the color decomposition of one-loop amplitudes involving multiple quark lines as described in Ref. [123]. This algorithm has been successfully applied to massless high-multiplicity processes involving an electroweak gauge boson [2, 3, 13].

3.1. Partial Amplitudes

The vertices of QCD Feynman rules are equipped with either fundamental generators $(T^a)_i^j$ or structure constants f^{abc} , where the indices of quarks are given by $\{i, j, \dots\}$ and those of anti-quarks by $\{\bar{i}, \bar{j}, \dots\}$. In order to treat both fundamental and adjoint color indices on the same footing, we rewrite the structure constants f^{abc} appearing in gluon

interactions in terms of the fundamental representation $(T^a)_i^{\bar{j}}$ using

$$f^{abc} = -\frac{i}{\sqrt{2}} \text{Tr} ([T^a, T^b] T^c). \quad (3.2)$$

with $\text{Tr}(T^a T^b) = \delta^{ab}$ such that $T^a = \frac{\lambda^a}{\sqrt{2}}$. Whenever contracted adjoint indices appear, we can apply the $SU(N_c)$ Fierz identity

$$\sum_a (T^a)_i^{\bar{j}} (T^a)_k^{\bar{l}} = \delta_i^{\bar{l}} \delta_k^{\bar{j}} - \frac{1}{N_c} \delta_i^{\bar{j}} \delta_k^{\bar{l}}, \quad (3.3)$$

and thereby reduce the possible forms of appearing color factors. They are constructed out of powers of N_C , traces of generators $\text{Tr}(T^a T^b \dots T^n)$, strings of generators with open fundamental indices $(T^a T^b \dots T^n)_i^{\bar{j}}$ and Kronecker delta functions $\delta_i^{\bar{j}}$. Here the gauge group parameter N_C is left unspecified and can be set to $N_C = 3$ for physical QCD predictions. A *partial amplitude* is defined as the kinematic terms multiplying a specific color structure, by which we mean a combination of color generators. The generic expression for amplitudes involving up to six-quarks can be found in [123]. As an example, for a two-quark amplitude at tree level, we have

$$\mathcal{A}_n^{\text{tree}}(1_q, 2_{\bar{q}}, 3, \dots, n) = \sum_{\sigma \in S_{n-2}} (T^{a_{\sigma(3)}} \dots T^{a_{\sigma(n)}})_{i_1}^{\bar{j}_2} A_n^{\text{tree}}(1_q, \sigma(3), \dots, \sigma(n), 2_{\bar{q}}), \quad (3.4)$$

where the coupling can be thought of as included in A_n^{tree} and we sum over all permutations S_{n-2} of the $n - 2$ gluons labels appearing in the partial tree amplitudes A_n^{tree} . The permutations in σ are also used for the mapping of the adjoint gluonic color indices. Note that for clarity, we suppress both helicity and color indices of the involved particles in the expressions for the amplitudes $\mathcal{A}_n^{\text{tree}}$. The color-decomposition of the corresponding one-loop amplitude additionally contains traces of fundamental generators and is given by

$$\begin{aligned} \mathcal{A}_n^{\text{1-loop}}(1_q, 2_{\bar{q}}, 3, \dots, n) = & \\ & \sum_{j=1}^{n-1} \sum_{\sigma \in \mathcal{P}} \text{Gr}_{2;n-2;j}(\sigma) A_{n;j}(\sigma(3), \dots, \sigma(j+1); 1_q, \sigma(j+2), \dots, \sigma(n), 2_{\bar{q}}), \end{aligned} \quad (3.5)$$

with the following color-structure groupings

$$\text{Gr}_{2;n-2;j}(\sigma) = \text{Tr}(T^{a_{\sigma(3)}} \dots T^{a_{\sigma(j+1)}}) (T^{a_{\sigma(j+2)}} \dots T^{a_{\sigma(n)}})_{i_1}^{\bar{j}_2}. \quad (3.6)$$

The combined sum in Eq. (3.5) runs over all distinct color structures: the outer sum over all different group theoretical factors and the inner sum over independent gluon orderings $\mathcal{P} = S_{n-2}/S_{n-2;j}$ that leave the trace in Eq. (3.6) invariant. As an explicit example, the one-loop color decomposition of $\mathcal{A}_4^{\text{1-loop}}(1_q, 2_{\bar{q}}, 3_g, 4_g)$ in terms of partial amplitudes yields

$$\begin{aligned} \mathcal{A}_4^{\text{1-loop}}(1_q, 2_{\bar{q}}, 3_g, 4_g) = & (T^3 T^4)_{i_1}^{\bar{i}_2} A_{4;1}^{\text{1-loop}}(1_q, 3_g, 4_g, 2_{\bar{q}}) + (T^4 T^3)_{i_1}^{\bar{i}_2} A_{4;1}^{\text{1-loop}}(1_q, 4_g, 3_g, 2_{\bar{q}}) \\ & + \text{Tr}(T^3 T^4) \delta_{i_1}^{\bar{i}_2} A_{4;3}^{\text{1-loop}}(3_g, 4_g; 1_q, 2_{\bar{q}}), \end{aligned} \quad (3.7)$$

where we have used the conventions $(T^a T^b \dots T^n)_i^j \rightarrow \delta_i^j$ for $n = 0$ and $\text{Tr}(T^a T^b \dots T^n) \rightarrow 1$ for $n = 0$ as well as the property $\text{Tr}(T^a) = 0$. The first list of particles in front of the semicolon is omitted if the color trace contribution is absent.

3.2. Primitive Amplitudes

Partial amplitudes can be further decomposed into gauge invariant, color-ordered basic building blocks, so called *primitive amplitudes* [122], with a fixed cyclic ordering of external legs. All partial amplitudes can be expressed by the set of primitive amplitudes of a given process. Since primitive amplitudes can contribute to several partial amplitudes, a caching mechanism for the primitives is appropriate. Explicit examples of how to generate the set of primitives and their relations to the partial amplitudes can be found in [11, 122], with a general algorithm of how to obtain them given in [123]. The Feynman rules used for the computation of amplitudes have to be changed due to our replacements (cf Eqs. (3.2) and (3.3)). The color-ordered Feynman rules can for example be found in [121] and in Appendix B.

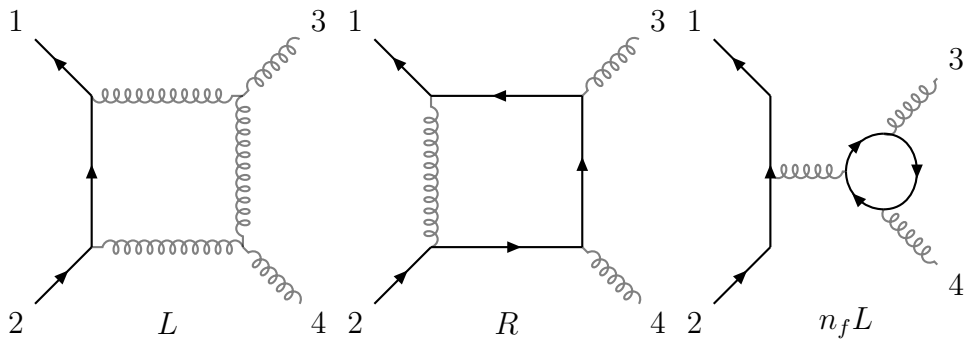


Figure 3.1: Primitive amplitudes are represented by parent diagrams specified by a routing label for the fermion lines. Here we show the parent diagrams that contribute to the partial amplitude $A_{4;1}^{\text{1-loop}}(1_q, 3_g, 4_g, 2_{\bar{q}})$, that is left-turner (L), right turner (R) and closed fermion loop with the line passing to the left of the loop ($n_f L$).

We represent primitive amplitudes by *parent diagrams*, that is color-ordered Feynman diagrams with the maximal number of loop propagators. Additionally, the routing of each fermion line which can either appear as a left- (L) or right-turner (R) or as a closed fermion loop (n_f), has to be specified. Amplitudes with multiple fermion lines therefore have multiple routing labels. As an explicit example, we give the decomposition of the partial amplitudes $A_{4;1}^{\text{1-loop}}(1_q, 3_g, 4_g, 2_{\bar{q}})$ and $A_{4;3}^{\text{1-loop}}(3_g, 4_g; 1_q, 2_{\bar{q}})$ which appeared in the color decomposition in Eq. (3.7), in terms of primitive amplitudes

$$A_{4;1}^{\text{1-loop}}(1_q, 3_g, 4_g, 2_{\bar{q}}) = N_c A^{[L]}(1_q, 3_g, 4_g, 2_{\bar{q}}) - \frac{1}{N_c} A^{[R]}(1_q, 3_g, 4_g, 2_{\bar{q}}) + n_f A^{[n_f L]}(1_q, 3_g, 4_g, 2_{\bar{q}}). \quad (3.8)$$

The right hand side is written in terms of primitive amplitudes only, where the superscripts $[L]$, $[R]$ and $[n_f]$ specify the quark routing in the primitive amplitude. The $[n_f]$ primitive contains contributions from both light flavors and heavy flavors turning in the loop and the external quark line passes to the left ($n_f L$) of the closed loop. In Fig. 3.1, we show the graphical representation of the parent diagrams contributing to this partial amplitude. The other partial amplitude in Eq. (3.7) can be decomposed as

$$A_{4;3}^{\text{1-loop}}(3_g, 4_g; 1_q, 2_{\bar{q}}) = \sum_{P(3,4)} (A^{[L]}(1_q, 3_g, 4_g, 2_{\bar{q}}) + A^{[L]}(1_q, 3_g, 2_{\bar{q}}, 4_g) + A^{[L]}(1_q, 2_{\bar{q}}, 3_g, 4_g)), \quad (3.9)$$

where we sum over the two permutations of gluon labels.

For more general topologies, we apply the decomposition algorithm presented in [123], which is applicable to massive quarks. By using symmetry properties amongst the primitive amplitudes, one can further reduce the number of fundamental building blocks that have to be computed. In computations with massive fermions, care has to be taken because not all symmetry properties of massless quarks hold for massive ones as well.¹

3.3. Assembly of Virtual Matrix Elements

In order to obtain the full virtual cross-section $d\sigma_V$, we need to interfere tree- and loop-level amplitudes as noted in Eq. (3.1). Therefore, open fundamental indices of tree and loop color factors are contracted and the resulting color factors are made up of products of traces of generators with repeated adjoint indices stemming from both tree and loop contributions. We then use the Fierz identity, Eq. (3.3), on the repeated adjoint indices

$$\begin{aligned} \text{Tr}(T^a T^a) &= (T^a)_j^{\bar{i}} (T^a)_i^{\bar{j}} = \delta_i^{\bar{i}} \delta_j^{\bar{j}} - \frac{1}{N_C} \delta_j^{\bar{i}} \delta_i^{\bar{j}} = N_C^2 - 1 \\ \text{Tr}(T^a A T^a B) &= \text{Tr}(A) \text{Tr}(B) - \frac{1}{N_C} \text{Tr}(AB), \end{aligned} \quad (3.10)$$

where A and B are products of generators. Therefore, the color factors reduce to positive and negative powers of N_C that multiply the products of tree and one-loop partial amplitudes.

For the *assembly* of virtual matrix elements, that is multiplying tree and one-loop partial amplitudes with the corresponding color factors, we use the approach of previous work [2, 3, 13, 123]. The color-decomposition therefore has to be done only once. For the remainder of this thesis, we work with color-ordered primitive amplitudes with a fixed cyclic ordering of external legs.

¹For example, the reversal of a fermion's arrow (cf. Eq. (2.23) in [123]) does not lead to a flip of the routing label for massive quark lines.

CHAPTER 4

Numerical Unitarity With Massive Quarks

In the following two chapters, we present a variant of the D -dimensional numerical unitarity method [11, 24, 30, 31, 33] applied to QCD one-loop amplitudes with massive quark pairs. Unitarity methods are based on both analyticity and unitarity of one-loop scattering amplitudes. Analyticity allows to reconstruct amplitudes as a function of kinematical invariants and mass parameters while unitarity guarantees that residues at the singular points factorize into tree amplitudes. The term numerical here refers to the variant of the unitarity approach suitable for numerical evaluation as opposed to analytic computations. Numerical unitarity with massless particles has been successfully applied at one loop to high-multiplicity processes [2, 3, 124] and recently using the techniques described in [41] also to the four- and five gluon amplitude at two loops [42, 43]. Nevertheless, implementations of unitarity with massive external and internal particles remain few. Analytic formulae have been obtained for $Wb\bar{b}$ [26] and $t\bar{t}$ production [27] and a numerical approach was applied to on-shell $t\bar{t}(+1 \text{ jet})$ production [28, 125]. The work presented in this thesis applies the method of numerical unitarity to high-multiplicity processes with massive quark flavors. In Chapter 9, we will for the first time present phenomenological results for $Wb\bar{b} + 2$ and 3 light jets using the here described methods. This is possible through a combination of the methods of numerical unitarity [30, 32, 33], together with an important extension of the algorithm, which concerns the careful treatment of internal and external polarization states in dimensional regularization. All details presented here have been implemented in C++ libraries which are the basis for a new version of the `BlackHat` library [32]. We overview the aspects of numerical unitarity most relevant for this thesis, and more details can be found in the reviews [126, 127] and references therein. The next Chapter 5, is devoted to the way we compute unitarity cuts in D -dimensions with massive particles.

4.1. Preliminaries

4.1.1. A Generic One-Loop Amplitude in D -Dimensions

We need to regularize one-loop amplitudes to keep track of divergencies. Following the approach of dimensional regularization, we move away from $D = 4$ dimensional space-time and continue momenta and polarization vectors of loop particles to $D \neq 4$ -dimensional space time. Without specifying *how* to choose the space-time dimensionality for the moment, we can write any generic n -particle one-loop amplitude in D -dimensional space-

time as

$$A_n^{\text{1-loop}} \sim \int \frac{d^D \ell}{(2\pi)^D} \frac{\mathcal{N}(p_1, p_2, \dots, p_N; \ell)}{D_1 D_2 \dots D_N}, \quad (4.1)$$

with the numerator function \mathcal{N} depending on the momenta of the external particles as well as on the loop momenta ℓ . The inverse propagators

$$D_i = (\ell_i^2 - m_i^2) = ((\ell + q_i)^2 - m_i^2) = \left((\ell + \sum_{j=1}^i p_j - q_0)^2 - m_i^2 \right), \quad (4.2)$$

build up the denominator, see Fig. 4.1, with region momenta q_i defined up to an arbitrary shift q_0 . All external momenta are defined to be outgoing throughout this thesis.

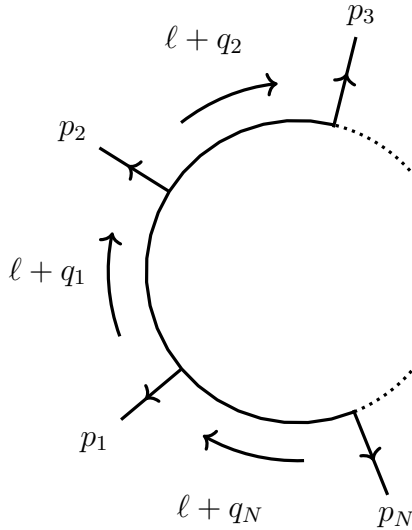


Figure 4.1: A generic one-loop amplitude, with region momenta q_i defined up to a shift q_0 . The momenta of all external particles are defined to be outgoing.

4.1.2. Dimensional Regularization

In dimensional regularization, we set

$$D \equiv 4 - 2\epsilon, \quad (4.3)$$

which results in a representation of the UV and IR divergent integrals in terms of poles in $1/\epsilon^n$. The final results we provide are regularized in the standard 't Hooft-Veltman scheme (HV) [128]¹. For intermediate calculations however, we employ the four-dimensional helicity scheme (FDH)², in which results are related to the HV scheme by a finite shift that we apply at the end of our calculation (cf. Sec. 6.5). For the purpose of this chapter, it suffices to define D -dimensional loop momenta ℓ and a decomposition into a 4-dimensional part

¹Here $D_s = D$. For more on dimensional regularization schemes, see Sec. 5.1.1.

²Here, we set $D_s = 4$ after performing the algebra of Dirac matrices.

and an orthogonal $(D - 4)$ -dimensional part [25], which we refer to as higher-dimensional part, defined by

$$\ell_{[D]}^\mu = \ell_{[4]}^\mu + \ell_{[D-4]}^\mu, \quad (4.4)$$

with $\ell_{[4]} \cdot \ell_{[D-4]} = 0$. The corresponding on-shell conditions read

$$\begin{aligned} \ell_{[D]}^2 &= \ell_{[4]}^2 + \ell_{[D-4]}^2 = m^2 \\ &= \ell_{[4]}^2 - \mu^2 = m^2, \end{aligned} \quad (4.5)$$

with the invariant mass of the higher-dimensional part $\ell_{[D-4]}^\mu$ conventionally named $\ell_{[D-4]}^2 = -\mu^2$. In FDH, external momenta are kept in $D = 4$ and contractions of those with the higher-dimensional part of the loop momentum are zero $\ell_{[D-4]} \cdot p_{i[4]} = 0$, i.e. there is no preferred direction in the $(D - 4)$ subspace of the D -dimensional momenta. Thus the only dependence of the numerator function \mathcal{N} in Eq. (4.1) on the higher dimensional part of the loop momentum comes through contractions of the form

$$\ell_{[D-4]}^2 = -\mu^2. \quad (4.6)$$

In particular, this implies a rotational invariance in the higher-dimensional subspace of the loop momenta in the integration since only the absolute square of it enters the numerator function³. For numerical purposes, we require finite dimensional representations of both metric tensor and Dirac algebra in order to compute one-loop amplitudes in FDH. This is the topic of Chapter 5.

4.1.3. Exploiting Unitarity as a Computational Method

The unitarity approach builds on the observation that integrands of one-loop amplitudes $A_n^{1\text{-loop}}(\ell)$ factorize into products of tree amplitudes in the factorization or on-shell limit:

$$\begin{aligned} \text{Res}_{i_1 \dots i_k} [A_n^{1\text{-loop}}(\ell)] &\equiv \lim_{\ell \rightarrow \ell_{i_1 \dots i_k}} (D_{i_1} \dots D_{i_k} A_n^{1\text{-loop}}(\ell)) \\ &= \sum_{\text{states}} (A_{n_1}^{\text{tree}}(\ell_k, \dots, -\ell_1) \times \dots \times A_{n_k}^{\text{tree}}(\ell_{k-1}, \dots, -\ell_k)), \end{aligned} \quad (4.7)$$

where the set of propagator momenta $\ell_{i_1 \dots i_k} = \{\ell_{i_1}, \dots, \ell_{i_k}\}$ in the loop simultaneously solves the on-shell conditions for the inverse propagators

$$D_{i_1}(\ell_{i_1}) = \dots = D_{i_k}(\ell_{i_k}) = 0. \quad (4.8)$$

The propagator momenta are thereby restricted to the on-shell phase spaces and the sum runs over the states associated to the full spectrum of the theory for each on-shell momentum. The systematic application of these unitarity cuts allows a computation of the coefficients of the expansion of one-loop amplitudes in terms of master integrals, as we will see in the following sections. The above is connected to the unitarity of the S -matrix, as worked out in [129].

³If one chooses a formulation in integer dimensions it thus suffices to use a 5-dimensional loop momentum

4.1.4. Master Integrals

Any one-loop amplitude in D -dimensional space time can be written as a sum of scalar master integrals [130–133]

$$A_n^{\text{1-loop}} = \sum_i \tilde{e}_i I_5^i + \sum_i \tilde{d}_i I_4^i + \sum_i \tilde{c}_i I_3^i + \sum_i \tilde{b}_i I_2^i + \sum_i \tilde{a}_i I_1^i, \quad (4.9)$$

where the summation runs over all scalar integral functions of the corresponding topology, and I_5, I_4, I_3, I_2, I_1 - pentagon, box, triangle, bubble and tadpole integrals respectively - are known. The pentagon functions I_5 can be expressed in terms of lower point functions $I_{n < 5}$ in one-loop computations, however, we require pentagon integrands and keep pentagons in intermediate steps of the computation. The master integrals on the right-hand side of Eq. (4.9) are defined as

$$I_n^i = \frac{\mu^{2\epsilon}}{ic_\Gamma} \int \frac{d^D \ell}{(2\pi)^D} \frac{1}{D_{i_1} D_{i_2} \dots D_{i_n}}, \quad (4.10)$$

with $c_\Gamma = (4\pi)^{-(2-\epsilon)} \Gamma^2(1-\epsilon)\Gamma(1+\epsilon)/\Gamma(1-2\epsilon)$. In the following, we suppress the prefactor appearing in the integrals for simplicity. A set of the IR and / or collinearly divergent scalar integrals for general masses can for example be found in [134]. Compared to a computation with massless external particles, the basis we employ contains more integrals. These are integrals with massive internal propagators as well as a new topology, the tadpole integral I_1 . For massless particles, the latter is scaleless and vanishes in dimensional regularization.

The extraction of the coefficients for the tadpole integral and the bubble integral with a single massive leg in one corner I_{2,m^2} , see Fig. 4.2, require a special treatment in the unitarity method. This is the topic of Section 4.4. Explicit formulae for these two integrals can be found in App. C.

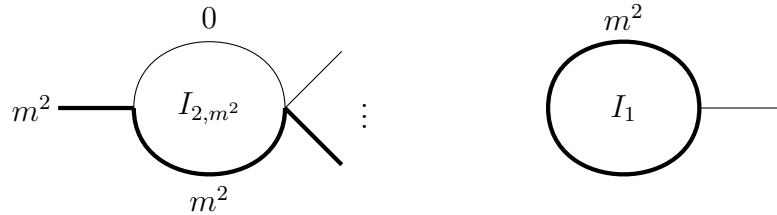


Figure 4.2: The extraction of the coefficients for the additional scalar integrals I_{2,m^2} and I_1 require a special treatment in the unitarity method. Thick lines refer to loop momenta with $\ell^2 = m^2$.

The number of inflow momenta for each integral in the basis of scalar master integrals is bounded from above by the space-time dimensionality D . Since we take external momenta and polarization vectors to be four dimensional, we maximally include a five-point function, the pentagon. Any higher-point function can be reduced to this set of integral functions. The knowledge of the coefficients $\tilde{e}_i, \tilde{d}_i, \tilde{c}_i, \tilde{b}_i, \tilde{a}_i$ completely defines the one-loop amplitude.

4.2. The Loop Integrand

We consider loop amplitudes before integration, that is the integrand of (4.1). In the construction due to OPP [29] and Ellis, Giele, Kunszt and Melnikov (EGKM) [30, 31], the generic expression for the integrand of a D -dimensional one-loop amplitude is

$$\begin{aligned} A_n^{\text{1-loop}}(\ell) \equiv \frac{\mathcal{N}(\ell)}{D_1 \dots D_n} = & \sum_{1 \leq i_1 < \dots < i_5 \leq n} \frac{\Delta_{i_1 i_2 i_3 i_4 i_5}^5(\ell)}{D_{i_1} D_{i_2} D_{i_3} D_{i_4} D_{i_5}} + \sum_{1 \leq i_1 < \dots < i_4 \leq n} \frac{\Delta_{i_1 i_2 i_3 i_4}^4(\ell)}{D_{i_1} D_{i_2} D_{i_3} D_{i_4}} \\ & + \sum_{1 \leq i_1 < \dots < i_3 \leq n} \frac{\Delta_{i_1 i_2 i_3}^3(\ell)}{D_{i_1} D_{i_2} D_{i_3}} + \sum_{1 \leq i_1 < \dots < i_2 \leq n} \frac{\Delta_{i_1 i_2}^2(\ell)}{D_{i_1} D_{i_2}} + \sum_{1 \leq i_1 \leq n} \frac{\Delta_{i_1}^1(\ell)}{D_{i_1}}, \end{aligned} \quad (4.11)$$

where inverse propagators are defined in Eq. (4.2). We suppress the dependence of the numerator tensors $\Delta^i(\ell)$ on external particles and polarization states. As a next step, we want to find a suitable parameterization of the numerator tensors $\Delta^i(\ell)$. It should satisfy the following criteria: all possible tensor insertions up to a certain rank should be covered and it should be easy to relate the basis to the coefficients $\tilde{e}_i, \tilde{d}_i, \tilde{c}_i, \tilde{b}_i, \tilde{a}_i$ of the scalar master integral decomposition (cf. Eq. 4.9). Such a basis of possible tensors can be found using the van Neerven - Vermaseren construction (NV) [132], for more detail see also App. A. In the NV construction, the D -dimensional space-time is decomposed into a physical space, spanned by the linearly independent external momenta flowing into the parent diagram, and its complement, the transverse space. The vectors n_i form an orthonormal basis that spans the space transverse to the physical momenta, $p_i \cdot n_j = 0$ and $n_i \cdot n_j = \delta_{ij}$. Together with the external momenta p_i the n_i form a basis of the four dimensional momentum space.

A suitable numerator parameterization for D -dimensional one-loop amplitudes involving massive particles is given by [30, 33]

$$\begin{aligned} \Delta_{i_1 i_2 i_3 i_4 i_5}^5(\ell) &= e_{i_1 i_2 i_3 i_4 i_5}^0 \mu^2 \\ \Delta_{i_1 i_2 i_3 i_4}^4(\ell) &= d_{i_1 i_2 i_3 i_4}^0 + d_{i_1 i_2 i_3 i_4}^1 t_1 \\ &+ (d_{i_1 i_2 i_3 i_4}^2 + d_{i_1 i_2 i_3 i_4}^3 t_1) \mu^2 + d_{i_1 i_2 i_3 i_4}^4 \mu^4 \\ \Delta_{i_1 i_2 i_3}^3(\ell) &= c_{i_1 i_2 i_3}^0 + c_{i_1 i_2 i_3}^1 t_1 + c_{i_1 i_2 i_3}^2 t_2 + c_{i_1 i_2 i_3}^3 (t_1^2 - t_2^2) \\ &+ t_1 t_2 (c_{i_1 i_2 i_3}^4 + c_{i_1 i_2 i_3}^5 t_1 + c_{i_1 i_2 i_3}^6 t_2) \\ &+ (c_{i_1 i_2 i_3}^7 t_1 + c_{i_1 i_2 i_3}^8 t_2 + c_{i_1 i_2 i_3}^9) \mu^2 \\ \Delta_{i_1 i_2}^2(\ell) &= b_{i_1 i_2}^0 + b_{i_1 i_2}^1 t_1 + b_{i_1 i_2}^2 t_2 + b_{i_1 i_2}^3 t_3 + b_{i_1 i_2}^4 (t_1^2 - t_3^2) \\ &+ b_{i_1 i_2}^5 (t_2^2 - t_3^2) + b_{i_1 i_2}^6 t_2 t_3 + b_{i_1 i_2}^7 t_1 t_2 + b_{i_1 i_2}^8 t_1 t_3 \\ &+ b_{i_1 i_2}^9 \mu^2 \\ \Delta_{i_1}^1(\ell) &= a_{i_1}^0 + a_{i_1}^1 t_1 + a_{i_1}^2 t_2 + a_{i_1}^3 t_3 + a_{i_1}^4 t_4, \end{aligned} \quad (4.12)$$

where $t_i = (n_i \cdot \ell)$. The terms μ^2 are the extra dimensional scalar product of the loop momentum and originate in a split-up of the loop momentum into four and $(D - 4)$ -dimensional part (cf. Eqs. (4.4) and (4.5)).

The terms in Eq. (4.12) that contain projections of the loop momentum into the transverse space integrate to zero (spurious terms). Lorentz-invariance⁴ restricts the possible results of the integration to tensors formed by external momenta p_i^μ and metric tensors $g^{\mu\nu}$. The contraction of the resulting tensor with any symmetric tensor of transverse basis vectors therefore yields a vanishing result. As an explicit example, we can integrate the spurious part of the box numerator $\Delta_{1234}^4(\ell)$ over a 4-dimensional loop momentum ℓ^μ ($\mu^2 = 0$) and get

$$\int \frac{d^4\ell}{(2\pi)^4} \frac{t_1}{D_1 D_2 D_3 D_4} = \int \frac{d^4\ell}{(2\pi)^4} \frac{\ell \cdot n_1}{D_1 D_2 D_3 D_4} \sim T(p_i) \cdot n_1 = 0, \quad (4.13)$$

with the tensor $T^\mu(p_i)$ being formed by linear combinations of external momenta. Since the transverse vectors are orthogonal to the physical space, the scalar product of $T^\mu(p_i)$ with the transverse vector n_1^μ must vanish. A similar reasoning holds for general tensors, see e.g. [126]. The remaining terms of the basis in Eq. (4.12) either plainly multiply scalar master integrals or scalar integrals with μ^n insertions, which we will treat later. The above basis is therefore naturally connected to the basis of scalar master integrals Eq. (4.9).

It remains to justify, why the above parameterization in Eq. (4.12) covers all possible tensor insertions. The tensors with components pointing along the physical space are dispensable. They lead to integrands of lower-point and scalar integrands as can be seen from the simplest case of

$$\ell \cdot q_2 = \frac{1}{2} (\ell^2 - (\ell - q_2)^2 + q_2^2) = \frac{1}{2} (D_1 - D_2 + q_2^2). \quad (4.14)$$

Inserting this numerator into the integrand, the inverse propagators cancel and we get

$$\frac{\ell \cdot q_2}{D_1 D_2 D_3 \cdots D_n} = \frac{1}{2} \left(\frac{1}{D_2 D_3 \cdots D_n} - \frac{1}{D_1 D_3 \cdots D_n} + \frac{q_2^2}{D_1 D_2 D_3 \cdots D_n} \right), \quad (4.15)$$

with lower-point integrands and a scalar integrand. The Passarino-Veltman reduction algorithm [131] exploits the above, namely that at one-loop, every scalar product of loop and external momenta can be expressed as a combination of propagators.

In consequence, the numerator tensors can only have components pointing along the transverse direction. Out of those, only a subset is linearly independent. As an example, the box numerator tensor could contain terms of the form

$$\Delta_{i_1 i_2 i_3 i_4}^4(\ell) = \cdots + \ell^\mu \ell^\nu n_{1\mu} n_{1\nu} + \ell^\mu \ell^\nu \ell^\rho n_{1\mu} n_{1\nu} n_{1\rho} + \cdots, \quad (4.16)$$

where the maximal rank of the tensor in Standard Model processes is equal to the number of inverse propagators in the diagram. Each of the above terms can be rewritten using the projection of the metric tensor into the transverse space (cf. App. A , Eq. (A.4)). The

⁴And parity invariance to exclude the epsilon tensor.

terms then have the following form

$$\ell^\mu \ell^\nu n_{1\mu} n_{1\nu} = \ell^2 - \sum_{i=1}^3 (\ell \cdot p_i)(\ell \cdot v_i), \quad (4.17)$$

where v_i are the so called dual vectors (see Appendix A) and the above terms contain inverse propagators and projections of the loop momentum onto the physical space $\ell \cdot p_i$. The latter again reduce, as in Eq. (4.15), to lower-point and scalar integrands. With the projection of the metric into the transverse space, one obtains an additional constraint on the numerator tensors for each topology. The number of tensors in the numerator of each topology is then determined by power counting and the additional constraint from the projection of the trace into the transverse space.

With the parameterization of Eq. (4.12), the integration over the loop momentum, and thereby the connection to the basis of master integrals, can be trivially performed. As an example, we do get for the integration over the box numerator in D -dimensions

$$\begin{aligned} \int \frac{d^D \ell}{(2\pi)^D} \frac{\Delta_{ijkl}^4(\ell)}{D_i D_j D_k D_l} &= \int \frac{d^D \ell}{(2\pi)^D} \frac{d_{ijkl}^0 + d_{ijkl}^1 t_1 + (d_{ijkl}^2 + d_{ijkl}^3 t_1) \mu^2 + d_{ijkl}^4 \mu^4}{D_i D_j D_k D_l} \\ &= \int \frac{d^D \ell}{(2\pi)^D} \frac{d_{ijkl}^0 + d_{ijkl}^2 \mu^2 + d_{ijkl}^4 \mu^4}{D_i D_j D_k D_l} \\ &= d_{ijkl}^0 I_{4,ijkl} + d_{ijkl}^2 I_{4,ijkl}[\mu^2] + d_{ijkl}^4 I_{4,ijkl}[\mu^4], \end{aligned} \quad (4.18)$$

where $I[\mu^2]$ denotes an insertions of μ^2 from the higher-dimensional part of the loop momentum.

By splitting the integration into the 4 and $D - 4$ -dimensional part, one can rewrite scalar master integrals with μ^2 insertions in terms of higher dimensional scalar integrals [31, 135] (see also appendix of [25])

$$\begin{aligned} I_{i\dots j}^{(D)}[\mu^2] &= \int \frac{d^D \ell}{(2\pi)^D} \frac{\mu^2}{D_i \dots D_j} = -\frac{(D-4)}{2} I_{i\dots j}^{(D+2)}[1] \\ I_{i\dots j}^{(D)}[\mu^4] &= \int \frac{d^D \ell}{(2\pi)^D} \frac{\mu^4}{D_i \dots D_j} = \frac{(D-4)(D-2)}{4} I_{i\dots j}^{(D+4)}[1]. \end{aligned} \quad (4.19)$$

With the identities in Eq. (4.19), different choices for the tensor basis are possible. We use the specific form of the pentagon numerator $\Delta^5(\ell)$ given in [135]. It is obtained by a dimensional shift identity on the D -dimensional scalar pentagon. As a result, one gets a μ^2 insertion on the pentagon numerator and a contribution to the scalar box coefficient, which we already absorbed into the coefficient d^0 . In total, we thus have five non-vanishing integrals with μ^2 insertions. They are multiplied by the coefficients e^0, d^2, d^4, c^9, b^9 . The six-dimensional scalar box and pentagon integrals are finite [133]. The integrals therefore

do not contribute to the amplitude in the limit $D = 4 - 2\epsilon \rightarrow 4$

$$\begin{aligned} \lim_{D \rightarrow 4} \frac{(D-4)}{2} I_{4,ijkl}^{(6)}[1] &= 0 \\ \lim_{D \rightarrow 4} \frac{(D-4)}{2} I_{5,ijklm}^{(6)}[1] &= 0. \end{aligned} \tag{4.20}$$

The 6-dimensional 2-point and 3-point as well as the 8-dimensional 4-point scalar integrals are UV divergent. Each of those integrals is multiplied by a factor $(D-4)$, cf. Eq. (4.19), that cancels the pole $1/\epsilon$. Therefore, these integrals produce finite, ϵ -independent contributions that are given by

$$\begin{aligned} \lim_{D \rightarrow 4} I_{4,ijkl}^{(D)}[\mu^4] &= \lim_{D \rightarrow 4} \frac{(D-4)(D-2)}{4} I_{4,ijkl}^{(D+4)}[1] \rightarrow -\frac{1}{6} \\ \lim_{D \rightarrow 4} I_{3,ijk}^{(D)}[\mu^2] &= \lim_{D \rightarrow 4} -\frac{(D-4)}{2} I_{3,ijk}^{(D+2)}[1] \rightarrow -\frac{1}{2} \\ \lim_{D \rightarrow 4} I_{2,ij}^{(D)}[\mu^2] &= \lim_{D \rightarrow 4} -\frac{(D-4)}{2} I_{2,ij}^{(D+2)}[1] \rightarrow \frac{(q_i - q_j)^2}{6} - \frac{m_i^2 + m_j^2}{2}, \end{aligned} \tag{4.21}$$

where we used Eq. (4.19). Historically, one splits one-loop amplitudes into a *cut constructable* part and a *rational* part when doing unitarity calculations [22, 23]. However, in this thesis we adopt the general D -dimensional picture as used in the relations in this section. Rational terms are generated by multiplying higher order terms (in ϵ) of the coefficients with the integrals, producing finite contributions. In a calculation in $D = 4$, all $\mathcal{O}(\epsilon)$ terms in the expansion of the coefficients are set to zero and the rational part cannot be reconstructed. The non-vanishing finite contributions to the rational part of one-loop amplitudes are given by the integrals in Eq. (4.21) multiplied by the corresponding coefficients and can only be reconstructed by D -dimensional unitarity cuts.

The $D = 4 - 2\epsilon$ -dimensional representation of the one-loop amplitude is thus given by

$$\begin{aligned} A_n^{\text{1-loop}} &= \sum_{1 \leq i_1 < \dots < i_4 \leq n} \left(d_{i_1 i_2 i_3 i_4}^0 I_{4,i_1 i_2 i_3 i_4}[1] - \frac{d_{i_1 i_2 i_3 i_4}^4}{6} \right) \\ &\quad + \sum_{1 \leq i_1 < \dots < i_3 \leq n} \left(c_{i_1 i_2 i_3}^0 I_{3,i_1 i_2 i_3}[1] - \frac{c_{i_1 i_2 i_3}^9}{2} \right) \\ &\quad + \sum_{1 \leq i_1 < \dots < i_2 \leq n} \left(b_{i_1 i_2}^0 I_{2,i_1 i_2}[1] + \left(\frac{(q_{i_1} - q_{i_2})^2}{6} - \frac{m_{i_1}^2 + m_{i_2}^2}{2} \right) b_{i_1 i_2}^9 \right) \\ &\quad + \sum_{1 \leq i_1 \leq n} a_{i_1}^0 I_{1,i_1} + \mathcal{O}(\epsilon), \end{aligned} \tag{4.22}$$

where we eliminated all vanishing integrals (cf. Eq. (4.20)). Furthermore, we used the explicit expressions in Eq. (4.21) for the non-vanishing integrals with μ^2 insertions. The rational coefficients $d_i^0, d_i^4, c_i^0, c_i^9, b_i^0, b_i^9, a_i^0$ are multiplying box, triangle, bubble and tadpole scalar integrals respectively and are functions of the external kinematics. Knowing these coefficients is tantamount to having computed the full color-ordered one-loop amplitude. The coefficients multiplying spurious numerator terms are relevant only at intermediate steps. Also those with μ^2 insertions with vanishing integrals in the limit $D = 4 - 2\epsilon$ do

not contribute to the final result, like the pentagon coefficient e^0 and the box coefficient d^2 , but are nevertheless needed for a consistent computation. We will next see how the systematic application of multiple unitarity cuts allows to determine all tensor coefficients and thereby reconstruct the full one-loop amplitude.

4.3. Generalized Unitarity Method

We employ the numerical unitarity method, which is based on a prescription of how to reconstruct the full one-loop amplitude by the consecutive application of pentuple, quadruple, triple, double and single cuts [11, 24]. We apply cuts at the level of the integrand of a one-loop amplitude, with the numerator parameterization given in Eq. (4.12). Central to this is the behavior of the one-loop integrand in the factorization limit of Eq. (4.7), i.e. it factorizes into the product of tree amplitudes. The numerator tensors $\Delta^i(\ell)$ in Eq. (4.12), are then given in terms of residues of multi-particle unitarity cuts, by

$$\begin{aligned}
 \Delta_{i_1 i_2 i_3 i_4 i_5}^5(\ell_{i_1 \dots i_5}) &= \text{Res}_{i_1 i_2 i_3 i_4 i_5} [A_n^{\text{1-loop}}(\ell_{i_1 \dots i_5})] , \\
 \Delta_{i_1 i_2 i_3 i_4}^4(\ell_{i_1 \dots i_4}) &= \text{Res}_{i_1 i_2 i_3 i_4} [A_n^{\text{1-loop}}(\ell_{i_1 \dots i_4})] - \sum_{j \neq i_1, i_2, i_3, i_4} \frac{\Delta_{i_1 i_2 i_3 i_4 j}^5(\ell_{i_1 \dots i_4})}{D_j} , \\
 \Delta_{i_1 i_2 i_3}^3(\ell_{i_1 \dots i_3}) &= \text{Res}_{i_1 i_2 i_3} [A_n^{\text{1-loop}}(\ell_{i_1 \dots i_3})] - \sum_{j \neq i_1, i_2, i_3} \frac{\Delta_{i_1 i_2 i_3 j}^4(\ell_{i_1 \dots i_3})}{D_j} \\
 &\quad - \sum_{\substack{j, k \neq i_1, i_2, i_3 \\ j < k}} \frac{\Delta_{i_1 i_2 i_3 j k}^5(\ell_{i_1 \dots i_3})}{D_j D_k} , \\
 \Delta_{i_1 i_2}^2(\ell_{i_1 i_2}) &= \text{Res}_{i_1 i_2} [A_n^{\text{1-loop}}(\ell_{i_1 i_2})] - \sum_{j \neq i_1, i_2} \frac{\Delta_{i_1 i_2 j}^3(\ell_{i_1 i_2})}{D_j} \tag{4.23} \\
 &\quad - \sum_{\substack{j, k \neq i_1, i_2 \\ j < k}} \frac{\Delta_{i_1 i_2 j k}^4(\ell_{i_1 i_2})}{D_j D_k} - \sum_{\substack{j, k, m \neq i_1, i_2 \\ j < k < m}} \frac{\Delta_{i_1 i_2 j k m}^5(\ell_{i_1 i_2})}{D_j D_k D_m} , \\
 \Delta_{i_1}^1(\ell_{i_1}) &= \text{Res}_{i_1} [A_n^{\text{1-loop}}(\ell_{i_1})] - \sum_{j \neq i_1} \frac{\Delta_{i_1 j}^2(\ell_{i_1})}{D_j} - \sum_{\substack{j, k \neq i_1 \\ j < k}} \frac{\Delta_{i_1 j k}^3(\ell_{i_1})}{D_j D_k} \\
 &\quad - \sum_{\substack{j, k, m \neq i_1 \\ j < k < m}} \frac{\Delta_{i_1 j k m}^4(\ell_{i_1})}{D_j D_k D_m} - \sum_{\substack{j, k, m, n \neq i_1 \\ j < k < m < n}} \frac{\Delta_{i_1 j k m n}^5(\ell_{i_1})}{D_j D_k D_m D_n} .
 \end{aligned}$$

The above equations are evaluated for a set of on-shell propagator momenta $\ell_{i_1 \dots i_k}$ as defined in Eq. (4.8). In order to isolate the contribution to a coefficient Δ^i from Eq. (4.23), care has to be taken to correctly subtract the contributions from topologies with more loop propagators to each residue. For example, the residue $\text{Res}_{i_1 i_2 i_3 i_4} [A_n^{\text{1-loop}}(\ell_{i_1 \dots i_4})]$ contains contributions from five-point topologies, that have to be subtracted. These *subtractions* rely on a hierarchical dependency between all topologies contributing to a specific primitive amplitude represented by a parent diagram. One can build the hierarchical de-

pendence by considering all possibilities of *pinching* propagators of a parent diagram. As an explicit example of Eq. (4.23), we give some of the numerators of a 4-point amplitude in terms of the residues and subtractions from higher point topologies⁵

$$\begin{aligned}\Delta_{1234}^4(\ell_{1234}) &= \text{Res}_{1234} [A_n^{\text{1-loop}}(\ell_{1234})] , \\ \Delta_{234}^3(\ell_{234}) &= \text{Res}_{234} [A_n^{\text{1-loop}}(\ell_{234})] - \frac{\Delta_{1234}^4(\ell_{234})}{D_1} , \\ \Delta_{23}^2(\ell_{23}) &= \text{Res}_{23} [A_n^{\text{1-loop}}(\ell_{23})] - \frac{\Delta_{123}^3(\ell_{23})}{D_1} - \frac{\Delta_{234}^3(\ell_{23})}{D_4} - \frac{\Delta_{1234}^4(\ell_{23})}{D_1 D_4} , \\ \Delta_3^1(\ell_3) &= \text{Res}_3 [A_n^{\text{1-loop}}(\ell_3)] - \frac{\Delta_{13}^2(\ell_3)}{D_1} - \frac{\Delta_{23}^2(\ell_3)}{D_2} - \frac{\Delta_{34}^2(\ell_3)}{D_4} \\ &\quad - \frac{\Delta_{123}^3(\ell_3)}{D_1 D_2} - \frac{\Delta_{134}^3(\ell_3)}{D_1 D_4} - \frac{\Delta_{234}^3(\ell_3)}{D_2 D_4} - \frac{\Delta_{1234}^4(\ell_3)}{D_1 D_2 D_4} .\end{aligned}\tag{4.24}$$

For the sake of brevity, we do not give explicit expressions for the loop momenta satisfying the cut conditions. Depending on the topology, the on-shell conditions in general do not fully constrain the loop-momentum but lead to a variety of loop momentum solutions, and moreover, require complex momenta to be satisfied. Parameterizations valid for massive particles and D -dimensional loop momenta can, for example, be found in [31, 126, 136].

Inverting the Unitarity Relations

Starting with the pentagon numerator Δ^5 , the unitarity relations Eq. (4.23) give a clear prescription of how to obtain the coefficients in the numerators Δ^i . In a numerical application of the unitarity method, we sample the loop momentum and obtain $\Delta^i(\ell_{j_1, \dots, j_i})$ computed for a specific choice of propagator momenta. In order to identify the scalar coefficients, by which the final one-loop amplitude is completely defined, we need to perform an inversion on the linear relations in Eq. (4.12). In particular, for a numerical implementation this implies evaluating the cuts in Eq. (4.23) multiple times depending on the tensor-rank.

The above is valid for general dimensionality D . In order to simplify the construction and reduce computing time, we do a *two-step procedure* [31] to obtain all coefficients. As a first step, we compute with a $D = 4$ dimensional on-shell phase-space, with all higher-dimensional contributions proportional to μ^2 vanishing. The numerator tensors in Eq. (4.12) simplify and start with Δ^4 . Note that this corresponds to a particular way of choosing the loop momentum. Depending on the rank, we then evaluate the unitarity relations on multiple on-shell momenta. The resulting system of equations can be solved by matrix inversion or the application of a discrete Fourier transform as for example described in [32]. As a second step, we compute the remaining numerator tensors on D -dimensional on-shell phase spaces and reuse the coefficients obtained for $D = 4$ in the inversion. The latter is possible since the coefficients e^i, d^i, c^i, b^i, a^i are independent of the loop momentum.

⁵There is no Δ^5 for a 4-point amplitude.

As an explicit example, we take the computation of the box coefficients d^i for a fixed arrangement of momenta flowing into the vertices of the parent diagram. We drop the indices associated to the external momenta and get

$$\begin{pmatrix} \Delta^4(\ell_1) \\ \Delta^4(\ell_2) \\ \Delta^4(\ell_3) \\ \Delta^4(\ell_4) \\ \Delta^4(\ell_5) \end{pmatrix} = \begin{pmatrix} 1 & t_{1;1} & 0 & 0 & 0 \\ 1 & t_{1;2} & 0 & 0 & 0 \\ 1 & t_{1;3} & \mu_3^2 & t_{2;3}\mu_3^2 & \mu_3^4 \\ 1 & t_{1;4} & \mu_4^2 & t_{2;4}\mu_4^2 & \mu_4^4 \\ 1 & t_{1;5} & \mu_5^2 & t_{2;5}\mu_5^2 & \mu_5^4 \end{pmatrix} \begin{pmatrix} d^0 \\ d^1 \\ d^2 \\ d^3 \\ d^4 \end{pmatrix}, \quad (4.25)$$

where the ℓ_i are solutions to the on-shell conditions in D -dimensions and the associated variables $t_{j,i}$ and μ_i calculated from loop momentum ℓ_i . We take the loop momentum solutions ℓ_1 and ℓ_2 being restricted to the 4-dimensional subspace that is with $\mu^2 = 0$. As described above, our *two-step procedure* gives us a lower block diagonal matrix by construction. As a first step, we compute the cuts $\Delta^4(\ell_1)$ and $\Delta^4(\ell_2)$. Those are cuts in $D = 4$ -dimensional space-time, which makes their computation numerically cheaper. We then invert the upper part of the matrix and obtain d^0 and d^1 . In particular, we can reconstruct all tadpole coefficients by working in $D = 4$, since they do not have μ^2 insertions. The second step then requires the evaluation of $\Delta^4(\ell_3)$, $\Delta^4(\ell_4)$ and $\Delta^4(\ell_5)$, where the loop momenta are D -dimensional momenta with $\mu^2 \neq 0$. We then invert the lower block of the matrix. The next Chapter 5 is devoted to the computation of the cuts in D -dimensions.

The advantage of this two-step process is twofold. It simplifies the inversion of the unitarity relations by turning them into a lower block diagonal matrix. And more importantly, it simplifies the calculation of the cuts $\Delta^i(\ell)$ for those loop momenta ℓ restricted to 4-dimensions by not having to extend the spinor algebra and momenta to higher dimensional space-time.

4.4. Massive Bubble and Tadpole Cuts

Among the new scalar integrals contained in the basis of master integrals for massive particles (cf. Sec. 4.1.4) are the tadpole integral I_1 and the bubble integral with a single massive leg in one corner I_{2,m^2} , which we refer to as massive one-leg bubble integral. The coefficients multiplying these integrals appear in the corresponding bubble and tadpole numerators in Eq. (4.12). Double and single cuts on the corresponding topologies are required to reconstruct these coefficients. In this section, we will see that some care has to be taken in order to treat these two new topologies in the numerical unitarity framework described above.

4.4.1. Massive One-Leg Bubble Cuts

In a direct application of numerical unitarity, external leg self-energy corrections would be included in double cuts on bubble topologies with one massive leg. We shall call these

massive one-leg bubbles. The double cut on a massive one-leg bubble leads to explicit divergent factors, as shown in Fig. 4.3. In traditional approaches to renormalization, Feynman diagrams with self-energy insertions on massive external legs are discarded. They are accounted for in wave function and mass renormalization. For a massless external leg, the corresponding scalar integral is scaleless and therefore vanishing in dimensional regularization. Double cuts on one-leg bubble topologies are therefore not considered for massless particles.

The one-loop amplitude on the massive one-leg bubble double cut factorizes into two tree amplitudes $A^{\text{tree}}(-\ell_{2,q}, 1_{\bar{q}}, \ell_{1,g})$ and $A^{\text{tree}}(-\ell_{1,g}, \dots, \ell_{2,\bar{q}})$, where the latter is not well defined, since it contains a divergent propagator. We split it into those parts multiplying the divergent propagator R and those free from it F

$$A^{\text{tree}}(-\ell_{1,g}, \dots, \ell_{2,\bar{q}}) = \frac{R(-\ell_{1,g}, \dots, \ell_{2,\bar{q}})}{(\ell_{1,g} - \ell_{2,\bar{q}})^2 - m_{\bar{q}}^2} + F(-\ell_{1,g}, \dots, \ell_{2,\bar{q}}), \quad (4.26)$$

with the invariant mass of the momenta flowing through the intermediate propagator being fixed by momentum conservation $(\ell_{1,g} - \ell_{2,\bar{q}})^2 = 1_{\bar{q}}^2 = m_{\bar{q}}^2$. Since it is equal to the quark mass, the first term in Eq. (4.26) is singular.

Three different possibilities on how to reconcile generalized unitarity and cuts of massive one-leg bubbles are known in the literature: First, the explicit removal of the unwanted contributions due to EGKM [33] and their inclusion by wave function and mass renormalization. Second, the introduction of a regulator for the divergent tree which has to be accounted for throughout the calculation, due to Britto and Mirabella [35]. Third, a recent proposal by Badger et al. [36] to match both infrared and ultraviolet poles in both $4 - 2\epsilon$ and $6 - 2\epsilon$ dimensions and thereby avoid the calculation of both one-leg massive bubbles and tadpoles. The latter comes at the cost of constructing an effective Lagrangian for the higher-dimensional calculation.

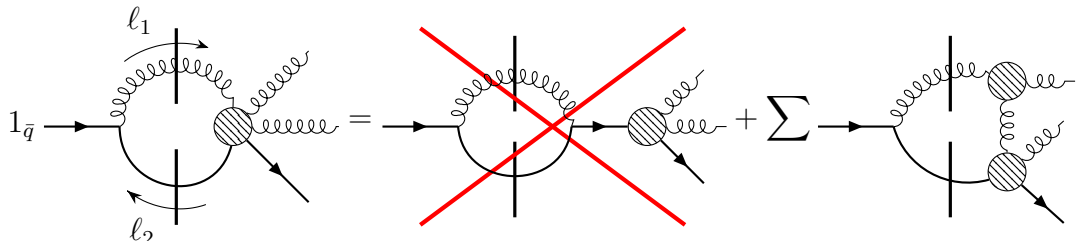


Figure 4.3: Double cut on a massive one-leg bubble topology. The blobs denote tree-like contributions and the sum in the right term runs over the possible ways to distribute the external particles on the two tree amplitudes. We discard contributions from external leg self-energy insertions.

We follow the proposition by EGKM [33] to remove the wave-function graph contribution to the double cut appearing in one-leg bubbles. This is particularly well suited for calculations employing Berends-Giele recursions for the tree generation. Computing the double cut trees, we interrupt the recursion whenever a wave-function graph situation is identified. We thereby remove any divergent tree contribution. In particular, this implies

that the two cut particles are not allowed to join in a vertex without previous interactions. Due to this removal, gauge invariance of the tree amplitude is broken and only restored after combination with the appropriate counterterms (cf. Sec. 6.3). This requires in particular to consistently compute in the same gauge, which for simplicity we choose to be Feynman gauge, i.e. the sum over polarization states is given by

$$\sum_{s=1}^{D_s} \epsilon_s^\mu \epsilon_s^\nu = -g^{\mu\nu}. \quad (4.27)$$

The above polarization sum includes unphysical degrees of freedom. In the discussed double-cut of Fig. 4.3 however, there is always a quark in the loop and therefore no additional ghost particles need to be introduced.

4.4.2. Massive Tadpole Cuts

The master integral basis for massive particles contains the scalar one-point integral I_1 , a tadpole. Its coefficients can be reconstructed by the application of single cuts. Note that the scalar one-point integral is not to be confused with *tadpole Feynman diagrams*. They have numerator insertions depending on the theory and vanish for both QED and QCD. In an application of unitarity single-cuts, vanishing tadpole Feynman diagrams would contribute. This section is concerned with the proper handling of single cuts. For massless particles, scalar one-point integrals are scaleless and vanish in dimensional regularization. Therefore, for massless processes, one does not have to deal with the described issues.

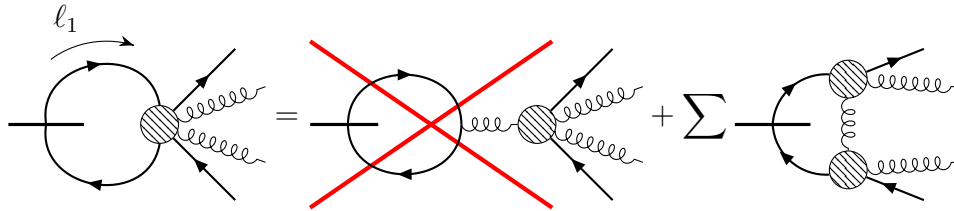


Figure 4.4: Single cut on a massive tadpole topology, with the first term on the left, R , denotes tadpole Feynman diagram contributions and the second one non-tadpole like terms N . The blobs denote tree-like contributions and the sum runs over all possibilities to distribute the external particles amongst the two blobs. We discard contributions from tadpole Feynman diagrams.

We use a direct approach to obtain tadpole coefficients by following the unitarity prescription, with explicit loop momentum parameterization given for example in [30]. An explicit prescription of how to deal with divergent contributions that appear in single cuts is not explicitly described in the literature. In this section, we will illustrate the source of these divergent contributions and propose a consistent scheme to compute single cuts based on the same principle that we applied for the double cut (cf. Sec. 4.4.1 and [33]). For processes with the particles in the loop having an identical mass m^2 , a second possibility

exists to obtain the single coefficient of the scalar tadpole integral by matching the UV pole structure [25, 36, 137]. The only source of UV divergencies of one-loop amplitudes are bubble and tadpole integrals, which are either independent of kinematical invariants or depend on the mass m^2 of loop particles. Knowing the coefficients of the bubble integrals and the UV pole structure of the full amplitude, one can deduce the coefficient of the scalar tadpole integral. For more details, see App. D.

There are two conceptual challenges in the direct unitarity approach when dealing with single cuts and both are related to tree-like contributions that diverge. The one-loop amplitude in Fig. 4.4 on the massive single cut corresponds to a single tree amplitude $A^{\text{tree}}(-\ell_{1,\bar{q}}, \dots, \ell_{1,q})$. This tree amplitude is not well defined, since it contains singular terms in *several* factorization channels. The first type corresponds to tadpole Feynman diagrams. These are not considered in traditional calculations based on Feynman diagrams since they vanish in dimensional regularization. By Lorentz invariance they must be proportional to the momentum p^μ of the gluon, which is zero $p^\mu = 0$ by momentum conservation. We can split the tree into the part R multiplying the apparently divergent propagator and the non-tadpole like term N and obtain

$$A^{\text{tree}}(-\ell_{1,\bar{q}}, \dots, \ell_{1,q}) = \frac{R(-\ell_{1,\bar{q}}, \dots, \ell_{1,q})}{p^2} + N(-\ell_{1,\bar{q}}, \dots, \ell_{1,q}), \quad (4.28)$$

where momentum conservation fixes the momentum p to be zero $p^\mu = 0$. We discard the tadpole Feynman diagram contributions appearing in the single cut. Again, the tree generation with a Berends-Giele recursion is beneficial. Whenever a situation is identified where the two cut quarks directly join into a vertex without any previous interaction, we stop the recursion and the tadpole Feynman diagram is discarded. The appearance of a tadpole Feynman diagram in the single cut has not been explicitly discussed in the literature, but can be seen as being contained in the treatment of the double cut introduced by EGKM in [33].

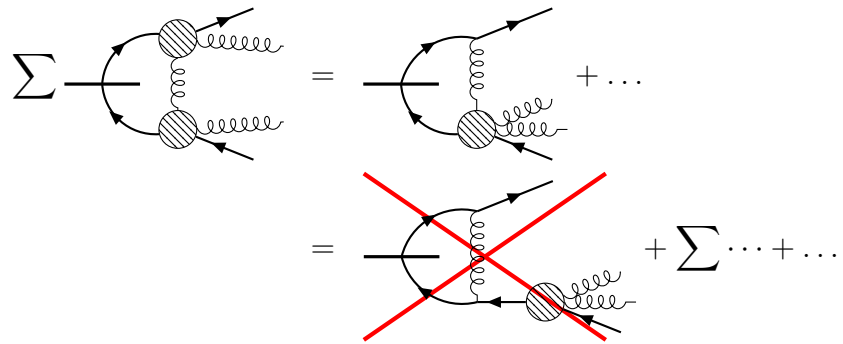


Figure 4.5: The non-tadpole like part N of the single cut contains contributions from external leg self-energy corrections that have to be removed. They are accounted for in the renormalization.

The second conceptual challenge is that the non-tadpole like term N in Eq. (4.28) also contains singular terms. They correspond to external leg self-energy Feynman diagrams. In Sec. 4.4.1, we saw that they contain a divergent propagator. The part N of Eq. (4.28) contains a sum over all possible ways of distributing the external legs to the two tree-like

subgraphs, represented by blobs. Amongst the Feynman diagrams contained therein, we have external leg self-energy contributions, as is apparent in the second line of Fig. 4.5. We apply the same treatment as in the previous Sec. 4.4.1 for massive one-leg bubbles. The singular contributions are removed by stopping the Berends-Giele recursion whenever such a configuration appears during the computation of the tree amplitude. Again, we explicitly break gauge invariance which is only restored after combination with the appropriate counter terms. The removal of these singular contributions from the single cut makes the direct application of numerical unitarity feasible.

4.5. Tree Amplitude Generation with Berends-Giele Recursions

Generalized unitarity relates color-ordered primitive one-loop amplitudes to the product of color-ordered tree amplitudes. An efficient and flexible way of computing tree amplitudes are Berends-Giele recursion relations [34] for off-shell currents. They were originally devised for pure gluon amplitudes but can easily be extended to an arbitrary spectrum. In algorithms based on off-shell recursion relations, so called currents with a single off-shell leg and n on-shell legs are related to those with fewer on-shell legs. The possible interactions between the currents are determined by the theory at hand. Berends-Giele recursions work for complex momenta as well as in any integer-dimensional space-time. Therefore, they are well suited for the application in generalized unitarity and we implemented a new tree generator in the `BlackHat` library for the computation of unitarity cuts for massive particles. Note, that the fine-grained control over the contributing Feynman diagrams to each current is beneficial for our treatment of double and single cuts with massive particles (cf. Sec. 4.4.2 and Sec. 4.4.1). In particular, the removal of certain Feynman diagrams does not affect the efficiency of the computation during the evaluation phase. Compared to on-shell recursions like BCFW [138, 139], that are based on factorization properties of the tree amplitudes, Berends-Giele recursion relations have the advantage of being flexible, e.g. with respect to the space-time dimensionality, and robust since they rely on a small set of rules to be implemented.

A Toy Example for Off-Shell Tree Recursions

The basic principle of BG recursions can easily be demonstrated in a vectorial toy example with a three-point interaction only. For simplicity we consider the example of a four-point tree amplitude $A^{\text{tree}}(1, 2, 3, 4)$ with a fixed order of external legs. We start by defining the *current* $J^\mu(2, 3, 4)$, which is constructed from an ordered on-shell tree amplitude by stripping one leg off. In this example we remove the external leg labeled by 1. To recover the tree amplitude, we multiply the current by both the wave function $\epsilon^\mu(1)$ of a massless spin-1 particle and the inverse propagator D_1 ⁶ of the removed external leg

$$A^{\text{tree}}(1, 2, 3, 4) = D_1 J^\mu(2, 3, 4) \epsilon_\mu(1). \quad (4.29)$$

⁶Numerically, the divergent propagator of the external leg is dropped in the final step of the recursion.

The recursive steps to construct the current $J^\mu(2, 3, 4)$ are graphically represented in Fig. 4.6. The external on-shell legs join into the shaded blob, representing a tree-like contribution. The main idea of the recursion is that the current leg must interact via one of the interactions furnished by the theory. In our simplified example, we insert the allowed three-point interaction. Then, we sum over all possible ways to distribute the ordered external legs to the subcurrents. The same reasoning is applied to the smaller subcurrents, cf. the second row. The endpoint of the recursion are the off-shell one-point currents $J^\mu(i) \equiv \epsilon^\mu(i)$.

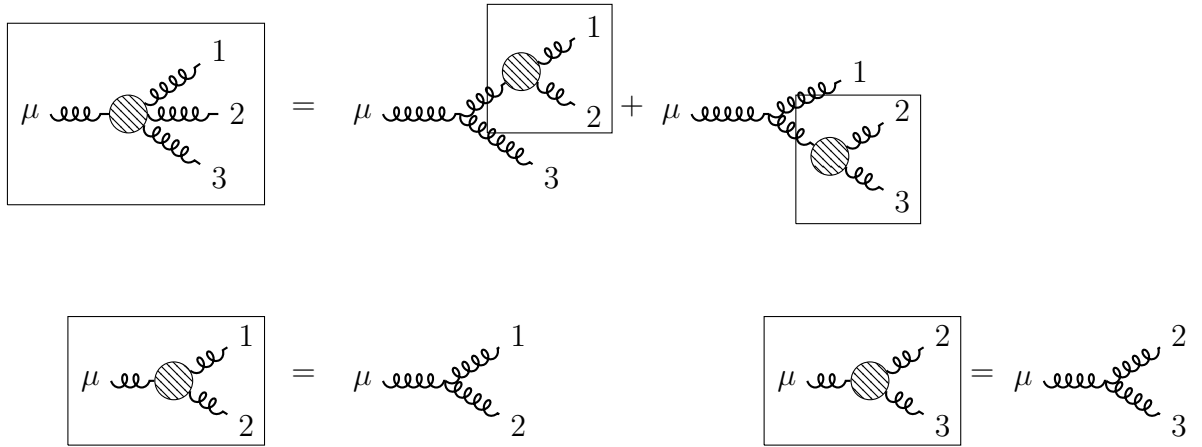


Figure 4.6: Berends-Giele recursion for a current $J^\mu(1, 2, 3)$ in a vectorial toy example with only three-point interactions.

We can easily generalize the recursive relation of our vectorial toy example to any number of external particles. The recursive relations between the current $J(n, \dots, m)$, containing $m-n$ external on-shell legs, and those currents containing less external legs can be written as

$$J^\mu(n, \dots, m) = \frac{g^{\mu\nu}}{D_{m,n}} \sum_{i=n}^{m-1} V_{\nu\rho\sigma}(-p_{m,n}, p_{n,i}, p_{i+1,m}) J^\rho(n, \dots, i) J^\sigma(i+1, \dots, m), \quad (4.30)$$

with the momenta sums defined as $p_{i,j} = \sum_{k=i}^j p_k$. The indices of the inverse propagator $D_{i,j}$ label the involved momenta sum $D_{i,j} = ip_{i,j}^2$ and we assume a momentum-dependent three-point interaction $V^{\nu\rho\sigma}(p_1, p_2, p_3)$. The Berends-Giele-like tree recursions thereby provide a systematic prescription to collect all the Feynman diagram contributions to a given color-ordered tree amplitude. The recursion relations are valid for complex momenta in any integer space-dimension and the currents can be multi-component objects representing vectors, spinors or scalars in any integer space-time dimension.

Tree-Level Recursions

The recursion relations of the previous subsection can easily be extended to the full QCD spectrum and an additional electroweak gauge boson, requiring recursive relations for different types of currents. We will present those for pure gluon currents and those

for currents composed of a single quark pair and additional gluons. Gluons interact via both three- and four-point interactions and thus the recursion relations read

$$J^\mu(n, \dots, m) = \frac{g^{\mu\nu}}{D_{m,n}} \left[\sum_{i=n}^{m-1} V_{\nu\rho\sigma}^{ggg}(-p_{m,n}, p_{n,i}, p_{i+1,m}) J^\rho(n, \dots, i) J^\sigma(i+1, \dots, m) \right. \\ \left. + \sum_{i=n}^{m-2} \sum_{j=i+1}^{m-1} V_{\nu\rho\sigma\delta}^{gggg} J^\rho(n, \dots, i) J^\sigma(i+1, \dots, j) J^\delta(j+1, \dots, m) \right]. \quad (4.31)$$

The color-ordered momentum dependent three-point interaction $V_{\nu\rho\sigma}^{ggg}(p_1, p_2, p_3)$ and the momentum independent four-point interaction $V_{\nu\rho\sigma\delta}^{gggg}$ are given in App. B. Momentum sums and the gluon propagator are defined as in the previous section. The recursion terminates with the polarization state of the gluon $J^\mu(i) \equiv \epsilon^\mu(i)$.

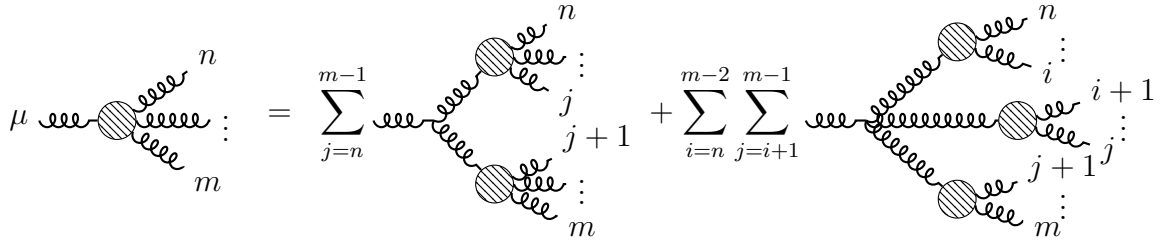


Figure 4.7: Berends-Giele recursion for a gluonic current $J^\mu(n, \dots, m)$. The sums run over all possible ways to distribute the on-shell legs with fixed cyclic ordering amongst the subcurrents.

Similar Berends-Giele recursions can be devised for tree amplitudes containing quark pairs. We have to distinguish currents with a quark off-shell leg and those with an anti-quark off-shell leg. Fig. 4.8 shows the Berends-Giele recursions for a quark current with n -gluons and a single quark line. The quark has two possibilities to interact. It can radiate a gluon to the left or to the right of the fermion line. These are related by a minus sign $V_\mu^{qg\bar{q}} = -V_\mu^{q\bar{q}g}$, see color-ordered Feynman rules in App. B. The recursion for the quark current $Q(g_1, g_2, \dots, g_{n_1}; \bar{q}; g_{n_1+1}, \dots, g_{n_1+n_2})$ therefore reads

$$Q = S^q(-p_{1,n_1+n_2}) \left[\sum_{j=1}^{n_1} V_\mu^{qg\bar{q}} Q(g_{j+1}, \dots, g_{n_1}; \bar{q}; g_{n_1+1}, \dots, g_{n_1+n_2}) J^\mu(g_1, \dots, g_j) \right. \\ \left. + \sum_{j=n_1}^{n_1+n_2-1} V_\mu^{q\bar{q}g} Q(g_1, \dots, g_{n_1}; \bar{q}; g_{n_1+1}, \dots, g_j) J^\mu(g_{j+1}, \dots, g_{n_1+n_2}) \right], \quad (4.32)$$

with the quark propagator given by $S^q(p) = \frac{i(p+m)}{p^2 - m^2}$ and momenta sums $p_{i,j} = \sum_{k=i}^j p_k$ defined as above. Fermion currents, propagators and interactions are objects in spinor space, which means that their relative positioning matters. We suppressed the related spinorial indices in Eq. (4.32).

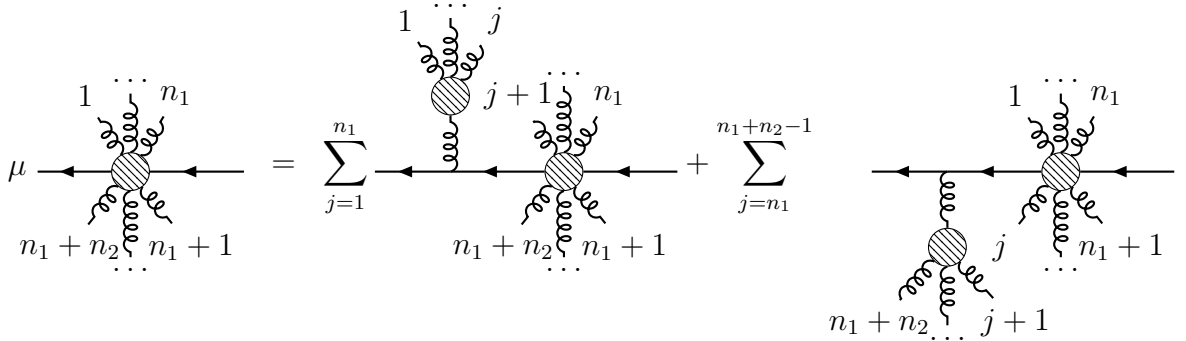


Figure 4.8: Berends-Giele recursion for the quark current Q . The vertices for radiating the gluon to the right $V_\mu^{qg\bar{q}}$ and to the left $V_\mu^{q\bar{q}g}$ of the fermion line are related by a minus sign. The sums run over all possibilities to distribute the on-shell legs with fixed cyclic ordering amongst the subcurrents.

The tree amplitude $A^{\text{tree}}(q; g_1, g_2, \dots, g_{n_1}; \bar{q}; g_{n_1+1}, \dots, g_{n_1+n_2})$ can thus be recovered from the quark current $Q(g_1, g_2, \dots, g_{n_1}; \bar{q}; g_{n_1+1}, \dots, g_{n_1+n_2})$ by

$$A^{\text{tree}} = \bar{u}(p_q) \left(-i(\not{p}_q - m) \right) Q. \quad (4.33)$$

Extending the Berends-Giele recursion relations to an arbitrary number of quark pairs poses no problem in a numerical implementation but their graphical representation can become quite cumbersome. Also the addition of a color-neutral gauge boson poses no problem in a flexible numerical implementation. Color-neutral particles are not strictly ordered, they have to be inserted at all possible positions between the colored particles with fixed cyclic ordering. Care has to be taken to consistently treat color-neutral particles during both color decomposition and tree generation. Explicit expressions for propagators and vertices for a W -boson can be found in App. B.

Multi-Cut Trees For Numerical Unitarity

In the context of a numerical unitarity application, tree amplitudes always appear as products of tree amplitudes in unitarity cuts. Adjacent tree amplitudes in the cut are connected by an on-shell leg, whose momentum enters the amplitudes with opposite signs. The sum over helicity states on the cut corresponds to the polarization state sum and is given by

$$\begin{aligned} P_g^{\mu\nu} &\equiv -g^{\mu\nu} = \sum_{s=\pm} \epsilon_s^{\ast\mu}(p) \epsilon_s^\nu(-p) \\ P_q(p) &\equiv (\not{p} + m) = \sum_{s=\pm} \bar{u}_s(p) v_s(-p), \end{aligned} \quad (4.34)$$

Instead of inserting explicit on-shell states for the cut leg, we replace the sum over helicity states on the cut by the corresponding polarization projectors $P_g^{\mu\nu}$ and $P_q(p)$ of Eq. (4.34).

We refer to the product of cut trees summed over helicities, with all but one state sum replaced by the corresponding projectors, as a *multi-cut tree*. In Fig. 4.9, the graphical representation of such a multi-cut tree appearing in the calculation of a quadruple cut is shown, where four loop propagators are set on-shell.

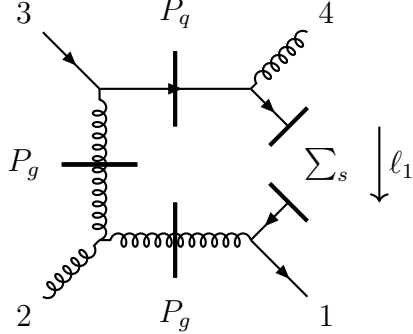


Figure 4.9: A multi-cut tree appearing in a quadruple cut, where the sum over polarization states is replaced by the corresponding projectors on all but one cut line.

The multi-cut tree for the quadruple cut in Fig. 4.9 thus corresponds to

$$\begin{aligned} & \sum_{s_1, s_2, s_3, s_4 = \pm} A^{\text{tree}}(-\ell_1, 1_q, \ell_2) A^{\text{tree}}(-\ell_2, 2_g, \ell_3) A^{\text{tree}}(-\ell_3, 3_{\bar{q}}, \ell_4) A^{\text{tree}}(-\ell_4, 4_g, \ell_1) \\ &= \sum_{s_1 = \pm} J_\mu(-\ell_1, 1_q, \ell_2) P_g^{\mu\nu} \text{MC}_{\nu\rho}(-\ell_2, 2_g, \ell_3) P_g^{\rho\sigma} \text{MC}_\sigma(-\ell_3, 3_{\bar{q}}, \ell_4) P_q(\ell_4) \bar{Q}(-\ell_4, 4_g, \ell_1), \end{aligned} \quad (4.35)$$

where we introduced *multi-currents* denoted by MC, that is an amplitude with two off-shell legs and therefore two open indices (we suppress spinorial indices for simplicity). The summation in the first line is over all spin states of internal cut particles and that in the second line only over the spin-states of the internal particle, whose polarization sum is not replaced by the corresponding projector. Depending on the legs that are stripped off, the indices can be spinorial, vectorial, a mixture of those or the current can be a scalar. The quark projector P_q and anti-fermion current \bar{Q} live in spinor space, whereas the gluon projector P_g and gluon current J^μ are vectors. Compared to computing tree amplitude by tree amplitude, the numerical implementation of multi-cut trees simplifies the book-keeping due to the smaller number of objects that are computed. Instead of computing several trees for each helicity configuration of internal cut legs, we only have to sum over the helicity configurations of the single cut leg with explicit on-shell states. Furthermore, handling the polarization sum by a projector reduces the number of operations for the computations in Feynman gauge. This is particularly relevant for a spectrum with an increased number of states. For example, we will see in the next chapter that our treatment of the rational terms leads to a massive spin-1 particle with three polarization states. The unphysical degrees of freedom circulating in the loop that are introduced by the gluonic polarization sum in Feynman gauge are canceled, since one cut-line is still computed with on-shell states. We implemented a caching mechanism for currents inside single tree amplitudes but also across all tree amplitudes required for the computation of a one-loop amplitude. In particular, this allows for the efficient evaluation of the latter.

CHAPTER 5

Dimensional Dependence of One-Loop Helicity Amplitudes

In this chapter, we describe an efficient algorithm for the numerical evaluation of dimensionally regulated QCD one-loop helicity amplitudes, that we use for the numerical evaluation of D -dimensional unitarity cuts. These cuts are a necessary ingredient to the numerical unitarity method described in the previous Chapter 4. The content of this chapter is also presented in [39].

There exist various dimensional regularization schemes. They mainly differ in their treatment of Lorentz vector indices associated to gauge particles. The 't Hooft-Veltman (HV) scheme [128] as well as the four-dimensional helicity (FDH) scheme [37, 38] keep external - or “observable” - particles in four dimensions. Therefore, only amplitudes with the four-dimensional helicity values \pm (and 0 for massive vector bosons) have to be computed, which simplifies the computation of QCD quantum corrections. The two schemes differ in the dimensionality of the spin space of unobserved loop particles D_s .¹ We limit the discussion in this chapter to helicity amplitudes computed in the FDH or HV scheme.

Existing computer algebra packages allow to perform the D_s -dimensional algebra of gamma matrices analytically [140, 141]. For massless particles at one-loop, considerable simplifications leading to an amplitude decomposition by particle content are known [23, 38, 142] and formulations for the computation of QCD one-loop amplitudes [135] have been used in NLO calculations, for example in [2, 3]. In numerical approaches for more general processes, however one is required to compute with explicit, integer dimensional representations of the Dirac algebra. The method of dimensional reconstruction [31, 33] allows to reconstruct the full D_s dependence of helicity amplitudes by computing in two different integer dimensions $D_s > 4$, which requires computations with large representations of the Dirac algebra for amplitudes with external fermions. At one-loop for example, amplitudes with external fermions must at least be computed in $D_s = 6$ and $D_s = 8$ dimensions, with the dimensionality of the representation of the Dirac algebra given by $D_t = 2^{D_s/2}$. For high-multiplicity processes, this can already cause considerable performance issues. For n -loop calculations, a direct application of dimensional reconstruction requires the computation in $n+1$ different D_s dimension. An efficient algorithm for dimensional reconstruction can be for example very relevant for the recently developed two-loop numerical unitarity method [43, 44].

The four-dimensional (re-) formulation (FDF) [40] of FDH avoids the problem of large representations of the Dirac algebra by providing a numerical prescription in terms of four-

¹In HV, D_s is set to $D_s = D = 4 - 2\epsilon$ and in FDH it is set to $D_s = 4$ after performing the Dirac algebra.

dimensional objects. However, it is currently not applicable to processes with multiple (massive) quark lines, as we will show. We provide some modifications to the FDF approach in order to make it applicable to more general processes.

In this chapter, we present a decomposition of one-loop helicity amplitudes by particle content, valid for one-loop amplitudes with multiple (massive) quark lines. It can be seen as an efficient algorithm for the computation of FDH/HV amplitudes that is amenable for numerical implementation. A similar decomposition using a supersymmetric decomposition of one-loop amplitudes was previously found for massless particles [23, 38, 135] and using the technique of dimensional reconstruction for pure gluon amplitudes at one [31] and two [143, 144] loops. Our prescription extends the above decompositions for one-loop amplitudes to the full QCD spectrum including massive quarks. In order to do so, we use explicit representations of the Dirac algebra in integer D_s dimensions [31]. We consider one-loop helicity amplitudes and reconstruct their D_s dependence. The starting point is a tensorial decomposition of gamma matrices in D_s dimensions. The consistent embedding of spinors of external particles in the higher-dimensional space used for internal (loop) particles is required. We show that a partial trace over the higher-dimensional parts of the respective gamma matrices fulfills the condition for a consistent embedding formulated by Veltman in [145]. Subsequently, we perform possible contractions between fermion lines analytically, and deduce an explicit computational prescription in terms of four-dimensional objects. Our prescription is amenable for generalized D -dimensional unitarity calculations and we implemented it in a new version of the `BlackHat` library. The results presented in Chapter 9 are computed using this library. Although we focus on QCD amplitudes, the arguments we use rely mostly on the Lorentz index structure of the involved particles and should be extendable to a broader class of theories.

This chapter is structured as follows: We first review the definition of the considered regularization schemes and provide explicit representations of the Dirac algebra and spinors in integer D_s . We show how the treatment of external states in the FDH scheme leads to a partial trace over the higher-dimensional part of spinor chains. Using a tensorial split-up of the Dirac matrices, we work out the D_s dependence of one-loop amplitudes. We also clarify the connection of our approach to the FDF method and show how an adaption of the FDF is required for the computation of amplitudes with multiple quark lines. Finally, we highlight details required for a numerical implementation.

5.1. Helicity Amplitudes in Integer D_s

5.1.1. Regularization Schemes

We follow the notation for different regularization schemes introduced in [146]. It is based on distinguishing a four-dimensional Minkowski space $S_{[4]}$, an infinite-dimensional space of loop momentum integration $QS_{[D]}$ with $D = 4 - 2\epsilon$ and an enlarged space ($D \leq D_s$) of internal spin states $QS_{[D_s]}$, such that

$$QS_{[D_s]} = QS_{[D]} \oplus QS_{[n_\epsilon]} = S_{[4]} \oplus QS_{[n_\epsilon - 2\epsilon]}, \quad n_\epsilon - 2\epsilon = D_s - 4. \quad (5.1)$$

Table 5.1.: Treatment of metric tensors used in propagator numerators and polarization sums in different regularization schemes. Virtual gluons in one-particle irreducible loop diagrams or initial and final state gluons in real correction diagrams that are collinear or soft are labeled “internal” whereas all others are labeled “external”. Conventional dimensional regularization (CDR) is listed for completeness, HV and FDH are treated in the text and $D = 4 - 2\epsilon$. In FDH, the dimensions D_s is set to $D_s = 4$ after the Dirac algebra is performed. Adapted from [147].

	CDR	HV	FDH
internal	$g_{[D]}^{\mu\nu}$	$g_{[D]}^{\mu\nu}$	$g_{[D_s]}^{\mu\nu}$
external	$g_{[D]}^{\mu\nu}$	$g_{[4]}^{\mu\nu}$	$g_{[4]}^{\mu\nu}$

We restrict the discussion to helicity amplitudes computed in FDH/HV, that is all external or regular fields are kept in $S_{[4]}$. Fields of unobserved virtual gluons or initial and final state gluons in real radiation diagrams that are collinear or soft are referred to as singular fields. They are extended to $QS_{[D_s]}$. For an overview of the considered schemes, see Table 5.1. For our calculation, we choose the dimensionality of $QS_{[D_s]}$ to be integer such that $\dim(QS_{[D_s]}) = D_s \in \mathbb{N}$.² Thus, we can find explicit representations of tensor and vector algebras, see next subsection. The structure of Eq. (5.1) motivates the following split-up

$$g_{[D_s]}^{\mu\nu} = g_{[4]}^{\mu\nu} + g_{[D_s-4]}^{\mu\nu}, \quad {}^{(D_t)}\Gamma_{[D_s]}^\mu = {}^{(D_t)}\Gamma_{[4]}^\mu + {}^{(D_t)}\Gamma_{[D_s-4]}^\mu, \quad (5.2)$$

where ${}^{(D_t)}\Gamma_{[D_s]}^\mu$ are gamma matrices. The integer dimensionality of the representation $D_t = 2^{D_s/2}$ is explicitly denoted by a left superscript in parentheses, and the subspace in which a vector is defined is denoted by a right subscript in brackets. Both are shown whenever appropriate. The metric tensors have the following properties

$$(g_{[\dim]})_\mu^\mu = \dim, \quad (g_{[4]})^{\mu\rho}(g_{[D_s-4]})_{\rho\nu} = 0, \quad (5.3)$$

and any object $A_{[D_s]}^\mu$ carrying a vector index, such as momenta or gamma matrices, can be projected onto the subspaces by

$$A_{[4]}^\mu = g_{[4]}^{\mu\nu} A_{\nu [D_s]}, \quad A_{[D_s-4]}^\mu = g_{[D_s-4]}^{\mu\nu} A_{\nu [D_s]}. \quad (5.4)$$

In order to obtain a one-loop amplitude in the FDH scheme, all sources of D_s -dependence have to be identified and only *after* this has been achieved D_s is set to $D_s = 4$. We note that amplitudes computed in the HV scheme are obtained by setting $D_s = D = 4 - 2\epsilon$ instead. Integrands of one-loop amplitudes regularized in the FDH or HV scheme can only depend on the $(D_s - 4)$ components of the loop momentum through contractions with itself, since external momenta are restricted to four-dimensions. In a numerical computation, we *trivially embed* external momenta in $QS_{[D_s]}$ by extending them with

²In general, the space $QS_{[D_s]}$ is formally infinite-dimensional with $D_s \in \mathbb{R}$.

zeros. Without loss of generality, one can thus exploit the rotational symmetry of the loop integration to write loop momenta in any integer $D_s > 4$ as

$$\ell_{[D]}^\mu = \ell_{[4]}^\mu + \ell_{[D-4]}^\mu \equiv \ell_{[4]}^\mu + i\mu n_4^\mu, \quad (5.5a)$$

$$\ell_{[D]}^2 = \ell_{[4]}^2 + \ell_{[D-4]}^2 \equiv \ell_{[4]}^2 - \mu^2, \quad (5.5b)$$

with the basis vector along the fifth direction of $\text{QS}_{[D_s]}$ denoted as n_4^μ , with $n_4^\mu = (0, 0, 0, 0, i)$ and $n_4^2 = 1$. In other words, the D -dimensional loop momentum can be represented by a five-dimensional vector.

5.1.2. Dirac Algebra and Spinor Representations in Integer D_s

In this section, we construct explicit, finite dimensional representations of both the Dirac algebra and the spinors in D_s -dimensional space-time. The Dirac algebra is defined by

$$\{\Gamma^\mu, \Gamma^\nu\} = 2g^{\mu\nu}, \quad \mu, \nu \in \{0, \dots, D_s - 1\}. \quad (5.6)$$

We construct explicit $D_t = 2^{D_s/2}$ dimensional representations of the Dirac algebra by a recursive procedure, see for example [148]. The gamma matrices of dimension $2D_t$ are related to a tensor product of the 2×2 Pauli matrices with the gamma matrices of lower dimension D_t by:

$${}^{(2D_t)}\Gamma^\mu = \begin{pmatrix} 1 & 0 \\ 0 & 1 \end{pmatrix} \otimes {}^{(D_t)}\Gamma^\mu, \quad \mu \in \{0, \dots, D_s - 1\}, \quad (5.7a)$$

$${}^{(2D_t)}\Gamma^{D_s} = \begin{pmatrix} 0 & i \\ i & 0 \end{pmatrix} \otimes {}^{(D_t)}\Gamma^*, \quad {}^{(2D_t)}\Gamma^{D_s+1} = \begin{pmatrix} 0 & 1 \\ -1 & 0 \end{pmatrix} \otimes {}^{(D_t)}\Gamma^*, \quad (5.7b)$$

with ${}^{(D_t)}\Gamma^*$ defined as

$${}^{(D_t)}\Gamma^* = i^{D_s/2-1} {}^{(D_t)}\Gamma^0 \dots {}^{(D_t)}\Gamma^{D_s-1}. \quad (5.7c)$$

Equivalently, a recursive definition for ${}^{(D_t)}\Gamma^*$ can be found

$${}^{(2D_t)}\Gamma^* = \begin{pmatrix} 1 & 0 \\ 0 & -1 \end{pmatrix} \otimes {}^{(D_t)}\Gamma^*, \quad (5.7d)$$

with ${}^{(D_t)}\Gamma^* {}^{(D_t)}\Gamma^* = {}^{(D_t)}\mathbb{1}$. As the starting point of the iteration, we choose the four-dimensional gamma matrices in the Weyl representation as well as the four-dimensional matrix γ_5 .

$${}^{(4)}\Gamma^\mu \equiv \gamma^\mu, \quad {}^{(4)}\Gamma^* \equiv \gamma_5. \quad (5.8)$$

As an explicit example, we show a representation of the Dirac algebra in $D_s = 6$ space-time dimensions. The gamma matrices are thus $D_t \times D_t$ dimensional matrices ($D_t = 2^{D_s/2} = 8$)

given by

$${}^{(8)}\Gamma^\mu = \begin{pmatrix} \gamma^\mu & 0 \\ 0 & \gamma^\mu \end{pmatrix} \quad \mu \in \{0, \dots, 3\}, \quad (5.9a)$$

$${}^{(8)}\Gamma^4 = \begin{pmatrix} 0 & i\gamma_5 \\ i\gamma_5 & 0 \end{pmatrix} \quad {}^{(8)}\Gamma^5 = \begin{pmatrix} 0 & \gamma_5 \\ -\gamma_5 & 0 \end{pmatrix}. \quad (5.9b)$$

Moreover, the iteration defined in Eq. (5.7) induces a block-diagonal structure of the gamma matrices. It is particularly simple for the first four gamma matrices with $\mu \leq 3$

$${}^{(D_t)}\Gamma_{[4]}^\mu = {}^{(D_t/4)}\mathbb{1} \otimes \gamma^\mu, \quad (5.10)$$

in other words the $D_t \times D_t$ dimensional gamma matrices consist of $\tilde{D}_t = D_t/4$ copies of the four dimensional gamma matrices γ^μ on the diagonal. We denote the left subspace in the tensor product in Eq. (5.10) as $\tilde{D}_t = D_t/4$ -space throughout this chapter. In the above example, the block-diagonal structure is clearly visible in Eq. (5.9a). This property is present for all $D_s > 4$ due to the form of the iteration in Eq. (5.7a). Likewise, the matrices with $\mu \geq 4$ can be decomposed as

$${}^{(D_t)}\Gamma_{[D_s-4]}^\mu = {}^{(\tilde{D}_t)}\mathfrak{g}^\mu \otimes \gamma_5, \quad (5.11)$$

where the \mathfrak{g}^μ represent the \tilde{D}_t -dimensional matrices obtained by the iteration in Eq. (5.7b). In the later sections, we require partial traces over the \tilde{D}_t -subspace of products of gamma matrices defined as

$$\text{Tr}_{\tilde{D}_t} \left[{}^{(\tilde{D}_t)}A \otimes {}^{(4)}B \right] = \text{Tr} \left[{}^{(\tilde{D}_t)}A \right] {}^{(4)}B. \quad (5.12)$$

In view of Eq. (5.10), it is obvious that the first four gamma matrices ${}^{(D_t)}\Gamma_{[4]}^\mu$ only contribute a unit matrix to the trace over \tilde{D}_t

$$\text{Tr}_{\tilde{D}_t} \left[{}^{(D_t)}\Gamma_{[4]}^\mu \right] = \text{Tr}_{\tilde{D}_t} \left[{}^{(D_t/4)}\mathbb{1} \otimes \gamma^\mu \right] = \text{Tr} \left[{}^{(\tilde{D}_t)}\mathbb{1} \right] \gamma^\mu = \tilde{D}_t \gamma^\mu. \quad (5.13)$$

However, partial \tilde{D}_t traces over ${}^{(D_t)}\Gamma_{[D_s-4]}^\mu$ give non-trivial contributions. To evaluate these, we note that the matrices ${}^{(\tilde{D}_t)}\mathfrak{g}^\mu$ again satisfy a Clifford relation

$$\left\{ {}^{(\tilde{D}_t)}\mathfrak{g}^\mu, {}^{(\tilde{D}_t)}\mathfrak{g}^\nu \right\} = 2g_{[D_s-4]}^{\mu\nu} {}^{(\tilde{D}_t)}\mathbb{1}, \quad {}^{(\tilde{D}_t)}\mathfrak{g}^\mu {}^{(\tilde{D}_t)}\mathfrak{g}_\mu = (D_s - 4) {}^{(\tilde{D}_t)}\mathbb{1} \quad (5.14)$$

which can be seen by inserting Eq. (5.11) into Eq. (5.6). As a consequence, one can show analogous to D_t dimensions that the trace over an odd number of ${}^{(\tilde{D}_t)}\mathfrak{g}^\mu$ vanishes

$$\text{Tr} \left[{}^{(\tilde{D}_t)}\mathfrak{g}^\mu \text{ (odd)} \right] = 0. \quad (5.15)$$

The only non-trivial and non-vanishing partial trace over gamma matrices required in this work evaluates to

$$\begin{aligned} \text{Tr}_{\tilde{D}_t} \left[{}^{(D_t)}\Gamma_{[D_s-4]}^\mu {}^{(D_t)}\Gamma_{[D_s-4]}^\nu \right] &= \text{Tr} \left[{}^{(\tilde{D}_t)}\mathbf{g}^\mu {}^{(\tilde{D}_t)}\mathbf{g}^\nu \right] (\gamma_5)^2 \\ &= \text{Tr} \left[{}^{(\tilde{D}_t)}\mathbb{1} \right] g_{[D_s-4]}^{\mu\nu} {}^{(4)}\mathbb{1} \\ &= \tilde{D}_t g_{[D_s-4]}^{\mu\nu} {}^{(4)}\mathbb{1}, \end{aligned} \quad (5.16)$$

where we used Eq. (5.11) and Eq. (5.14). No further trace relations are required for the arguments presented in the later sections.

Spinor States

We are interested in unitarity cuts in D_s dimensions, and thus need explicit spinor states for the cut particles. The generic construction in D_s dimensions for the $D_t/2$ independent fermionic states must satisfy the polarization sum

$$\sum_{k=1}^{D_t/2} u_k \bar{u}_k = {}^{(D_t)}\ell + m {}^{(D_t)}\mathbb{1}, \quad (5.17)$$

as well as the Dirac equation. For the construction of spinor states, we use an arbitrary light-like D -dimensional reference momentum $q_{k,[D]}$ with $q_{k,[D]} \cdot \ell_{[D]} \neq 0$. We denote the associated reference spinors as ${}^{(D_t)}q_k$, which are D_t component objects. We construct spinor states in higher-dimensional space time by acting with the inverse Dirac operator on reference spinors ${}^{(D_t)}q_k$

$${}^{(D_t)}u_k(\ell, q) = \frac{1}{\sqrt{N}} \left({}^{(D_t)}\ell + m {}^{(D_t)}\mathbb{1} \right) {}^{(D_t)}q_k \quad (5.18a)$$

$${}^{(D_t)}\bar{u}_k(\ell, q) = \frac{1}{\sqrt{N}} {}^{(D_t)}\bar{q}_k \left({}^{(D_t)}\ell + m {}^{(D_t)}\mathbb{1} \right), \quad (5.18b)$$

with a suitable normalization N . By construction, the Dirac equation in D_s dimensions is satisfied by the above states. A suitable basis for the $D_t/2$ light-like reference spinors can be obtained by a recursive definition

$${}^{(2D_t)}q_k = \begin{pmatrix} 1 \\ 0 \end{pmatrix} \otimes {}^{(D_t)}q_k \quad {}^{(2D_t)}q_{k+D_t/4} = \begin{pmatrix} 0 \\ 1 \end{pmatrix} \otimes {}^{(D_t)}q_k \quad (5.19a)$$

$${}^{(2D_t)}\bar{q}_k = (1 \ 0) \otimes {}^{(D_t)}\bar{q}_k \quad {}^{(2D_t)}\bar{q}_{k+D_t/4} = (0 \ 1) \otimes {}^{(D_t)}\bar{q}_k, \quad (5.19b)$$

with the index k ranging from $k = 0$ to $(D_t/4 - 1)$. We choose the starting point in $D_s = 4$ as the Weyl spinors

$${}^{(4)}q_1 \equiv |q, +\rangle \equiv |q\rangle, \quad {}^{(4)}q_2 \equiv |q, -\rangle \equiv |q], \quad (5.20a)$$

$${}^{(4)}\bar{q}_1 \equiv \langle q, +| \equiv [q|, \quad {}^{(4)}\bar{q}_2 \equiv \langle q, -| \equiv \langle q|. \quad (5.20b)$$

The naive application of the above construction also holds for four-dimensional momenta. Since the first four gamma matrices in Eq. (5.10) are diagonal in the \tilde{D}_t -space, one can rewrite these spinor states as $D_t/4$ identical pairs inserted in different positions in the spinor space. We split the index k labeling the states that ranges from $k = 0, \dots, (D_t/2 - 1)$ and get an index i with $i \in \{0, 1\}$ corresponding to external helicity states and a \tilde{D}_t -index j with $j = 0, \dots, (D_t/4 - 1)$ such that $k = i + 2j$ and obtain

$$\begin{aligned} {}^{(D_t)}u_{i,j}(p_{[4]}) &= e_j \otimes {}^{(4)}u_i(p_{[4]}) \equiv |j\rangle \otimes |p, i\rangle = |p, i, j\rangle, & i &= 0, 1, \\ {}^{(D_t)}\bar{u}_{i,j}(p_{[4]}) &= e_j^T \otimes {}^{(4)}\bar{u}_i(p_{[4]}) \equiv \langle j| \otimes \langle p, i| = \langle p, i, j|, & j &= 0, \dots, (D_t/4 - 1), \end{aligned} \quad (5.21)$$

with e_j being the j -th unit vector in the $(D_t/4)$ -dimensional space

$$e_j = (0, \dots, 1, \dots, 0)^T. \quad (5.22)$$

The states defined above are orthogonal in the \tilde{D}_t -space:

$$\langle p_1, i_1, j_1 | p_2, i_2, j_2 \rangle = \langle p_1, i_1 | p_2, i_2 \rangle \delta_{j_1 j_2}. \quad (5.23)$$

γ_5 in D_s dimensions

For completeness, we give the matrix γ_5 in D_s dimensions in the 't Hooft-Veltman [128] / Breitenlohner-Maison [149] (BMHV) prescription

$${}^{(D_t)}\Gamma_5 = {}^{(\tilde{D}_t)}\mathbb{1} \otimes \gamma_5, \quad (5.24)$$

such that the following relations hold for any dimension D_s

$$\left\{ {}^{(D_t)}\Gamma_5, {}^{(D_t)}\Gamma_{[4]}^\mu \right\} = 0, \quad \left[{}^{(D_t)}\Gamma_5, {}^{(D_t)}\Gamma_{[D_s-4]}^\mu \right] = 0, \quad (5.25)$$

together with

$$\text{Tr} [\Gamma_5 \Gamma^\mu \Gamma^\nu \Gamma^\rho \Gamma^\sigma] \neq 0. \quad (5.26)$$

A proper treatment of the spurious anomalies associated to the fact that Γ_5 does not anticommute with other Dirac matrices has to be ensured [150]. However, we consider $Wb\bar{b}$ production at NLO in this work, where no spurious anomalies occur since no D_s dimensional trace over γ_5 appears.

Nomenclature

In the following we will refer to various dimensionalities which we list here.

- D : Dimension of the loop momentum integration $D = 4 - 2\epsilon$.
- D_s : Dimension of the spin space of unobserved loop particles $D_s \geq D > 4$.

- D_t : Dimension of representations of the Dirac algebra in integer D_s is $D_t = 2^{D_s/2}$.
- \tilde{D}_t : Dimension of the left factor in tensorial split-ups of gamma matrices $\tilde{D}_t = D_t/4$.

5.1.3. One-loop Matrix Elements

We use the known decomposition of any *string* or product of n Dirac matrices in a D_t dimensional representation

$${}^{(D_t)}S^{\mu_1 \dots \mu_n} = {}^{(D_t)}\Gamma^{\mu_1} \dots {}^{(D_t)}\Gamma^{\mu_n} \quad (5.27)$$

in the basis of antisymmetric combinations of Dirac matrices and the unit matrix

$$\left\{ {}^{(D_t)}\mathbb{1}, {}^{(D_t)}\Gamma^{[\nu_1]}, {}^{(D_t)}\Gamma^{[\nu_1 \nu_2]}, \dots, {}^{(D_t)}\Gamma^{[\nu_1 \dots \nu_{D_s}]} \right\}, \quad \nu_i \in \{0, \dots, D_s - 1\}. \quad (5.28)$$

The basis elements are defined by

$${}^{(D_t)}\Gamma^{[\nu_1 \dots \nu_m]} \equiv \frac{1}{m!} \sum_{\sigma \in \mathcal{P}_m} \text{sgn}(\sigma) {}^{(D_t)}\Gamma^{\sigma_1} \dots {}^{(D_t)}\Gamma^{\sigma_m}, \quad (5.29)$$

where the summation runs over all permutations and the parity $\text{sgn}(\sigma)$ of each permutation is given by the number of inversions in it and evaluates to $+1$ or -1 for even and odd permutations respectively. The number of basis elements required is bounded from above by the dimensionality of D_s and only antisymmetric combinations of $m \leq D_s$ Dirac matrices have to be considered. The decomposition of a string of n matrices in D_s dimensions thus reads

$${}^{(D_t)}S^{\mu_1 \dots \mu_n} = \alpha^{\mu_1 \dots \mu_n} {}^{(D_t)}\mathbb{1} + \alpha_{\nu_1}^{\mu_1 \dots \mu_n} {}^{(D_t)}\Gamma^{[\nu_1]} + \alpha_{\nu_1 \nu_2}^{\mu_1 \dots \mu_n} {}^{(D_t)}\Gamma^{[\nu_1 \nu_2]} + \dots + \alpha_{\nu_1 \dots \nu_{D_s}}^{\mu_1 \dots \mu_n} {}^{(D_t)}\Gamma^{[\nu_1 \dots \nu_{D_s}]} \quad (5.30)$$

For the special case of $D_s = 4$ dimensions the number of basis elements is reduced leading to the simpler decomposition:

$${}^{(4)}S^{\mu_1 \dots \mu_n} = \alpha^{\mu_1 \dots \mu_n} {}^{(4)}\mathbb{1} + \alpha_{\nu_1}^{\mu_1 \dots \mu_n} {}^{(4)}\Gamma^{[\nu_1]} + \alpha_{\nu_1 \nu_2}^{\mu_1 \dots \mu_n} {}^{(4)}\Gamma^{[\nu_1 \nu_2]} + \dots + \alpha_{\nu_1 \dots \nu_4}^{\mu_1 \dots \mu_n} {}^{(4)}\Gamma^{[\nu_1 \dots \nu_4]}, \quad (5.31)$$

note that in general the basis elements in four-dimensions can be simplified. However, we do not require these simplifications nor the explicit form of the coefficients α for the argument presented. From the tensorial split-up of the first four gamma matrices, see Eq. (5.10), it becomes clear that we can define a *trivial embedding* of the basis elements of the four-dimensional basis in D_t dimensions by

$${}^{(4)}\Gamma^{[\nu_1 \dots \nu_m]} = \frac{1}{\tilde{D}_t} \text{Tr} \left[{}^{(\tilde{D}_t)}\mathbb{1} \right] {}^{(4)}\Gamma^{[\nu_1 \dots \nu_m]} = \frac{1}{\tilde{D}_t} \text{Tr}_{\tilde{D}_t} \left[{}^{(D_t)}\Gamma^{[\nu_1 \dots \nu_m]} \right]. \quad (5.32)$$

An important observation is that the basis elements ${}^{(D_t)}\Gamma^{[\nu_1 \dots \nu_m]}_{[4]}$ are part of the D_t -dimensional basis and we can thus split the expansion of a string in D_t dimensions into a

direct sum

$${}^{(D_t)}S^{\mu_1 \dots \mu_n} = {}^{(D_t)}S_{[4]}^{\mu_1 \dots \mu_n} \oplus {}^{(D_t)}S_{[D_s-4]}^{\mu_1 \dots \mu_n}, \quad (5.33)$$

where ${}^{(D_t)}S_{[4]}^{\mu_1 \dots \mu_n}$ is expanded in basis elements $\left\{ {}^{(D_t)}\mathbb{1}, {}^{(D_t)}\Gamma_{[4]}^{[\nu_1]}, \dots, {}^{(D_t)}\Gamma_{[4]}^{[\nu_1 \dots \nu_4]} \right\}$ with $\nu_i \in \{0, \dots, 3\}$ and ${}^{(D_t)}S_{[D_s-4]}^{\mu_1 \dots \mu_n}$ in all other basis elements of the full basis in D_t dimensions.

A well-defined treatment of one-loop helicity amplitudes in integer dimensions in the FDH or HV scheme requires an embedding of spinors of external particles. Fields associated to external particles in these schemes are defined to be in four-dimensions, cf. Table 5.1. Conversely, gamma matrices originating in interactions of loop particles are D_s dimensional, that is they are $D_t \times D_t$ dimensional matrices. Therefore, the spinors of external particles need to be embedded in the D_t dimensional space in order to get a well-defined computation amenable for numerical evaluation. To this end, we follow the requirement for the D_t dimensional basis elements of the above expansion Eq. (5.33) formulated by Veltman [145]. That is, basis elements that are connected with spinors u and \bar{u} representing particles in four dimensions need to satisfy:

$${}^{(D_t)}\bar{u} {}^{(D_t)}\Gamma_{[D_s-4]}^{[\mu_1 \dots \mu_m]} {}^{(D_t)}u \stackrel{!}{=} 0, \quad \forall {}^{(D_t)}\Gamma_{[D_s-4]}^{[\mu_1 \dots \mu_m]} \in {}^{(D_t)}S_{[D_s-4]}^{\mu_1 \dots \mu_n}. \quad (5.34)$$

We have checked in relevant cases to numerical one-loop calculations ($D_s = 6, 8$), but have not proven in general, that no states u and \bar{u} satisfying Eq. (5.34) can be found. However, a normalized, partial trace over the \tilde{D}_t space of the respective expansion fulfills exactly the requirement of Eq. (5.34):

$$\frac{1}{\tilde{D}_t} \text{Tr}_{\tilde{D}_t} \left[{}^{(D_t)}S_{[D_s-4]}^{\mu_1 \dots \mu_n} \right] = 0 \quad (5.35)$$

$$\frac{1}{\tilde{D}_t} \text{Tr}_{\tilde{D}_t} \left[{}^{(D_t)}S_{[4]}^{\mu_1 \dots \mu_n} \right] = {}^{(4)}S_{[4]}^{\mu_1 \dots \mu_n} \neq 0. \quad (5.36)$$

In Eq. (5.35), we used that basis elements are either antisymmetric in the \tilde{D}_t space with respect to at least a single pair of indices or contain a single gamma matrix with $\mu \geq 4$. In both cases, the basis elements vanish in a partial trace over \tilde{D}_t . The second relation in Eq. (5.36) follows by construction, as shown in Eq.(5.32).

A partial trace over the \tilde{D}_t space of each fermion line thus amounts to a valid embedding of external spinors in D_s dimensions. A similar result without referencing an explicit representation of the gamma matrices was derived in [141, 142]. A one-loop helicity amplitude in D_s dimensions is thus given by

$$\mathcal{A}_{[D_s], \text{ext} \in S_{[4]}}^{(\text{1-loop})} \equiv \frac{1}{\tilde{D}_t^n} \sum_{\vec{j}} \mathcal{A}_{[D_s]}^{(\text{1-loop})}(\vec{j}), \quad (5.37)$$

where we sum over the \tilde{D}_t -index of all n fermion lines, $\vec{j} = (j_{l_1}, \dots, j_{l_n})$, corresponding to a partial trace over the \tilde{D}_t subspace on each fermion line. We construct amplitudes with identical quarks from the ones with distinct quarks by appropriate superposition.

In this way the prescription of Eq. (5.37) can be implemented, as it is well defined for distinct-quark amplitudes.

5.1.4. Gluon Propagator in Axial Gauge

We use the color-stripped gluon propagator in D_s dimensional ghost-free, axial gauge (for a review see [151]) in the form given by

$$D_{\text{axial},[D_s]}^{\mu\nu} = \frac{i}{\ell_{[D]}^2} \left[-g_{[D_s]}^{\mu\nu} + \frac{\ell_{[D]}^\mu \eta_{[D]}^\nu + \ell_{[D]}^\nu \eta_{[D]}^\mu}{\ell_{[D]} \cdot \eta_{[D]}} - \frac{\eta_{[D]}^2 \ell_{[D]}^\mu \ell_{[D]}^\nu}{(\ell_{[D]} \cdot \eta_{[D]})^2} \right], \quad (5.38)$$

with the D dimensional reference vector $\eta_{[D]}^\mu$. We choose the particular reference vector $\eta_{[D]}^\mu = i\mu n_4^\mu$ with $\eta_{[D]}^2 = -\mu^2$, as defined in Eq. (5.5). Splitting the metric and loop momentum into four- and higher-dimensional components, the above expression simplifies to

$$D_{\text{axial},[D_s]}^{\mu\nu} = \frac{i}{\ell_{[4]}^2 - \mu^2} \left[-g_{[4]}^{\mu\nu} + \frac{\ell_{[4]}^\mu \ell_{[4]}^\nu}{\mu^2} - g_{[D_s-5]}^{\mu\nu} \right] \equiv D_{\text{mg},[4]}^{\mu\nu} + D_{\text{sc},[D_s-5]}^{\mu\nu}, \quad (5.39)$$

where the subscripts stand for “massive” gluon (mg) and scalar (sc). When interpreting μ^2 , being part of the loop momentum beyond four dimensions, as a mass, then the propagator resembles the one of a massive vector boson. Due to this analogy, in the following we refer to the gluons with polarizations in four dimensions as “massive” gluons. In Eq. (5.39) we used the fact that the higher-dimensional components of the metric can be written as

$$g_{[D_s-4]}^{\mu\nu} = \sum_{k=4}^{D_s-1} n_k^\mu n_k^\nu. \quad (5.40)$$

The D_s dimensional gluon propagator in axial gauge thus decomposes into the propagator of a “massive” spin-1 particle in four dimensions and scalar propagators of higher-dimensional components.³ Moreover, the only non-vanishing contractions of the components $n_{k \geq 5}$ of $g_{[D_s-5]}^{\mu\nu}$ are with itself via metric tensors, since external polarizations and momenta as well as the “massive” gluon propagator are four-dimensional, and the loop momentum is five-dimensional. As a consequence, there are no interactions between scalar lines and “massive” gluons. The three-gluon vertex in D_s dimensions, with two gluons polarized along n_k , corresponds to a scalar-scalar-gluon vertex

$$V_{\mu\nu\rho}^{ggg}(p_1, p_2, p_3) \epsilon_1^\mu n_k^\nu n_k^\rho \sim \epsilon_1^\mu (p_2 - p_3)_\mu, \quad (5.41)$$

³For on-shell loop momenta with $\ell_{[D]}^2 = 0$, one can use light-cone gauge and choose a massless reference vector $\eta_{[D]}^\mu = \ell_{[4]}^\mu - \ell_{[D-4]}^\mu$, which leads to the same split-up of the polarization sum into “massive” gluon and scalar [40]. For off-shell momenta however a “global” reference momentum leading to the described split-up is only possible in axial gauge.

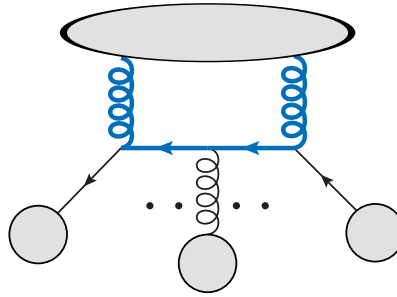


Figure 5.1.: A schematic subdiagram of a fermion line entering and leaving the loop giving rise to a generic spinor string. The grey circles represent tree-like contributions and lines carrying loop momentum are thick and colored (blue).

and a similar argument leads to a scalar-scalar-gluon-gluon vertex when considering the four-gluon vertex. Thus the propagation of “massive”, four-dimensional gluons and each scalar degree of freedom decouples along each D_s dimensional gluon line.

5.2. Establishing the Dimensional Dependence

In this section, we establish the explicit D_s dependence of one-loop amplitudes by analyzing all possible non-trivial contributions to traces over \tilde{D}_t in equation (5.37). They can be grouped in four different classes depending on the type of particles in the loop: closed gluon loops, one fermion line entering the loop, two or more fermion lines entering the loop, and closed fermion loops.

It is beneficial to use the split of the axial gauge gluon propagator in D_s dimensions induced by the specific choice of reference momentum, as discussed in Sec. 5.1.4. A D_s -dimensional gluon line in the loop thus decouples into a four dimensional, “massive” gluon with mass μ^2 and $(D_s - 5)$ colored, scalar components, since also gluonic vertices respect the split-up. The decomposition of pure gluon amplitudes by particle content, with the split-up into a “massive” gluon amplitude in four-dimensions⁴ and a scalar amplitude, was previously established in [23] and is purely restated here. In the remainder of this section, we establish a decomposition valid for the full QCD spectrum including several (massive) quark lines.

When fermion lines enter (and leave) the loop, they contribute generic strings of Dirac matrices to Feynman diagrams (Fig. 5.1). The source of Dirac matrices contributing to the partial trace over \tilde{D}_t in Eq. (5.37) is twofold. Vertices of quarks coupled to gluons carrying loop momentum are proportional to ${}^{(D_t)}\Gamma_{[D_s]}^\mu$ and quark propagators carrying

⁴Corresponding to a massless gluon in five-dimensions in Feynman gauge in [31].

loop momentum can be written, using relations (5.5), as

$${}^{(D_t)}S_q(\ell_{[D]}) = \frac{i}{\ell_{[D]}^2 - m^2} \left(\ell_{[D]\mu} {}^{(D_t)}\Gamma_{[D_s]}^\mu + m \cdot {}^{(D_t)}\mathbb{1} \right) \quad (5.42)$$

$$= \frac{i}{\ell_{[4]}^2 - \mu^2 - m^2} \left({}^{(D_t)}\ell_{[4]} + m \cdot {}^{(D_t)}\mathbb{1} + \mu {}^{(D_t)}\Gamma^4 \right). \quad (5.43)$$

The only non-trivial contribution of Eq. (5.42) comes from $\mu {}^{(D_t)}\Gamma^4$, since the two other terms are proportional to a unit matrix in the \tilde{D}_t -space. For the tensorial split-up of the matrices ${}^{(D_t)}\Gamma^4$ in quark propagators, we adapt Eq. (5.11) for later convenience to

$${}^{(D_t)}\Gamma^4 = {}^{(\tilde{D}_t)}\mathfrak{g}^4 \otimes \gamma_5 = \left(-i {}^{(\tilde{D}_t)}\mathfrak{g}^4 \right) \otimes (i\gamma_5), \quad (5.44)$$

such that $(-i\mathfrak{g}^4) \cdot (-i\mathfrak{g}^4) = 1$.

A generic spinor string $T_{[D_s]}^{\mu\nu}$, with indices coupled to D_s -dimensional gluons in the loop left uncontracted, is according to the prescription we found in the previous Section 5.1.3, see Eq. (5.37), of the form

$$T_{[D_s]}^{\mu\nu} = \text{Tr}_{\tilde{D}_t} [M_n^{\mu\nu}], \quad (5.45)$$

with

$$M_n^{\mu\nu} = \langle p_1, i_1 | \dots {}^{(D_t)}\Gamma_{[D_s]}^\mu \left(\prod_{k=1}^n {}^{(D_t)}\Gamma_{[D_s]}^4 \dots \right) {}^{(D_t)}\Gamma_{[D_s]}^\nu \dots | p_2, i_2 \rangle. \quad (5.46)$$

The dots \dots represent any number of D_t -dimensional gamma matrices from vertices and propagators that contribute only a unit matrix to the partial trace over \tilde{D}_t . The number of insertions of ${}^{(D_t)}\Gamma^4$ from quark propagators is denoted by n , see Eq. (5.42).

The partial trace of $M_n^{\mu\nu}$ over \tilde{D}_t in Eq. (5.45) can be evaluated explicitly using the tensor product structure of gamma matrices shown in Eqs. (5.10) and (5.11). It is only non-vanishing for an even number of \mathfrak{g}^μ matrices in the trace, as shown in Eq. (5.15). We distinguish four cases depending on whether the matrices \mathfrak{g}^μ in the partial trace originate in insertions from the quark propagator or in vertex couplings to the higher-dimensional scalar components of a D_s -dimensional gluon. We start with a restriction of the open indices of Eq. (5.45) to $\mu, \nu \leq 3$, corresponding to a coupling of the spinor string to two “massive” gluons, which leads to

$$T_{[D_s]}^{\mu\nu} = \text{Tr}_{\tilde{D}_t} [M_n^{\mu\nu}] = \text{Tr} [(-i\mathfrak{g}^4)^n] (\dots \gamma^\mu \dots \gamma^\nu \dots), \quad \mu, \nu \leq 3, \quad (5.47a)$$

$$= \tilde{D}_t (\dots \gamma^\mu \dots \gamma^\nu \dots), \quad n \text{ even}, \quad (5.47b)$$

which is only non-vanishing for an even number n of ${}^{(D_t)}\Gamma^4$ insertions from quark propagators. We used Eqs. (5.10) and (5.44) such that $(-i\mathfrak{g}^4) \cdot (-i\mathfrak{g}^4) = 1$. The expression in parentheses denotes the remaining four-dimensional part of the spinor string. We explicitly show the four-dimensional matrices at the two uncontracted vertices. The four-dimensional parts $i\gamma_5$ of the insertions from quark propagators are not explicitly shown and accounted for in the quark propagator. We proceed in the same manner with the remaining cases. A restriction of both open indices to $\mu, \nu \geq 4$, corresponding to a coupling

to two scalars, leads to

$$T_{[D_s]}^{\mu\nu} = \text{Tr}_{\tilde{D}_t} [M_n^{\mu\nu}] = \text{Tr} [\mathfrak{g}^\mu (-i \mathfrak{g}^4)^n \mathfrak{g}^\nu] (\cdots \gamma_5 \cdots \gamma_5 \cdots), \quad \mu, \nu \geq 4, \quad (5.48a)$$

$$= \tilde{D}_t (\cdots \gamma_5 \cdots \gamma_5 \cdots) g_{[D_s-4]}^{\mu\nu}, \quad n \text{ even}, \quad (5.48b)$$

which is again only non-vanishing for even powers n of $(D_t)\Gamma^4$ insertions from quark propagators. We used the same relations as for the previous case and additionally Eq. (5.16) to evaluate the non-trivial trace over \tilde{D}_t . Lastly, we treat the two related cases of $\mu \leq 3, \nu \geq 4$ and vice versa, corresponding to the coupling of a spinor string to both a “massive” gluon and a scalar. The expression for the spinor string is given by

$$T_{[D_s]}^{\mu\nu} = \text{Tr}_{\tilde{D}_t} [M_n^{\mu\nu}] = \begin{cases} \text{Tr} [\mathfrak{g}^\mu (-i \mathfrak{g}^4)^n] (\cdots \gamma_5 \cdots \gamma^\nu \cdots) & \mu \geq 4, \nu \leq 3, \\ \text{Tr} [(-i \mathfrak{g}^4)^n \mathfrak{g}^\nu] (\cdots \gamma^\mu \cdots \gamma_5 \cdots) & \mu \leq 3, \nu \geq 4, \end{cases} \quad (5.49a)$$

$$= -i \tilde{D}_t \begin{cases} (\cdots \gamma_5 \cdots \gamma^\nu \cdots) g_{[D_s-4]}^{\mu 4}, & n \text{ odd}, \\ (\cdots \gamma^\mu \cdots \gamma_5 \cdots) g_{[D_s-4]}^{\nu 4}, & \end{cases} \quad (5.49b)$$

where we used the same relations as above to evaluate the partial trace.

The resulting expressions of Eqs. (5.47b), (5.48b) and (5.49b) are contracted with the remainder of the loop diagram $D_{[D_s]}^{\mu\nu}$, which we write as $(\{\cdots\}_{[4]\mu\nu} + \{\cdots\}g_{[D_s-5]\mu\nu})$. In this relation, we used the decoupling of scalars and “massive” gluons described around Eq. (5.39). $\{\cdots\}_{[4]\mu\nu}$ is a four-dimensional tensor denoting a contribution from the latter and $\{\cdots\}g_{[D_s-5]\mu\nu}$ is a tensor denoting the scalar contribution. For a single fermion line entering the loop, we have a single spinor string $T_{[D_s]}^{\mu\nu}$ and the contraction is of the form

$$T_{[D_s]}^{\mu\nu} D_{[D_s]\mu\nu} = T_{[D_s]}^{\mu\nu} \left(\{\cdots\}_{[4]\mu\nu} + \{\cdots\}g_{[D_s-5]\mu\nu} \right) = \tilde{D}_t (d_{gl} + (D_s - 5) d_{sc}), \quad (5.50)$$

where d_{gl} is a diagram with all D_s dimensional gluons replaced by “massive” gluons and d_{sc} a diagram with all D_s dimensional gluons replaced with scalars. In the second equality we used Eqs. (5.47b), (5.48b) and (5.49b) and the property of the metric tensor

$$g_{[D_s-4]}^{\mu\nu} g_{[D_s-5]\nu\mu} = g_{\mu[D_s-5]}^\mu = (D_s - 5). \quad (5.51)$$

For loop diagrams with multiple quark lines entering the loop, the split-up of D_s -dimensional gluons leads to mixed diagrams with both “massive” gluons and scalars coupling to the same spinor string that have to be considered in general. However, it turns out that the contraction of a fermion line with a “massive” gluon on one side and with a scalar on the other side vanishes. In this situation, the cases of Eq. (5.49b) are used, and the contraction with both a “massive” gluon and a scalar propagator leads to:

$$g_{[D_s-5]}^{\mu\nu} g_{[D_s-4]\nu 4} = g_{[D_s-5]}^{\mu 4} = 0. \quad (5.52)$$

Therefore, also for multiple fermion lines in the loop the diagrams in which all D_s -dimensional gluons are replaced by “massive” gluons and those with all D_s -dimensional gluons replaced by scalars can be treated independently. Diagrams with scalars in the

loop pick up a factor of $(D_s - 5)$ from contractions across multiple lines, see Eq (5.51). The additional prefactor \tilde{D}_t from the partial trace over each spinor string in Eqs. (5.47b), (5.48b) and (5.49b) cancels with that in Eq. (5.37).

Summing up, we found that all diagrams under consideration exhibit the same dimensional dependence and respect the decoupling of “massive” gluons and scalars. Hence a one-loop amplitude with any number of external quark pairs⁵ can be written in arbitrary D_s as

$$\mathcal{A}_{\text{ext} \in S_{[4]}}^{[D_s]} = (\mathcal{A}_{\text{gl}} + (D_s - 5) \mathcal{A}_{\text{sc}}), \quad (5.53)$$

where \mathcal{A}_{gl} is a sum of diagrams with “massive” gluons and \mathcal{A}_{sc} is a sum of diagrams with scalars in the loop. Both \mathcal{A}_{gl} and \mathcal{A}_{sc} are defined in terms of four-dimensional objects in addition with the requirement of only even number of $(D_s - 4)$ -dimensional loop momenta insertions from the quark propagator Eq. (5.42) on *each* fermion line. The latter is in general impossible to satisfy with *only* four-dimensional representations of the Dirac algebra. We provide further details of a numerical computation of \mathcal{A}_{gl} and \mathcal{A}_{sc} in Sec. 5.4.

Once the full dimensional dependence is established by Eq. (5.53), we can use it to *define* an amplitude for continuous D_s . An FDH amplitude is obtained by setting $D_s = 4$:

$$\mathcal{A}^{\text{FDH}} = \mathcal{A}_{\text{gl}} - \mathcal{A}_{\text{sc}}. \quad (5.54)$$

The connection to the method of dimensional reconstruction [31] can be made clear by using Eq. (5.53) with the following

$$\mathcal{A}^{\text{FDH}} = 2\mathcal{A}_{\text{ext} \in S_{[4]}}^{[6]} - \mathcal{A}_{\text{ext} \in S_{[4]}}^{[8]} = \mathcal{A}_{\text{ext} \in S_{[4]}}^{[6]} - 2\mathcal{A}_{\text{sc}}, \quad (5.55)$$

which is valid for all QCD one-loop amplitudes. We used Eq. (5.53) and the above can be further compressed to Eq. (5.54).

It remains to analyze diagrams with a closed fermion loop. For those, no D_s -dimensional vector index contractions appear and the only possible dimensional dependence is an additional total factor of \tilde{D}_t from the loop trace. To see this in detail, we analyze a generic contribution to the D_s -dimensional loop trace which is of the form

$$\begin{aligned} T_{n_f [D_s]}^{\mu_1 \dots \mu_n} &= \text{Tr}_{\tilde{D}_t} \left[\left(-i^{(\tilde{D}_t)} \mathfrak{g}^4 \right) \dots \left(-i^{(\tilde{D}_t)} \mathfrak{g}^4 \right) \right] \text{Tr}_4 [\gamma^{\mu_1} \dots \gamma^{\mu_n}] \\ &= \tilde{D}_t \text{Tr}_4 [\gamma^{\mu_1} \dots \gamma^{\mu_n}]. \end{aligned} \quad (5.56)$$

Both traces above are only non-vanishing for even powers of $i^{(\tilde{D}_t)} \mathfrak{g}^4$ from propagator insertions. Odd numbers of higher-dimensional loop momenta insertions lead to vanishing traces over odd numbers of γ_5 in the four-dimensional trace. The requirement to have only even powers of $i^{(\tilde{D}_t)} \mathfrak{g}^4$ insertions can thus be satisfied with a purely four-dimensional calculation and a four-dimensional quark propagator carrying a dependence on μ (cf. Sec. 5.4).

⁵For now we exclude diagrams with closed fermion loops, which we will discuss later.

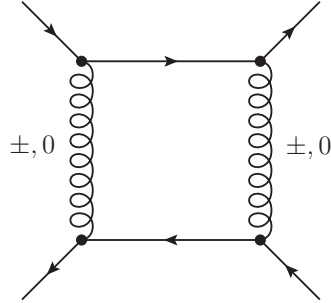


Figure 5.2.: Diagram for the exchange of two “massive” gluons between two quark lines in the FDF. It contains terms that are proportional to μ^2 , which vanish in the FDH scheme.

We get the simple relation

$$\mathcal{A}_{\text{nf}}^{\text{FDH}} = \frac{1}{\tilde{D}_t} \mathcal{A}_{\text{nf}}^{[D_s]} = \mathcal{A}_{\text{nf}}^{[4]}. \quad (5.57)$$

We implemented the approach discussed in this section in the `BlackHat` library. A detailed verification of NLO QCD virtual matrix elements computed with the above prescription is performed in Chapter 8. We do so by comparing all QCD processes with up to 7 partons as well as those with the associated emission of a W^\pm boson⁶ with publicly available tools.

5.3. Remarks on the FDF Scheme

In this section, we discuss the connection of our prescription formulated in the previous section to the recently proposed four-dimensional (re-)formulation (FDF) of FDH [40]. It provides a computational prescription in four dimensions together with selection rules, which have to be evaluated at the level of Feynman diagrams⁷. The scheme is defined with the additional requirement to remove odd powers of μ from the integrand. For testing purposes, we have implemented the FDF method in the context of our numerical unitarity calculation. We find that for amplitudes with gluons and a single quark line, the application of the FDF prescription is equivalent to Eq. (5.54), which can be seen by computing the relevant selection rule factors.

However, for processes involving multiple quark lines, the requirement to remove odd powers of μ is in general not sufficient to circumvent the obstruction discussed below Eq. (5.53). As an example we consider the evaluation of the diagram in Fig. 5.2, that is the exchange of two “massive” gluons (cf. Sec. 5.1.4) between two quark lines. If both quark lines are massive, there is a non-vanishing contribution of the form

$$\langle p_2 | \gamma^\mu (i\mu\gamma_5) \gamma^\nu | p_1 \rangle \langle p_4 | \gamma^\rho (i\mu\gamma_5) \gamma^\sigma | p_3 \rangle D_{\mu\rho}^{\text{mg}} D_{\nu\sigma}^{\text{mg}} \sim \mu^2 \dots . \quad (5.58)$$

⁶Chiral couplings can be incorporated using the ’t Hooft-Veltman prescription, see Section 5.1.2.

⁷The evaluation of the selection rules has to be done only once for a given process, comparable to the color algebra.

Terms with odd numbers of μ insertions, that combine to even powers of μ across multiple lines, generically appear in FDF with two or more massive quark lines. In FDH however, these terms are removed at each line by the partial traces over \tilde{D}_t . They thus constitute a genuine difference between the FDF and the FDH scheme.

In the following, we propose a modification of the FDF prescription to correctly reproduce one-loop FDH amplitudes with multiple (massive) quark lines. In the FDF, one performs the substitutions

$$g_{[D_s-4]}^{\mu\nu} \rightarrow G^{AB}, \quad \gamma_{[D_s-4]}^\mu \rightarrow \gamma_5 \Gamma^A, \quad \ell_{[D_s-4]}^\mu \rightarrow i\mu Q^A, \quad (5.59)$$

where symbols Γ^A do not have a finite-dimensional representation. The FDF is then based on the formulation of selection rules for the objects G^{AB} , Γ^A and Q^A . Amongst them, the replacements of Eq. (5.59) lead to the selection rule

$$\ell_{[D_s-4]} \ell_{[D_s-4]} = -\mu^2 Q^A \Gamma^A Q^B \Gamma^B = -\mu^2 \rightarrow Q^A \Gamma^A = 1. \quad (5.60)$$

However the last transition is ad hoc, since the above equation allows more solutions in general. For example, one can easily find a non-unit matrix that squares to a unit matrix. The corrected selection rule drawn from Eq. (5.60) is thus

$$Q^A \Gamma^A Q^B \Gamma^B = 1. \quad (5.61)$$

We propose to replace the selection rule in Eq. (5.60) with that in Eq. (5.61). Together with the rules to contract indices across different quark lines equivalent to Eqs. (5.47b), (5.48b) and (5.49b), the FDF becomes a valid (re-)formulation of FDH applicable to amplitudes with multiple quark lines. An implementation of the FDF is thus equivalent to the one described in the Section 5.4.

5.4. Implementation Details

In this section, we describe details required for a numerical implementation of the prescription that we presented in Sec. 5.2, see Eq. (5.54) and Eq. (5.57). It allows to compute one-loop QCD amplitudes involving multiple (massive) quark lines regularized in the FDH scheme in a compact way.

An FDH amplitude is given by the difference of an amplitude with all D_s dimensional gluons replaced by a four-dimensional “massive” gluon in the loop and one with scalar particles in the loop, see Eq. (5.54). These amplitudes are defined in terms of four-dimensional objects. Additionally, the requirement of even numbers of $(D_s - 4)$ -dimensional loop momentum insertions from quark propagators on each fermion line has to be enforced. We propose to keep track of the number of $(D_s - 4)$ insertions from quark propagators to enforce this requirement. One way to achieve this numerically is to use a double copy of fermionic states and vertices and to adapt the μ -dependent piece of the propagator to

switch between upper and lower components, see Feynman rules in Table 5.2.⁸ For external and internal fermionic particles, the states are constructed as described in Sec. 5.1.2 with $D_s = 6$. For external particles, only the states with \tilde{D}_t -index $j = 0$ are considered, which projects out terms with even numbers of insertions of $(D_s - 4)$ -dimensional loop momenta. One can equally think of this as keeping track of even powers of μ .

An additional simplification can be exploited for massless quark lines, since odd numbers of γ_5 matrices in a massless spinor chain vanish

$$\langle p_1, i_1 | \cdots \gamma_5 \cdots | p_2, i_2 \rangle = 0, \quad p_1^2 = p_2^2 = 0, \quad (5.62)$$

and the requirement to have only even numbers of $(D_s - 4)$ -dimensional loop momentum insertions is automatically fulfilled. In this situation, it suffices to compute with a $D_s = 4$ dimensional representation of gamma matrices in vertices and the quark propagator

$${}^{(4)}S_q(\ell_{[D]}) = \frac{i \left({}^{(4)}\not{\ell}_{[4]} + i\mu\gamma_5 + m \right)}{\ell_{[4]}^2 - \mu^2 - m^2}, \quad (5.63)$$

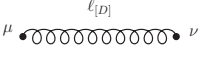
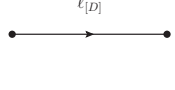
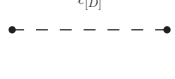
on massless fermion lines. A similar simplification applies to closed fermion loops. Odd numbers of higher-dimensional loop momenta insertions lead to vanishing traces over odd numbers of γ_5 . Consequently, the requirement of having even numbers of insertions is always fulfilled and it suffices to compute in four-dimensions with the quark propagator of Eq. (5.63). To illustrate the prescription, we show in Eqs. (5.64)-(5.67) the schematic computation of FDH amplitudes in terms of “massive” gluon and scalar amplitudes with even numbers of $(D_s - 4)$ -dimensional loop momenta insertions. We show the examples of gluon and closed fermion diagrams, as well as those with (multiple) quark lines entering the loop. The dimension D_t of fermion states in the loop is written between parentheses.

In summary, in this chapter we provide a compact algorithm for the computation of NLO QCD amplitudes regularized in FDH. We find a simple and computationally efficient decomposition of amplitudes by particle content in the loop. D_s dimensional gluons circulating in the loop are replaced by a “massive” four-dimensional gluon as well as a colored scalar. In a numerical implementation, we propose to keep track of even powers of μ by using a $D_s = 6$ -dimensional representation of the Dirac algebra for vertices and propagators. Our central result is a generalization of the previously known decomposition for gluons [23] to the full QCD spectrum, and is in particular valid for multiple massive quark lines. We furthermore clarify the connection between dimensional reconstruction methods and the FDF [40] and find equivalence for gluon amplitudes and those with a single quark line. For multiple quark lines however, the FDF contains terms that constitute a genuine difference with respect to FDH. We provide an adaption of the selection rules and thereby make the FDF applicable to amplitudes with multiple quark lines.

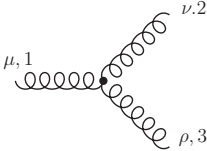
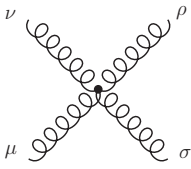
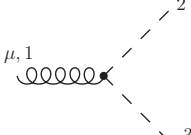
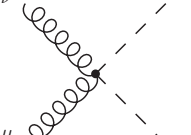
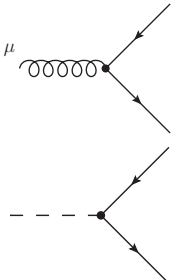
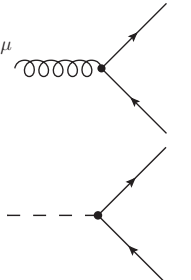
⁸This is related to a calculation in $D_s = 6$ dimensions but differs in the treatment of external states.

Table 5.2.: Color-ordered QCD Feynman rules for the computation of FDH one-loop amplitudes. Shown are the rules for “massive” gluons and scalars in the loop. The requirement to have even numbers of insertions of higher-dimensional loop momentum along each fermion line is enforced by construction.

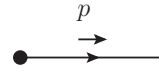
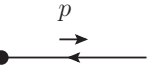
Propagators

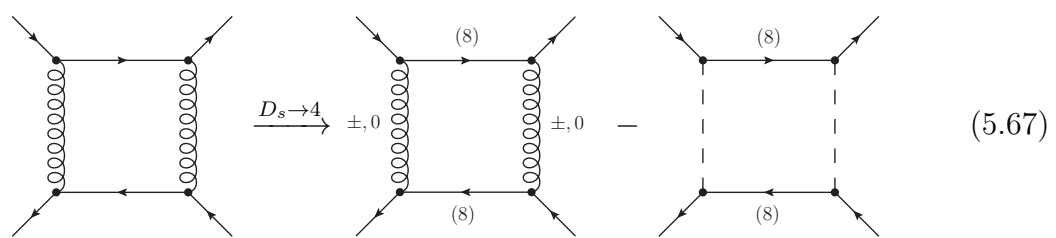
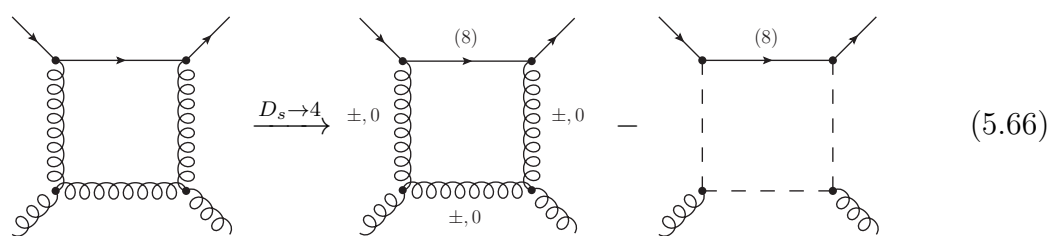
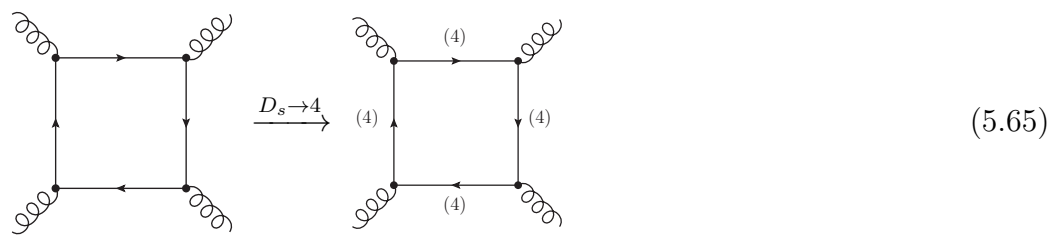
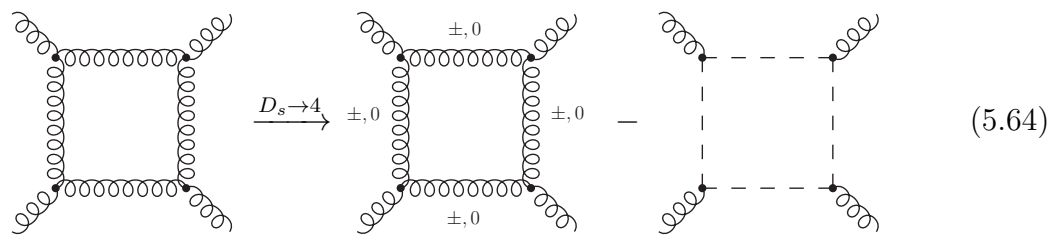
	$= \frac{i}{\ell_{[4]}^2 - \mu^2} \left[-g_{[4]}^{\mu\nu} + \frac{\ell_{[4]}^\mu \ell_{[4]}^\nu}{\mu^2} \right]$
	$= \frac{i}{\ell_{[4]}^2 - \mu^2 - m^2} \left[{}^{(2)}\mathbb{1} \otimes \left({}^{(4)}\ell_{[4]} + m {}^{(4)}\mathbb{1} \right) + \begin{pmatrix} 0 & 1 \\ 1 & 0 \end{pmatrix} \otimes i\mu\gamma_5 \right]$
	$= \frac{-i}{\ell_{[4]}^2 - \mu^2}$

Vertices

	$= \frac{i}{\sqrt{2}} \left[g_{[4]}^{\mu\nu}(p_{1[4]} - p_{2[4]})^\rho + g_{[4]}^{\nu\rho}(p_{2[4]} - p_{3[4]})^\mu + g_{[4]}^{\rho\mu}(p_{3[4]} - p_{1[4]})^\nu \right]$		
	$= ig_{[4]}^{\mu\rho}g_{[4]}^{\nu\sigma} - \frac{i}{2} \left[g_{[4]}^{\mu\nu}g_{[4]}^{\rho\sigma} + g_{[4]}^{\mu\sigma}g_{[4]}^{\nu\rho} \right]$		
	$= \frac{i}{\sqrt{2}} (p_{2[4]} - p_{3[4]})^\mu$		$= -\frac{i}{2} g_{[4]}^{\mu\nu}$
	$= \frac{i}{\sqrt{2}} {}^{(2)}\mathbb{1} \otimes \gamma^\mu$		$= -\frac{i}{\sqrt{2}} {}^{(2)}\mathbb{1} \otimes \gamma^\mu$
	$= \frac{i}{\sqrt{2}} {}^{(2)}\mathbb{1} \otimes \gamma_5$		$= -\frac{i}{\sqrt{2}} {}^{(2)}\mathbb{1} \otimes \gamma_5$

Outgoing Fields

	$= \begin{pmatrix} {}^{(4)}\bar{u}(p), & 0 \end{pmatrix}$		$= \begin{pmatrix} {}^{(4)}v(p) \\ 0 \end{pmatrix}$
---	---	--	---



CHAPTER 6

Renormalization

In order to arrive at physical predictions, we need to *renormalize* QCD one-loop amplitudes. Renormalization refers to the process of connecting the initial Lagrangian parameters, so called bare parameters, to physical quantities that can be measured in experiment. In a renormalizable theory, UV divergencies stemming from virtual corrections drop out once the bare parameters are connected to physical ones. The SM, and thus QCD, is a renormalizable theory [128, 152].

We renormalize one-loop amplitudes for processes involving massive quarks in a mixed scheme. The strong coupling is renormalized in the $\overline{\text{MS}}$ scheme and we apply a shift to decouple massive quark loops from the running of α_s . The wave-function and mass renormalization is done in the on-shell scheme. The mass renormalization is performed at the level of each color-ordered amplitude. Previously, we explicitly broke gauge invariance of the amplitudes by removing external leg self-energy Feynman diagrams from tree amplitudes that appeared in double cuts on one-leg bubble topologies (cf. Sec. 4.4). After recombination with the corresponding mass counterterms, gauge invariance of the one-loop amplitudes is restored. The coupling renormalization and massive quark decoupling as well as wave-function renormalization lead to a shift proportional to the tree amplitude. We provide all renormalization constants in FDH to be consistent with the computation of the one-loop amplitudes.

Furthermore, in Sec. 6.6 we work out the correct Root [153] n -tuple weights [82] for massive one-loop amplitudes. Using n -tuple files allows for an efficient a-posteriori reevaluation of matrix elements with different renormalization and factorization scales as well as couplings and parton distribution functions.

6.1. Multiplicative Renormalization

We will briefly review the standard multiplicative renormalization procedure (more details can be found in many textbooks [83, 84, 104]). In particular, we will see that mass counterterms have to be computed at the level of each color-ordered amplitude whereas the other renormalizations result in a shift proportional to the tree amplitude. We reparameterize the bare parameters in the Lagrangian by

$$\begin{aligned} \psi_0 &= \sqrt{Z_2} \psi_R, & A_0^\mu &= \sqrt{Z_3} A_R^\mu, \\ m_0 &= Z_m m_R, & g_0 &= Z_g g_R, \end{aligned} \tag{6.1}$$

where ψ_0 is the bare fermion field, A_0^μ the bare QCD gauge field, m_0 the bare mass and g_0 the bare strong coupling. In perturbation theory, we expand the renormalization constants Z_i and get to first order

$$\begin{aligned} Z_2 &\equiv 1 + \delta_2, & Z_3 &\equiv 1 + \delta_3, \\ Z_m &\equiv 1 + \delta_m, & Z_g &\equiv 1 + \delta_g, \end{aligned} \quad (6.2)$$

which leads to a split up of the Lagrangian. We get the original Lagrangian in which bare parameters are replaced by renormalized ones, and in addition, the so called *counterterm* Lagrangian that collects all terms in the renormalization constants δ_i and generates counterterm Feynman rules. The renormalization constants multiplying the counterterm Feynman rules for QCD vertices are given by

$$\begin{aligned} Z_{3g} - 1 &= Z_3^{3/2} Z_g - 1 \equiv \frac{3}{2} \delta_3 + \delta_g, \\ Z_{4g} - 1 &= Z_3^{4/2} Z_g^2 - 1 \equiv 2\delta_3 + 2\delta_g, \\ Z_{2q1g} - 1 &= Z_2 Z_3^{1/2} Z_g - 1 \equiv \delta_2 + \frac{1}{2} \delta_3 + \delta_g, \end{aligned} \quad (6.3)$$

for the three- and four-valent gluon interaction Z_{3g} and Z_{4g} as well as the quark-gluon interaction Z_{2q1g} . The Feynman rules for two-particle counterterms in Feynman gauge are given in Fig. 6.1.

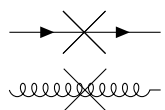
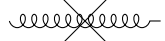
	$i((\not{p} - m_R)\delta_2 - \delta_m m_R) = P_{ct}^q(p) _{\delta_2} + P_{ct}^q(p) _{\delta_m}$
	$-ip^2\delta_3 g^{\mu\nu} = P_{ct}^{g,\mu\nu}(p)$

Figure 6.1: Feynman rules for QCD two-particle counterterms in Feynman gauge. The renormalization constants δ_i are defined in Eq. (6.2).

In principle, one has to compute all possible counterterms as specified by the counterterm Feynman rules. However, the simple counting exercise of Sec. 6.2.1 reveals that wavefunction and coupling renormalization of QCD one-loop amplitudes lead to a renormalization shift proportional to the tree. The remaining mass renormalization counterterms have to be computed explicitly, as spelled out in Sec. 6.3.

6.2. Coupling and Wave-Function Renormalization

6.2.1. Renormalization Shifts Proportional to Tree Amplitudes

We first observe that the combination of two propagators of the QCD spectrum with a counterterm insertion leads, for the parts independent of δ_m , to the original propagator multiplied by a renormalization constant. In particular, the counterterm insertion on

fermion propagators is given by

$$\begin{aligned} P^q(p)P_{\text{ct}}^q(p)|_{\delta_2}P^q(p) &= \frac{i(\not{p} + m_R)}{p^2 - m_R^2} (i(\not{p} - m_R)\delta_2) \frac{i(\not{p} + m_R)}{p^2 - m_R^2} \\ &= -\delta_2 \frac{i(\not{p} + m_R)}{p^2 - m_R^2} = -\delta_2 P^q(p), \end{aligned} \quad (6.4)$$

and that on gluon propagators by

$$\begin{aligned} P_{\mu\nu}^g(p)P_{\text{ct}}^{g,\nu\rho}P_{\rho\sigma}^g(p) &= \frac{-ig_{\mu\nu}}{p^2} (-ip^2\delta_3 g^{\nu\rho}) \frac{-ig_{\rho\sigma}}{p^2} \\ &= -\delta_3 \frac{-ig_{\mu\sigma}}{p^2} = -\delta_3 P_{\mu\sigma}^g(p). \end{aligned} \quad (6.5)$$

It remains to show that the multiplicative renormalization factor of each Feynman diagram is purely determined by the number and species of external particles. In order to do so, we count vertices and propagators of QCD tree amplitudes and multiply them with the corresponding renormalization factors, cf. Eqs. (6.3)-(6.5). We start with pure gluon amplitudes with n external particles. For each Feynman diagram contributing to the amplitude, we have

$$n = n_3 + 2n_4 + 2, \quad (6.6)$$

where n_3 and n_4 are the number of three- and four-valent gluon interactions. The number of gluon propagators $n_{\text{p,g}}$ is related to the number of vertices by

$$n_{\text{p,g}} = n_3 + n_4 - 1. \quad (6.7)$$

Therefore, the renormalization constants multiplying each Feynman diagram are given by

$$\begin{aligned} R(n, n_3, n_4, n_{\text{p,g}}) &= n_4 (2\delta_3 + 2\delta_g) + n_3 \left(\frac{3}{2}\delta_3 + \delta_g \right) - n_{\text{p,g}}\delta_3 \\ &= \frac{n}{2}\delta_3 + (n-2)\delta_g \equiv R(n), \end{aligned} \quad (6.8)$$

where we used Eqs. (6.6) and (6.7) as well as the counterterm Feynman rules. Thus the renormalization constants multiplying each Feynman diagram are only dependent on the number of external legs. Wave-function and coupling renormalization of pure gluon amplitudes are therefore proportional to the corresponding tree amplitude.

We perform a similar counting exercise for processes involving both quarks and gluons. For a Feynman diagram of n particles, with N_g gluons, N_q quarks, n_3 and n_4 gluon vertices and n_{qg} quark-gluon vertices, we get the relation

$$n = N_g + N_q = n_3 + 2n_4 + n_{\text{qg}} + 2. \quad (6.9)$$

The number of both gluon ($n_{\text{p,g}}$) and quark ($n_{\text{p,q}}$) propagators is given by

$$n_{\text{p,g}} = n_3 + n_4 + \left(\frac{N_q}{2} - 1 \right), \quad n_{\text{p,q}} = n_{\text{qg}} - 1 - \left(\frac{N_q}{2} - 1 \right). \quad (6.10)$$

The multiplicative renormalization factor $R(N_g, N_q, n_3, n_4, n_{\text{qg}}, n_{\text{p,g}}, n_{\text{p,q}})$ of each Feynman diagram with N_g gluons and N_q quarks therefore reads

$$\begin{aligned} R(\dots) &= n_4 (2\delta_3 + 2\delta_g) + n_3 \left(\frac{3}{2}\delta_3 + \delta_g \right) + n_{\text{qg}} \left(\delta_2 + \frac{1}{2}\delta_3 + \delta_g \right) - n_{\text{p,g}}\delta_3 - n_{\text{p,q}}\delta_2 \\ &= \frac{N_g}{2}\delta_3 + \frac{N_q}{2}\delta_2 + (n-2)\delta_g \\ &\equiv R(N_g, N_q), \end{aligned} \quad (6.11)$$

where we have used Eqs. (6.9) and (6.10) and the counterterm Feynman rules. As above, the wave-function and coupling renormalization shift for amplitudes containing quarks and gluons is proportional to a tree amplitude.

6.2.2. Renormalization Constants

Gluon Wave-Function Renormalization

We renormalize the gluon wave function in the on-shell scheme. The renormalization constant is fixed by the requirement that the residue of the gluon propagator is one. As a side effect, we do not have to calculate self-energy corrections on external gluon legs. The renormalization constant in the on-shell scheme calculated in FDH is given by

$$Z_3^{\text{os}} = 1 + \delta_3 = 1 - g_s^2 c_\Gamma \frac{2}{3} \left(\frac{1}{\epsilon} + \log \left(\frac{\mu^2}{m_{\text{os}}^2} \right) \right) + \mathcal{O}(g_s^4, \epsilon), \quad (6.12)$$

with a heavy quark with on-shell mass m_{os} running in the closed loop and the prefactor $c_\Gamma = (4\pi)^{-(2-\epsilon)} \Gamma(1+\epsilon) \Gamma^2(1-\epsilon)/\Gamma(1-2\epsilon)$ appearing in all integrals and renormalization constants. As we saw in Eq. (6.11), each of the N_g external gluons contributes a factor of $\frac{1}{2}\delta_3$ and we get contributions from each flavor in closed massive quark loops. Therefore the renormalization shift to a one-loop amplitude involving n particles and N_g gluons is given by

$$\begin{aligned} R_{\text{wf, gluon}} &= -g_s^2 c_\Gamma N_g \sum_{i=1}^{N_{hf}} \left(\frac{1}{3\epsilon} + \frac{1}{3} \log \left(\frac{\mu^2}{m_{i,\text{os}}^2} \right) \right) \mathcal{A}^{\text{tree}}(1, \dots, n) \\ &= -g_s^2 c_\Gamma N_g \Delta_3 \mathcal{A}^{\text{tree}}(1, \dots, n), \end{aligned} \quad (6.13)$$

where N_{hf} denotes the number of heavy-quark flavors with mass $m_{i,\text{os}}$.

Massive Quark Wave-Function Renormalization

We use the on-shell scheme to renormalize the massive quark wave function and the renormalization constant in FDH is given by

$$Z_2^{\text{os}} = 1 + \delta_2 = 1 - g_s^2 c_\Gamma C_F \left(\frac{3}{\epsilon} + 3 \log \left(\frac{\mu^2}{m_{\text{os}}^2} \right) + 5 \right) + \mathcal{O}(g_s^4, \epsilon), \quad (6.14)$$

with $C_F = \frac{N_C^2 - 1}{2N_C}$. Each massive external fermion contributes a factor of $\frac{1}{2}\delta_2$, see Eq. (6.11). Therefore, the renormalization shift to a one-loop amplitude involving n particles including external massive quarks is given by

$$\begin{aligned} R_{\text{wf, quark}} &= -g_s^2 c_\Gamma \sum_{i=1}^{N_{hf}} N_{Q_i} \frac{1}{2} C_F \left(\frac{3}{\epsilon} + 3 \log \left(\frac{\mu^2}{m_{i,\text{os}}^2} \right) + 5 \right) \mathcal{A}^{\text{tree}}(1, \dots, n) \\ &= -g_s^2 c_\Gamma \sum_{i=1}^{N_{hf}} N_{Q_i} \frac{\Delta_{2,i}}{2} \mathcal{A}^{\text{tree}}(1, \dots, n), \end{aligned} \quad (6.15)$$

where N_{hf} denotes the number of heavy-quark flavors and N_{Q_i} the number of external quarks of flavor i with on-shell mass $m_{i,\text{os}}$.

Coupling Renormalization

The coupling renormalization constant is fixed by a calculation of the vacuum polarization. We use the $\overline{\text{MS}}$ scheme, where the renormalization constant for the coupling computed in FDH is given by

$$Z_g^{\overline{\text{MS}}} = 1 + \delta_g = 1 - g_s^2 c_\Gamma \frac{1}{2} \left(\frac{11N_c - 2(N_f + N_{hf})}{3\epsilon} - \frac{N_c}{3} \right) + \mathcal{O}(\epsilon, g_s^4), \quad (6.16)$$

with N_f denoting the number of light and N_{hf} the number of heavy-quark flavors. The finite shift $\frac{N_c}{3}$ stems from the translation of the gauge coupling from standard $\overline{\text{MS}}$ to the FDH variant. As we saw in Eq. (6.11), each power N_{g_s} of the strong coupling g_s contributes to the renormalization shift

$$\begin{aligned} R_{\text{coupling}} &= -g_s^2 c_\Gamma \frac{N_{g_s}}{2} \left(\frac{11N_c - 2(N_f + N_{hf})}{3\epsilon} - \frac{N_c}{3} \right) \mathcal{A}^{\text{tree}}(1, \dots, n) \\ &= -g_s^2 c_\Gamma N_{g_s} \Delta_{\alpha_s} \mathcal{A}^{\text{tree}}(1, \dots, n). \end{aligned} \quad (6.17)$$

For pure QCD amplitudes, the power of g_s is given by $N_{g_s} = n - 2$ and that of α_s by $N_{\alpha_s} = N_{g_s}/2$. For amplitudes involving electroweak gauge bosons, the counting is reduced accordingly.

Heavy-Quark Decoupling

We work in the decoupling scheme [154]. That is, we require that heavy quarks decouple from the running of α_s at energies $E \ll m_{hf}$. Consequently, the appropriate $\overline{\text{MS}}$ coefficients for the running of α_s should be the same as in absence of the heavy quarks. Therefore, diagrams with a heavy quark loop are subtracted at zero momentum transfer and the decoupling shift for an n -particle amplitude with $\frac{n-2}{2}$ powers of the strong coupling α_s and N_{hf} decoupled heavy-quark flavors is given by

$$\begin{aligned} R_{\text{decoupling}} &= g_s^2 c_\Gamma N_{\alpha_s} \sum_{i=1}^{N_{hf}} \frac{2}{3} \log\left(\frac{\mu^2}{m_{i,\text{os}}}\right) \mathcal{A}^{\text{tree}}(1, \dots, n) \\ &= -g_s^2 c_\Gamma N_{\alpha_s} \sum_{i=1}^{N_{hf}} \Delta_i \mathcal{A}^{\text{tree}}(1, \dots, n), \end{aligned} \quad (6.18)$$

where the sum runs over heavy quark flavors N_{hf} and N_{α_s} denotes the power of the coupling α_s . For processes involving electroweak gauge bosons, the counting is reduced accordingly.

6.3. Mass Renormalization

For processes involving massive quarks, we need to renormalize the bare mass parameter. Its renormalization cannot be represented as a contribution proportional to the tree amplitude. For convenience we combine the computation of these contributions with the bubble diagrams. We explicitly compute mass-counterterm contributions using a dedicated recursive tree-like computation at the level of primitive loop amplitudes. The only source to the δ_m counterterm is the two-particle QCD counterterm interaction, cf. Fig. 6.1 and Eq. (6.3)

$$P_{\text{ct}}^q(p)|_{\delta_m} = -im_R \delta_m. \quad (6.19)$$

For double cut topologies with a gluon and a massive quark cut line, the mass counterterm is computed by replacing the two cut lines of the bubble with fermion propagators and the above insertion of Eq. (6.19) as shown in Fig. 6.2. The counterterm for a double cut topology with legs $1_g, \dots, j_{\bar{q}}$ joining in vertex one and $(j+1)_g, \dots, n_q$ in vertex two is thus computed by

$$\text{CT}_{1_g, \dots, j_{\bar{q}}; (j+1)_g, \dots, n_q} = Q(1_g, \dots, j_{\bar{q}}) P_{\text{ct}}^q(P_{1j})|_{\delta_m} \bar{Q}((j+1)_g, \dots, n_q), \quad (6.20)$$

where we denoted the momentum sum $P_{ij} = \sum_{k=i}^j p_k$ and Q and \bar{Q} denote quark and anti-quark Berends-Giele currents respectively. By adding these counterterms to each color-ordered one-loop amplitude, gauge invariance is restored at the level of primitive amplitudes, after initially being broken by the removal of external leg self-energy insertions

in one-leg bubble cuts, cf. Sec. 4.4.

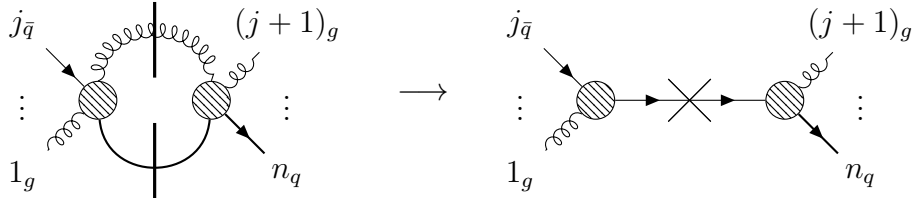


Figure 6.2: Generation of mass counterterms. For double cut topologies with a gluon and fermion cut line, we compute the corresponding counterterm by joining the two currents $Q(1_g, \dots, j_{\bar{q}})$ and $\bar{Q}((j+1)_g, \dots, n_q)$ with the fermion two-particle counterterm interaction.

We renormalize the mass in the *on-shell scheme*. The renormalization constant Z_m , computed in Feynman gauge and expressed in FDH is given by

$$\begin{aligned} Z_m^{\text{os}} &= 1 + \delta_m = 1 - C_F g_s^2 c_{\Gamma} \left(\frac{\mu^2}{m_{\text{os}}^2} \right)^{\epsilon} \left(\frac{3}{\epsilon} + 5 \right) + \mathcal{O}(g_s^4) \\ &= 1 - C_F g_s^2 c_{\Gamma} \left(\frac{3}{\epsilon} + 3 \log \left(\frac{\mu^2}{m_{\text{os}}^2} \right) + 5 \right) + \mathcal{O}(g_s^4, \epsilon). \end{aligned} \quad (6.21)$$

The color factor C_F evaluates to $C_F = 1$ if we compute the counter terms for color-ordered particles. In the on-shell scheme, the renormalization constant Z_m^{os} is fixed such that the pole of the propagator is described by the renormalized mass m_{os} , thereby fixing the finite terms.

6.4. Summary of Renormalization

In summary, we renormalize one-loop amplitudes in a mixed scheme. For external states we use the on-shell scheme and the gluon wave-function renormalization receives contributions from all active heavy quark flavors. We renormalize the mass in the on-shell scheme and compute mass renormalization counterterms explicitly at the level of each color-ordered amplitude. The QCD coupling is renormalized in $\overline{\text{MS}}$, where we decouple massive quarks from the running of α_s . The renormalized one-loop amplitude is obtained by combining all tree-like renormalization shifts with the mass renormalized one-loop amplitude

$$\begin{aligned} \mathcal{A}_{(\text{ren})}^{\text{1-loop}} &= \mathcal{A}_{(\text{mass ren})}^{\text{1-loop}} + R_{\text{wf,quark}} + R_{\text{wf,gluon}} + R_{\text{coupling}} + R_{\text{decoupling}} \\ &= \mathcal{A}_{(\text{mass ren})}^{\text{1-loop}} - g_s^2 c_{\Gamma} \left(\sum_{i=1}^{N_{hf}} N_{Q_i} \frac{\Delta_{2,i}}{2} + N_g \Delta_3 + N_{\alpha_s} \left(\Delta_{\alpha_s} + \sum_{i=1}^{N_{hf}} \Delta_i \right) \right) \mathcal{A}^{\text{tree}}, \end{aligned} \quad (6.22)$$

where N_{hf} denotes the number of heavy flavors, N_{Q_i} the number of external heavy quarks of flavor i , N_g the number of external gluons and N_{α_s} the power of α_s (at Born level). The renormalization constants in the FDH scheme are summarized in Table 6.1.

Table 6.1.: Renormalization constants used in this thesis. Here μ is the renormalization scale, m_i are the masses for heavy quarks, N_f is the number of light flavors, N_{hf} the number of heavy flavors, and N_c the number of colors. A common factor of $-g_s^2 c_\Gamma$ has been factored out.

Renormalization	Scheme	Constant
Heavy-quark wave function	on-shell	$\Delta_{2,i} = \frac{N_c^2 - 1}{2N_c} \left(\frac{3}{\epsilon} + 3 \log \frac{\mu^2}{m_i^2} + 5 \right)$
Light-quark wave function	on-shell	0 (UV+IR cancellation)
Quark mass	on-shell	$\Delta_{m_i} = \Delta_{2,i}$
Gluon wave function	on-shell	$\Delta_3 = \sum_{i=1}^{N_{hf}} \left(\frac{1}{3\epsilon} + \frac{1}{3} \log \frac{\mu^2}{m_i^2} \right)$
QCD coupling	$\overline{\text{MS}}$	$\Delta_{\alpha_s} = \frac{1}{\epsilon} \left(\frac{11}{3} N_c - \frac{2}{3} (N_f + N_{hf}) \right) - \frac{N_c}{3}$
Decoupling shift	—	$\Delta_i = -\frac{2}{3} \log \frac{\mu^2}{m_i^2}$

6.5. Scheme Shift From FDH to 't Hooft-Veltman

We use the FDH variant of dimensional regularization in intermediate steps to regularize UV and IR divergences. At the end we convert the renormalized amplitude to the HV scheme [128] which is often more convenient for comparisons and interfacing with Monte-Carlo generators. The conversion of a renormalized one-loop amplitude $\mathcal{A}_{(ren)}^{1\text{-loop}}$ is performed by a finite shift, see e.g. [147]

$$\mathcal{A}_{(ren)}^{1\text{-loop}, \text{HV}} = \mathcal{A}_{(ren)}^{1\text{-loop}, \text{FDH}} - g_s^2 c_\Gamma \left(N_g \frac{N_c}{6} + N_q \frac{N_c^2 - 1}{4N_c} \right) \mathcal{A}^{\text{tree}}, \quad (6.23)$$

where N_g denotes the number of gluons and N_q the number of light quarks in the respective amplitude.

6.6. Scale Variation Using N -tuple Data

We provide NLO results in the form of Root [153] n -tuple files [82]. The n -tuple files allow to reevaluate generic IR-safe observables with different renormalization and factorization scales as well as different PDFs. They store the relevant information to reevaluate observables without recomputing the short-distance matrix elements, which is possible due to the particular simple form of the parts of the virtual matrix element that

depend on μ_R . This possibility for a-posteriori variations of scales and PDFs make the efficient estimation of uncertainties associated to NLO predictions possible.

In this section, we analyze the dependence of virtual cross sections on the unphysical renormalization scale. We neglect the implicit dependence via the strong coupling for this discussion, since it amounts to a global prefactor and can be treated as described in [82]. In particular, we identify additional renormalization terms with μ_R dependence which are present in calculations with massive external particles and have to be considered in order to supply the correct data for n -tuple files.

The dependence of the virtual cross section on the unphysical scale μ_R is introduced in dimensional regularization to enforce a mass dimension of one for the gauge couplings $g \rightarrow \mu_R^\epsilon g$. As a consequence, there is an explicit dependence on μ_R in virtual NLO matrix elements. We can write an unrenormalized, one-loop amplitude, with couplings stripped off, as

$$\mathcal{A}^{\text{1-loop}}(\mu_R) = \tilde{\mu}_R^{2\epsilon} \left[\frac{a_2}{\epsilon^2} + \frac{a_1}{\epsilon} + a_0 \right], \quad (6.24)$$

where we use the dimensionless scale $\tilde{\mu}_R = \frac{\mu_R}{\text{GeV}}$ to simplify the argument in the following. We generically have ratios of renormalization scale μ_R and involved physical scales, from which we build dimensionless quantities by

$$\left(\frac{\mu_R}{s} \right)^{2\epsilon} = \tilde{\mu}_R^{2\epsilon} \left(\frac{\text{GeV}}{s} \right)^{2\epsilon}. \quad (6.25)$$

Note, that Eq. (6.24) is valid for any number of involved physical scales. We then expand $(\tilde{\mu}_R)^{2\epsilon}$ and obtain

$$\tilde{\mu}_R^{2\epsilon} = 1 + \log(\tilde{\mu}_R^2)\epsilon + \frac{1}{2} \log(\tilde{\mu}_R^2)^2 \epsilon^2 + \mathcal{O}(\epsilon^3), \quad (6.26)$$

such that the explicit $\tilde{\mu}_R$ dependence of Eq. (6.24) becomes transparent

$$\mathcal{A}^{\text{1-loop}}(\mu_R) = \left[\frac{a_2}{\epsilon^2} + \frac{a_1 + a_2 \log(\tilde{\mu}_R^2)}{\epsilon} + a_0 + a_1 \log(\tilde{\mu}_R^2) + \frac{1}{2} a_2 \log(\tilde{\mu}_R^2)^2 \right]. \quad (6.27)$$

This formula contains double and single poles due to infrared divergencies as well as single poles due to ultraviolet divergencies. The difference of the finite part of the amplitude computed at two distinct scales $\mu_{R,1}$ and $\mu_{R,2}$ is then given by

$$\begin{aligned} \mathcal{A}_{|\epsilon=0}^{\text{1-loop}}(\mu_{R,2}) - \mathcal{A}_{|\epsilon=0}^{\text{1-loop}}(\mu_{R,1}) &= a_1 \log \left(\frac{\tilde{\mu}_{R,2}^2}{\tilde{\mu}_{R,1}^2} \right) + \frac{1}{2} a_2 \left[\log(\tilde{\mu}_{R,2}^2)^2 - \log(\tilde{\mu}_{R,1}^2)^2 \right] \\ &= [a_1 + a_2 \log(\tilde{\mu}_{R,1}^2)] \log \left(\frac{\tilde{\mu}_{R,2}^2}{\tilde{\mu}_{R,1}^2} \right) + \frac{1}{2} a_2 \log \left(\frac{\tilde{\mu}_{R,2}^2}{\tilde{\mu}_{R,1}^2} \right)^2, \end{aligned} \quad (6.28)$$

which we can parameterize in terms of the weights w_1 and w_2

$$w_1 \equiv a_1 + a_2 \log(\tilde{\mu}_{R,1}^2) = \mathcal{A}_{|\epsilon=-1}^{\text{1-loop}}, \quad w_2 \equiv a_2 = \mathcal{A}_{|\epsilon=-2}^{\text{1-loop}}. \quad (6.29)$$

The above parameterization has the advantage, that only ratios of renormalization scales have to be considered and no explicit dimensionless scales have to be constructed. The finite part of an unrenormalized one-loop amplitude at scale $\tilde{\mu}_{R,2}$ can thus be extrapolated from that at scale $\tilde{\mu}_{R,1}$ by adding the terms in Eq. (6.28)

$$\mathcal{A}_{|\epsilon^0}^{1\text{-loop}}(\mu_{R,2}) = \mathcal{A}_{|\epsilon^0}^{1\text{-loop}}(\mu_{R,1}) + w_1 \log\left(\frac{\tilde{\mu}_{R,2}^2}{\tilde{\mu}_{R,1}^2}\right) + \frac{1}{2}w_2 \log\left(\frac{\tilde{\mu}_{R,2}^2}{\tilde{\mu}_{R,1}^2}\right)^2. \quad (6.30)$$

The above considerations are independent of whether the involved particles are massive or not. In the renormalization procedure, see the previous sections, additional sources of μ_R dependence are introduced. Whereas mass and wave-function renormalization lead to terms in which the logarithmic dependence in the finite part has the same prefactor as the single pole, the shift due to charge renormalization has no dependence on μ_R but contributes to the single pole. Its schematic contributions in an ϵ expansion ($\epsilon^{-1}, \epsilon^0$) is given by

$$R_{\text{charge}} = (a_{1,c}, a_{0,c}), \quad (6.31)$$

with coefficients a_i that do not contain any logarithms. The decoupling shift for massive quarks however has finite logarithms but no contribution to the single pole

$$R_{\text{decoupling}} = (0, a_{0,dec} \log(\tilde{\mu}_R^2)). \quad (6.32)$$

The weight w_1 should correctly parameterize simple logs of μ_R in the finite part. To account for the absence of μ_R dependence in the charge renormalization and the fact that the decoupling shift does not have a single-pole contribution, the weights for renormalized amplitudes are defined as

$$w_1 = \hat{\mathcal{A}}_{|\epsilon^{-1}}^{1\text{-loop}} - a_{1,c} + a_{0,dec}, \quad w_2 = \hat{\mathcal{A}}_{|\epsilon^{-2}}^{1\text{-loop}}. \quad (6.33)$$

With these weights, one can use Eq. (6.28) to extrapolate the virtual cross section to different values of μ_R for processes involving massive particles.

We provide the weights in Eq. (6.33) for each phase space point together with the finite part of the matrix element squared. They are stored in n -tuple files alongside information like the phase-space point, the involved partons, the factorization and renormalization scales, the Bjorken-x and the corresponding PDF weights. We make extensive use of a-posteriori scale variations in the phenomenological results presented in the following Chapters 7-11.

Part 2:

$Wb\bar{b} + n$ Jet Production ($n = 0, 1, 2, 3$)

CHAPTER 7

Introduction to $Wb\bar{b} + n$ Jet Production

In this part of the thesis, we present phenomenological predictions obtained using the methods presented in Chapters 3–6. In particular, we provide NLO QCD predictions for $Wb\bar{b}$ production in association with up to three light jets at the LHC, as shown in Ref. [21]. These processes have diverse final states including leptons, heavy and light jets and missing transverse energy, and so they provide a natural testing ground for precise measurements of complex signatures at the LHC. Furthermore, $Wb\bar{b}$ signatures are reducible and irreducible backgrounds to HW associated production, with the Higgs boson decaying into a bottom-quark pair ($b\bar{b}$). Due to its relevance for constraining the coupling of the Higgs to b quarks, this process receives currently increased attention by both LHC experiment. We provide results as a function of the light-jet multiplicity and thus add jet probes to the core production process. This allows to construct ratio observables [4, 155–158] which give a further handle to improve the understanding of these QCD processes.

The earliest NLO QCD studies of $Wb\bar{b}$ production appeared about twenty years ago [80] and were already included in the first version of the MCFM program [159]. Those initial predictions were performed in the context of the four-flavor number scheme (4FNS) though they approximate all quarks but the top quark to be massless (employing the one-loop helicity amplitudes of Ref. [11]). Results including full b -mass effects appeared in Refs. [14, 79] with on-shell W bosons and subsequent refinements in Refs. [26, 160]. NLO QCD corrections for $Wb\bar{b} + 1$ -jet production were obtained in Ref. [15]. Also studies with more inclusive samples of b jets have been carried out. In Ref. [161] NLO QCD corrections were computed for $W + b + 1$ -light jet production, while NLO QCD results were presented for W production in association with a single b jet in Refs. [162, 163]. Several experimental measurements on this process have been carried out by the CDF experiment for W production with one or two b jets [164] (including samples with light jets), by the D0 experiment for inclusive W production with a single b jet [165], by the ATLAS experiment for W with up to two b jets [75] and also by the CMS experiment for W and two b jets [76, 77].

The prediction we provide in Ref. [21], and show in this part of the thesis, present for the first time NLO QCD corrections to $Wb\bar{b} + 2$ -jet and $Wb\bar{b} + 3$ -jet production, and for completeness we recompute the cases with zero and one light jet. These $\mathcal{O}(\alpha_s)$ corrections are computed to the corresponding leading-order (LO) results at $\mathcal{O}(\alpha_s^{2+n}\alpha_f^2)$, with n the number of light jets in the process. At higher orders in the fine-structure constant α_f , the same collider signatures can be obtained from processes involving top quarks which we do not consider here. Since the early calculations of inclusive $Wb\bar{b}$ production [14, 79, 80] it has been observed that the NLO QCD corrections are quite large. This is mainly due to the opening of a gluon-initiated channel as part of the real contributions to the NLO QCD

corrections, as well as to the release of a LO kinematical constraint which fixes the p_T of the W boson to that of the $b\bar{b}$ system. In other words, these processes suffer from giant K -factors [9]. The corrections to $Wb\bar{b} + 1$ -jet production on the other hand show better behavior [15], and it is expected that for even larger light-jet multiplicities, K -factors will be more moderate. We show that this is indeed the case in our results.

Initial attempts to obtain reliable predictions in spite of giant K -factors for $Wb\bar{b}$ production have focused on exclusive analyses [14], including jet vetoes. But sensitivity to the p_T^{veto} cut tends to spoil the convergence of the perturbative series [166]. Instead, we employ exclusive sums [81] as an alternative to stabilize these predictions, considering exclusive combinations of up to two light jets. The perturbative series for exclusive-sum observables is better behaved, as confirmed by comparison to LHC data for $W + 1$ -jet production [59, 61]. Results based on exclusive sums can contain some large next-to-next-to-leading order (NNLO) corrections, and so in the lack of a full NNLO QCD study of $Wb\bar{b}$ production, our results represent a useful parton-level prediction for $Wb\bar{b}$ observables. We put particular emphasis on observables associated to $H(\rightarrow b\bar{b})W$ production, that is we study the $p_T^{b\bar{b}}$, p_T^W , and $M_{b\bar{b}}$ exclusive-sum distributions.

We obtained our results using the `BlackHat` library [32] after a significant upgrade and the addition of new algorithms, as described in Chapters 3–6. Most notably, the new version of the program allows to compute one-loop matrix elements including massive fermions. For the real-emission corrections we use the massive-dipole formalism [167], as implemented in the `COMIX` package [168] which is part of the `SHERPA` Monte Carlo program [78]. We store our results in a set of n -tuple files [82] which allow fast a-posteriori studies of our results, including scale variations, PDF and α_s reweighting as well as the evaluation of additional observables.

This part of the thesis is organized as follows. In the present chapter, we give our calculational setup, details about coupling schemes and input parameters employed as well as the choices for the renormalization and factorization scales. In Chap. 8, we validate our new matrix elements and provide thorough checks against automated tools and higher-precision targets. In Chap. 9, we present and analyze the results obtained.

7.1. Calculational Setup

We provide NLO QCD prediction for the production of $Wb\bar{b}$ in association with n light jets ($n = 0, 1, 2, 3$) at the LHC $\sqrt{s} = 13$ TeV. We treat the decay of the charged vector boson to a massless charged-lepton and its corresponding (anti-)neutrino at the amplitude level. The partonic subprocesses of Born and virtual contributions can be obtained from the following subprocesses

$$n = 0 : \quad 0 \rightarrow Wb\bar{b}q\bar{q}' , \tag{7.1a}$$

$$n = 1 : \quad 0 \rightarrow Wb\bar{b}q\bar{q}'g , \tag{7.1b}$$

$$n = 2 : \quad 0 \rightarrow Wb\bar{b}q\bar{q}'gg , \quad 0 \rightarrow Wb\bar{b}q\bar{q}'Q\bar{Q} , \tag{7.1c}$$

$$n = 3 : \quad 0 \rightarrow Wb\bar{b}q\bar{q}'ggg , \quad 0 \rightarrow Wb\bar{b}q\bar{q}'Q\bar{Q}g , \tag{7.1d}$$

by crossing. Light-quark flavors are denoted by the labels q and Q and we consider bottom quarks to be massive (except when explicitly stated otherwise). We include contributions from closed fermions loops of light quarks as well as top and bottom quarks. In Fig. 7.1 we show sample Feynman diagrams for the seven-parton amplitudes. Real-emission subprocesses are obtained from the above list by adding a gluon or replacing a gluon by a $Q'\bar{Q}'$ pair.

We generate fixed order parton-level predictions and do not include parton-shower effects. All observables considered will be constructed from events containing exactly two observable b jets, defined in an infrared safe way [169]. We do not introduce any corrections due to possible mistagging of heavy and/or light jets.

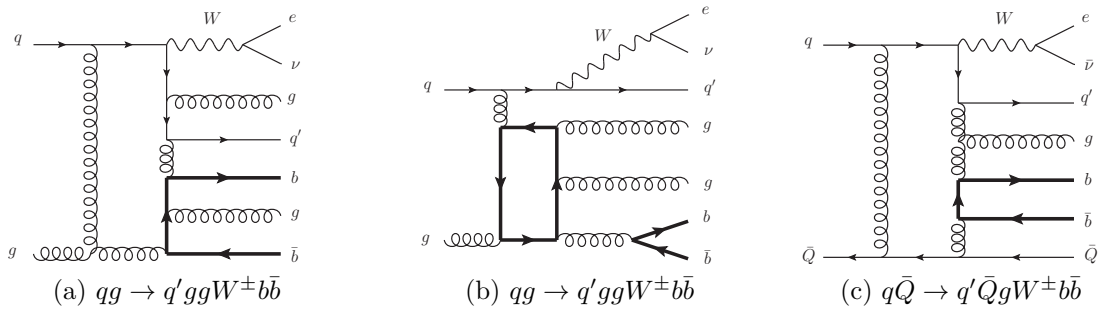


Figure 7.1.: Sample one-loop diagrams contributing to $pp \rightarrow W b\bar{b} + 3\text{-jet}$ production. Massive quark lines are printed thick and the diagram (b) displays a contribution from closed loops of top and bottom quarks.

7.2. Monte Carlo Integration

We obtain NLO QCD predictions by using the **SHERPA** Monte Carlo program [78] to integrate Born, virtual and real-radiation matrix elements. The virtual matrix elements are provided by our new **BlackHat** library. In order to increase the efficiency of the phase-space integration, we exploit the color structure of virtual matrix elements by splitting them into leading and subleading color terms [12, 123]. The subleading color terms are computationally expensive. However, due to their color suppression, they need to be evaluated less often to reach a given total statistical-integration error and we sample the two parts independently over phase space.

Before a numerical integration can be performed, the infrared singularities that appear in real-emission corrections have to be canceled explicitly against their counterparts in virtual matrix elements. In our calculation, we use the subtraction scheme based on massive dipoles [167]. In particular, we use the automated implementation provided by the **COMIX** package [168], which is part of the **SHERPA** library [78]. The latter implementation has been checked extensively, for example in the recent calculation of $t\bar{t}$ production in association with up to three light jets [170].

Furthermore, we use the **SHERPA** library to handle subprocess generation and mappings, the integration techniques necessary to deal with complex final-state phase spaces as well as the internal analysis package. All results that we provide are fixed-order parton-level predictions and we include neither parton-shower effects nor hadronization corrections or other non-perturbative effects. We use the flexible **ROOT** [153] n -tuple file format to store our results. This allows for a-posteriori variations of the strong coupling, PDFs and choices of renormalization and factorization scales in our NLO QCD results. The n -tuple format was developed in Ref. [82] and the correct definition of the weights for one-loop amplitudes involving massive particles can be found in Sect. 6.6.

7.3. Input Parameters: Partons Distributions, Couplings and Masses

For our predictions we use PDFs from CT14 [171], with LO (CT14llo_NF4) and NLO (CT14nlo_NF4) PDF sets, as implemented in the LHAPDF library [172]. The corresponding strong coupling is given by $\alpha_s(M_Z) = 0.125$ at LO and $\alpha_s(M_Z) = 0.1128$ at NLO. We evolve $\alpha_s(\mu)$ with the QCD beta function for four massless quark flavors, for all μ . This is achieved by introducing a decoupling shift for massive quarks, see Chap. 6. We use a one-loop running of α_s at LO and a two-loop running at NLO. We choose the quark masses consistent with the PDF sets and use a bottom-quark mass of $m_b = 4.75$ GeV and a top-quark mass of $m_t = 172$ GeV. The top-quark mass appears in closed-loop contributions.

The electroweak parameters are obtained in the G_μ scheme [173] at leading order in the electroweak coupling. This fixes the W -boson couplings to fermions with the SM input parameters as specified in Table 7.1. We compute the parameters $\alpha_f(M_Z)$, $\sin^2(\theta_W)$ and g_W^2 using the tree-level relations

$$\begin{aligned}\sin^2(\theta_W) &= \left(1 - \frac{M_W^2}{M_Z^2}\right) , & \alpha_f(M_Z) &= \frac{\sqrt{2}}{\pi} G_F M_W^2 \sin^2(\theta_W) , \\ g_W^2 &= \frac{4\pi\alpha_f(M_Z)}{\sin^2(\theta_W)} .\end{aligned}\tag{7.2}$$

Mass and width of the W boson are specified in Table 7.1 and the lepton-pair invariant mass follows a relativistic Breit-Wigner distribution. We approximate the CKM matrix by a unit matrix. This results in a small change of the total cross sections for the setup we use, as estimated by LO evaluations with the full CKM matrix. We find that these differences are of the order 1% for $Wb\bar{b}$ production and below 0.5% for $Wb\bar{b} + 1$ -jet and $Wb\bar{b} + 2$ -jet production.

We include contributions from virtual bottom and top quarks, and we confirm the expected percent-level effect on cross-sections [3, 13, 174]. We work with a single massless lepton pair, an approximation that can be applied to the electron or muon families and we treat all light quarks (u, d, s, c) as massless particles.

Parameter	Value
G_F	$1.1663787 \times 10^{-5} \text{ GeV}^{-2}$
M_W^{OS}	80.385 GeV
M_Z^{OS}	91.1876 GeV
Γ_W	2.085 GeV
$\alpha_f(M_Z)$	1/132.23 (calculated)
$\sin^2(\theta_W)$	0.22290 (calculated)
g_W^2	0.42635 (calculated)

Table 7.1.: Electroweak parameters used in this work. We use the G_μ scheme with real parameters and leading order relations. The input parameters are chosen in accordance with 2016 PDG values [107].

7.4. Kinematics, Observables and Exclusive Sums

In our phenomenological analysis, we use several standard observables. The pseudorapidity η and the angular separation between any two objects (partons, jets, leptons) ΔR are given by

$$\eta = -\ln \left(\tan \frac{\theta}{2} \right), \quad \Delta R = \sqrt{(\Delta\phi)^2 + (\Delta\eta)^2}, \quad (7.3)$$

where θ denotes the polar angle with respect to the beam axis, $\Delta\phi$ the difference in the azimuthal angle in the plane transverse to the beam axis and $\Delta\eta$ the difference in the pseudorapidities. Furthermore, the transverse energy of the W boson E_T^W and the total partonic transverse energy \hat{H}'_{T} are given by

$$E_T^W = \sqrt{M_W^2 + (p_T^W)^2}, \quad \hat{H}'_{\text{T}} = \sum_j p_{\text{T}}^j + E_{\text{T}}^W, \quad (7.4)$$

where the sum runs over all final state partons j , independent of whether or not they are inside a jet that passes the cuts. The scalar transverse momentum p_T of a parton is given by $p_T = \sqrt{p_x^2 + p_y^2}$. The total partonic transverse energy is not directly measurable. Nevertheless, it is a suitable candidate for choosing unphysical renormalization and factorization scales since changing the cuts does not affect the matrix element at a given phase-space point. We define jet invariant masses by

$$M_{ij}^2 = \left(p_i^{\text{jet}} + p_j^{\text{jet}} \right)^2, \quad (7.5)$$

and jets are labeled in order of decreasing transverse momentum p_T . The transverse mass of the W boson is computed from the kinematics of its decay products

$$M_T^W = \sqrt{2E_T^e E_T^\nu (1 - \cos(\Delta\phi_{e\nu}))} . \quad (7.6)$$

The predictions we show in Section 9.3 are based on exclusive sums [81]. We can exploit our high-multiplicity results to build these observables. The main idea is to replace tree-like contributions in NLO corrections by the corresponding full NLO results. In order to avoid double counting, one combines exclusive (with respect to the presence of an extra light jet) predictions σ_n^{exc} for all but the last multiplicity under consideration, and an inclusive prediction σ_n^{inc} for the last. We use exclusive sums for observables in $Wb\bar{b}+X$ production (0 light jets) and use our high-multiplicity results to define the exclusive sums labeled ‘NLO+’ and ‘NLO++’:

$$\sigma_0^{\text{NLO+}} = \sigma_0^{\text{exc}} + \sigma_1^{\text{inc}} , \quad \sigma_0^{\text{NLO++}} = \sigma_0^{\text{exc}} + \sigma_1^{\text{exc}} + \sigma_2^{\text{inc}} . \quad (7.7)$$

7.5. Dynamical Scale Choice

We use a standard approach to dynamical scale setting with a functional form of the central scale defined by $\mu_0 = \hat{H}'_T/2$, see Eq. (7.4), and we keep factorization and renormalization scales equal, $\mu_R = \mu_F = \mu_0$. We compute the renormalization and factorization scale dependence of cross sections by using correlated variations around the central scale μ_0 by factors of $(1/2, 1/\sqrt{2}, 1, \sqrt{2}, 2)$. An independent variation of those scales lead to similar results as with the correlated variations. We will label results for leading-order QCD with the central scale $\mu_0 = \hat{H}'_T/2$ by “LO” and the corresponding results at next-to-leading order QCD by “NLO”.

CHAPTER 8

Validation of the New Matrix Elements

We implemented the virtual matrix elements required for $Wb\bar{b}$ production in association with up to three light jets in a new version of the `BlackHat` library [32], which includes significant upgrades for the computation of loop amplitudes with massive particles. The library is based on the methods presented in Chapters 3-6 of this thesis. In this chapter, we provide thorough checks of the virtual matrix elements required for $Wb\bar{b} + n\text{-jet}$ ($n = 0, 1, 2, 3$) by comparing to both higher-precision targets and automated tools. We partly showed the checks presented in this chapter in Ref. [21].

8.1. Numerical Stability of Virtual Matrix Elements

Previous computations with numerical unitarity have shown a good numerical stability even for high-multiplicity one-loop matrix elements (see for example [2, 12]). However, there exist regions of phase space where on-shell loop-momentum parameterizations (which can e.g. be found in [136]) can break down. In particular, this occurs if Gram determinants¹, which are found in on-shell solutions to the loop momentum, are close to zero. This type of configuration can lead to incomplete cancellations of large contributions and thereby induce a loss of numerical precision.

We implemented a rescue system to control the precision of the computation, which identifies unstable phase-space points by performing checks at several stages of the calculation. With some minor adaptations we use the same implementation as described in [12, 32]. Whenever any of those checks fails, we switch to a higher precision computation locally (i.e. only for the part which failed the check), using higher-precision arithmetic as provided by the QD library [175]. The fraction of time spent on these recomputations is normally small. Specifically, we test the vanishing of higher-rank tensor coefficients. Tensors with rank greater than n , for n -point topologies ($n = 1, 2, 3, 4, 5$) must vanish given the interactions governed by the renormalizable QCD Lagrangian. Computing the value of an additional higher-rank tensor coefficient comes without much extra cost. We apply this check at the level of bubble coefficients. Through subtractions, this captures any loss of precision in the computation of the higher-point topologies related to the specific bubble and allows to recompute only the numerically unstable part of the computation. Furthermore, we check that parts of the known IR and UV divergence structure [176] of a given matrix element have been reproduced correctly. This assess the precision at

¹The Gram matrix is the matrix of all possible inner products of external momenta and its determinant is called the Gram determinant.

the level of a complete amplitude calculation. In consequence, this check demands a full recomputation in the case of failure.

We study the numerical stability of our new massive one-loop matrix elements by comparing results computed in standard production mode with computations fully performed in quadruple precision [175] (up to 32 digits of precision).

We produce distributions of the logarithmic relative error δ

$$\delta = \log_{10} \left(\frac{|d\sigma_V^{\text{prod}} - d\sigma_V^{\text{HP}}|}{|d\sigma_V^{\text{HP}}|} \right) \quad (8.1)$$

for the poles $1/\epsilon^2$, $1/\epsilon^1$ and the finite part ϵ^0 , with ϵ being the dimensional regularization parameter. The superscripts “prod” and “HP” mean standard production evaluation and quadruple floating-point evaluation respectively. We sample over physical phase space, as defined for the phenomenological study in the next Chapter 9, and compute for $\mathcal{O}(10^5)$ events for sample subprocesses of the most complex types in our calculations.

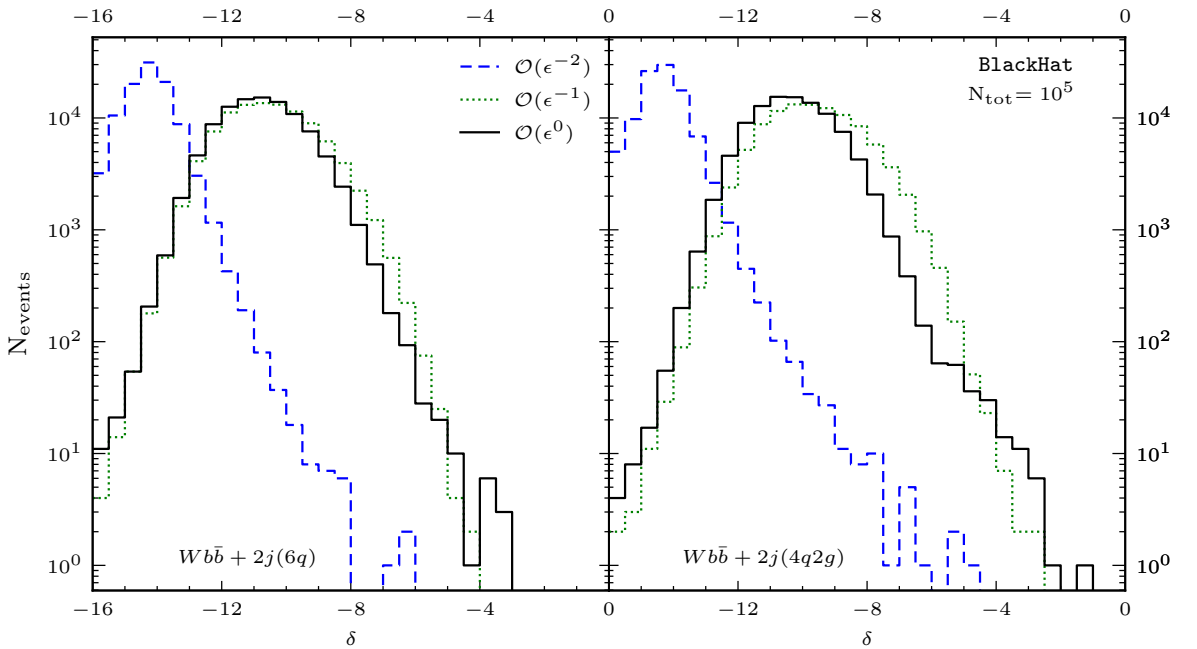


Figure 8.1.: Relative logarithmic error distributions of full-color matrix elements for two types of subprocesses contributing to $Wb\bar{b} + 2$ -jet production, that is $0 \rightarrow Wb\bar{b}q\bar{q}'Q\bar{Q}$ (left) and $0 \rightarrow Wb\bar{b}q\bar{q}'gg$ (right). We use a set of 10^5 phase-space points sampled for the LHC with $\sqrt{s} = 13$ TeV in the same way as the phenomenological study presented in Chapter 9. We use a dedicated calculation in quadruple precision for computing target results to compare against. The dashed (blue) line represents the precision of the double pole, the dotted (green) line represents the single pole and the solid (black) line the precision of the finite piece of the calculation.

In Fig. 8.1 and Fig. 8.2, we show results for $Wb\bar{b} + 2\text{-jet}$ and $Wb\bar{b} + 3\text{-jet}$ production, respectively. We include the two types of subprocesses for $Wb\bar{b} + 2\text{-jet}$: those with four quarks and two gluons (associated by crossing two partons into the final state to the process $0 \rightarrow Wb\bar{b}q\bar{q}'gg$), and those with six quarks ($0 \rightarrow Wb\bar{b}q\bar{q}'Q\bar{Q}$). For $Wb\bar{b} + 3\text{-jet}$ we show the cases with four quarks and three gluons ($0 \rightarrow Wb\bar{b}q\bar{q}'ggg$), and with six quarks and one gluon ($0 \rightarrow Wb\bar{b}q\bar{q}'Q\bar{Q}g$). Each figure shows the estimated precision of the computation of the double and single pole as well as the finite piece for each amplitude. The double pole is commonly computed with an accuracy of 14 digits, while the single pole and the finite piece distributions peak at about 10 digits.

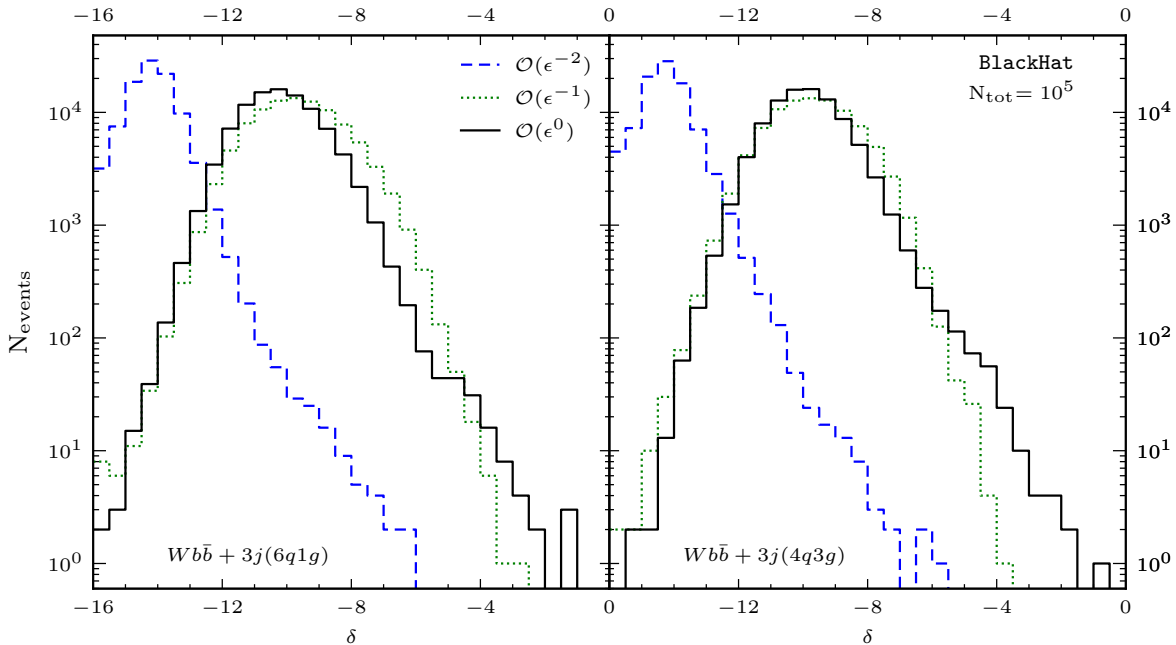


Figure 8.2.: As in Fig. 8.1 but for $Wb\bar{b} + 3\text{-jet}$ production. This time, we consider only leading-color contributions to the one-loop matrix elements. To the left we show subprocesses associated to $0 \rightarrow Wb\bar{b}q\bar{q}'Q\bar{Q}g$, and on the right the ones associated to $0 \rightarrow Wb\bar{b}q\bar{q}'ggg$.

Overall, our computation has a very good precision, with less than 1 in 10^4 phase-space points computed to an accuracy worse than three digits. We attribute some of the few points in the low-precision tail to the fact that the scale set by the bottom mass m_b and other scales of the problem s_{ij} at sufficiently high energy are separated by several orders of magnitude. The ratios of the form $(m_b^2/s_{ij})^k$ enter loop-momentum parameterizations and can cause loss of precision. However, we have observed that the contribution of the points in the low-precision tail is significantly smaller than the total statistical errors for the observables studied.

	Process	$\Delta_{V,\epsilon^{-2}}$	$\Delta_{V,\epsilon^{-1}}$	Δ_{V,ϵ^0}
$n = 0$	$u\bar{d} \rightarrow e^+ \bar{\nu}_e b\bar{b}$	$9.508 \cdot 10^{-14}$	$5.925 \cdot 10^{-13}$	$3.338 \cdot 10^{-12}$
	$d\bar{u} \rightarrow e^- \nu_e b\bar{b}$	$9.989 \cdot 10^{-14}$	$6.602 \cdot 10^{-13}$	$3.507 \cdot 10^{-12}$
$n = 1$	$u\bar{d} \rightarrow e^+ \bar{\nu}_e b\bar{b}g$	$6.577 \cdot 10^{-13}$	$4.114 \cdot 10^{-11}$	$5.329 \cdot 10^{-10}$
	$d\bar{u} \rightarrow e^- \nu_e b\bar{b}g$	$7.224 \cdot 10^{-13}$	$4.515 \cdot 10^{-11}$	$6.012 \cdot 10^{-10}$
$n = 2$	$u\bar{d} \rightarrow e^+ \bar{\nu}_e b\bar{b}d\bar{d}$	$4.709 \cdot 10^{-12}$	$2.711 \cdot 10^{-10}$	$3.217 \cdot 10^{-9}$
	$u\bar{d} \rightarrow e^+ \bar{\nu}_e b\bar{b}s\bar{s}$	$5.351 \cdot 10^{-12}$	$2.185 \cdot 10^{-10}$	$3.100 \cdot 10^{-9}$
	$u\bar{d} \rightarrow e^+ \bar{\nu}_e b\bar{b}gg$	$1.036 \cdot 10^{-11}$	$7.192 \cdot 10^{-10}$	$1.007 \cdot 10^{-8}$
	$d\bar{u} \rightarrow e^- \nu_e b\bar{b}dd\bar{d}$	$5.300 \cdot 10^{-12}$	$2.524 \cdot 10^{-10}$	$2.774 \cdot 10^{-9}$
	$d\bar{u} \rightarrow e^- \nu_e b\bar{b}s\bar{s}$	$5.260 \cdot 10^{-12}$	$1.965 \cdot 10^{-10}$	$2.773 \cdot 10^{-9}$
	$d\bar{u} \rightarrow e^- \nu_e b\bar{b}gg$	$9.867 \cdot 10^{-12}$	$6.525 \cdot 10^{-10}$	$8.646 \cdot 10^{-9}$
$n = 3$	$u\bar{d} \rightarrow e^+ \bar{\nu}_e b\bar{b}dd\bar{g}$	$6.412 \cdot 10^{-11}$	$2.211 \cdot 10^{-9}$	$7.703 \cdot 10^{-8}$
	$u\bar{d} \rightarrow e^+ \bar{\nu}_e b\bar{b}ggg$	$1.347 \cdot 10^{-10}$	$3.023 \cdot 10^{-9}$	$2.762 \cdot 10^{-7}$
	$d\bar{u} \rightarrow e^- \nu_e b\bar{b}dd\bar{g}$	$6.571 \cdot 10^{-11}$	$2.077 \cdot 10^{-9}$	$7.432 \cdot 10^{-8}$
	$d\bar{u} \rightarrow e^- \nu_e b\bar{b}ggg$	$1.530 \cdot 10^{-10}$	$3.031 \cdot 10^{-9}$	$2.783 \cdot 10^{-7}$

Table 8.1.: The logarithmically averaged relative deviation of poles in ϵ as well as the finite part of virtual matrix elements computed with `BlackHat` and `RECOLA`. We averaged over 1000 randomly chosen phase-space points. Shown are the deviations for exemplary subprocesses contributing to $Wb\bar{b} + n\text{-jet}$ ($n = 0, 1, 2, 3$).

8.2. Phase-Space Point Comparison Against Automated Tools

We carried out a number of checks with the new implementation of `BlackHat`. We systematically reproduced matrix elements that were implemented in the earlier versions of the library such as those for $V+\text{jets}$, jets and $VV+\text{jets}$ production ($V = W, Z$) and found excellent agreement. Furthermore, the explicit cancellation of infrared poles of renormalized one-loop matrix elements is checked by comparing to the integrated subtraction terms as performed with the `SHERPA` library.

We reproduced the results for primitive amplitudes including a top-quark pair and three gluons as presented by Ellis *et al.* in [33]. Even more, we cross checked fully interfered, matrix-element squared results against automated tools available on the market. In particular, this includes comparisons of all one-loop matrix elements necessary for $pp \rightarrow t\bar{t} + (\leq 2)\text{-jet}$ and $pp \rightarrow b\bar{b} + (\leq 2)\text{-jet}$ at NLO QCD with the `RECOLA` [177] and `OpenLoops` [178] libraries (both powered by the `Collier` library [179]), as well as all the ones needed for $Wb\bar{b} + (\leq 3)\text{-jet}$ with `RECOLA`.

For the latter comparison of virtual matrix elements required for $Wb\bar{b} + (\leq 3)$ -jet with **RECOLA**, we compute the logarithmically averaged relative deviation

$$\log_{10} \Delta_V = \frac{1}{N_{tot}} \sum_{j=1}^{N_{tot}} \log_{10} \left(\frac{|d\sigma_{V,\text{BlackHat}}^j - d\sigma_{V,\text{RECOLA}}^j|}{|d\sigma_{V,\text{RECOLA}}^j|} \right) \quad (8.2)$$

where N_{tot} denotes the total number of phase space points considered. We compare for exemplary subprocesses contributing to $Wb\bar{b} + n$ -jet ($n = 0, 1, 2, 3$) and sample over 1000 randomly chosen phase-space points for each of the subprocesses considered. In Table 8.1, we show Δ_V for both single pole $1/\epsilon^2$ and double pole $1/\epsilon^1$ as well as the finite part ϵ^0 .

Overall we find good agreement for all subprocesses considered between the results computed with **RECOLA** and **BlackHat**. The average relative deviation increases with the multiplicity of light jets n since more particles in the final state lead to an increased complexity due to more contributions to the calculation. Also the presence of external gluons makes the agreement worse. The average relative deviation for the case $n = 0$ lies around $\mathcal{O}(10^{-14})$ for the double pole, $\mathcal{O}(10^{-13})$ for the single pole and $\mathcal{O}(10^{-12})$ for the finite term, corresponding to an agreement of 12 digits on average. For the highest multiplicity case $n = 3$, it decreases to around $\mathcal{O}(10^{-10})$ for the double pole, $\mathcal{O}(10^{-9})$ for the single pole and $\mathcal{O}(10^{-7})$ for the finite term, corresponding to an agreement of 7 digits on average. Whereas we have good control over the precision of our calculation with **BlackHat**, see previous Sec. 8.1, no corresponding precision data for **RECOLA** is publicly available. A similar comparison against **OpenLoops** [178] for the lower multiplicity cases $n \leq 2$ shows a comparable agreement.

8.3. Validation of Integrated Total Cross Sections

We complete the validation of our new matrix elements by dedicated comparisons at the level of physical observables against the **MCFM** program [159] for the inclusive production of $Wb\bar{b}$ at NLO QCD at the LHC with $\sqrt{s} = 13$ TeV. We find agreement at the permil level for both total cross sections and differential distributions. The matrix-elements implemented in **MCFM** were first reported in [26], where analytic expressions for the QCD NLO corrections for $Wb\bar{b}$ including decay correlations and a non-zero bottom mass were found.

For our comparison, we use the renormalization and factorization scale $\mu_R = \mu_F = M_W$. We use the 5-flavor **MSTW2008** LO (**MSTW2008lo**) and NLO (**MSTW2008nlo**) PDFs [180] interfaced through **LHADPF** 6.1.3 [172] at the respective orders with $\alpha_s(M_Z) = 0.133551$ (LO) and $\alpha_s(M_Z) = 0.114904$ (NLO).

We use real values for the electroweak parameters as specified in Tab. 7.1. However, for this comparison we use a non-diagonal CKM matrix in the Wolfenstein parameterization [181] with the parameter $\lambda = 0.2272$. All light quarks (u, d, s, c) are treated as massless and bottom quarks are treated massive if they appear in the final state. The mass of the bottom quark is set according to the PDF to $m_b = 4.75$ GeV. We do include contributions from closed top quark loops, with the top mass set to $m_t = 173.5$ GeV. Bottom quarks

in virtual closed loops are treated as massless particles in accordance with the scheme implemented in MCFM.

We reconstruct b-jets by using the `anti- k_T` algorithm [120] as implemented in the package `Fastjet` [182, 183], with jet-radius parameter $R = 0.5$. We require the b-jets to have a minimum transverse-momentum of $p_T > 25$ GeV.

We integrated three statistically independent samples. The total integrated cross section in pb for both $W^-b\bar{b}$ and $W^+b\bar{b}$ are shown in Table 8.2. The values in parenthesis next to the central value denote the uncertainty associated to the numerical integration. The results obtained by MCFM and `BlackHat+SHERPA` are integrated to about 0.1%.

Run	$W^-b\bar{b}$ LO	$W^-b\bar{b}$ NLO	K -factor	$W^+b\bar{b}$ LO	$W^+b\bar{b}$ NLO	K -factor
MCFM 1	1.0961(7)	2.3613(23)	2.154	1.7644(11)	3.6788(37)	2.085
MCFM 2	1.0972(8)	2.3542(21)	2.146	1.7644(12)	3.6790(42)	2.085
MCFM 3	1.0968(7)	2.3562(39)	2.148	1.7655(11)	3.6766(34)	2.082
BlackHat 1	1.0973(3)	2.3618(25)	2.152	1.7652(6)	3.6877(48)	2.089
BlackHat 2	1.0962(5)	2.3596(30)	2.153	1.7643(9)	3.6804(56)	2.086
BlackHat 3	1.0966(5)	2.3649(36)	2.157	1.7640(8)	3.6809(40)	2.087

Table 8.2.: Total integrated cross-section at LO and NLO for $W^-b\bar{b}$ production (left) and $W^+b\bar{b}$ production (right) in pb as well as the ratio of the NLO to LO result (K -factor). Shown are the results of three statistically independent runs of MCFM and `BlackHat+SHERPA`. The uncertainty associated to the numerical integration is given in parenthesis next to the central value.

The results agree to the expected level, in particular in light of the small absolute difference of the cross-sections. The agreement after numerical integration validates the setup of `BlackHat+SHERPA` against MCFM.

CHAPTER 9

Results for the LHC with $\sqrt{s} = 13$ TeV

In this chapter, we present the phenomenological results for $Wb\bar{b}$ production in association with up to three jets at the LHC $\sqrt{s} = 13$ TeV, as shown in Ref. [21]. First, we analyze effects of a finite b -mass by comparing results obtained in both the four-flavor number (4FNS) and five-flavor number (5FNS) scheme. Secondly, we present results for total and differential cross sections and study their renormalization- and factorization-scale dependence. And lastly, we present a series of observables associated to HW production measurements and show predictions of exclusive sums, which combine cross sections of distinct light-jet multiplicities and assess their theoretical uncertainty based on scale dependence, higher-order contributions and PDF errors.

9.1. Effects of a Finite Bottom-Quark Mass

The effects of a finite b quark mass in $Wb\bar{b}$ production have been studied since the early NLO QCD calculations in Ref. [14]. We consider situations with two well defined b jets, where the effects of a finite bottom-quark mass are expected to be small since ratios of invariants involving m_b^2 are typically small. However, the effect of a finite b quark mass is important for inclusive b -jet production at hadron colliders (see for example Refs. [161–163]).¹ We leave the study of inclusive b -jet production in association with multiple light jets using our matrix elements to future work.

In this section, we analyze the effects of a finite mass of the bottom quark m_b in our results. To this end, we compare both total cross-sections and differential distributions computed in two different schemes. In the four-flavor number scheme (4FNS) bottom quarks are consistently treated as massive particles that can appear in the final-state and as virtual particles in loop diagrams. Corresponding PDFs, and the DGLAP equations to evolve them, consider only four quark flavors (d, u, s and c) and the gluon as partons. For the 4FNS calculation, we use our default setup (as described in Section 7.3). We compare to a computation in the five-flavor number scheme (5FNS), where bottom quarks are consistently treated as massless particles in the hard scattering matrix elements. The corresponding PDF sets thus have five quark flavors and the gluon as partons.

We perform an analysis for $Wb\bar{b}$ and $Wb\bar{b} + 1$ -jet production with the aim of confirming the findings of Ref. [14] also for $Wb\bar{b} + 1$ -jet. Note in particular that apart from real-emission diagrams for $Wb\bar{b} + 1$ -jet, the considered diagrammatic content is the same in the

¹Here, only one b -jet is required to pass a p_T cut whereas the other b -jet remains unrestricted. In some regions of phase space the $b\bar{b}$ jet invariant mass can become not much larger than $2m_b$ and effects of a finite b -mass are sizeable.

4FNS and the 5FNS for both these processes, since no bottom-initiated diagrams exist. We can thus attribute appearing difference to b -mass effects in matrix elements, phase space generation, differences in PDFs and the corresponding running couplings. Given the similar diagrammatic content, it might be interesting in the future to also compare $Wb\bar{b} + 2$ -jet and $Wb\bar{b} + 3$ -jet production, for which no such limitation exists, in the two flavor-number schemes. We leave this more systematic comparison of the 4FNS vs. 5FNS to future work.

The two schemes are characterized by a different organization of the perturbative series used for computing observables. Given that for example $\alpha_s^{N_f=4}(M_Z^2)$ has a value of about 0.113 and $\alpha_s^{N_f=5}(M_Z^2)$ of 0.118, differences between the two schemes can potentially appear. Nevertheless, we will see that in regions where characteristic scales Q^2 are such that the ratios m_b^2/Q^2 are small, we find good agreement at NLO QCD between the 4FNS and the 5FNS. This shows that the differing terms in the perturbative series are small for the observables considered in this study (a dedicated study of the different perturbative contributions appearing in these different schemes appeared in Ref. [184]).

In our analysis of the 4FNS and 5FNS calculations, we require two b jets and n light jets, as defined by the anti- k_T jet algorithm [120] with $R = 0.4$. We apply the following event selection cuts, with the same cuts applied to b and light jets

$$\begin{aligned} p_T^{\text{jet}} &> 15 \text{ GeV}, & |\eta^{\text{jet}}| &< 2.4, \\ p_T^e &> 25 \text{ GeV}, & |\eta^e| &< 2.5, \\ p_T^\nu &> 20 \text{ GeV}, & M_T^W &> 20 \text{ GeV}. \end{aligned} \quad (9.1)$$

We define b jets (in both massive or massless cases) by quark-flavor content of the jets in an infrared-safe manner according to [169]. In the 5FNS calculations, we use PDFs from CT14 [171], denoted by `CT14l1o` at LO and `CT14nlo` at NLO and include closed massive top loops. Closed bottom loops in the 5FNS are computed with massless quarks.

jets	massive LO	massive NLO	K -factor	massless LO	massless NLO	K -factor
0	$0.81177(32)^{+0.1379}_{-0.1113}$	$1.6804(20)^{+0.3071}_{-0.2300}$	2.07	$0.95905(41)^{+0.1507}_{-0.1247}$	$2.0051(44)^{+0.3527}_{-0.2673}$	2.09
1	$0.96210(93)^{+0.3630}_{-0.2457}$	$1.3748(82)^{+0.2422}_{-0.2200}$	1.43	$1.1756(19)^{+0.4279}_{-0.2940}$	$1.7132(80)^{+0.2907}_{-0.2636}$	1.46

Table 9.1.: LO and NLO QCD cross sections for $W^-b\bar{b}+0, 1\text{-jet}+X$ production within the 4FNS (massive) and the 5FNS (massless). Results with dynamical scale $\hat{H}'_T/2$ are shown together with their respective K -factors. Kinematical cuts are specified in eq. (9.1). The number in parenthesis next to the central value gives the corresponding statistical integration error. Super and subscripts denote scale variations.

In Table 9.1 we show the results at the level of total cross sections as computed in the 4FNS and 5FNS. We observe a clear deviation between the central results, with the 5FNS results producing total cross sections about 20% larger. However, the structure of the corrections, both by the size of the K -factor and by the scale sensitivity at NLO, is very similar.

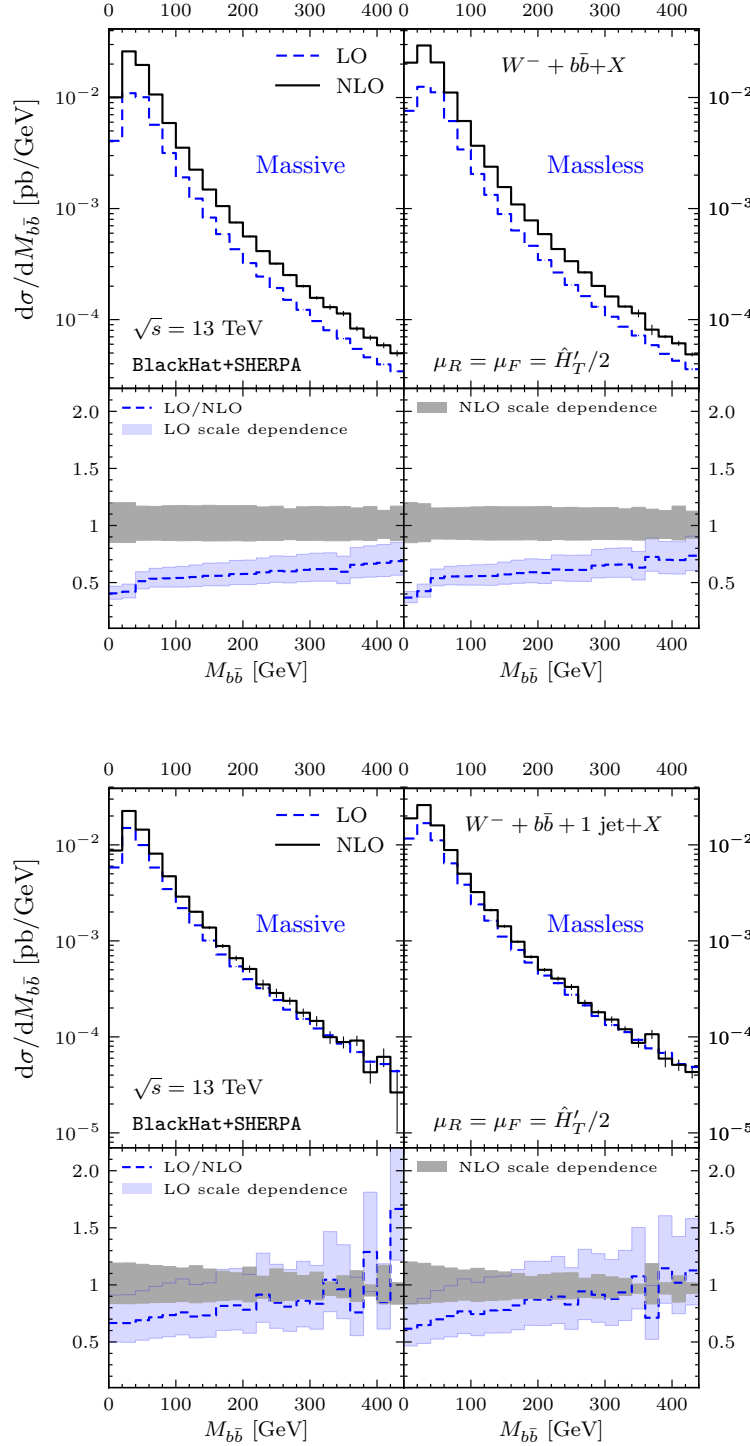


Figure 9.1.: The invariant mass spectra for the $b\bar{b}$ system in $W^-b\bar{b}$ (top) and $W^-b\bar{b}+1\text{-jet}$ (bottom) production at the LHC at $\sqrt{s} = 13$ TeV, for calculations performed at LO and NLO QCD order within the 4FNS (left) and the 5FNS (right). In the upper panel of each figure, we show the LO (dashed blue) and NLO (solid black) results with thin vertical lines representing the numerical integration errors. The bottom panels show the scale-dependence bands normalized to the NLO result in blue for LO and gray for NLO.

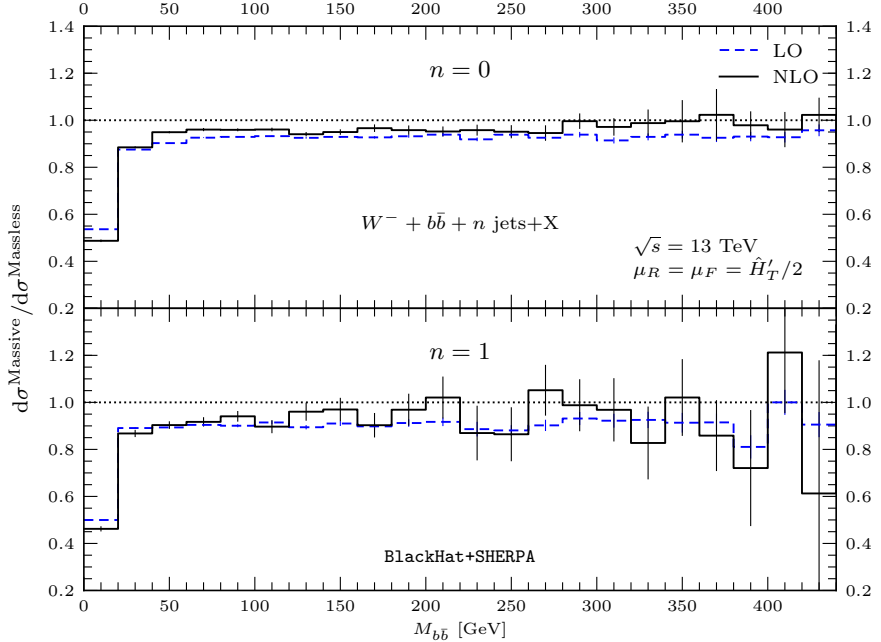


Figure 9.2.: Ratio of the invariant mass spectrum of the $b\bar{b}$ system in a 4FNS calculation to a 5FNS one, for $W^- b\bar{b}$ (top) and $W^- b\bar{b}+1\text{-jet}$ (bottom) production. The ratios are taken at LO (dashed blue line) and at NLO (solid black line). Statistical errors are shown as thin vertical lines. We include a dotted horizontal line at a ratio value of 1.

In the following, we show that this difference on the level of total cross sections can be largely attributed to regions of phase space in which m_b^2 cannot be considered a small quantity. We do so by looking at the structure of our results over phase space and find that the effects are quite similar at LO and at NLO, as originally shown in [14]. In particular, we show distributions in the invariant mass of the $b\bar{b}$ system, but similar effects are found for example for the p_T distributions of the leading and subleading b jets.

In Fig. 9.1 we show the $M_{b\bar{b}}$ distribution for $W^- b\bar{b}$ and $W^- b\bar{b}+1\text{-jet}$ production computed at LO and NLO in both the 4FNS and 5FNS. $Wb\bar{b}$ production exhibits large radiative corrections, as visible in the ratio panels, while the results for $Wb\bar{b}+1\text{-jet}$ production show less structure over phase space.

In order to highlight the differences between the two calculations, we show the ratio of massive calculation (4FNS) to massless calculation (5FNS) in Fig. 9.2. We notice that the differences observed at the level of the total cross sections can be mostly attributed to the regions of small $M_{b\bar{b}}$. For values of $M_{b\bar{b}}$ above 50 GeV, the ratios stabilize rapidly at about 0.95 for $Wb\bar{b}$ production and at 0.9 for $Wb\bar{b}+1\text{-jet}$ production, whereas we have a strong deviation for lower values, with the massless calculation more than doubling the massive one. The discrepancy is to be expected, since in these regions, phase-space constraints the production of massive b quarks and m_b effects in the matrix elements are noticeable.

The mass effects are not affected by quantum corrections, as we can deduce from the similarity of the LO and NLO ratios. The deviation from 1 at large $M_{b\bar{b}}$ is smaller

than the scale-dependence bands of the NLO results. Notice that the 4FNS and 5FNS have by construction different renormalization schemes. Also, it is important to mention that the intrinsic difference of the global QCD analyses to produce 4FNS and 5FNS PDF sets induce discrepancies both in α_s and the gluon-PDF that can account for the massless results increase of about 5% for $Wb\bar{b}$ production and of about 10% for $Wb\bar{b}+1$ -jet production. The PDF uncertainties associated to the global QCD analysis are relatively small, at the level of 1 or 2% as we will show in Section 9.3.

9.2. Results for $Wb\bar{b}$ Production in Association with Light Jets

In this section we present NLO QCD results for $Wb\bar{b}$ production in association with up to three light jets in pp collisions at the LHC Run-II with $\sqrt{s} = 13$ TeV. We show total cross sections and differential distributions as a function of the light-jet multiplicity. We obtain our results by applying the following kinematical cuts

$$\begin{aligned} p_T^{\text{jet}} &> 25 \text{ GeV}, & |\eta^{\text{jet}}| &< 2.4, \\ p_T^e &> 25 \text{ GeV}, & |\eta^e| &< 2.5, \\ p_T^\nu &> 20 \text{ GeV}, & M_T^W &> 20 \text{ GeV}, \end{aligned} \quad (9.2)$$

where the same cuts are applied to both light and b jets. The computational setup is described in Chap. 7 and renormalization and factorization scales are chosen to be equal and are dynamically set to $\mu = \hat{H}'_{\text{T}}/2$, according to Eq. (7.4). Jets are defined by using the anti- k_T jet algorithm [120] with $R = 0.4$, as implemented in the `FastJet` package [183].

9.2.1. Total Cross Sections

In Table 9.2, we present total partonic cross sections for the inclusive production of both W^- and W^+ accompanied by two b jets and zero to three light jets. We give the numerical integration uncertainty in parenthesis and quote the scale dependence in superscripts and subscripts. In separate columns, we show the ratio of NLO to LO results, the so called K -factors, which quantify the total size of the NLO corrections.

We observe that the size of quantum corrections is large for $Wb\bar{b}$ production and the NLO QCD corrections increase the total cross section by a factor of 2. The scale dependence of the LO cross section of $Wb\bar{b}$ is around 20% and thus not representative of the associated theoretical uncertainties. The large quantum corrections for the above process can be understood as the result of an opening of gluon-initiated channels [14, 79, 80]. Furthermore, kinematical constraints are present at LO for $Wb\bar{b}$ production and released at NLO, as we will discuss for the $p_T^{b\bar{b}}$ and p_T^W observables in Section 9.3. Also for $Wb\bar{b}+1$ -jet a gluon-gluon initiated channel is opened up, but with milder impact, and for the larger multiplicity processes all subprocesses are present at LO. Hence, quantum corrections are

jets	$W^- b\bar{b}$ LO	$W^- b\bar{b}$ NLO	K -factor	$W^+ b\bar{b}$ LO	$W^+ b\bar{b}$ NLO	K -factor
0	$0.33278(12)^{+0.0619}_{-0.0490}$	$0.67719(60)^{+0.1288}_{-0.1000}$	2.03	$0.48573(19)^{+0.0925}_{-0.0727}$	$0.97175(85)^{+0.1877}_{-0.1411}$	2.00
1	$0.36153(13)^{+0.1408}_{-0.0945}$	$0.50484(63)^{+0.0851}_{-0.0800}$	1.40	$0.52095(23)^{+0.2034}_{-0.1362}$	$0.72740(99)^{+0.1277}_{-0.1167}$	1.40
2	$0.18501(44)^{+0.1053}_{-0.0626}$	$0.22604(87)^{+0.0407}_{-0.0400}$	1.22	$0.27663(68)^{+0.1569}_{-0.0934}$	$0.3340(17)^{+0.0599}_{-0.0647}$	1.21
3	$0.07204(25)^{+0.0540}_{-0.0289}$	$0.08288(89)^{+0.0189}_{-0.0200}$	1.15	$0.11493(59)^{+0.0855}_{-0.0459}$	$0.1286(17)^{+0.0280}_{-0.0307}$	1.12

Table 9.2.: Total cross sections (in pb) for $W^\pm b\bar{b} + 0, 1, 2, 3$ -jet + X production at LO and NLO QCD. The scale dependence is shown as super and subscripts and the corresponding statistical integration error is shown in parenthesis next to the central value. We show results obtained with the dynamical scale $\hat{H}'_T/2$ together with their respective K -factors, that is ratios of NLO to LO results. The setup is specified in Chapter 7, and kinematical cuts can be found in Eq. (9.2).

n	$W^+ b\bar{b}$ n/ $W^- b\bar{b}$ n		$W^- b\bar{b}$ n/(n - 1)		$W^+ b\bar{b}$ n/(n - 1)	
	LO	NLO	LO	NLO	LO	NLO
0	1.45962(78)	1.4350(18)	—	—	—	—
1	1.44098(83)	1.4409(27)	1.08640(55)	0.7455(17)	1.07253(64)	0.7485(12)
2	1.4952(51)	1.4776(95)	0.5117(12)	0.4478(21)	0.5310(13)	0.4592(24)
3	1.5952(99)	1.551(27)	0.3894(16)	0.3667(44)	0.4155(24)	0.3850(54)

Table 9.3.: Ratios of LO and NLO QCD total cross sections. The second and third columns show charge ratios of LO and NLO cross sections as a function of the number of associated light jets n . The last four columns show jet production ratios, that is ratios of the cross section of a process to that with one less jet, for both $W^- b\bar{b}$ and $W^+ b\bar{b}$ in association with n light jets. The number in parenthesis gives the corresponding statistical integration error.

milder for the higher multiplicity cases. We thus expect quantum corrections for processes with even more light jets to be under relatively good perturbative control.

In Table 9.3 we show several ratios of LO and NLO total cross sections. We show W^+/W^- charge ratios in columns 2 and 3 as a function of the number of light jets. These ratios are relatively stable with respect to quantum corrections, which has been explored in similar processes as a way to make precise determinations of ratios of u/d PDFs (see for example Ref. [185]). They also show some stability as a function of the number of jets, with a slight monotonic increase given the larger mean values of Bjorken x sampled as a consequence of the larger invariant mass necessary to produce the corresponding final states.

We also explore jet-production ratios in $W^\pm b\bar{b}$ production in association with light jets in columns 4–7 of Table 9.3, that is ratios of the cross section of a process to that with one less jet. As discussed previously, the results for $n = 1$ are special given the large NLO corrections for $Wb\bar{b}$ production. The opening of an initial-state channel and the release of a kinematical constraint, makes the $Wb\bar{b} + 1\text{-jet}/Wb\bar{b}$ ratio clearly sensitive to quantum corrections. A similar observation was made in studies of these ratios in $W + n\text{-jet}$ (light jet) production [4], where the ratio $(W + 2\text{-jet})/(W + 1\text{-jet})$ was sensitive to quantum corrections. Only the calculation of NLO QCD correction to $W + 5\text{-jet}$ production [2] gave some indication of a possible jet-ratio universality. For our results, the inclusion of NLO QCD corrections to $W + b\bar{b} + 4\text{-jet}$ production in the future might reveal similar structure for inclusive $Wb\bar{b}$ production.

In all our results, we include the full-color information and only exploit the decomposition in a color expansion for efficiency of the computation. Interestingly, $Wb\bar{b}$ production with light jets is largely dominated by virtual contributions in our setup, and so a leading-color approximation would only be accurate at the order of 10% for physical observables. This is in contrast to W production in association with light jets, where the leading-color approximation for one-loop matrix elements gives a very good approximation for physical observables (at the level of 1 to 3%) [2]. We attribute this difference to the unlike dominant subprocesses.

9.2.2. Scale Dependence

In Fig. 9.3 we show the dependence of total cross sections in $W^-b\bar{b}$ and $W^+b\bar{b}$ production in association with up to three light jets on the renormalization and factorization scale as a function of the light-jet multiplicity. The central dynamical scale is $\mu_0 = \mu_R = \mu_F = \hat{H}'_T/2$ (defined in Eq. (7.4)) and we vary by factors of $(1/2, 1/\sqrt{2}, 1, \sqrt{2}, 2)$ around the central scale. We observe a very similar scale variation for both species of vector boson, for W^+ and W^- . For all multiplicities with $n \geq 1$, we observe that the LO cross sections have a monotonically increasing scale dependence. As noted previously, $Wb\bar{b}$ production is special given the opening of a gluon-initiated channel at NLO, which is reflected in the associated scale dependence.

The dynamical scale $\hat{H}'_T/2$ increases on average monotonically with multiplicity. For vector boson production in association with massless jets, this scale choice has been observed to produce relatively stable NLO results over a wide range of kinematical configurations relevant to the LHC and future colliders [2, 13, 186, 187]. For the LHC in particular, it has been observed that for massless jet production the scale $\hat{H}'_T/2$ typically produced NLO cross sections lying on the locus of the scale-dependence curves. Contrary to that we observe that for $Wb\bar{b} + n\text{-jet}$ ($n = 0, 1, 2, 3$) production, the NLO cross section at the central scale appears consistently on the right of the scale-dependence plateau. We assert, in particular considering the similarities of the massive and massless results studied in Section 9.1, that this difference has little to do with the presence of a massive jet and it is actually due to the type of subprocesses contributing. In light-jet production the dominant subprocesses are the ones with a single fermion line. In the case of

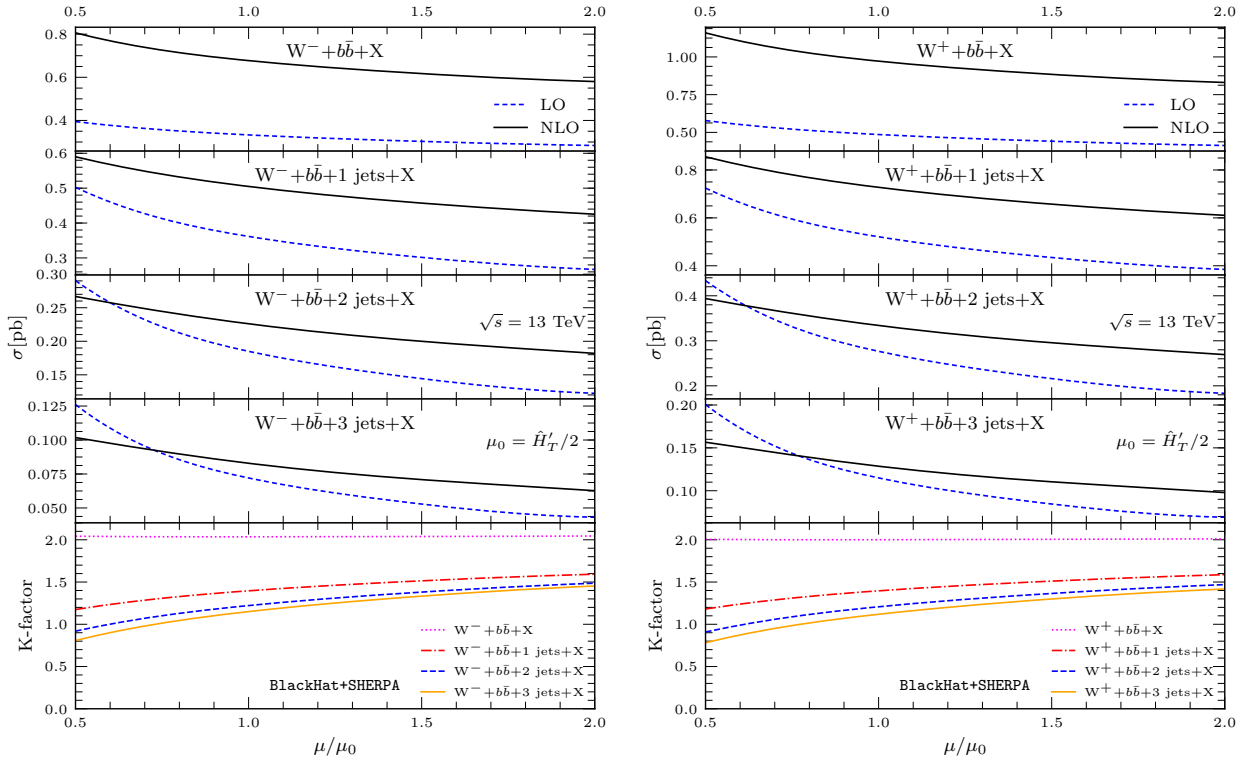


Figure 9.3.: Renormalization- and factorization-scale dependence of total cross sections for $W^- b\bar{b}+0, 1, 2, 3-jet+ X production to the left and $W^+ b\bar{b}+0, 1, 2, 3-jet+ X production to the right. We use the central scale $\mu_0 = \mu_r = \mu_f = \hat{H}'_T/2$. In the upper four panels, we show the dependence of LO (dashed blue line) and NLO (solid black line) predictions on the scale μ . The lower panel shows the respective K -factor (ratio of NLO/LO).$$

$Wb\bar{b}+n$ -jet ($n = 0, 1, 2, 3$) production in turn, the dominant subprocesses are those with two fermionic lines (the ones with most gluons involved).

9.2.3. Differential Cross Sections

This section is devoted to the study of NLO results for several differential distributions and we will thereby highlight the impact of NLO QCD corrections on fixed-order predictions over phase space. The structure of corrections is similar for the W^\pm species and we will in general only show results for one of them.

In Figs. 9.4 and 9.5 we show the jet- p_T spectra of leading and subleading b jets (ordered by p_T) respectively, for inclusive $W^- b\bar{b}$ production in association with $n = 0, 1, 2, 3$ jets. In the upper panel of the figures, we show LO and NLO distributions as dashed (blue) and solid (black) lines respectively. The bottom panels show the scale-dependence bands normalized to the central NLO result (LO in blue and NLO in gray). Numerical

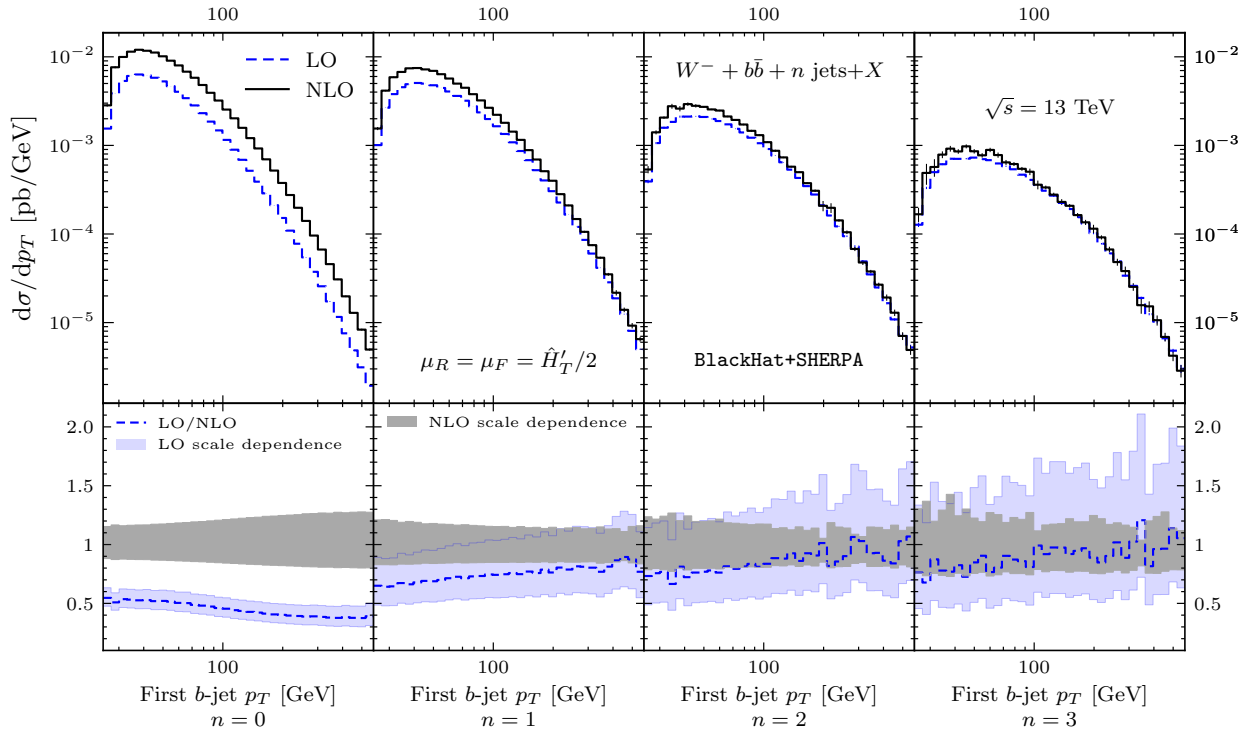


Figure 9.4.: The p_T distributions of the leading b jet (ordered by p_T) in inclusive $W^- b\bar{b}+0, 1, 2, 3$ -jet production at the LHC at $\sqrt{s} = 13$ TeV. Light jet multiplicity increases from left to right. In the upper panels the dashed (blue) line shows the LO result and the solid (black) line the NLO result. Vertical thin lines show the statistical error from the numerical integration. In the bottom panels we show the scale-dependence bands normalized to the NLO result, in blue for LO and gray for NLO.

integration errors for each bin are shown as thin vertical lines (when visible). We show all distributions in this section in a similar manner.

We observe that the NLO corrections have structure beyond the K -factors studied at the level of total cross sections in the previous subsection. In most of the p_T distributions of b jets, shape differences are present between LO and NLO results. Typically, the LO predictions become harder. This trend is reduced with light-jet multiplicity and for the highest-multiplicity process considered, $Wb\bar{b} + 3$ -jet production, the LO/NLO shape difference is reduced. An exception to this observation is the leading b jet p_T in $Wb\bar{b}$ production. As expected, the scale dependence of NLO results is reduced compared to LO results (apart from $Wb\bar{b}$, as discussed for total cross sections) and in the high-multiplicity samples, NLO results lie inside LO bands. This confirms the relatively good perturbative control for the high-multiplicity samples.

In Fig. 9.6 we show the p_T distribution of the softest light jet in inclusive $W^+ b\bar{b}+1, 2, 3$ -jet production. We observe a reduction of the scale sensitivity with the inclusion of QCD corrections, with LO and NLO bands overlapping. The quantum corrections for these distributions are rather flat. This feature is similar to observations for softest jet p_T distributions in $W + n$ -light-jet production.

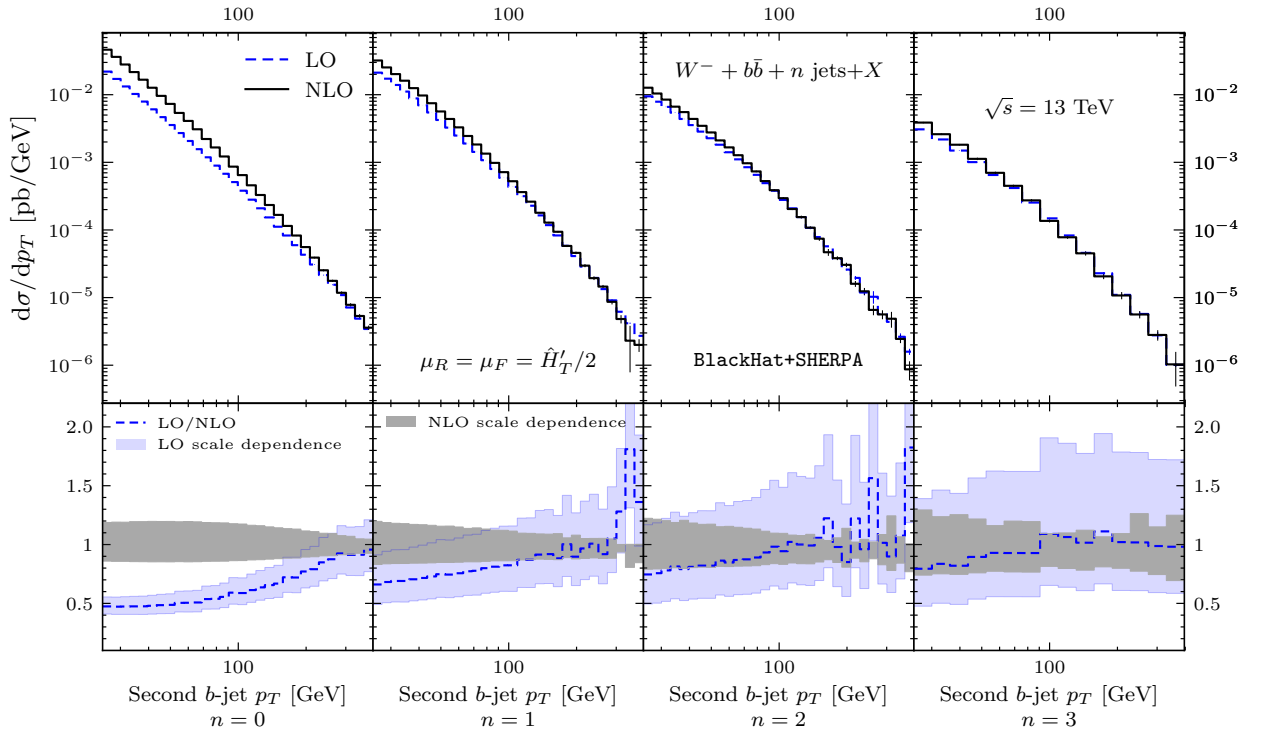


Figure 9.5.: The p_T distributions of the subleading b jet (ordered by p_T) in inclusive $W^-b\bar{b}+0, 1, 2, 3$ -jet production at the LHC at $\sqrt{s} = 13$ TeV. Format as in Fig. 9.4.

The total hadronic activity in a detector is an interesting observable for many BSM scenarios, as well as for experimental studies at hadron colliders. In Fig. 9.7 we show distributions in this observable, including all hadronic activity from light and b jets in $W^-b\bar{b}+0, 1, 2, 3$ -jet production. As we would expect from previous discussions, strikingly large and phase-space dependent NLO corrections appear for $Wb\bar{b}$. Interestingly, a remnant of these large effects remains in $Wb\bar{b} + 1$ -jet production in this observable. For $Wb\bar{b} + 1$ -jet, the QCD corrections are not as large as for $Wb\bar{b}$, but at around 1 TeV for H_T^{jets} , we still observe a differential K -factor reaching two, with the shape difference ending at about 400 GeV. The large-multiplicity processes on the other hand show much less structure. In particular, enhancements due to soft W emission are present already at LO in this case.

Lastly, we show in Fig. 9.8 distributions in the ΔR separation between first b jet and charged lepton l^- . Most of the angular variables that we studied are similar to this one, showing little structure in the QCD corrections. However, we find an effect when a certain kinematic constraint is imposed at LO and released by the QCD corrections, as visible on the left most plots of Fig. 9.8. In the LO ΔR_{bl^-} distribution for $W^-b\bar{b}$ production, the parent W and gluon that give rise to the leptons and b jets respectively are produced with $\Delta\phi$ (the difference in azimuthal angle) equal to π . Also, the $\Delta\eta$ distribution peaks at around zero and decreases monotonically. The resulting ΔR_{bl^-} distribution thus has the feature of a sharply decaying distribution at LO. This constraint is lifted at NLO by

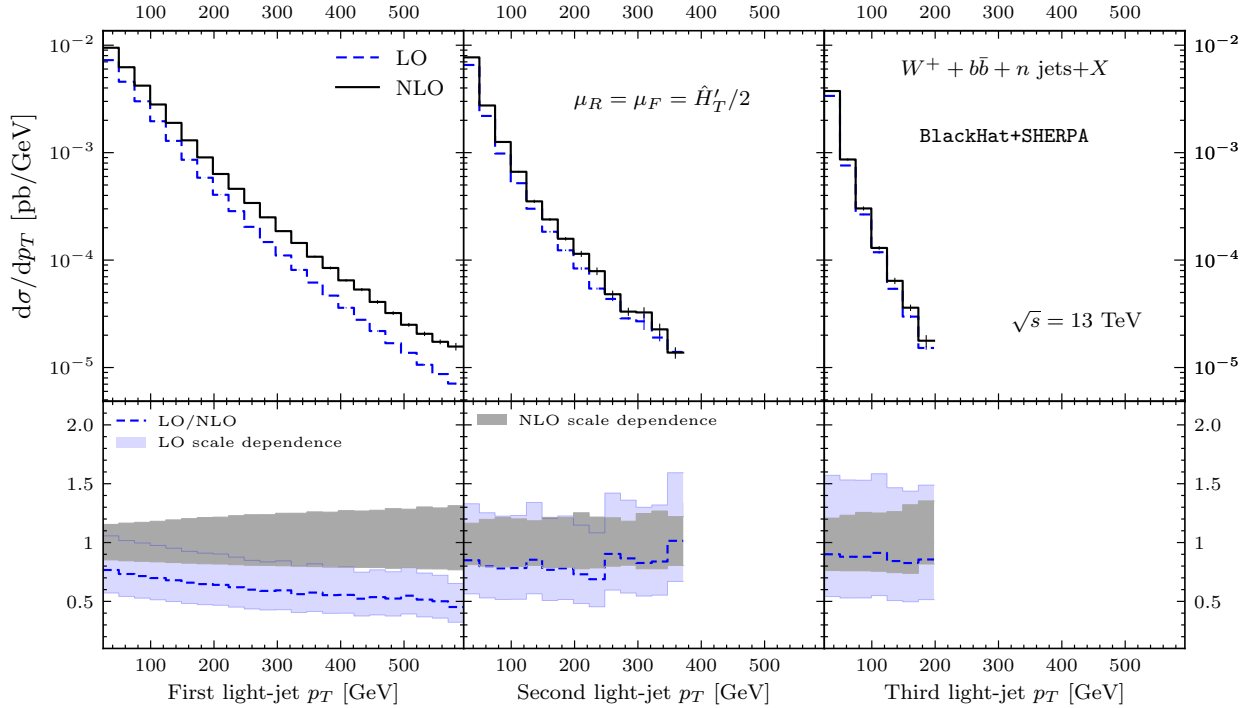


Figure 9.6.: The p_T distributions of the softest light jets in inclusive $W^+b\bar{b}+1, 2, 3$ -jet production. Format as in Fig. 9.4.

real corrections. Also the higher-multiplicity cases of $Wb\bar{b}+1, 2, 3$ -jet production do not exhibit a similar feature.

9.3. Backgrounds to HW Production

Many of the properties of the Higgs boson have been studied at the LHC, and so far all measurements appear in good agreement with the predictions of the SM (see for example Ref. [188]). However, it will be important to further constrain the strength of the Yukawa coupling y_b of the Higgs boson to b quarks, given that a Higgs boson with mass M_h around 125 GeV decays about half of the time into a $b\bar{b}$ pair. In the main production channel of the Higgs, through gluon-gluon fusion, one faces a huge background from pure QCD $b\bar{b}$ production. Therefore, considering the associated $H(\rightarrow b\bar{b})W$ production can help solidify the evidence for the Higgs decaying to b quarks [73]. Important for this approach is of course that irreducible backgrounds with the same signature, such as $Wb\bar{b}$ production in the SM, can be kept under control. We aim to contribute to this quest with the predictions provided in this section.

In this section, we study three observables that are important for HW analyses, in the context of our high-multiplicity results: On the one hand, $p_T^{b\bar{b}}$ and $M_{b\bar{b}}$, which are associated to the $b\bar{b}$ system and, when producing a Higgs, are associated with the p_T distributions of the Higgs and the mass of the Higgs. Furthermore, we study p_T^W , which helps to characterize the accompanying W boson. At high energies and multiplicities,

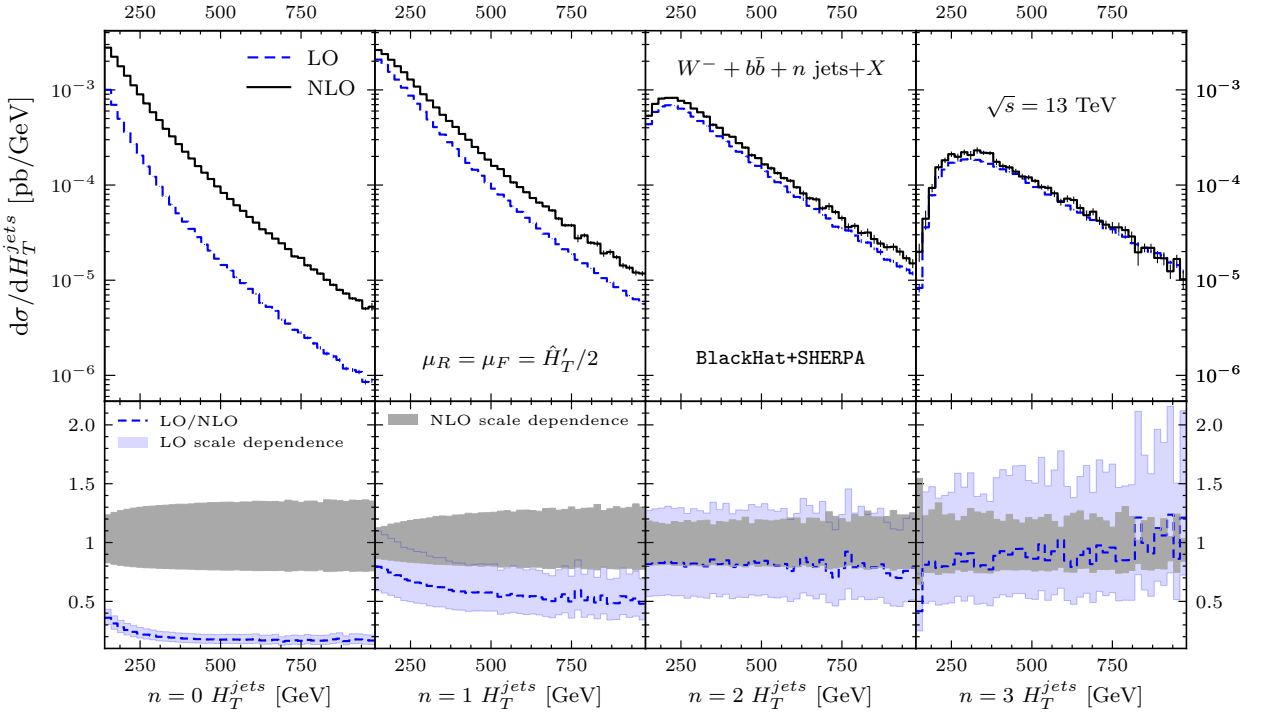


Figure 9.7.: Distributions of total transverse jet energy H_T^{jets} of light and b jets for inclusive $W^- b\bar{b} + 0, 1, 2, 3$ -jet production at the LHC at $\sqrt{s} = 13$ TeV. Format as in Fig. 9.4.

resonant top contributions, as studied for example in [189], are equally present. In the context of HW production the focus is on the non-resonant backgrounds, where top contributions are also sizable. They can be of similar order to the contributions presented here, even though they are formally suppressed by powers of α_f/α_s . A more systematic study of HW backgrounds should thus include non-resonant top contribution, which we leave to future work.

We have seen in this chapter and it has been understood since a long time that NLO QCD correction to $Wb\bar{b}$ production have large contributions associated to processes with an extra light jet. Previous approaches used exclusive results in the number of light jets [14], which explicitly vetoed events with extra jets. This prescription however suffers from its sensitivity associated to the p_T^{veto} cut [166]. We choose to follow a different approach. Instead of imposing a veto cut to stabilize the predictions, we effectively replace the extra light-jet contributions to generic observables, which are effectively LO, by their corresponding results including NLO QCD corrections. In higher-order corrections these contributions are naturally added and our predictions will be outdated once NNLO predictions for $Wb\bar{b}$ production become available in the future.

We apply the ‘exclusive sums’ technique which was studied in [81]. In particular, this technique is expected to be of benefit when tree-like contribution, with an extra light jet, to NLO corrections are rather large. Notice that in measurements of W +light jets some of the predictions from exclusive sums have been compared to LHC data, see for example [59, 61], usually in the context of $W + 1$ -jet production. By now those computations are outdated,

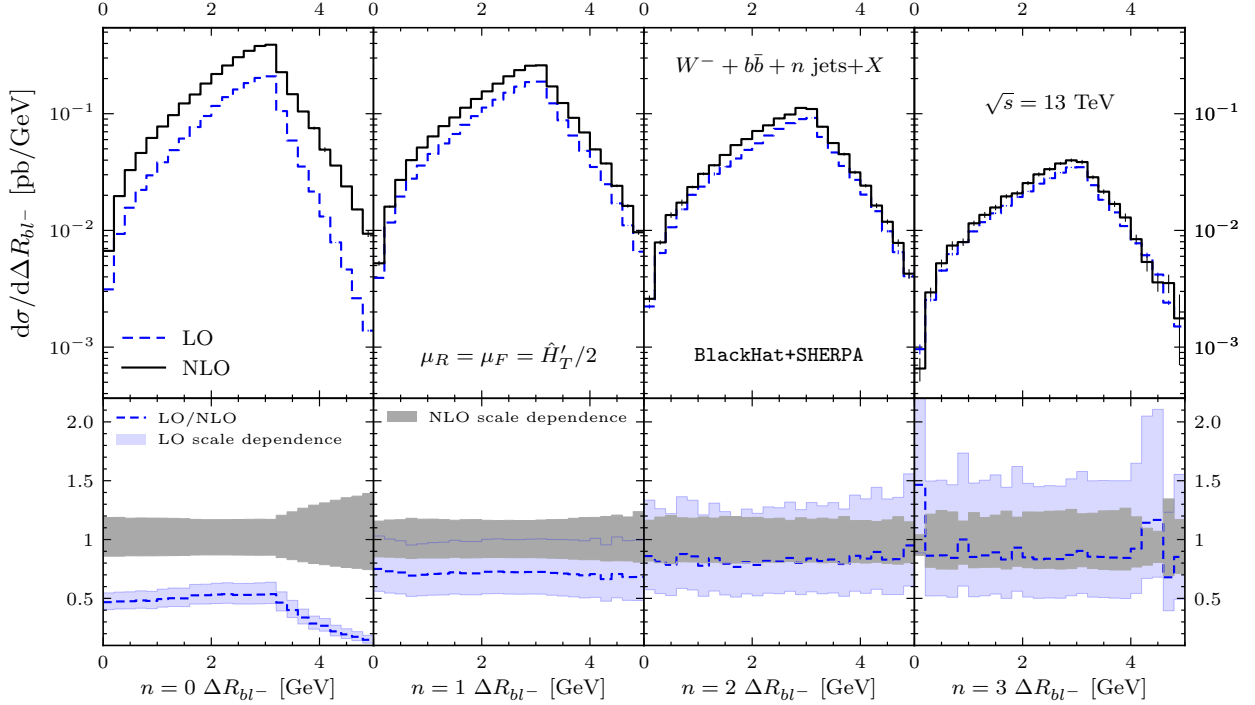


Figure 9.8.: Distributions in the ΔR_{bl-} separation between first b jet (ordered in p_T) and charged lepton for inclusive $W^- b\bar{b} + n$ jets production. Format as in Fig. 9.4.

given the recent NNLO QCD calculation presented in Ref. [18]. Other approaches studied to get more realistic predictions for the comparison to LHC data are the application of a parton-shower [15], or using a matched and merged version for example with the MEPS@NLO [190] or FxFx technique [191].

In this section, we focus on predictions for $Wb\bar{b}+X$ production. We denote fixed-order results for those as usual with the labels LO and NLO. Furthermore, we employ exclusive sums as defined in Eq. (7.7), for which we use labels NLO+ and NLO++. The latter serves as a proxy for the size of even higher-order corrections and thus to estimate the theoretical uncertainty.

In order to characterize theoretical uncertainties in a more complete way, we also explore PDF uncertainties associated to the observables under consideration. To that end, we estimate the associated PDF uncertainties from the error sets of the pseudo-PDF set PDF4LHC15_nlo_nf4_30 [192], which have been produced as a by-product of the major PDF sets according to the so called ‘PDF4LHC’ recommendations. Since the PDF error we find are small compared to other theoretical uncertainties, we do not go beyond this restricted error set for our estimations. Further uncertainties are associated to the value of m_b and α_s , but those are expected to be rather small compared to missing higher-order corrections.

In Fig. 9.9, we show the distribution of transverse momentum of the $b\bar{b}$ system. The upper panel contains all our predictions, that is the central NLO+ prediction as well as LO, NLO and NLO++. In the second panel, we show the corresponding scale-dependence

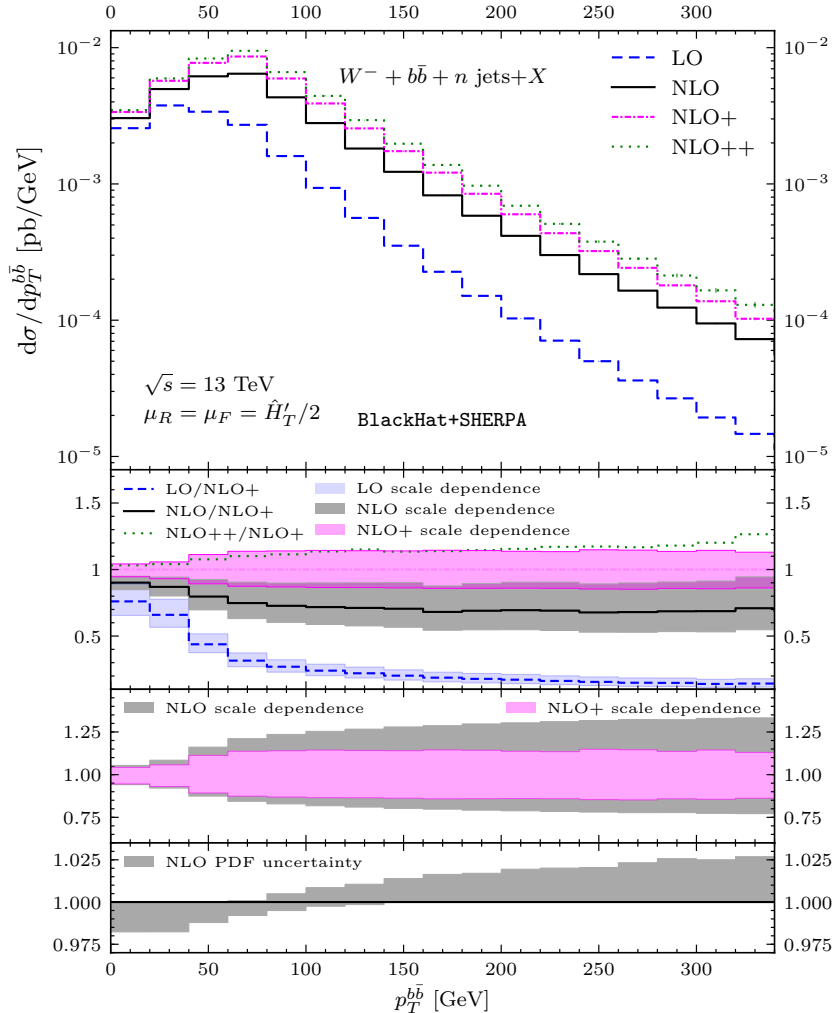


Figure 9.9.: The p_T distribution of the $b\bar{b}$ system in inclusive $W^- b\bar{b}$ production, computed at LO (dashed blue line) and NLO (solid black line) as well as by employing the exclusive sums NLO+ (dashed-dot magenta line) and NLO++ (dotted green line). The second panel shows scale dependence bands normalized by NLO+, and the third panel shows results normalized by the corresponding central value. The bottom panel shows the associated PDF uncertainties normalized to our NLO results.

bands at LO, NLO and NLO+, all normalized by NLO+, as well as the central value for NLO++. In the third panel we show the scale-dependence bands at NLO and NLO+, normalized by the respective central value. Lastly, in the bottom panel, we show the PDF uncertainties, which are below 2% for the range of p_T^{bb} shown (we normalize the PDF uncertainties by the NLO result). The NLO+ predictions have smaller scale-dependence bands at the level of 13%, which is a reduction compared to those of the fixed-order NLO result. No adequate prediction is given by the LO result. The NLO and NLO+ bands overlap, but show a difference in shape, particularly at low values of p_T^{bb} . The estimation of higher-order corrections through scale variations and by the NLO++ results are of the same order of magnitude.

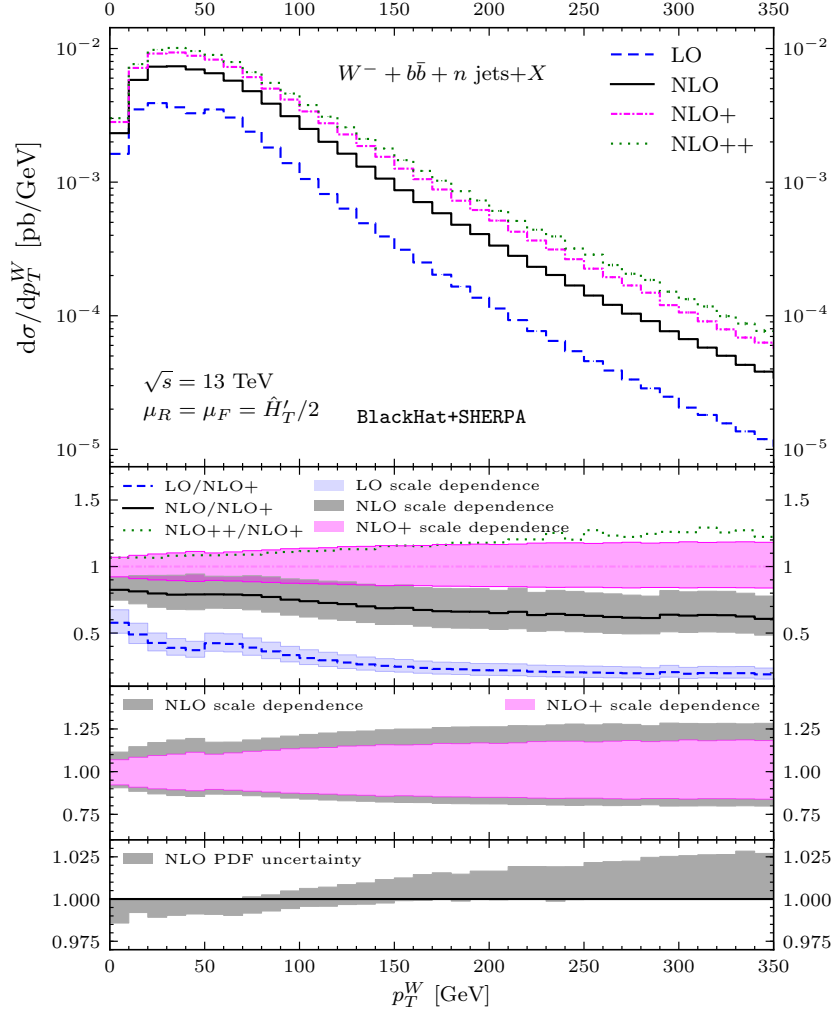


Figure 9.10.: The p_T of the W boson in inclusive $W^- b\bar{b}$ production. Format as in Fig. 9.9.

We observe the release of a kinematical constraint at NLO for the $p_T^{b\bar{b}}$ observable. At LO, the massive b -quark pair originates in a gluon splitting and $p_T^{b\bar{b}}$ and p_T^W are back-to-back. At NLO, real radiation emission relaxes this constraint and yields large corrections, due to a soft enhancement for low p_T^W . The release of this constraint together with the opening of a gluon-initiated channel give rise to a giant K -factor [9]. The kinematical constraint in $Wb\bar{b}$ is similar to those appearing in $V+1$ light jet (see e.g. Refs. [2, 13, 186]). The characteristics of the NLO results for $Wb\bar{b}$ production are thus expected [193].

In Fig. 9.10, we show the distribution in the transverse momentum of the vector boson p_T^W in the same format. We find similar results as for $p_T^{b\bar{b}}$: the NLO+ uncertainty estimation is marginally overlapping with the NLO predictions and has a scale sensitivity of the order of the NLO++ predictions. We estimate theoretical uncertainties to about 17% in the range of p_T^W shown (as compared to the 25% of the NLO results). As before, PDF uncertainties are subleading, appearing at 3% and below.

The last observable we show in Fig. 9.11 is the distribution in $M_{b\bar{b}}$, which exhibits similar features to the observables studied previously in this section. Here, we estimate

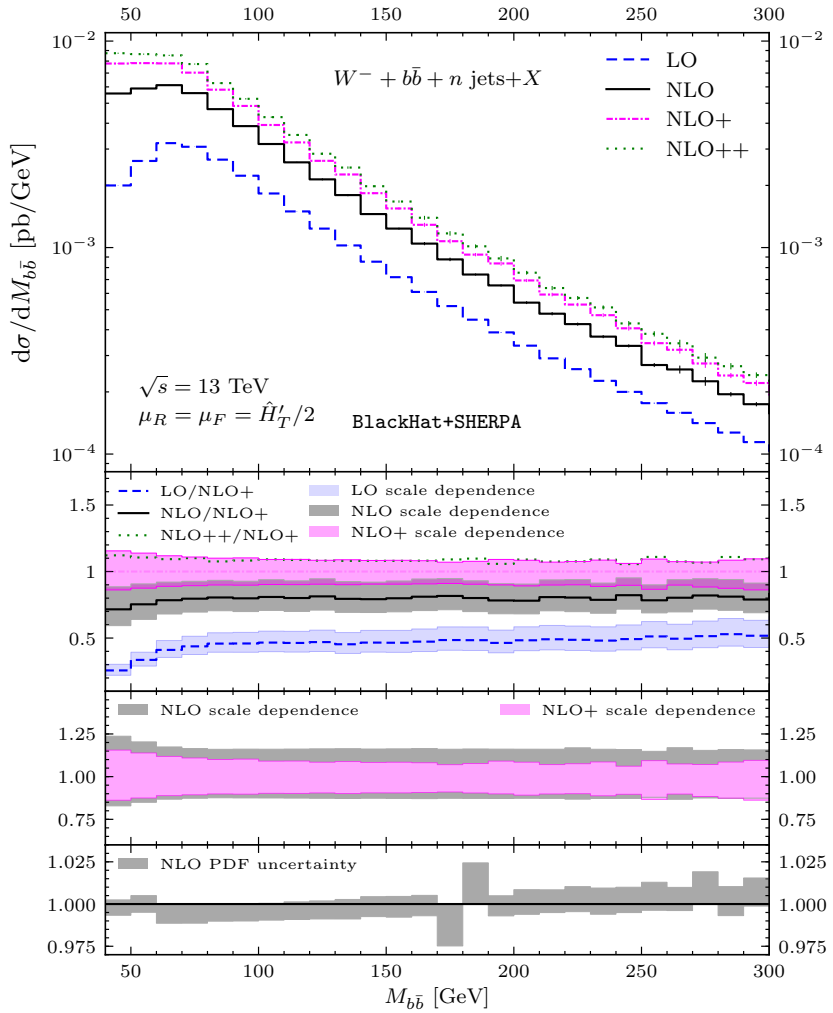


Figure 9.11.: The invariant mass of the $b\bar{b}$ system in inclusive $W^- b\bar{b}$ production. Format as in Fig. 9.9.

the uncertainties associated with scale sensitivity and missing higher-order effects to about 10% or slightly smaller. The PDF uncertainties are tiny, being at 1% or smaller.

Part 3:

Weak Vector Boson Production with Many Jets at the LHC $\sqrt{s} = 13$ TeV

CHAPTER 10

Introduction to $V + \text{Jets}$ Production

Electroweak vector boson production in association with multiple light jets has been extensively studied during the 7 and 8 TeV runs of the LHC by both the ATLAS and CMS experiments [54–68, 194]. Recently, the first measurements of this process class at an energy of 13 TeV have been presented by both collaborations [69, 70]. These studies highlight the extent to which theoretical predictions produced by either dedicated calculations or by general Monte Carlo event generators can describe total rates and differential distributions for signatures that involve leptons, missing transverse energy and many light jets. Such characterizations are of key importance given that searches for new physics carried out at hadron colliders target similar final states.

In recent years high precision results have become available with the NNLO QCD prediction for vector-boson production with a single jet [18–20]. Also other refinements to NNLO QCD and NLO electroweak corrections for this process are developed which for example have been used to describe backgrounds for dark matter searches [195]. Calculations for the high-multiplicity processes with four and five jets [2, 3] in the final state remain the state of the art at NLO QCD. The NLO electroweak corrections have been computed for up to three light jets [196, 197], and combined with QCD merging [198]. The matching to parton showers has been carried out for up to three jets in the final state [199], and multi-jet merging has been studied with up to two jets [190, 191, 200].

In this part of the thesis we show dedicated predictions for the 13 TeV LHC for $W + n$ -jet and $Z + m$ -jet production with $n \leq 5$ and $m \leq 4$, as shown in [71]. We use existing one-loop matrix elements from the original `BlackHat` library [32]¹ and provide results in publicly available Root [153] n -tuple files. In particular we study theoretical uncertainties related to scale sensitivity and PDF dependence of our predictions. To this end, we compare results obtained by using fixed-order dynamical scales based on the total partonic transverse energy as well as different variants of the `MinLO` method [5], as implemented in `SHERPA` [78] and a private implementation [201]. A recent study of on-shell $t\bar{t}$ production in association with up to three light jets [170] has performed a similar comparison and the results obtained were largely consistent between the choices of dynamical scales. We extend the comparison of fixed-order scales with the `MinLO` method to high-multiplicity processes with four or five light jets in the final state, where many scales are present. This type of comparison considers two very different approaches to the issue of scale choices and thereby helps to solidify the picture of uncertainties associated to the spurious dependence on unphysical renormalization and factorization scales.

¹As opposed to the new version of `BlackHat` [21] which can handle massive quarks that was presented in the other parts of this thesis.

In this Chapter 10 we summarize our calculational setup, showing all kinematical information employed. We also present the implementation of dynamical scales applied. In Chapter 11 we present our results for total and differential cross sections as well as for observable ratios and study their scale dependence and uncertainties associated to PDFs.

10.1. Basic Setup

The overall calculations are managed by the **SHERPA** package [78] and the required one-loop matrix elements are provided by the original **BlackHat** library [32], as opposed to the new version of **BlackHat** [21] which can handle massive quarks that was presented in the other parts of this thesis. Both Born and real-emission contributions are computed by the matrix-element generator **COMIX** [168], which also provides the necessary Catani-Seymour subtraction terms [202]. More details on the computational setup can be found in Refs. [2] and [3]. We include all contributing subprocesses and confirm in particular that 8-quark finite contributions to the real part in $W^\pm + 5$ -jet production are negligible [2]. Our results are stored in Root [153] n -tuple files and are publicly available. We use an extension [203] of the n -tuple file format [82] which allows for extended reweighting procedures.

We use **CT14 LO** (**CT14llo**) and **NLO** (**CT14nlo**) PDFs [171] at the respective orders, including the corresponding definition of the strong coupling α_s . To explore PDF uncertainties, we use the corresponding **CT14nlo** error set and compare to predictions generated with the PDF error sets of **ABM** [204], **MMHT** [205] and **NNPDF 3.1** [206]. The lepton-pair invariant mass follows a relativistic Breit-Wigner distribution, with $M_W = 80.385$ GeV and $M_Z = 91.1876$ GeV, and the widths are given by $\Gamma_Z = 2.4952$ GeV and $\Gamma_W = 2.085$ GeV. We employ a diagonal CKM matrix and use real values for the electroweak parameters.

We treat all light quarks (u, d, s, c, b) as massless particles and do not include contributions from real or virtual top quarks. We expect this to have a percent-level effect on cross-sections [3, 13, 21, 174]. We use the leading-color approximation [123] for the $V + 4, 5$ -jets one-loop matrix elements which we find to be precise at the level of 2% of the total cross section in lower jet-multiplicity calculations. We quote results for a single lepton (pair) flavor and both leptons are treated as massless, an approximation that can be applied to the electron or muon families. Results presented are produced in fixed-order parton-level perturbation theory and we do not apply any non-perturbative corrections to account for effects associated to underlying event or hadronization.

10.2. Kinematical Cuts

We present NLO QCD results for $pp \rightarrow V + n$ jets at the LHC with a center-of-mass energy of $\sqrt{s} = 13$ TeV, with $n \leq 5$ and $n \leq 4$ for $V = W^\pm$ and Z , respectively. We apply the following kinematical cuts:

$$p_T^{\text{jet}} > 30 \text{ GeV}, \quad |\eta^{\text{jet}}| < 3. \quad (10.1)$$

Jets are defined using the anti- k_{T} algorithm [120] with $R = 0.4$. In general, we order jets in the transverse momentum p_{T} and label them according to their hardness. For all charged leptons we require:

$$p_{\text{T}}^l > 20 \text{ GeV}, \quad |\eta^l| < 2.5. \quad (10.2)$$

The transverse mass of W^\pm bosons is defined by $M_{\text{T}}^W = \sqrt{2E_{\text{T}}^l E_{\text{T}}^\nu (1 - \cos(\Delta\phi_{l\nu}))}$ and we impose the following cuts on processes involving a W^\pm boson:

$$p_{\text{T}}^\nu > 20 \text{ GeV}, \quad M_{\text{T}}^W > 20 \text{ GeV}. \quad (10.3)$$

For processes involving a Z boson, we impose the following constraint on the invariant mass of its decay products:

$$66 \text{ GeV} < M_{l+l^-} < 116 \text{ GeV}. \quad (10.4)$$

10.3. Dynamical Scale Choices

In this section, we define the fixed-order scales employed, and present a variant of the MiNLO [5] procedure, which we will label MiNLO'. Finally we summarize the nomenclature used to label all dynamical scales considered.

10.3.1. Fixed-Order Scales

We use two dynamical fixed-order scales. On the one hand, we use a scale based on the total partonic transverse energy $\mu_0 = \hat{H}_{\text{T}}'/2$, defined in Eq. (7.4) and Section 7.5 of the previous part of this thesis. This scale choice has proven to be a sensible choice for weak-vector-boson production in association with jets as it tends to reduce the shape changes and global size of quantum corrections when going from LO to NLO (see for example [2–4]). On the other hand, we use an additional scale denoted as

$$\hat{S}_{\text{T}} = \frac{1}{2} \sum_j p_{\text{T}}^j + E_{\text{T}}^V, \quad (10.5)$$

where the sum runs over all final state partons. The scale \hat{S}_{T} differs from $\hat{H}_{\text{T}}'/2$ by the prefactor of E_{T}^V . It is designed to match the invariant mass of the lepton pair in kinematic configurations with very small hadronic transverse energy, and in events of di-jet type the transverse momentum of the hardest QCD jet. We use a conventional variation of the central scale by factors $(1/2, 1/\sqrt{2}, 1, \sqrt{2}, 2)$ to assess the scale dependence, keeping factorization and renormalization scales equal. In Subsection 10.3.3 we provide our notation used to refer to the different scales employed.

10.3.2. The MiNLO' Procedure

In our study, we compare results obtained with the fixed-order scales described in the previous subsection to those obtained with a dynamical scale choice based on the recent MiNLO [5] reweighting procedure. We use the implementation in **SHERPA** [78] that was validated in [170] and denote it schematically as MiNLO' since it differs in some aspects from the original formulation. Additionally, we compare to the original formulation of the MiNLO method [5] for processes with fewer than three jets in the final state by using the implementation of [201]. In contrast to the MiNLO' implementation, the original MiNLO variant uses the Sudakov factors of [207] and unordered clustering histories are treated in a different manner.

The MiNLO reweighting procedure is inspired by the next-to-leading logarithmic (NLL) branching formalism of Ref. [115]. It builds on an event-by-event identification of the most likely branching history of the Born kinematics leading to the full $V + n$ -parton final state using a k_T -type clustering algorithm. In order to reflect the nature of QCD interactions, only $1 \rightarrow 2$ branchings consistent with elementary interaction vertices are allowed in the MiNLO procedure. Successive branchings take place at scales q_1, q_2, \dots, q_N , where the nodal scales q_i correspond to the k_T measure of the jet algorithm. The strong coupling associated to each node in the branching tree is evaluated at the respective nodal scale q_i . In addition, we require a strong ordering of the nodal scales in the k_T clustering in the MiNLO' implementation. If an inverted scale hierarchy is encountered the clustering is terminated. In this case we set the scale of the remaining $V + m$ -parton (with $m < n$) “core” interaction, μ_{core} , to $\hat{H}_{\text{T}}'/2$ (or when explicitly stated, to \hat{S}_{T}) by default. This biases the scale choice for events with many hard scales towards $\hat{H}_{\text{T}}'/2$ (\hat{S}_{T}), an effect that will be further discussed in Chapter 11. Note in particular that at very high energies there may be configurations where no clustering can be performed at all: For example a $V + 2$ jet event with $p_{T,j1} \approx p_{T,j2} \gg m_{T,W}$ or a $V + 5$ jet event where $p_{T,j1} \approx p_{T,j2} \approx \dots \approx p_{T,j5}$ and $y_{j1} \ll y_{j2} \ll \dots \ll y_{j5}$. This is a considerable source of uncertainty because of the large available phase space at the LHC. In general, the clustering procedure for a leading-order process of $\mathcal{O}(\alpha_s^N)$ will yield a branching history with $M \leq N$ ordered nodal scales $q_1 \dots q_M$ and a core interaction of $\mathcal{O}(\alpha_s^{N-M})$ with scale $\mu_{\text{core}} > q_M$. We then set the global renormalization scale μ_R to the geometric mean $\mu_R^N = \mu_{\text{core}}^{N-M} \prod_{i=1}^M q_i$.

We then assign no-branching probabilities in the form of NLL Sudakov form factors to both intermediate lines (connecting branching nodes i and j) and external lines to reflect the fact that no radiation above a resolution scale, given by the lowest nodal k_T value in the clustering, should occur. External lines connected to the i -th branching are multiplied by a factor $\Delta_a(q_{\min}, q_i)$, where the lowest branching scale $q_1 = q_{\min}$ is identified as the resolution scale. Intermediate lines connecting nodes $j < i$ are dressed by factors $\Delta_a(q_{\min}, q_i)/\Delta_a(q_{\min}, q_j)$. Internal lines connected to the primary process are assigned form factors between their respective scales and μ_{core} . The factorization scale μ_F used in the evaluation of the PDFs is set to the lowest scale, $\mu_F = q_1$. In the MiNLO' implementation, we use a physical definition of the Sudakov form factors, which is given

by

$$\Delta_a(Q_0, Q) = \exp \left\{ - \int_{Q_0}^Q \frac{dq}{q} \frac{\alpha_s(q)}{\pi} \sum_{b=q,g} \int_0^{1-q/Q} dz \left(z P_{ab}(z) + \delta_{ab} \frac{\alpha_s(q)}{2\pi} \frac{2C_a}{1-z} K \right) \right\}, \quad (10.6)$$

where [208]

$$K = \left(\frac{67}{18} - \frac{\pi^2}{6} \right) C_A - \frac{10}{9} T_R n_f, \quad (10.7)$$

and $a = g, q$ corresponds to massless gluons and quarks, respectively. Eq. (10.6) does not exceed unity and can therefore be interpreted as a no-branching probability between the scales Q_0 and Q , while maintaining the correct limiting behavior for $Q_0 \ll Q$.

The **MiNLO** method generalized the above to NLO and thus requires some modifications [5]. Virtual corrections and integrated IR-subtraction terms are treated identically to the leading order case. Real-emission events have branching histories with $M+1 \leq N+1$ ordered branchings, but they are treated as Born-like M -parton events for the purpose of scale definition. This is achieved by discarding the softest branching, i.e. if the $M+1$ step branching history is given by $q_0 < q_1 < \dots < q_K$, we set the resolution scale to q_1 . Consequently, the softest emission at NLO (with scale q_0) is neither dressed with Sudakov factors nor does it enter the definitions of μ_R and μ_F . The value of the additional strong coupling at NLO (the $N+1$ -th power) appearing in both real and virtual corrections is set to the average of all other values of α_s , i.e. $N \alpha_s^{(N+1)} = (N-M) \alpha_s(\mu_{core}) + \sum_{i=1}^M \alpha_s(q_i)$.

In order to retain NLO accuracy of the full calculation, the Born configuration receives correction terms that are proportional to the first-order expansion of the Sudakov factors, Eq. (10.6). Conventional scale uncertainties associated to the **MiNLO** method are estimated using variations of μ_R and μ_F by constant factors of two. The scale of the strong coupling in the Sudakov form factors remains fixed at the integration variable, q , while it is varied in all other parts of the calculation, including the **MiNLO** counterterms used to subtract the $\mathcal{O}(\alpha_s)$ expansion of the Sudakov factors. Factorization scale variations in the **MiNLO'** procedure have been discussed extensively in [170]. We perform them in the same manner, i.e. we set q_1 equal to μ_F .

10.3.3. Nomenclature for Dynamical Scales Explored

Throughout this part of the thesis, we set renormalization and factorization scales equal $\mu_R = \mu_F = \mu_0$ for fixed-order scales. The results labeled “LO” and “NLO” use the central scale $\mu_0 = \hat{H}'_T/2$ by default, where \hat{H}'_T is defined in Eq. (7.4). When necessary, to distinguish the usage of the fixed-order scales defined in Section 10.3.1, we write “(N)LO $\hat{H}'_T/2$ ” or “(N)LO \hat{S}_T ”, where \hat{S}_T is defined in Eq. (10.5).

In the **MiNLO'** procedure described in Section 10.3.2 the default core scale is $\mu_{core} = \hat{H}'_T/2$. When considering variations of this choice we explicitly write “Mi(N)LO' $\hat{H}'_T/2$ ” or “Mi(N)LO' \hat{S}_T ”. We also compare to the original formulation of the **MiNLO** method [5] for processes with fewer than three jets in the final state. Compared to our implementation,

this variant uses the Sudakov factors of [207] and unordered clustering histories are treated in a different manner. Following the previous naming convention, we label those results as “ $M_i(N)LO \hat{H}'_T/2$ ” or “ $M_i(N)LO \hat{S}_T$ ” depending on the choice of core scale μ_{core} employed.

CHAPTER 11

Results for $V + \text{Jets}$ Production

In this chapter, we present phenomenological results for the production of a weak vector boson V in association with up to 5 jets for $V = W^+$ and W^- , and with up to 4 jets for $V = Z$ at the LHC $\sqrt{s} = 13$ TeV, as shown in Ref. [71]. We first present our results for total cross sections and differential distributions and then for a series of observable ratios. In particular, we explore uncertainties associated to renormalization and factorization scales by using different functional forms for the dynamical scales, as laid out in Section 10.3. In general the structure of QCD corrections is very similar for the different vector bosons W^\pm and Z and we often show results only for one type of weak vector boson.

11.1. Total Cross Sections

We quote total cross sections in Tables 11.1, 11.2 and 11.3 for the production of a weak vector boson V in association with up to 5 jets for $V = W^+$ and W^- , and with up to 4 jets for $V = Z$, respectively. We include results obtained with a central scale $\hat{H}'_T/2$ as well as those obtained with **MiNLO'** (see section 10.3.3 for the nomenclature that we use for the different dynamical scales considered). Furthermore, in Table 11.4 we show jet production ratios [4, 155–158] for all vector boson types, that is ratios of total cross sections for the production for $V + n$ jets to the production of $V + (n - 1)$ jets.

The scale dependence of LO cross sections for the scale choice $\mu_0 = \hat{H}'_T/2$ is monotonically increasing with jet multiplicity. The LO scale dependence for $V + 1$ jet, which appears at around 4% is not representative of the associated theoretical uncertainties, in particular due to kinematical constraints that are released at NLO. In this situation, at LO the p_T of the vector boson matches the one from the unique jet. Real contributions at NLO release this constraint, producing a soft enhancement that tends to produce large corrections [9, 12, 209]. The total cross section at the central scale choice for the dynamical scale $\mu_0 = \hat{H}'_T/2$ lies near the plateau of the NLO scale dependence. Resultingly, the uncertainty estimates based on lower/upper values of the cross sections seem slightly small. If we quote the absolute deviations with respect to this value, we can estimate NLO scale sensitivity at the order of 10% (running from about 6% to 16%, depending on multiplicity).

The total cross sections with **MiLO'** are similar to the corresponding LO results. However, the absolute predictions tend to be larger for **MiLO'** with the excess increasing slightly with multiplicity. The central prediction of the **MiNLO'** results agree well with the NLO results. Moreover, their ratio is relatively stable as a function of jet multiplicity.

jets	W^+ LO	W^+ NLO	W^+ MiLO'	W^+ MiNLO'	MiLO'/LO	MiNLO'/NLO
1	$588.49(33)^{+23.77}_{-27.07}$	$764.9(16)^{+37.8}_{-27.1}$	$591.50(35)^{+20.70}_{-25.36}$	$799.1(18)^{+49.9}_{-35.1}$	1.005(1)	1.045(3)
2	$197.23(27)^{+44.64}_{-34.42}$	$197.78(66)^{+1.80}_{-7.82}$	$205.01(28)^{+46.95}_{-36.46}$	$211.44(78)^{+9.50}_{-12.07}$	1.039(2)	1.069(5)
3	$57.07(10)^{+22.82}_{-15.23}$	$49.54(27)^{+0.00}_{-3.13}$	$59.09(11)^{+26.02}_{-16.89}$	$52.32(41)^{+0.19}_{-3.95}$	1.035(3)	1.056(10)
4	$16.408(50)^{+9.344}_{-5.566}$	$12.14(22)^{+0.00}_{-1.59}$	$17.287(56)^{+11.768}_{-6.516}$	$12.78(24)^{+0.00}_{-2.87}$	1.054(5)	1.053(27)
5	$4.579(45)^{+3.399}_{-1.829}$	$3.06(14)^{+0.00}_{-0.72}$	$4.908(56)^{+4.691}_{-2.233}$	$3.21(14)^{+0.00}_{-0.52}$	1.072(16)	1.049(66)

Table 11.1.: LO and NLO QCD results for inclusive $W^+ + 1, 2, 3, 4, 5$ -jet total cross sections (in pb). We quote results for the two dynamical scales, $\hat{H}_T'/2$ and MiNLO', as well as their ratios. Details of the setup are given in section 10.2. We determine the conventional scale dependence by varying both μ_R and μ_F by factors of 2 and $\sqrt{2}$ up and down. The statistical integration error is given in parenthesis.

jets	W^- LO	W^- NLO	W^- MiLO'	W^- MiNLO'	MiLO'/LO	MiNLO'/NLO
1	$446.68(22)^{+17.48}_{-20.29}$	$582.0(11)^{+25.6}_{-18.6}$	$448.82(23)^{+15.07}_{-18.92}$	$608.2(12)^{+34.6}_{-24.5}$	1.005(1)	1.045(3)
2	$141.67(14)^{+31.89}_{-24.67}$	$144.53(39)^{+1.03}_{-5.46}$	$147.40(15)^{+33.40}_{-26.08}$	$154.11(46)^{+5.91}_{-8.40}$	1.040(1)	1.066(4)
3	$39.029(55)^{+15.653}_{-10.448}$	$34.34(16)^{+0.00}_{-2.10}$	$40.889(61)^{+17.99}_{-11.70}$	$36.20(22)^{+0.03}_{-2.64}$	1.048(2)	1.054(8)
4	$10.513(23)^{+6.035}_{-3.585}$	$8.22(13)^{+0.00}_{-0.86}$	$11.399(27)^{+7.797}_{-4.314}$	$8.85(19)^{+0.00}_{-1.85}$	1.084(3)	1.077(29)
5	$2.747(12)^{+2.059}_{-1.103}$	$1.971(56)^{+0.004}_{-0.298}$	$3.063(14)^{+2.949}_{-1.400}$	$2.105(59)^{+0.000}_{-0.788}$	1.115(7)	1.068(43)

Table 11.2.: As in Table 11.1 but for inclusive $W^- + 1, 2, 3, 4, 5$ -jet total cross sections.

jets	Z LO	Z NLO	Z MiLO'	Z MiNLO'	MiLO'/LO	MiNLO'/NLO
1	$112.264(60)^{+4.121}_{-4.876}$	$142.79(15)^{+5.12}_{-3.70}$	$112.615(43)^{+3.390}_{-4.448}$	$148.48(17)^{+7.21}_{-5.04}$	1.003(1)	1.040(2)
2	$36.140(38)^{+7.931}_{-6.178}$	$36.811(65)^{+0.228}_{-1.339}$	$36.780(28)^{+8.076}_{-6.382}$	$38.962(68)^{+1.555}_{-2.147}$	1.018(1)	1.058(3)
3	$10.4844(76)^{+4.1227}_{-2.7702}$	$9.175(44)^{+0.000}_{-0.578}$	$11.1242(87)^{+4.847}_{-3.166}$	$9.612(50)^{+0.000}_{-0.617}$	1.061(1)	1.048(7)
4	$2.9597(37)^{+1.6698}_{-0.9989}$	$2.331(29)^{+0.000}_{-0.246}$	$3.3050(43)^{+2.248}_{-1.247}$	$2.439(37)^{+0.000}_{-0.668}$	1.117(2)	1.046(21)

Table 11.3.: As in Table 11.1 but for inclusive $Z + 1, 2, 3, 4$ -jet total cross sections.

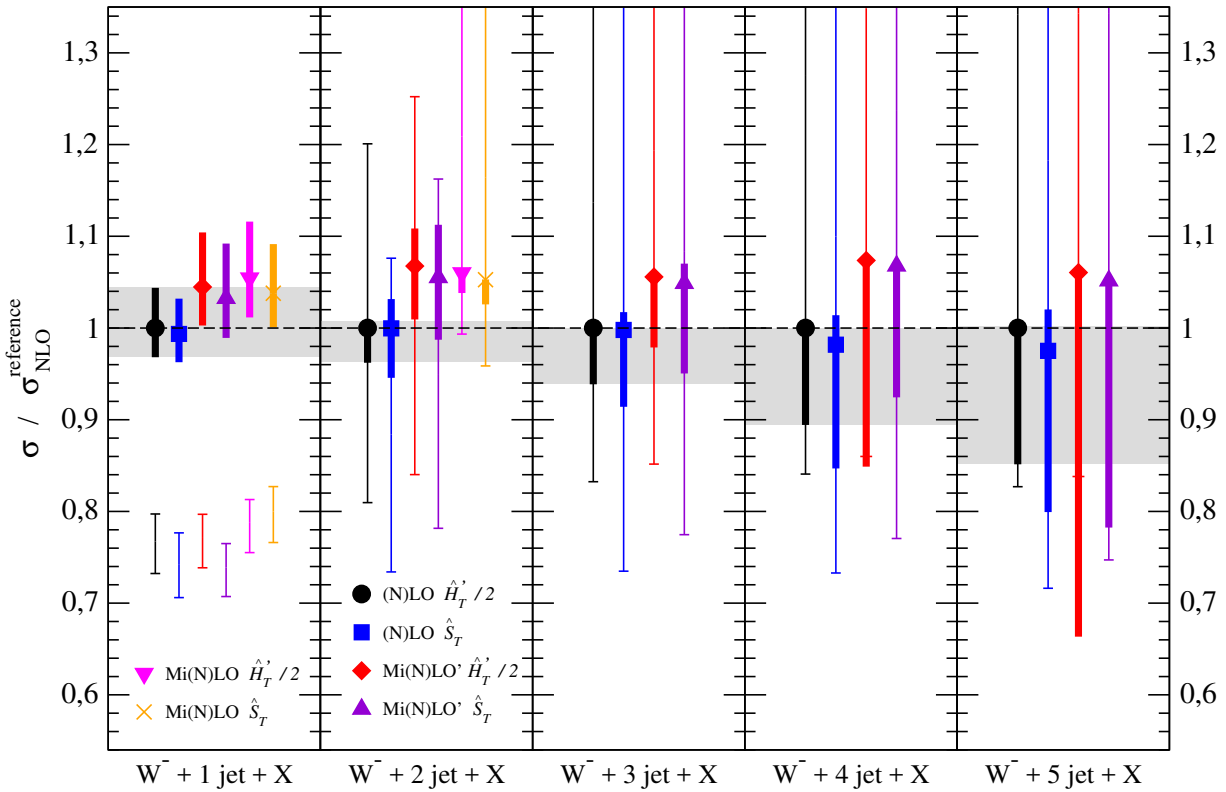


Figure 11.1.: Scale dependence of total cross sections for inclusive $W^- + 1, 2, 3, 4, 5$ -jet production considering all scales defined in section 10.3.3 for both LO and NLO results. The corresponding symbols and colors are specified in the legend of the plot. The LO scale-dependence bands are represented by thin lines (in certain cases extending outside of the range plotted) while the thick lines represent NLO bands. We normalized all results to the corresponding NLO $\hat{H}'_T/2$ result for each jet multiplicity and the gray bands show the NLO $\hat{H}'_T/2$ scale-dependence band.

$W^+ n/(n-1)$				$W^- n/(n-1)$				$Z n/(n-1)$		
n	LO	NLO	MiNLO'	LO	NLO	MiNLO'	LO	NLO	MiNLO'	
2	0.3351(5)	0.259(1)	0.265(1)	0.3172(4)	0.248(1)	0.253(1)	0.3219(4)	0.2578(5)	0.2624(5)	
3	0.2894(6)	0.250(2)	0.247(2)	0.2755(5)	0.238(1)	0.235(2)	0.2901(4)	0.249(1)	0.247(1)	
4	0.288(1)	0.245(5)	0.244(5)	0.2694(7)	0.239(4)	0.244(5)	0.2823(4)	0.254(3)	0.254(4)	
5	0.279(3)	0.252(12)	0.251(11)	0.261(1)	0.240(8)	0.238(8)	—	—	—	

Table 11.4.: LO, NLO and MiNLO' QCD jet production ratios for W^\pm as well as Z/γ^* . The ratio is taken for a given process to that with one fewer jet. The setup is specified in section 10.2. The number in parenthesis next to the ratio gives the corresponding statistical integration error.

We display total cross sections and the corresponding scale variations for W^- production in association with jets for all scales considered in this analysis in Fig. 11.1. We observe that in particular the MiLO' and MiNLO' predictions exhibit a considerable variation for different choices of μ_{core} , both in their central value and in the associated conventional scale uncertainty. The sensitivity on the core scale can be traced to the procedure for the identification of ordered clustering hierarchies (cf. Sec. 10.3.2). The clustering is terminated as soon as an inverted scale hierarchy is encountered and the remaining “core” process as evaluated at μ_{core} . For events with many hard scales, this biases the scale choice towards μ_{core} , and therefore the precise definition of μ_{core} plays a significant role [210]. On average, the choice of \hat{S}_T increases μ_{core} and thus permits more clusterings in high-multiplicity final states and therefore induces more associated Sudakov form factors. Resultingly, both central value of the prediction and the related scale uncertainty are reduced on average.

In Table 11.4 we show jet-production ratios. In these ratios many uncertainties associated to scale sensitivity and PDF dependence cancel. Also systematic uncertainties in experimental analyses associated with luminosity measurements cancel. Overall, we observe a remarkable stability of these ratios at NLO for both scale choices $\hat{H}'_T/2$ and MiNLO', with the ratio for all of them being around a value of 0.25. This universality is present for NLO ratios in V +jet production even though the corresponding LO ratios deviate considerably. One can use this universality of the jet production ratios for tests of the SM and they can be exploited to make extrapolations of total and differential cross sections to larger jet-multiplicity processes [4].

11.2. Scale Dependence

In Fig. 11.2 we display the dependence of total cross sections in W^- production in association with up to 5 jets on renormalization and factorization scales. Both LO and MiLO' results are very sensitive to these scales. However, we find a remarkable stability for both NLO and MiNLO' results, with the central prediction lying at the plateau of the NLO curves for $W^-+3,4$ and 5 jets, thus minimizing the scale variations (for a discussion of this effect, see [12]).

The LO results obtained with the two scale choices are largely consistent in both normalization and scale sensitivity since the difference between the results is smaller than the respective factor-two scale variations. MiLO' results are slightly larger compared to the LO results obtained with $\hat{H}'_T/2$. We attribute this to the fact that the smaller average renormalization scales for large jet multiplicity in MiLO' and the correspondingly large strong couplings are not entirely compensated by the suppression from Sudakov form factors. We also note that the two LO results differ slightly in their variation. Whereas the scale uncertainty at low multiplicity associated to LO and MiLO' results are comparable, the MiLO' results exhibit larger scale variations with increased multiplicity.

The NLO results obtained with both dynamical scales are mostly consistent. For the case of multiplicities with more than 2 jets, the differences between the two scale choices lie within the respective factor-two scale variations. For the case of $W + 2$ -jet production,

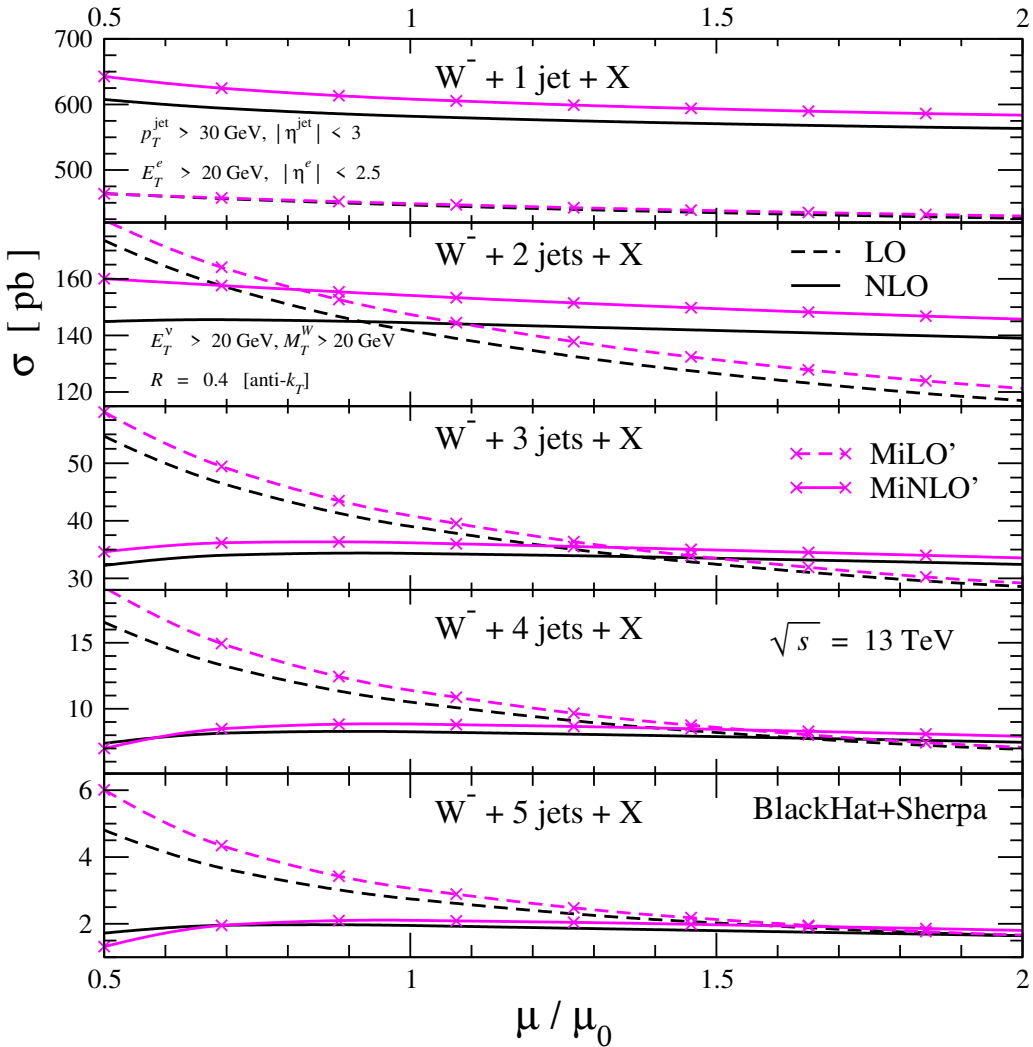


Figure 11.2.: Renormalization- and factorization-scale dependence of total cross sections for inclusive $W^- + 1, 2, 3, 4, 5$ -jet production. For each multiplicity, we show the dependence of predictions at LO as dashed (black) lines and at NLO as solid (black) lines with $\mu_0 = \mu_r = \mu_f = \hat{H}'_T/2$, while predictions for MiLO' are shown as dashed-crossed (magenta) lines and those for MiNLO' as solid-crossed (magenta) lines.

we observe an approximately 15% discrepancy which can be taken as an estimate for the total scale uncertainty associated with this prediction. We furthermore observe that with increasing multiplicity, the bands associated to the uncertainty of the respective scale choice seem to behave differently between $\hat{H}'_T/2$ and the MiNLO' scheme. In general, the scale uncertainty obtained by factor-two variations grows with multiplicity, a trend that is slightly more pronounced for the MiNLO' scale choice.

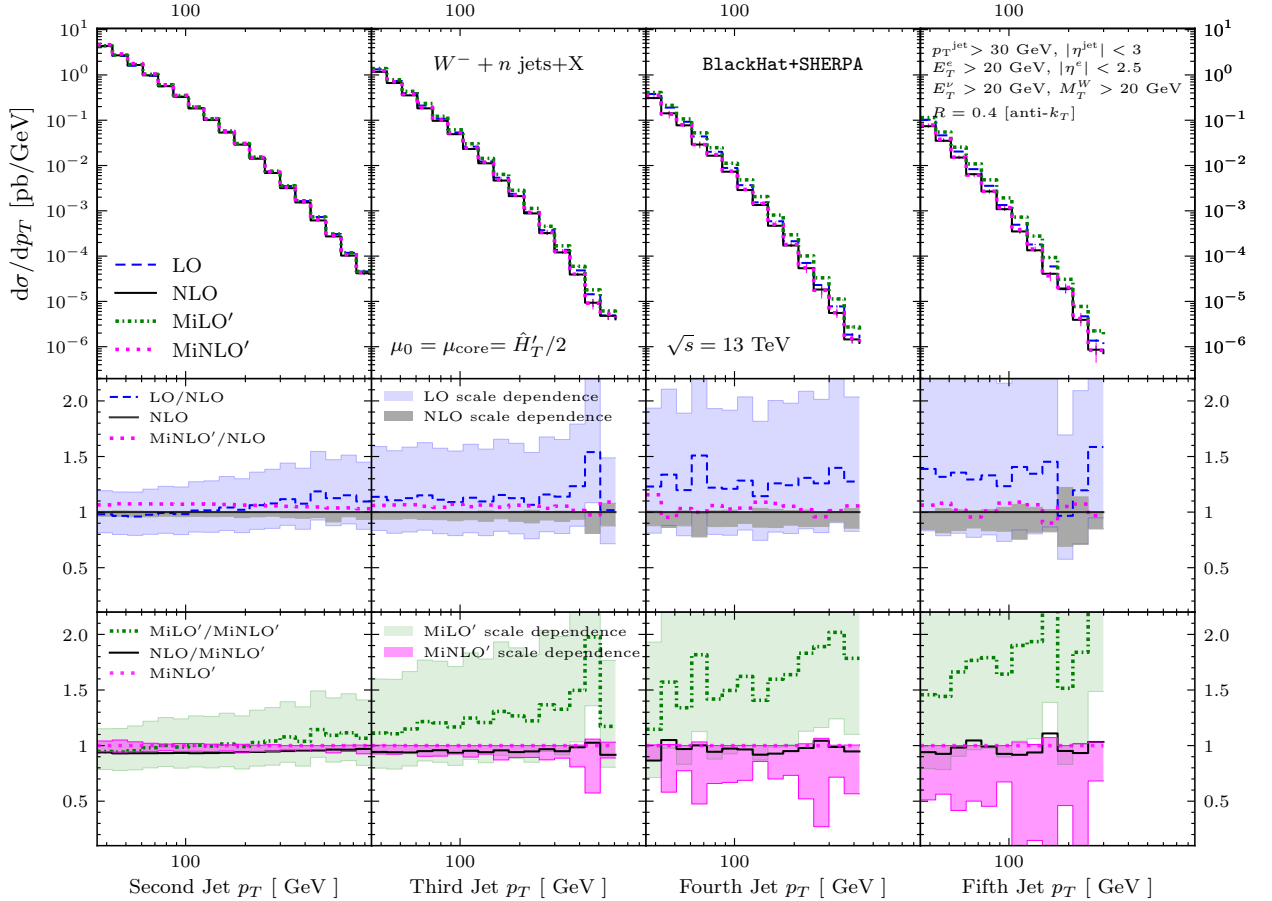


Figure 11.3.: The p_T spectra of the softest jet (ordered in p_T) in inclusive samples of $W^- + n$ jets ($n = 2, 3, 4, 5$) at the LHC at $\sqrt{s} = 13$ TeV. In the upper panels, we show NLO predictions as solid (black) lines, MiNLO' predictions as dotted (magenta) lines, while LO predictions are shown as dashed (blue) lines and MiLO' predictions as dash-dotted (green) lines. In the central panels, we show predictions for both LO and MiNLO' distribution as well as scale-dependence bands at NLO (grey) and LO (blue) normalized to the central NLO prediction. Similarly in the bottom panels, we show predictions for MiLO' and NLO distributions as well as scale dependence bands for MiLO' (green) and MiNLO' (magenta) normalized to the central MiNLO' predictions.

11.3. Differential Cross Sections

In this section we present several differential cross sections and show the impact that next-to-leading order corrections have on fixed-order predictions over phase space. We show results only for the W^- weak vector boson, as in general the structure of QCD corrections is very similar for the different vector bosons W^\pm and Z . We include (N)LO and Mi(N)LO' results and do not show results for the scale choice \hat{S}_T , since they are rather consistent with the ones obtained with $\hat{H}_T/2$.

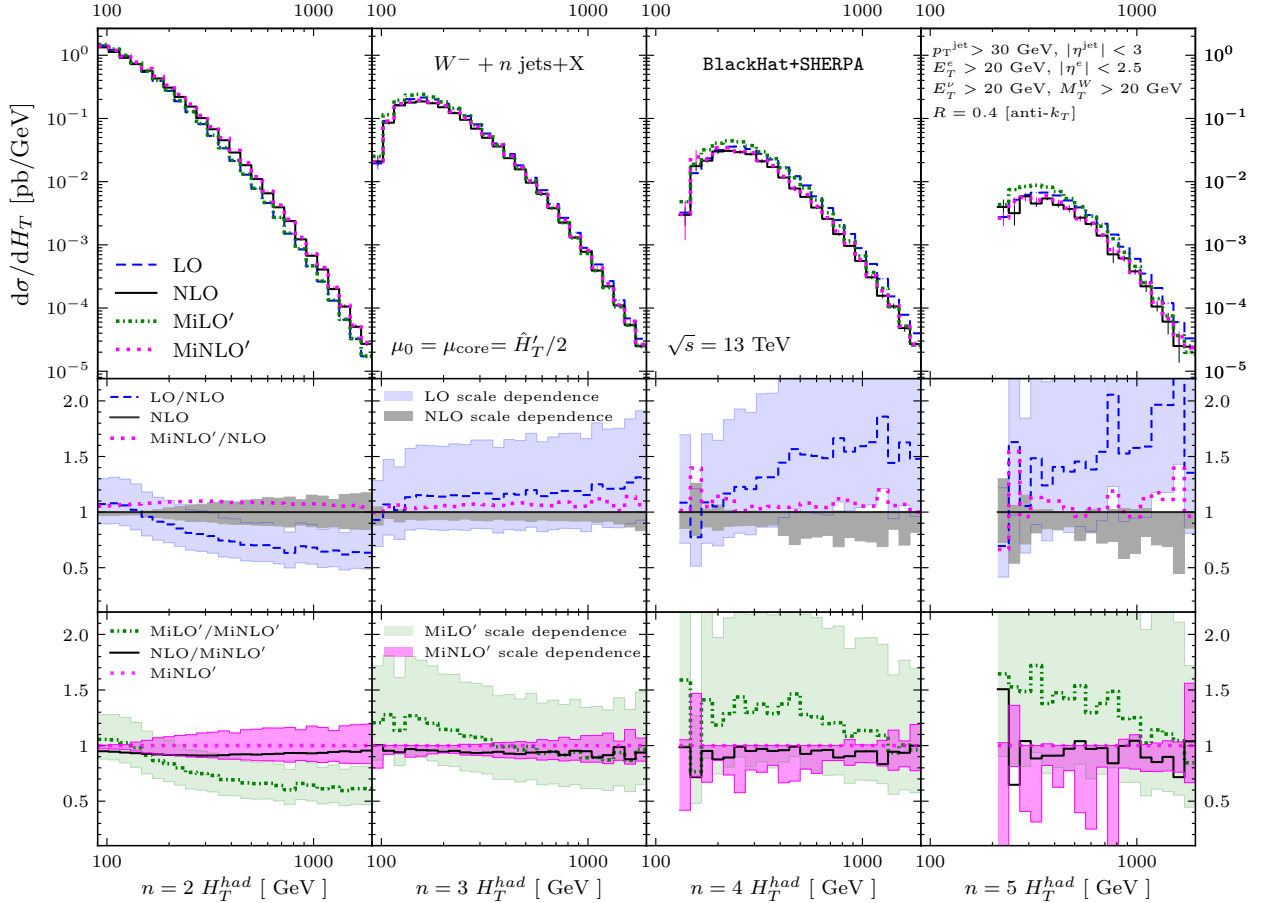


Figure 11.4.: Distribution in the total hadronic transverse energy H_T^{had} in inclusive samples of $W^- + 2, 3, 4, 5$ -jets. Format as in Figure 11.3.

In Fig. 11.3 we show p_T spectra of the softest jet (ordered in p_T) for the production of $W^- + n$ jets with n ranging from $n = 2$ to $n = 5$. Solid (black) lines show NLO predictions, dotted (magenta) lines MiNLO' predictions, while dashed (blue) lines show LO predictions and dash-dotted lines MiLO' predictions. The thin vertical lines represent the estimate of statistical integration errors. In the middle panels, we show ratios of LO, NLO and MiNLO' to the NLO result including scale dependence bands at LO (blue) and NLO (grey). Similarly, the lower panels show ratios of MiLO', NLO and MiNLO' to the MiNLO' results and scale dependences for MiLO' (green) and MiNLO' (magenta). Previous studies at lower energies (see for example [2]) have shown that the n -th jet p_T spectrum in an inclusive $V + n$ jets sample tends to have rather small distortions due to QCD corrections (as long as $n > 1$). We can confirm this result with our current study, with the LO to NLO ratios being flat over a wide p_T range. It is clear that although LO results employing an $\hat{H}'_T/2$ dynamical scale have similar shapes to the NLO results, their normalization is badly determined, following the trend described in the previous section on total cross sections. Furthermore, we notice that MiNLO' results are in good agreement with NLO results regarding both shape and normalization over the seven orders of magnitude shown for the differential cross sections. Using the $\hat{H}'_T/2$ scale-dependence band as well as its deviation with respect to the MiNLO' result as a measure of the associated uncertainties,

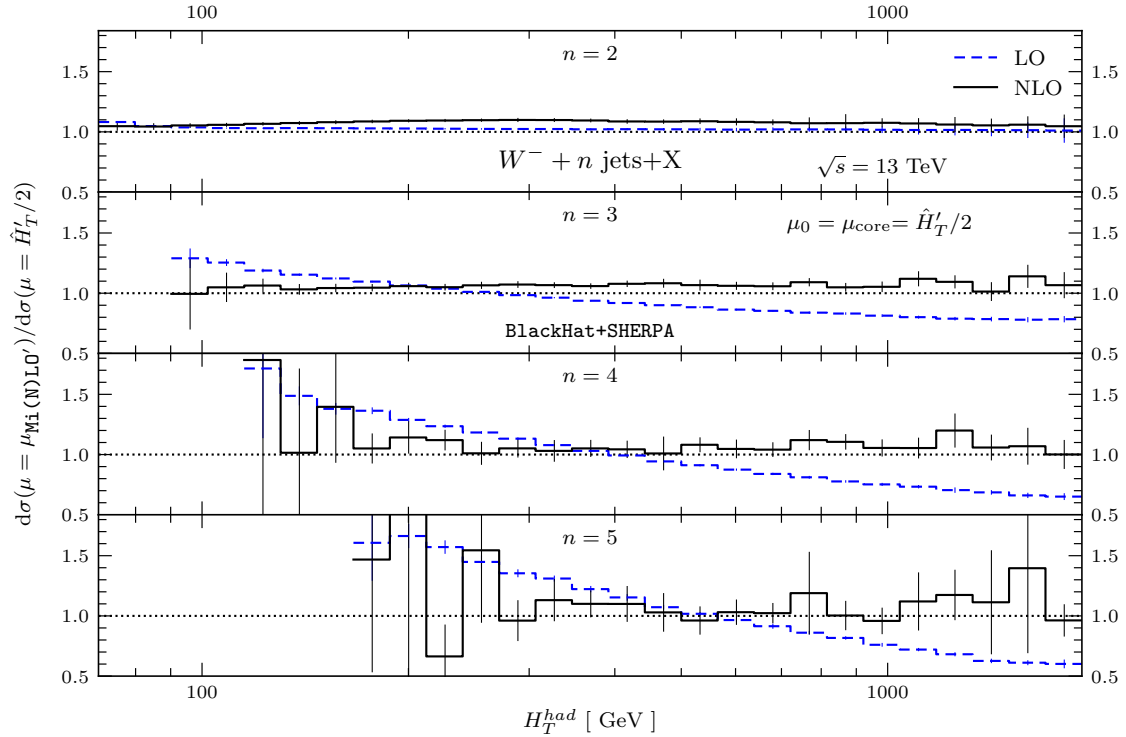


Figure 11.5.: Ratio of the distribution in the total hadronic transverse energy H_T^{had} in inclusive samples of $W^- + n$ -jet production ($n = 2, 3, 4$ and 5) comparing the MiNLO' and $\hat{H}'_T/2$ scale choice.

we can confirm the relatively good theoretical control over NLO prediction for these observables and estimate related uncertainties to the order of 15%.

In Fig. 11.4 we study the differential distribution in the total hadronic transverse energy H_T^{had} as well as ratios thereof between $\text{Mi}(N)\text{LO}'$ and $\hat{H}'_T/2$ scale choices in Fig. 11.5. The format of Fig. 11.4 is as in Fig. 11.3, that is we show in side-by-side panels results for $W^- + n$ jets, with $n = 2, 3, 4$ and 5 . For $n \geq 3$, we find that the corrections to the H_T^{had} spectrum change the shape of the distributions relatively mild in general, which can be seen by looking at both LO to NLO ratios as well as MiNLO' to NLO ratios. Notice that the fluctuations at NLO for small values of H_T^{had} for increasing multiplicity are just due to the fact that near threshold the integration errors grow large. On the other hand, the $n = 2$ LO predictions have a large shape difference compared to the NLO results. These changes are similar to the corresponding observable for $n = 1$ for which it is well known that large corrections appear from configurations with many jets in the final state [9]. The widening of the NLO scale band indeed shows that real contributions are large in the tail of the distributions, making this observable sensitive to quantum corrections. In principle a computation of NNLO QCD correction to $V + 2$ jets would be desirable in order to stabilize the predictions.

We notice an interesting behavior in the ratios of H_T^{had} distributions between $\text{Mi}(N)\text{LO}'$ and $\hat{H}'_T/2$ scale choices as shown in Fig. 11.5. At NLO, these ratios are quite stable and lie around 1. For the $n = 2$ case, the ratio between MiLO' and LO results is also stable

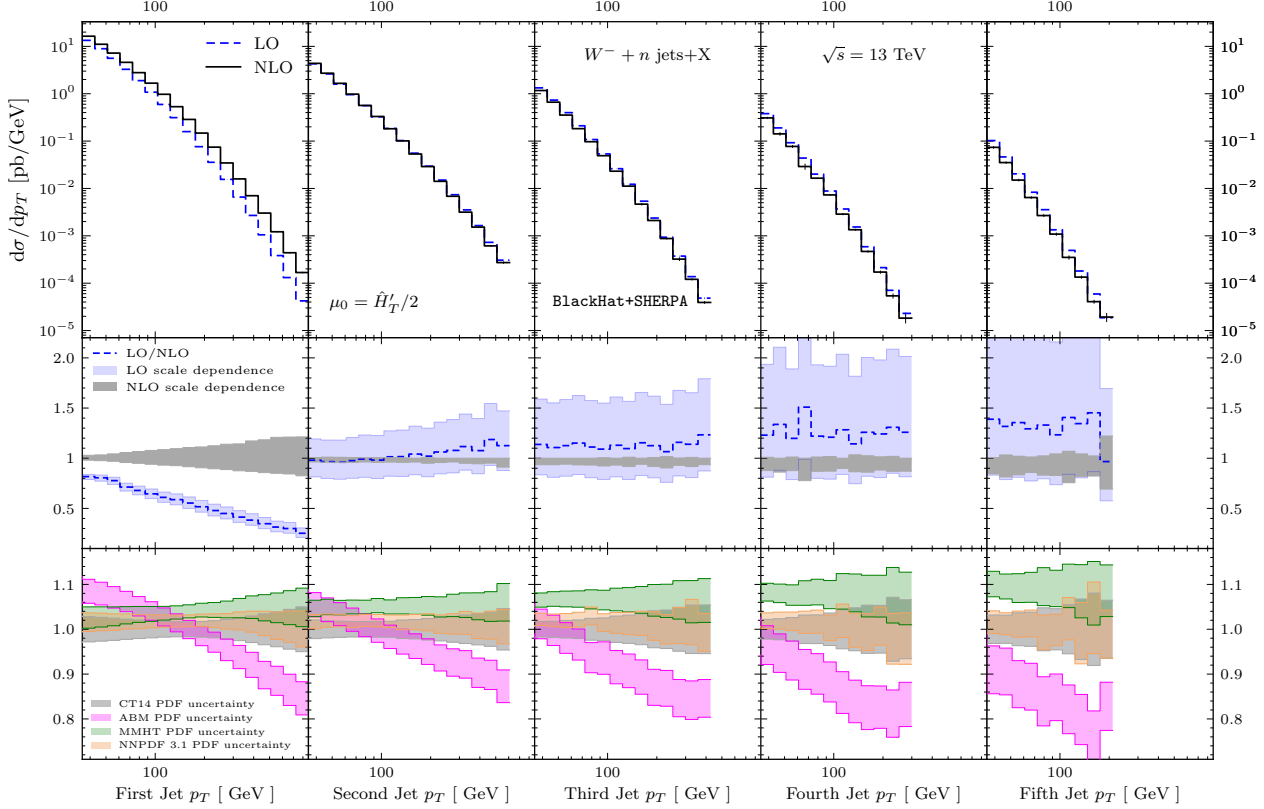


Figure 11.6.: PDF uncertainty for the p_T distribution of the softest jet in an inclusive sample of $W^- + n$ jets ($n = 1, 2, 3, 4, 5$) at the LHC at $\sqrt{s} = 13$ TeV. In the upper panels, we show NLO predictions as solid (black) lines and LO predictions as dashed (blue) lines. The central panels show the scale-dependence bands at NLO (grey) and LO (blue) normalized to the central NLO prediction. The lower panels show the NLO PDF uncertainty for CT14 (gray), ABM (magenta), MMHT (green) and NNPDF 3.1 (orange) PDF sets, normalized to the results obtained with CT14.

and lies around 1. However, for the higher multiplicity cases the LO ratios become tilted with a negative slope. This trend becomes more pronounced with light-jet multiplicity. We attribute this to the fact that very large values of H_T^{had} are mostly generated in events of di-jet type with largely disparate scales of jet production, i.e. $p_{T,j1} \approx p_{T,j1} \gg p_{T,j3}, \dots, p_{T,jn}$. In the **MiLO'** method, this induces Sudakov suppression factors that reduce the corresponding high- H_T^{had} tails compared to the LO prediction. However, these factors improve the agreement of **MiLO'** with the **MiNLO'** prediction as visible in the bottom panels of Fig. 11.4.

In Figure 11.6 we explore uncertainties associated to the choice of PDFs and show the PDF uncertainty bands for n th-jet p_T spectra in an inclusive sample of $W^- +$ jets for $\hat{H}'_T/2$, analogous to the distributions shown in Fig. 11.3. The additional bottom panel shows the NLO PDF uncertainty bands for CT14 (gray) [171], ABM (magenta) [204], MMHT (green) [205] and NNPDF 3.1 (orange) [206] PDF sets, all normalized to the central value obtained with CT14. We generated the data for Fig. 11.6 by creating a

nbr. of jets	1	2	3	4	5
CT14	1.000	1.000	1.000	1.000	1.000
ABM	1.070	1.039	1.000	0.960	0.920
MMHT	1.029	1.049	1.066	1.080	1.095
NNPDF 3.1	1.016	1.018	1.020	1.020	1.016

Table 11.5.: NLO QCD total cross sections for inclusive $W^- + 1, 2, 3, 4, 5$ -jet production for different choices of PDF sets, normalized to the results for CT14. This data was generated by creating a fastNLO table [211] from the n -tuple data.

fastNLO table [211] from our n -tuple data. We also quote the central values for total cross sections obtained with the different choices of PDF sets, normalized to the results for CT14, in Tab. 11.5.

In our samples, PDF uncertainties can reach up to 10% and most of the error sets overlap. However, both central values and uncertainty bands of the ABM results lie outside the uncertainty bands of all other PDF sets. Also, the MMHT bands lie systematically higher than the others, a trend that is more pronounced in the large-multiplicity cases. All uncertainty bands increase for larger p_T as the effective mass sampled for the corresponding events grows and the PDFs are evaluated for larger values of the Bjorken x , with less data available to constrain the PDF fits. PDF uncertainties are thus of the same order as NLO scale uncertainties, in particular for the high-multiplicity processes, where we observe a considerable spread between the different PDF sets. At the level of normalized NLO QCD total cross sections this is shown in Tab. 11.5.

11.4. Cross Section Ratios

In this section, we study the differential jet ratio for W^- production as well as differential ratios of both W^-/W^+ and Z/W production. These observable ratios feature reduced uncertainties compared to basic observables such as cross sections or differential distributions. In particular, experimental uncertainties related to jet energy scale, lepton efficiency, acceptance and proton-proton luminosity should be greatly reduced. Also the observable ratios are expected to suffer less from theoretical uncertainties from uncalculated higher-order corrections. Furthermore, non-perturbative effects are expected to largely cancel in these observable ratios. When comparing parton-level result to experimental data, these non-perturbative effect such as hadronization of the outgoing partons or effects induced by the underlying event have to be accounted for. In consequence, these ratios can help to better understand the structure of quantum corrections to processes with a vector boson in association with multiple jets and as shown in [4] they exhibit certain universal features that can be exploited in phenomenological studies at hadron colliders.

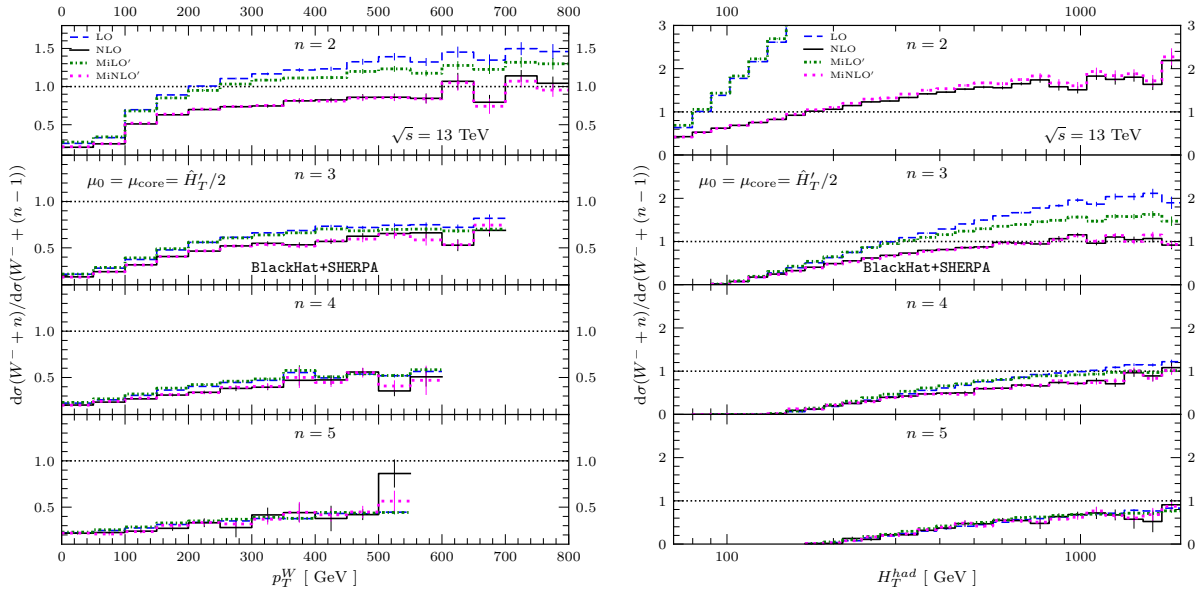


Figure 11.7.: Ratios of $W^- + n$ -jet to $W^- + (n-1)$ -jet cross sections as a function of the transverse momentum p_T^W of the W^- -boson on the left, and as a function of the hadronic transverse energy H_T^{had} on the right with $n = 2$ (top panel) to $n = 5$ (bottom panel). LO results are shown as dashed (blue) lines and NLO results as solid (black) lines, while MiLO' results are shown as dash-dotted (green) lines and MiNLO' results as dotted (magenta) lines.

11.4.1. Jet Ratios

In Figure 11.7, we show differential jet-production ratios of $W^- + n$ -jet to $W^- + (n-1)$ -jet production with up to $n = 5$ jets as a function of the W^- -boson transverse momentum p_T^W in the left panel and of the total hadronic transverse energy H_T in the right panel. We show ratios for both scale choices with $\hat{H}'_T/2$ at LO shown as dashed (blue) lines and at NLO as solid (black) lines, while MiLO' ratios are shown as dash-dotted (green) lines and those for MiNLO' as dotted (magenta) lines.

We observe that the $W^- + 2$ -jet / $W^- + 1$ -jet ratio ($n = 2$) as a function of p_T^W shows large NLO corrections. This is mainly due to the large corrections appearing at NLO [9], which are related to the release of a kinematical constraint as described in the previous sections. The corresponding corrections at NNLO [18–20] are stabilized. In the lowest p_T region (up to the order of the W mass), the ratios lie around a value of 0.25, roughly independent of the number of jets. In this region, the NLO corrections are modest for all displayed multiplicities, which is in agreement with the total cross sections displayed in Tab. 11.2. The ratios grow monotonically with p_T^W and are stabilized for $n \geq 3$ for large p_T^W . The increase is less pronounced for the higher-multiplicity cases and the ratio stabilizes for $n = 5$ around a value 0.5. In the low-multiplicity cases ($n \leq 3$) and for large values of p_T^W , the ratio for MiLO' lies below that for LO. The LO ratios in the higher-multiplicity cases as well as all those of NLO and MiNLO' agree very well.

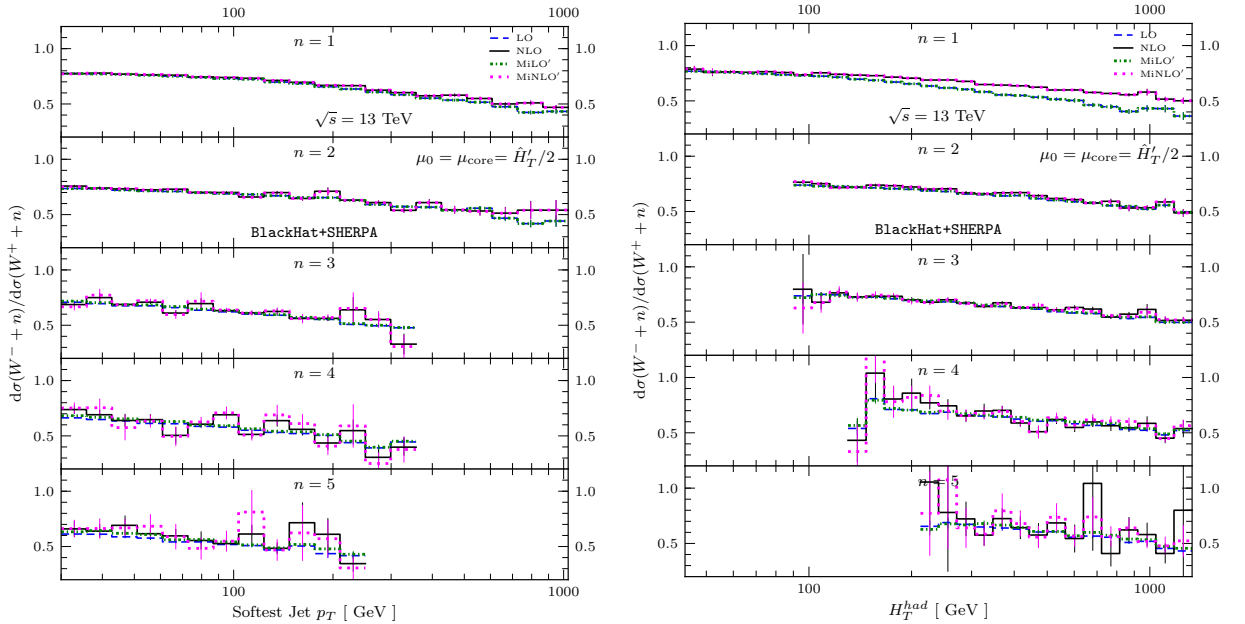


Figure 11.8.: The charge ratios of $W^- + n\text{-jet}$ to $W^+ + n\text{-jet}$ cross sections as a function of the softest-jet p_T on the left, and as a function of the hadronic transverse energy H_T^{had} on the right, for results from $n = 2$ (top panel) to $n = 5$ (bottom panel). Format as in Figure 11.7.

In the right panel of Fig. 11.7, we show the differential ratios in H_T^{had} . Similar to the p_T^W ratios, we observe that for $n = 2$ the ratio in H_T^{had} is not stable under the fixed-order quantum corrections. Even at NLO, the differential jet production ratio is larger than 1 for a large range of H_T^{had} that is shown. We expect this observable to stabilize if higher-multiplicity results are included either through NNLO or even higher-order calculations, or through multi-jet merging at NLO. Around the threshold, all ratios lie at a value of the same order. With increasing H_T^{had} they increase monotonically and stabilize at NLO for $n \geq 3$ for large values of H_T^{had} . We observe a characteristic behavior of the ratios in the high H_T^{had} region. Such events tend to be populated by multiple jets and the H_T^{had} distributions in these jet bins tend to overlap [4], which results in the ratio tending to 1.0. As for the previous observable, MiNLO' and NLO ratios agree very well, with some discrepancy between LO and MiLO' ratios for the lower-multiplicity cases.

11.4.2. Vector-Boson Ratios

In this subsection we show vector-boson ratios of W^- to W^+ production as well as Z to W^+ production. These ratios can help in the extraction of valence-quark PDF information for large values of Bjorken x [4, 185] due to the different coupling of the vector bosons to initial quarks.

We display differential ratios as a function of both the transverse momentum p_T of the softest jet (left panel) as well as the total hadronic energy H_T^{had} (right panel) for W^- to W^+ production accompanied with up to five jets in Fig. 11.8 and Z to W^+ production

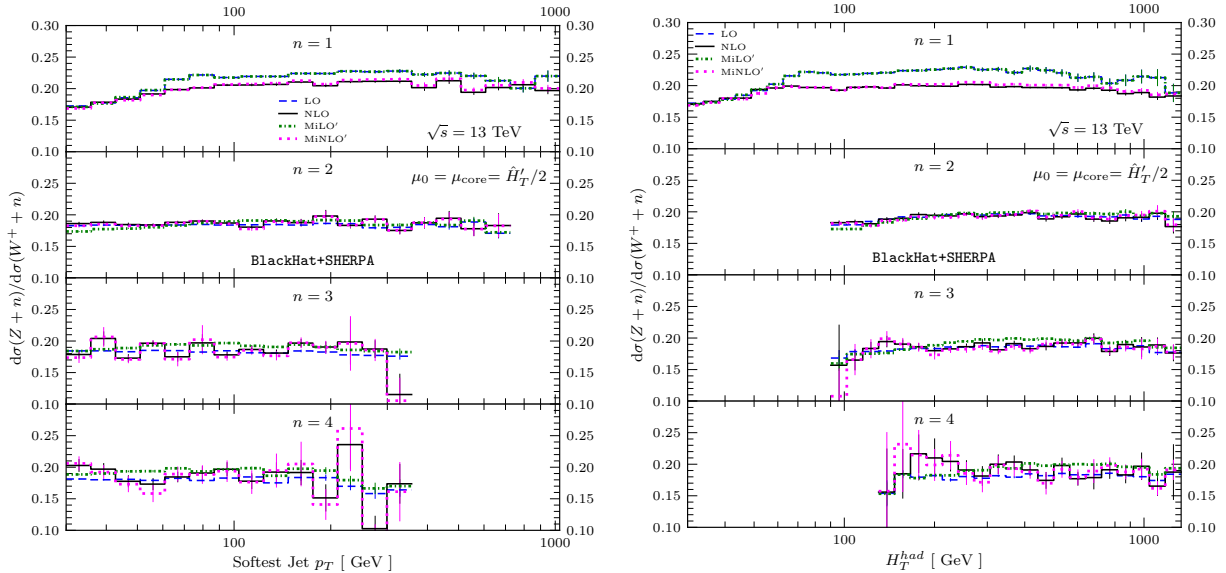


Figure 11.9.: The ratios of $Z + n$ -jet to $W^+ + n$ -jet cross sections as a function of the softest-jet p_T on the left, and as a function of the hadronic transverse energy H_T^{had} on the right. We present results from $n = 1$ (top panel) to $n = 4$ (bottom panel). Format as in Figure 11.7.

with up to four jets in Fig. 11.9. We show ratios for both scale choices with those for $\hat{H}_T'/2$ shown at LO as dashed (blue) lines and at NLO as solid (black) lines, while MiLO' ratios are shown as dash-dotted (green) lines and those for MiNLO' as dotted (magenta) lines. Ratios of Z to W production have been studied experimentally for example in [63].

The ratios of W^-/W^+ production as a function of the transverse momentum for low values of p_T lie around a value of roughly the same order for all shown multiplicities n . With increasing p_T , we observe a monotonic decrease of the corresponding ratio. We attribute this decrease to the different couplings of W^\pm bosons to initial quarks, which together with the dominance of u quarks over d quarks at large values of Bjorken x leads to a suppression of this ratio. NLO corrections to the transverse momentum ratios are mild and the results for both scale choices agree very well. We observe a similar behavior for the differential ratios as a function of the total hadronic energy H_T^{had} . In particular, the ratios decrease monotonically with increasing H_T^{had} , and take values of the same order at low H_T^{had} for all multiplicity, also the results for both scale choices agree very well. However, we observe noticeable NLO correction for the $n = 1$ case in the high H_T^{had} tail.

The ratios of Z to W^+ production in Figure 11.9 are quite flat over the full range of variables shown, which is in contrast to the W^-/W^+ ratios in Figure 11.8. This can be traced to the fact that the Z boson has an appreciable coupling to initial u quarks, as the W^+ boson. The values of Z/W^+ ratios as a function of both the variables shown lie around roughly the same value for all multiplicities n shown. For the $n = 1$ case, a slight decrease of the Z/W^+ ratio can be observed in the low p_T region and there are also noticeable quantum corrections in this case. For all the Z/W^+ ratios, the results for both scale choices agree very well. In general, the quantum corrections in the Z/W^+ observable ratios are quite mild, which makes them excellent choices for new-physics searches.

CHAPTER 12

Summary and Outlook

The processes of electroweak-gauge-boson production in association with many light- and b -jets have diverse final states and are abundantly produced at the LHC. They therefore constitute a natural testing ground for perturbative QCD and more generally the Standard Model over several orders of magnitude. The study of these processes at the LHC thus helps to improve the understanding of both theoretical and experimental techniques, e.g. our understanding of heavy-jet production. Furthermore, these processes are background to many interesting signatures, for example HW associated production with a subsequent decay of the Higgs into a bottom-quark pair as well as many searches for new physics with multi-particle final states.

The theoretical description of these high-multiplicity processes represents a challenging task. In particular, the computation of the required QCD $\mathcal{O}(\alpha_s)$ corrections represents a difficult task due to the many scales that are present such as the bottom mass. We used the numerical unitarity approach [22, 25, 29–31, 33] to compute virtual matrix elements, which required several extensions of the method, and which allowed us to make a first computation for massive final states in association with many jets and multiple quark lines. In general, NLO QCD corrections help to considerably reduce the spurious dependence on unphysical renormalization and factorization scales. Associated to it is the question which scale to use in a fixed-order calculation. New ideas for scale setting such as the parton-shower-inspired `MiNLO` method [5] are an interesting alternative to traditional approaches to scale setting. The application and comparison of different functional forms of dynamical scales for high-multiplicity processes helps to improve the understanding of uncertainties associated to NLO QCD calculations.

In this thesis, we presented NLO QCD predictions for $Wb\bar{b}$ production in association with two and three light jets [21], and we also included results with zero or one extra light jet for completeness. We find that the NLO QCD corrections for the high-multiplicity processes of $Wb\bar{b} + 2$ -jet and $Wb\bar{b} + 3$ -jet production are mild and the remaining renormalization and factorization scale dependence reduces from LO to NLO. In contrast, the K -factor for NLO QCD corrections is large in inclusive $Wb\bar{b}$ production [14, 79, 80], which led us to explore possible improvements to observables for the $Wb\bar{b}$ process by using exclusive sums [81]. We focused on the context of this process being background to $H(\rightarrow b\bar{b})W$ associated production and showed that exclusive-sum predictions for key observables give reduced uncertainties associated to missing higher-order corrections. We found that uncertainties associated to PDFs are subleading in the generic kinematical regimes we studied. We provide n -tuple sets for the predictions obtained by a new `BlackHat` version in combination with `SHERPA` [78], which can be used in future analyses of the $Wb\bar{b} + n$ -jet signatures.

To achieve these state-of-the-art NLO QCD results for $Wb\bar{b} + n\text{-jet}$ ($n = 0, 1, 2, 3$) production, we needed to extend previous applications of the numerical unitarity method to the case of multiple massive fermion lines. For that we presented all relevant ingredients that we used and developed. In particular, the previous application of the numerical unitarity method with massive quarks by Melnikov et al [33] did not reach this level of complexity and we provide a complete set of methods for the first time. In order to deal with explicitly divergent double cuts, we used the prescription of Ref. [33]. In the application of single cuts we also encountered divergent contributions associated to tadpole Feynman diagrams. We extended the prescription of Ref. [33] to this case and removed the divergent expressions by adjusting the Berends-Giele tree generation.

Furthermore, we efficiently evaluated D -dimensional unitarity cuts by reducing the D_s -dimensional Dirac algebra and states to lower dimensions [39]. In order to do so, we found a correct numerical implementation of the HV/FDH scheme for massive external fermions, which builds on a consistent embedding of the external fermion states. The resulting decomposition of one-loop helicity amplitudes by particle content allowed us to avoid the overhead of computing in higher-dimensional representations of the Dirac algebra. We have implemented the above in a new version of the `BlackHat` library.

Moreover, we have performed a dedicated study of weak-vector-boson production in association with light jets at the $\sqrt{s} = 13$ TeV LHC [71] that we presented in this thesis. We have provided NLO QCD predictions for $W^\pm + n\text{-jet}$ and $Z + m\text{-jet}$ production in association with $n \leq 5$ and $m \leq 4$ light jets. We used available matrix elements from `BlackHat` [32] in combination with `SHERPA` and extended previous predictions [2, 3] to the energy configuration of LHC Run-II. We provided a study of uncertainties associated to renormalization and factorization scales by employing several functional forms of dynamical scales and by conventional variations of the central scale. To this end, we used the fixed-order scale $\hat{H}_T'/2$ and compared the results with the more physically motivated MiNLO' reweighting procedure (adaption of the original formulation in [5]). This is the first time such a comparison is carried out in the context of processes with the high jet multiplicity of four and five jets. We find that NLO results obtained with $\hat{H}_T'/2$ and MiNLO' are largely consistent in both shapes and normalization for total cross sections and differential distributions. We also computed several observable ratios and found that jet production ratios have an increased stability compared to the results at $\sqrt{s} = 7$ TeV. In general, the good agreement between the two scale choices confirms that NLO QCD predictions in high multiplicity processes give the first reliable predictions. It will be interesting to see more comparisons of our results with LHC data such as the ones recently shown in Ref. [69].

Finally, we discuss possible extensions of the general approach of numerical unitarity with massive quarks presented in this thesis. We have matrix elements for several interesting phenomenological processes available in our new version of the `BlackHat` library. They allow for the computation of NLO QCD corrections to challenging processes such as on-shell $t\bar{t} + b\bar{b}$ +jet production, on-shell $t\bar{t}$ production in association with up to four light jets, inclusive Wb +jets production and other applications with massive quarks and vector bosons in the future. Also $Zb\bar{b}$ production in association with two light jets should be accessible with some minor modifications of our new matrix elements. In this thesis, we presented a comparison of 4FNS and 5FNS for $Wb\bar{b}$ and $Wb\bar{b} + 1\text{-jet}$ production. This

comparison could easily be extended to the higher-multiplicity cases of $Wb\bar{b}$ + 2-jet and $Wb\bar{b}$ + 3-jet production. In particular, b -initiated subprocesses start to play a more dominant role for these high-multiplicity cases. It would be interesting to see how this affects the comparison of 4FNS and 5FNS and whether we can confirm our conclusions for the comparison in the higher-multiplicity cases.

On the conceptual side, the correct numerical implementation of the HV/FDH scheme for massive quarks and our resulting algorithm for a decomposition of QCD one-loop amplitudes by particle content [39] can be beneficial for the computational efficiency of one- and two-loop amplitudes in the future. In particular, an application in the numerical unitarity approach at two-loops seems to be feasible and well in line with the ongoing research activities here in Freiburg. This might open the route to two-loop amplitudes with massive external quarks. More generally, in order to verify both theory predictions and experimental techniques at the LHC, it will be interesting to study and compare data with predictions for high-multiplicity processes including b jets, like the ones presented in this work. For example, the results based on exclusive sums for $Wb\bar{b}$ production presented in this thesis might help to further constrain the coupling of the Higgs to bottom quarks.

APPENDIX A

The Van Neerven-Vermaseren Basis

In the van Neerven-Vermaseren (NV) construction [132], the D -dimensional space-time is decomposed into a physical space and its complement, the transverse space. The NV construction is used for integrand parameterizations [30, 126]. Consider r inflow momenta p_1, \dots, p_r . The physical space is then spanned by these r momenta and has dimensions $D_p = \min(D, r - 1)$, since the r momenta are in general linearly dependent and one degree of freedom is absorbed by momentum conservation $\sum_{i=1}^r p_i = 0$. Whenever $r > D$, one can find additional relations to reduce the higher point scalar integrals to lower point ones [130]. For example, if $D = 4$, one finds a basis with a maximal rank of 4. The physical space therefore forms a lower dimensional subspace whenever $r \leq D$. The complement to the physical space is called transverse space and has dimension $D_t = \max(0, D - r + 1)$, such that

$$D = D_p + D_t. \quad (\text{A.1})$$

We assume that the momenta p_1, \dots, p_r are ordered, such that the first D_p vectors are linearly independent. The corresponding dual vectors are called v_1, \dots, v_{D_p} . The transverse basis vectors are denoted n_1, \dots, n_{D_t} and we have the following properties

$$\begin{aligned} n_i \cdot n_j &= \delta_{ij}, & n_i \cdot p_j &= 0, \\ v_j \cdot n_i &= 0, & v_j \cdot p_i &= \delta_{ij}. \end{aligned} \quad (\text{A.2})$$

For the case that $r > D$, the space is parameterized solely in terms of linearly independent vectors p_i . The metric tensor is thus decomposed in the NV basis as

$$g^{\mu\nu} = \sum_{i=1}^{D_p} p_i^\mu v_i^\nu + \sum_{i=1}^{D_t} n_i^\mu n_i^\nu, \quad (\text{A.3})$$

with the projector into the transverse space consequently given by

$$(g_\perp)^{\mu\nu} \equiv \sum_{i=1}^{D_t} n_i^\mu n_i^\nu = g^{\mu\nu} - \sum_{i=1}^{D_p} p_i^\mu v_i^\nu. \quad (\text{A.4})$$

One can thus decompose the loop momentum in the NV basis as

$$\ell^\mu = \sum_{i=1}^{D_p} (\ell \cdot p_i) v_i^\mu + \sum_{i=1}^{D_t} (\ell \cdot n_i) n_i^\mu, \quad (\text{A.5})$$

with the projections of the loop momentum on the transverse space $t_i(\ell) = (\ell \cdot n_i)$. In actual computations with $D > 4$, only a specific combination of the projection on the transverse space is relevant. Since external particles remain in 4-dimensions, the additional components of the loop momentum are only relevant in contractions of the loop momentum with itself

$$\mu^2 = -\ell_{[D-4]}^2 \equiv \sum_{i=5}^D (\ell \cdot n_i)^2, \quad (\text{A.6})$$

for explicit integer D -dimensions. Only this combination is of relevance in $D \neq 4$ -dimensional calculations. The $n_{i>4}$ are the transverse vectors of the $D - 4$ -dimensional space. One can split up the decomposition into a 4-dimensional part and a $D - 4$ -dimensional part and gets for the projector into the transverse space

$$(g_\perp)^{\mu\nu} = \sum_{i=1}^{D_t} n_i^\mu n_i^\nu = \sum_{i=1}^{4-r+1} n_i^\mu n_i^\nu + \sum_{i=5}^d n_i^\mu n_i^\nu. \quad (\text{A.7})$$

APPENDIX B

Color-Ordered Feynman Rules

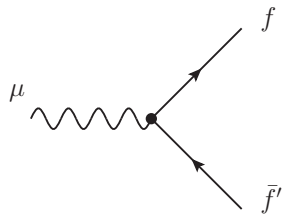
In this appendix we list the color-truncated QCD Feynman rules, which can for example be found in Ref. [121], in Table B.2. They are required for the calculation of color-ordered amplitudes. We assume all vertices are cyclically ordered and momenta are outgoing. We use the light-cone decomposition for massive momenta

$$p = p^\flat + \frac{m^2}{2p \cdot q} q, \quad q^2 = 0, \quad (\text{B.1})$$

with an arbitrary $p \cdot q \neq 0$ light-like reference momentum q and use the spinor-helicity formalism, as for example presented in Ref. [212, 213]. Furthermore, we list the Feynman rule for the electroweak vertex used in this thesis in Table B.1. The full set of SM Feynman rules can for example be found in Ref. [84, 104].

Table B.1.: Feynman rule for the electroweak vertex used in this work with outgoing momenta, adapted from Ref. [104]. V_{ij} denote entries of the CKM matrix.

Electroweak Vertex



$$= ie\gamma^\mu \left(C_L \frac{1 - \gamma_5}{2} + C_R \frac{1 + \gamma_5}{2} \right)$$

	$V f f'$	$\gamma f_i \bar{f}_j$	$Z f_i \bar{f}_j$	$W^+ u_i \bar{d}_j$	$W^- d_j \bar{u}_i$	$W^+ \nu_i \bar{l}_j$	$W^- l_j \bar{\nu}_i$
C_L	$-Q_f \delta_{ij}$	$g_f^- \delta_{ij}$	$\frac{1}{\sqrt{2}s_w} V_{ij}$	$\frac{1}{\sqrt{2}s_w} V_{ji}^*$	$\frac{1}{\sqrt{2}s_w} \delta_{ij}$	$\frac{1}{\sqrt{2}s_w} \delta_{ji}$	
C_R	$-Q_f \delta_{ij}$	$g_f^+ \delta_{ij}$	0	0	0	0	

where $g_f^+ = -\frac{s_w}{c_w} Q_f$, $g_f^- = \frac{I_{W,f}^3 - s_w^2 Q_f}{s_w c_w}$, $s_w = \sin(\theta_W)$, $c_w = \cos(\theta_W)$.

Table B.2.: Color-truncated QCD Feynman rules in Feynman gauge.

Propagators

$$\begin{array}{c} p \\ \mu \bullet \overbrace{\circ \circ \circ \circ \circ \circ \circ \circ \circ}^p \nu \end{array} = \frac{-ig^{\mu\nu}}{p^2}$$

$$\begin{array}{c} p \\ \bullet \xrightarrow{p} \bullet \end{array} = \frac{i(\not{p} + m)}{p^2 - m^2}$$

Vertices

$$\begin{array}{c} \nu, 2 \\ \mu, 1 \quad \text{---} \quad \rho, 3 \\ \text{---} \quad \text{---} \quad \text{---} \end{array} = \frac{i}{\sqrt{2}} [g^{\mu\nu}(p_1 - p_2)^\rho + g^{\nu\rho}(p_2 - p_3)^\mu + g^{\rho\mu}(p_3 - p_1)^\nu]$$

$$\begin{array}{c} \nu \quad \rho \\ \mu \quad \sigma \\ \text{---} \quad \text{---} \end{array} = i \left[g^{\mu\rho}g^{\nu\sigma} - \frac{1}{2}(g^{\mu\nu}g^{\rho\sigma} + g^{\mu\sigma}g^{\nu\rho}) \right]$$

$$\begin{array}{c} \mu \\ \text{---} \quad \text{---} \end{array} = \frac{i}{\sqrt{2}} g_s \gamma^\mu \quad \begin{array}{c} \mu \\ \text{---} \quad \text{---} \end{array} = -\frac{i}{\sqrt{2}} g_s \gamma^\mu$$

Outgoing Fields

$$\begin{array}{c} p \\ \bullet \xrightarrow{p} \text{---} \end{array} \quad \left\{ \begin{array}{l} \bar{u}_+ = [p^\flat] + \frac{m}{\langle qp^\flat \rangle} \langle q | \\ \bar{u}_- = \langle p^\flat | + \frac{m}{[qp^\flat]} [q] \end{array} \right. \quad \begin{array}{c} p \\ \bullet \xleftarrow{p} \text{---} \end{array} \quad \left\{ \begin{array}{l} v_+ = [p^\flat] - \frac{m}{\langle p^\flat q \rangle} |q\rangle \\ v_- = |p^\flat\rangle - \frac{m}{[p^\flat q]} [q] \end{array} \right.$$

$$\begin{array}{c} p \\ \bullet \overbrace{\circ \circ \circ \circ \circ \circ \circ \circ}^\mu \end{array} \quad \left\{ \begin{array}{l} \epsilon_+^* = \frac{[q|\gamma^\mu|p\rangle}{\sqrt{2}[pq]} \\ \epsilon_-^* = \frac{\langle q|\gamma^\mu|p]}{\sqrt{2}\langle qp\rangle} \end{array} \right.$$

APPENDIX C

Results for Selected Scalar Integrals

Among the additional scalar integrals appearing in the master integral decomposition in Section 4.1.4 for processes involving massive quarks are the tadpole integral $I_1(m^2)$ and the bubble integral with a single massive leg in one corner $I_2(m^2; 0, m^2)$. For vanishing masses, both integrals are scaleless and vanish in dimensional regularization. They are given in dimensional regularization with $D = 4 - 2\epsilon$ by

$$I_1(m^2) \equiv I_1 = \frac{\mu_R^{2\epsilon}}{ic_\Gamma} \int \frac{d^D \ell}{(2\pi)^D} \frac{1}{(\ell^2 - m^2)} = m^2 \left(\frac{1}{\epsilon} + \log \left(\frac{\mu_R^2}{m^2} \right) + 1 \right) + \mathcal{O}(\epsilon), \quad (\text{C.1})$$

and

$$I_2(m^2; 0, m^2) \equiv I_{2,m^2} = \frac{\mu_R^{2\epsilon}}{ic_\Gamma} \int \frac{d^D \ell}{(2\pi)^D} \frac{1}{\ell^2((\ell - p)^2 - m^2)} = \left(\frac{1}{\epsilon} + \log \left(\frac{\mu_R^2}{m^2} \right) + 2 \right) + \mathcal{O}(\epsilon), \quad (\text{C.2})$$

where the small imaginary part $i\epsilon$ in the inverse propagators is understood implicitly as $D_i = (\ell_i^2 - m_i^2 + i\epsilon)$ and $c_\Gamma = (4\pi)^{-(2-\epsilon)} \Gamma^2(1 - \epsilon) \Gamma(1 + \epsilon) / \Gamma(1 - 2\epsilon)$. The integrals are taken from Ref. [134].

APPENDIX D

Tadpole Coefficients From UV matching

In an application of numerical unitarity to processes with a single mass circulating in the loop, one can avoid the computation of single cuts in order to extract the tadpole coefficient.¹ Instead, as proposed in Ref. [25, 137], one can match the known *UV* singularity structure of the mass-renormalized amplitude [176] to the *UV* poles of tadpole, bubble and renormalization contributions. The *UV*-divergent part of the tadpole integral and bubble integrals are given in Eq. (C.1) and Eq. (C.2) of Appendix C by

$$I_{1| \frac{1}{\epsilon}} = \tilde{I}_1 = m^2 \quad I_{2,i| \frac{1}{\epsilon}} = \tilde{I}_{2,i} = 1 \quad (\text{D.1})$$

for all i and are in particular independent of other kinematical invariants. Since tadpole and bubble integrals as well as mass renormalization counterterms are the only sources of *UV* divergencies for mass-renormalized one-loop amplitudes, one can deduce the tadpole coefficient by matching the known *UV*-pole structure of each primitive amplitude [176] to the *UV*-poles of the combined bubble, tadpole and renormalization contributions

$$\begin{aligned} \mathcal{A}_{|\text{UV}}^{\text{mass ren.}} &= \sum_i b_i^0 \tilde{I}_{2,i} + a^0 \tilde{I}_1 + \alpha_{\text{mass ren.}} \\ \Rightarrow a^0 &= \frac{1}{m^2} \left(\mathcal{A}_{|\text{UV}}^{\text{mass ren.}} - \sum_i b_i^0 - \alpha_{\text{mass ren.}} \right), \end{aligned} \quad (\text{D.2})$$

with the mass renormalization contribution $\alpha_{\text{mass ren.}}$. In practice, this implies extracting the *UV* pole structure of primitive amplitudes from that of the full amplitude [176] as laid out in Ref. [127]. In the work presented in this thesis we do not apply this technique but follow the straightforward application of numerical unitarity and compute single cuts explicitly. In particular since this is independent of the number of masses in the loop.

¹For more complex processes with different masses in the loop one has several tadpole coefficients.

Bibliography

- [1] M. Czakon, D. Heymes, and A. Mitov, “Dynamical scales for multi-TeV top-pair production at the LHC,” *JHEP* **04**, 071 (2017), arXiv:1606.03350 [hep-ph].
- [2] Z. Bern, L. J. Dixon, F. Febres Cordero, S. Höche, H. Ita, D. A. Kosower, D. Maître, and K. J. Ozeren, “Next-to-Leading Order $W+5$ -Jet Production at the LHC,” *Phys. Rev.* **D88**, 014025 (2013), arXiv:1304.1253 [hep-ph].
- [3] H. Ita, Z. Bern, L. J. Dixon, F. Febres Cordero, D. A. Kosower, and D. Maître, “Precise Predictions for $Z + 4$ Jets at Hadron Colliders,” *Phys. Rev.* **D85**, 031501 (2012), arXiv:1108.2229 [hep-ph].
- [4] Z. Bern, L. J. Dixon, F. Febres Cordero, S. Höche, H. Ita, D. A. Kosower, and D. Maître, “Extrapolating W -Associated Jet-Production Ratios at the LHC,” *Phys. Rev.* **D92**, 014008 (2015), arXiv:1412.4775 [hep-ph].
- [5] K. Hamilton, P. Nason, and G. Zanderighi, “MINLO: Multi-Scale Improved NLO,” *JHEP* **10**, 155 (2012), arXiv:1206.3572 [hep-ph].
- [6] S. Catani, F. Krauss, R. Kuhn, and B. R. Webber, “QCD matrix elements + parton showers,” *JHEP* **11**, 063 (2001), arXiv:hep-ph/0109231 [hep-ph].
- [7] S. J. Brodsky and X.-G. Wu, “Scale Setting Using the Extended Renormalization Group and the Principle of Maximum Conformality: the QCD Coupling Constant at Four Loops,” *Phys. Rev.* **D85**, 034038 (2012), [Erratum: *Phys. Rev.* D86, 079903(2012)], arXiv:1111.6175 [hep-ph].
- [8] M. Mojaza, S. J. Brodsky, and X.-G. Wu, “Systematic All-Orders Method to Eliminate Renormalization-Scale and Scheme Ambiguities in Perturbative QCD,” *Phys. Rev. Lett.* **110**, 192001 (2013), arXiv:1212.0049 [hep-ph].
- [9] M. Rubin, G. P. Salam, and S. Sapeta, “Giant QCD K-factors beyond NLO,” *JHEP* **09**, 084 (2010), arXiv:1006.2144 [hep-ph].
- [10] W. T. Giele, E. W. N. Glover, and D. A. Kosower, “Higher order corrections to jet cross-sections in hadron colliders,” *Nucl. Phys.* **B403**, 633–670 (1993), arXiv:hep-ph/9302225 [hep-ph].
- [11] Z. Bern, L. J. Dixon, and D. A. Kosower, “One loop amplitudes for $e^+ e^-$ to four partons,” *Nucl. Phys.* **B513**, 3–86 (1998), arXiv:hep-ph/9708239 [hep-ph].
- [12] C. F. Berger, Z. Bern, L. J. Dixon, F. Febres Cordero, D. Forde, T. Gleisberg, H. Ita, D. A. Kosower, and D. Maître, “Next-to-Leading Order QCD Predictions for $W+3$ -Jet Distributions at Hadron Colliders,” *Phys. Rev.* **D80**, 074036 (2009), arXiv:0907.1984 [hep-ph].

Bibliography

- [13] C. F. Berger, Z. Bern, L. J. Dixon, F. Febres Cordero, D. Forde, T. Gleisberg, H. Ita, D. A. Kosower, and D. Maitre, “Precise Predictions for $W + 4$ Jet Production at the Large Hadron Collider,” *Phys. Rev. Lett.* **106**, 092001 (2011), arXiv:1009.2338 [hep-ph].
- [14] F. Febres Cordero, L. Reina, and D. Wackerlo, “NLO QCD corrections to W boson production with a massive b-quark jet pair at the Tevatron p anti-p collider,” *Phys. Rev.* **D74**, 034007 (2006), arXiv:hep-ph/0606102 [hep-ph].
- [15] G. Luisoni, C. Oleari, and F. Tramontano, “ $Wb\bar{b}j$ production at NLO with POWHEG+MiNLO,” *JHEP* **04**, 161 (2015), arXiv:1502.01213 [hep-ph].
- [16] J. M. Campbell and R. K. Ellis, “Next-to-leading order corrections to W^+ 2 jet and Z^+ 2 jet production at hadron colliders,” *Phys. Rev.* **D65**, 113007 (2002), arXiv:hep-ph/0202176 [hep-ph].
- [17] C. F. Berger, Z. Bern, L. J. Dixon, F. Febres Cordero, D. Forde, T. Gleisberg, H. Ita, D. A. Kosower, and D. Maitre, “Next-to-Leading Order QCD Predictions for Z, γ^* + 3-Jet Distributions at the Tevatron,” *Phys. Rev.* **D82**, 074002 (2010), arXiv:1004.1659 [hep-ph].
- [18] R. Boughezal, C. Focke, X. Liu, and F. Petriello, “ W -boson production in association with a jet at next-to-next-to-leading order in perturbative QCD,” *Phys. Rev. Lett.* **115**, 062002 (2015), arXiv:1504.02131 [hep-ph].
- [19] R. Boughezal, J. M. Campbell, R. K. Ellis, C. Focke, W. T. Giele, X. Liu, and F. Petriello, “ Z -boson production in association with a jet at next-to-next-to-leading order in perturbative QCD,” *Phys. Rev. Lett.* **116**, 152001 (2016), arXiv:1512.01291 [hep-ph].
- [20] A. Gehrmann-De Ridder, T. Gehrmann, E. W. N. Glover, A. Huss, and T. A. Morgan, “ Z +jet production at NNLO,” *Proceedings, 13th DESY Workshop on Elementary Particle Physics: Loops and Legs in Quantum Field Theory (LL2016): Leipzig, Germany, April 24-29, 2016*, PoS **LL2016**, 056 (2016), arXiv:1607.01749 [hep-ph].
- [21] F. R. Anger, F. Febres Cordero, H. Ita, and V. Sotnikov, “NLO QCD Predictions for $Wb\bar{b}$ Production in Association with up to Three Light Jets at the LHC,” (2017), arXiv:1712.05721 [hep-ph].
- [22] Z. Bern, L. J. Dixon, D. C. Dunbar, and D. A. Kosower, “One loop n point gauge theory amplitudes, unitarity and collinear limits,” *Nucl. Phys.* **B425**, 217–260 (1994), arXiv:hep-ph/9403226 [hep-ph].
- [23] Z. Bern, L. J. Dixon, D. C. Dunbar, and D. A. Kosower, “Fusing gauge theory tree amplitudes into loop amplitudes,” *Nucl. Phys.* **B435**, 59–101 (1995), arXiv:hep-ph/9409265 [hep-ph].
- [24] R. Britto, F. Cachazo, and B. Feng, “Generalized unitarity and one-loop amplitudes in $N=4$ super-Yang-Mills,” *Nucl. Phys.* **B725**, 275–305 (2005), arXiv:hep-th/0412103 [hep-th].

- [25] Z. Bern and A. G. Morgan, “Massive loop amplitudes from unitarity,” *Nucl. Phys.* **B467**, 479–509 (1996), arXiv:hep-ph/9511336 [hep-ph].
- [26] S. Badger, J. M. Campbell, and R. K. Ellis, “QCD corrections to the hadronic production of a heavy quark pair and a W-boson including decay correlations,” *JHEP* **03**, 027 (2011), arXiv:1011.6647 [hep-ph].
- [27] S. Badger, R. Sattler, and V. Yundin, “One-Loop Helicity Amplitudes for $t\bar{t}$ Production at Hadron Colliders,” *Phys. Rev.* **D83**, 074020 (2011), arXiv:1101.5947 [hep-ph].
- [28] K. Melnikov and M. Schulze, “NLO QCD corrections to top quark pair production and decay at hadron colliders,” *JHEP* **08**, 049 (2009), arXiv:0907.3090 [hep-ph].
- [29] G. Ossola, C. G. Papadopoulos, and R. Pittau, “Reducing full one-loop amplitudes to scalar integrals at the integrand level,” *Nucl. Phys.* **B763**, 147–169 (2007), arXiv:hep-ph/0609007 [hep-ph].
- [30] R. K. Ellis, W. T. Giele, and Z. Kunszt, “A Numerical Unitarity Formalism for Evaluating One-Loop Amplitudes,” *JHEP* **03**, 003 (2008), arXiv:0708.2398 [hep-ph].
- [31] W. T. Giele, Z. Kunszt, and K. Melnikov, “Full one-loop amplitudes from tree amplitudes,” *JHEP* **04**, 049 (2008), arXiv:0801.2237 [hep-ph].
- [32] C. F. Berger, Z. Bern, L. J. Dixon, F. Febres Cordero, D. Forde, H. Ita, D. A. Kosower, and D. Maître, “An Automated Implementation of On-Shell Methods for One-Loop Amplitudes,” *Phys. Rev.* **D78**, 036003 (2008), arXiv:0803.4180 [hep-ph].
- [33] R. K. Ellis, W. T. Giele, Z. Kunszt, and K. Melnikov, “Masses, fermions and generalized D -dimensional unitarity,” *Nucl. Phys.* **B822**, 270–282 (2009), arXiv:0806.3467 [hep-ph].
- [34] F. A. Berends and W. T. Giele, “Recursive Calculations for Processes with n Gluons,” *Nucl. Phys.* **B306**, 759–808 (1988).
- [35] R. Britto and E. Mirabella, “External leg corrections in the unitarity method,” *JHEP* **01**, 045 (2012), arXiv:1109.5106 [hep-ph].
- [36] S. Badger, C. Brønnum-Hansen, F. Buciuni, and D. O’Connell, “A unitarity compatible approach to one-loop amplitudes with massive fermions,” *JHEP* **06**, 141 (2017), arXiv:1703.05734 [hep-ph].
- [37] Z. Bern and D. A. Kosower, “The Computation of loop amplitudes in gauge theories,” *Nucl. Phys.* **B379**, 451–561 (1992).
- [38] Z. Bern, A. De Freitas, L. J. Dixon, and H. L. Wong, “Supersymmetric regularization, two loop QCD amplitudes and coupling shifts,” *Phys. Rev.* **D66**, 085002 (2002), arXiv:hep-ph/0202271 [hep-ph].
- [39] F. R. Anger and V. Sotnikov, “On the Dimensional Regularization of QCD Helicity Amplitudes With Quarks,” In preparation.

- [40] R. A. Fazio, P. Mastrolia, E. Mirabella, and W. J. Torres Bobadilla, “On the Four-Dimensional Formulation of Dimensionally Regulated Amplitudes,” *Eur. Phys. J.* **C74**, 3197 (2014), [arXiv:1404.4783 \[hep-ph\]](#).
- [41] H. Ita, “Two-loop Integrand Decomposition into Master Integrals and Surface Terms,” *Phys. Rev.* **D94**, 116015 (2016), [arXiv:1510.05626 \[hep-th\]](#).
- [42] S. Abreu, F. Febres Cordero, H. Ita, M. Jaquier, and B. Page, “Subleading Poles in the Numerical Unitarity Method at Two Loops,” *Phys. Rev.* **D95**, 096011 (2017), [arXiv:1703.05255 \[hep-ph\]](#).
- [43] S. Abreu, F. Febres Cordero, H. Ita, M. Jaquier, B. Page, and M. Zeng, “Two-Loop Four-Gluon Amplitudes with the Numerical Unitarity Method,” *Phys. Rev. Lett.* **119**, 142001 (2017), [arXiv:1703.05273 \[hep-ph\]](#).
- [44] S. Abreu, F. Febres Cordero, H. Ita, B. Page, and M. Zeng, “Planar Two-Loop Five-Gluon Amplitudes from Numerical Unitarity,” (2017), [arXiv:1712.03946 \[hep-ph\]](#).
- [45] S. Chatrchyan *et al.* (CMS), “Search for New Physics with Jets and Missing Transverse Momentum in pp collisions at $\sqrt{s} = 7$ TeV,” *JHEP* **08**, 155 (2011), [arXiv:1106.4503 \[hep-ex\]](#).
- [46] G. Aad *et al.* (ATLAS), “Search for squarks and gluinos using final states with jets and missing transverse momentum with the ATLAS detector in $\sqrt{s} = 7$ TeV proton–proton collisions,” *Phys. Lett.* **B710**, 67–85 (2012), [arXiv:1109.6572 \[hep-ex\]](#).
- [47] S. Chatrchyan *et al.* (CMS), “Search for new physics in the multijet and missing transverse momentum final state in proton-proton collisions at $\sqrt{s}= 8$ TeV,” *JHEP* **06**, 055 (2014), [arXiv:1402.4770 \[hep-ex\]](#).
- [48] G. Aad *et al.* (ATLAS), “Search for squarks and gluinos with the ATLAS detector in final states with jets and missing transverse momentum using $\sqrt{s} = 8$ TeV proton–proton collision data,” *JHEP* **09**, 176 (2014), [arXiv:1405.7875 \[hep-ex\]](#).
- [49] V. Khachatryan *et al.* (CMS), “Search for supersymmetry in the multijet and missing transverse momentum final state in pp collisions at 13 TeV,” *Phys. Lett.* **B758**, 152–180 (2016), [arXiv:1602.06581 \[hep-ex\]](#).
- [50] M. Aaboud *et al.* (ATLAS), “Search for squarks and gluinos in final states with jets and missing transverse momentum using 36 fb^{-1} of $\sqrt{s}=13$ TeV pp collision data with the ATLAS detector,” (2017), [arXiv:1712.02332 \[hep-ex\]](#).
- [51] G. Aad *et al.* (ATLAS), “ATLAS Run 1 searches for direct pair production of third-generation squarks at the Large Hadron Collider,” *Eur. Phys. J.* **C75**, 510 (2015), [Erratum: *Eur. Phys. J.* C76,no.3,153(2016)], [arXiv:1506.08616 \[hep-ex\]](#).
- [52] M. Aaboud *et al.* (ATLAS), “Search for bottom squark pair production in proton–proton collisions at $\sqrt{s} = 13$ TeV with the ATLAS detector,” *Eur. Phys. J.* **C76**, 547 (2016), [arXiv:1606.08772 \[hep-ex\]](#).

- [53] M. Aaboud *et al.* (ATLAS), “Search for supersymmetry in events with b -tagged jets and missing transverse momentum in pp collisions at $\sqrt{s} = 13$ TeV with the ATLAS detector,” *JHEP* **11**, 195 (2017), arXiv:1708.09266 [hep-ex].
- [54] G. Aad *et al.* (ATLAS), “Study of jets produced in association with a W boson in pp collisions at $\sqrt{s} = 7$ TeV with the ATLAS detector,” *Phys. Rev.* **D85**, 092002 (2012), arXiv:1201.1276 [hep-ex].
- [55] G. Aad *et al.* (ATLAS), “Measurement of the production cross section for Z/γ^* in association with jets in pp collisions at $\sqrt{s} = 7$ TeV with the ATLAS detector,” *Phys. Rev.* **D85**, 032009 (2012), arXiv:1111.2690 [hep-ex].
- [56] G. Aad *et al.* (ATLAS), “Measurement of the production cross section for W -bosons in association with jets in pp collisions at $\sqrt{s} = 7$ TeV with the ATLAS detector,” *Phys. Lett.* **B698**, 325–345 (2011), arXiv:1012.5382 [hep-ex].
- [57] G. Aad *et al.* (ATLAS), “A measurement of the ratio of the W and Z cross sections with exactly one associated jet in pp collisions at $\sqrt{s} = 7$ TeV with ATLAS,” *Phys. Lett.* **B708**, 221–240 (2012), arXiv:1108.4908 [hep-ex].
- [58] G. Aad *et al.* (ATLAS), “A measurement of the ratio of the production cross sections for W and Z bosons in association with jets with the ATLAS detector,” *Eur. Phys. J.* **C74**, 3168 (2014), arXiv:1408.6510 [hep-ex].
- [59] G. Aad *et al.* (ATLAS), “Measurements of the W production cross sections in association with jets with the ATLAS detector,” *Eur. Phys. J.* **C75**, 82 (2015), arXiv:1409.8639 [hep-ex].
- [60] G. Aad *et al.* (ATLAS), “Measurement of the production cross section of jets in association with a Z boson in pp collisions at $\sqrt{s} = 7$ TeV with the ATLAS detector,” *JHEP* **07**, 032 (2013), arXiv:1304.7098 [hep-ex].
- [61] M. Aaboud *et al.* (ATLAS), “Measurement of differential cross sections and W^+/W^- cross-section ratios for W boson production in association with jets at $\sqrt{s} = 8$ TeV with the ATLAS detector,” (2017), arXiv:1711.03296 [hep-ex].
- [62] V. Khachatryan *et al.* (CMS), “Differential cross section measurements for the production of a W boson in association with jets in proton–proton collisions at $\sqrt{s} = 7$ TeV,” *Phys. Lett.* **B741**, 12–37 (2015), arXiv:1406.7533 [hep-ex].
- [63] S. Chatrchyan *et al.* (CMS), “Jet Production Rates in Association with W and Z Bosons in pp Collisions at $\sqrt{s} = 7$ TeV,” *JHEP* **01**, 010 (2012), arXiv:1110.3226 [hep-ex].
- [64] S. Chatrchyan *et al.* (CMS), “Event shapes and azimuthal correlations in $Z +$ jets events in pp collisions at $\sqrt{s} = 7$ TeV,” *Phys. Lett.* **B722**, 238–261 (2013), arXiv:1301.1646 [hep-ex].
- [65] V. Khachatryan *et al.* (CMS), “Measurements of jet multiplicity and differential production cross sections of $Z +$ jets events in proton-proton collisions at $\sqrt{s} = 7$ TeV,” *Phys. Rev.* **D91**, 052008 (2015), arXiv:1408.3104 [hep-ex].

- [66] V. Khachatryan *et al.* (CMS), “Measurements of differential cross sections for associated production of a W boson and jets in proton-proton collisions at $\sqrt{s} = 8$ TeV,” *Phys. Rev.* **D95**, 052002 (2017), arXiv:1610.04222 [hep-ex].
- [67] V. Khachatryan *et al.* (CMS), “Comparison of the $Z/\gamma + \text{jets}$ to $\gamma + \text{jets}$ cross sections in pp collisions at $\sqrt{s} = 8$ TeV,” *JHEP* **10**, 128 (2015), [Erratum: JHEP04,010(2016)], arXiv:1505.06520 [hep-ex].
- [68] V. Khachatryan *et al.* (CMS), “Measurements of differential production cross sections for a Z boson in association with jets in pp collisions at $\sqrt{s} = 8$ TeV,” *JHEP* **04**, 022 (2017), arXiv:1611.03844 [hep-ex].
- [69] M. Aaboud *et al.* (ATLAS), “Measurements of the production cross section of a Z boson in association with jets in pp collisions at $\sqrt{s} = 13$ TeV with the ATLAS detector,” *Eur. Phys. J.* **C77**, 361 (2017), arXiv:1702.05725 [hep-ex].
- [70] A. M. Sirunyan *et al.* (CMS), “Measurement of the differential cross sections for the associated production of a W boson and jets in proton-proton collisions at $\sqrt{s} = 13$ TeV,” *Phys. Rev.* **D96**, 072005 (2017), arXiv:1707.05979 [hep-ex].
- [71] F. R. Anger, F. Febres Cordero, S. Höche, and D. Maître, “Weak Vector Boson Production with Many Jets at the LHC $\sqrt{s} = 13$ TeV,” (2017), arXiv:1712.08621 [hep-ph].
- [72] G. Aad *et al.* (ATLAS), “Measurements of the Higgs boson production and decay rates and coupling strengths using pp collision data at $\sqrt{s} = 7$ and 8 TeV in the ATLAS experiment,” *Eur. Phys. J.* **C76**, 6 (2016), arXiv:1507.04548 [hep-ex].
- [73] M. Aaboud *et al.* (ATLAS), “Evidence for the $H \rightarrow b\bar{b}$ decay with the ATLAS detector,” *JHEP* **12**, 024 (2017), arXiv:1708.03299 [hep-ex].
- [74] G. Aad *et al.* (ATLAS), “Performance of b -Jet Identification in the ATLAS Experiment,” *JINST* **11**, P04008 (2016), arXiv:1512.01094 [hep-ex].
- [75] G. Aad *et al.* (ATLAS), “Measurement of the cross-section for W boson production in association with b-jets in pp collisions at $\sqrt{s} = 7$ TeV with the ATLAS detector,” *JHEP* **06**, 084 (2013), arXiv:1302.2929 [hep-ex].
- [76] V. Khachatryan *et al.* (CMS), “Measurement of the production cross section of a W boson in association with two b jets in pp collisions at $\sqrt{s} = 8$ TeV,” *Eur. Phys. J.* **C77**, 92 (2017), arXiv:1608.07561 [hep-ex].
- [77] S. Chatrchyan *et al.* (CMS), “Measurement of the production cross section for a W boson and two b jets in pp collisions at $\sqrt{s}=7$ TeV,” *Phys. Lett.* **B735**, 204–225 (2014), arXiv:1312.6608 [hep-ex].
- [78] T. Gleisberg, S. Höche, F. Krauss, M. Schönherr, S. Schumann, F. Siegert, and J. Winter, “Event generation with Sherpa 1.1,” *JHEP* **02**, 007 (2009), arXiv:0811.4622 [hep-ph].

- [79] F. Febres Cordero, L. Reina, and D. Wackerlo, “W- and Z-boson production with a massive bottom-quark pair at the Large Hadron Collider,” *Phys.Rev.* **D80**, 034015 (2009), arXiv:0906.1923 [hep-ph].
- [80] R. K. Ellis and S. Veseli, “Strong radiative corrections to W b anti-b production in p anti-p collisions,” *Phys.Rev.* **D60**, 011501 (1999), arXiv:hep-ph/9810489 [hep-ph].
- [81] J. Alcaraz Maestre *et al.*, “W+Jets Production at the LHC: A Comparison of Perturbative Tools, in: The SM and NLO Multileg and SM MC Working Groups: Summary Report,” in *Proceedings, 7th Les Houches Workshop on Physics at TeV Colliders: Les Houches, France, May 30-June 17, 2011* (2012) pp. 1–220, arXiv:1203.6803 [hep-ph].
- [82] Z. Bern, L. J. Dixon, F. Febres Cordero, S. Höche, H. Ita, D. A. Kosower, and D. Maitre, “Ntuples for NLO Events at Hadron Colliders,” *Comput. Phys. Commun.* **185**, 1443–1460 (2014), arXiv:1310.7439 [hep-ph].
- [83] M. E. Peskin and D. V. Schroeder, *An Introduction to quantum field theory* (Addison-Wesley, Reading, USA, 1995).
- [84] M. D. Schwartz, *Quantum Field Theory and the Standard Model* (Cambridge University Press, 2014).
- [85] G. S. Guralnik, C. R. Hagen, and T. W. B. Kibble, “Global Conservation Laws and Massless Particles,” *Phys. Rev. Lett.* **13**, 585–587 (1964).
- [86] T. W. B. Kibble, “Symmetry breaking in nonAbelian gauge theories,” *Phys. Rev.* **155**, 1554–1561 (1967).
- [87] P. W. Higgs, “Broken symmetries, massless particles and gauge fields,” *Phys. Lett.* **12**, 132–133 (1964).
- [88] P. W. Higgs, “Broken Symmetries and the Masses of Gauge Bosons,” *Phys. Rev. Lett.* **13**, 508–509 (1964).
- [89] F. Englert and R. Brout, “Broken Symmetry and the Mass of Gauge Vector Mesons,” *Phys. Rev. Lett.* **13**, 321–323 (1964).
- [90] P. W. Higgs, “Spontaneous Symmetry Breakdown without Massless Bosons,” *Phys. Rev.* **145**, 1156–1163 (1966).
- [91] G. Aad *et al.* (ATLAS), “Observation of a new particle in the search for the Standard Model Higgs boson with the ATLAS detector at the LHC,” *Phys. Lett.* **B716**, 1–29 (2012), arXiv:1207.7214 [hep-ex].
- [92] S. Chatrchyan *et al.* (CMS), “Observation of a new boson at a mass of 125 GeV with the CMS experiment at the LHC,” *Phys. Lett.* **B716**, 30–61 (2012), arXiv:1207.7235 [hep-ex].
- [93] S. Dittmaier and M. Schumacher, “The Higgs Boson in the Standard Model - From LEP to LHC: Expectations, Searches, and Discovery of a Candidate,” *Prog. Part. Nucl. Phys.* **70**, 1–54 (2013), arXiv:1211.4828 [hep-ph].

- [94] J. Goldstone, “Field Theories with Superconductor Solutions,” *Nuovo Cim.* **19**, 154–164 (1961).
- [95] J. Goldstone, A. Salam, and S. Weinberg, “Broken Symmetries,” *Phys. Rev.* **127**, 965–970 (1962).
- [96] S. L. Glashow, “Partial Symmetries of Weak Interactions,” *Nucl. Phys.* **22**, 579–588 (1961).
- [97] S. Weinberg, “A Model of Leptons,” *Phys. Rev. Lett.* **19**, 1264–1266 (1967).
- [98] A. Salam, “Weak and Electromagnetic Interactions,” *Conf. Proc. C680519*, 367–377 (1968).
- [99] S. L. Glashow, J. Iliopoulos, and L. Maiani, “Weak Interactions with Lepton-Hadron Symmetry,” *Phys. Rev. D2*, 1285–1292 (1970).
- [100] J. J. van der Bij, “A Cosmotopological relation for a unified field theory,” *Phys. Rev. D76*, 121702 (2007), arXiv:0708.4179 [hep-th].
- [101] A. Huss, *Mixed QCD-electroweak $\mathcal{O}(\alpha_s\alpha)$ corrections to Drell-Yan processes in the resonance region*, Ph.D. thesis, Freiburg U. (2014).
- [102] N. Cabibbo, “Unitary Symmetry and Leptonic Decays,” *Phys. Rev. Lett.* **10**, 531–533 (1963).
- [103] M. Kobayashi and T. Maskawa, “CP Violation in the Renormalizable Theory of Weak Interaction,” *Prog. Theor. Phys.* **49**, 652–657 (1973).
- [104] M. Bohm, A. Denner, and H. Joos, *Gauge theories of the strong and electroweak interaction* (2001).
- [105] H. Lehmann, K. Symanzik, and W. Zimmermann, “On the formulation of quantized field theories,” *Nuovo Cim.* **1**, 205–225 (1955).
- [106] R. P. Feynman, “Very high-energy collisions of hadrons,” *Phys. Rev. Lett.* **23**, 1415–1417 (1969).
- [107] C. Patrignani *et al.* (Particle Data Group), “Review of Particle Physics,” *Chin. Phys. C40*, 100001 (2016).
- [108] L. D. Landau, “On analytic properties of vertex parts in quantum field theory,” *Nucl. Phys.* **13**, 181–192 (1959).
- [109] T. Kinoshita, “Mass singularities of Feynman amplitudes,” *J. Math. Phys.* **3**, 650–677 (1962).
- [110] T. D. Lee and M. Nauenberg, “Degenerate Systems and Mass Singularities,” *Phys. Rev.* **133**, B1549–B1562 (1964).
- [111] Y. L. Dokshitzer, “Calculation of the Structure Functions for Deep Inelastic Scattering and e+ e- Annihilation by Perturbation Theory in Quantum Chromodynamics.” Sov. Phys. JETP **46**, 641–653 (1977).

- [112] V. N. Gribov and L. N. Lipatov, “Deep inelastic e p scattering in perturbation theory,” Sov. J. Nucl. Phys. **15**, 438–450 (1972).
- [113] G. Altarelli and G. Parisi, “Asymptotic Freedom in Parton Language,” Nucl. Phys. **B126**, 298–318 (1977).
- [114] T. Sjostrand, “Monte Carlo Generators,” in *High-energy physics. Proceedings, European School, Aronsborg, Sweden, June 18-July 1, 2006* (2006) pp. 51–74, arXiv:hep-ph/0611247 [hep-ph].
- [115] S. Catani, Y. L. Dokshitzer, M. H. Seymour, and B. R. Webber, “Longitudinally invariant K_t clustering algorithms for hadron hadron collisions,” Nucl. Phys. **B406**, 187–224 (1993).
- [116] S. D. Ellis and D. E. Soper, “Successive combination jet algorithm for hadron collisions,” Phys. Rev. **D48**, 3160–3166 (1993), arXiv:hep-ph/9305266 [hep-ph].
- [117] Y. L. Dokshitzer, G. D. Leder, S. Moretti, and B. R. Webber, “Better jet clustering algorithms,” JHEP **08**, 001 (1997), arXiv:hep-ph/9707323 [hep-ph].
- [118] M. Wobisch and T. Wengler, “Hadronization corrections to jet cross-sections in deep inelastic scattering,” in *Monte Carlo generators for HERA physics. Proceedings, Workshop, Hamburg, Germany, 1998-1999* (1998) pp. 270–279, arXiv:hep-ph/9907280 [hep-ph].
- [119] G. P. Salam and G. Soyez, “A Practical Seedless Infrared-Safe Cone jet algorithm,” JHEP **05**, 086 (2007), arXiv:0704.0292 [hep-ph].
- [120] M. Cacciari, G. P. Salam, and G. Soyez, “The Anti- $k(t)$ jet clustering algorithm,” JHEP **04**, 063 (2008), arXiv:0802.1189 [hep-ph].
- [121] M. L. Mangano and S. J. Parke, “Multiparton amplitudes in gauge theories,” Phys. Rept. **200**, 301–367 (1991), arXiv:hep-th/0509223 [hep-th].
- [122] Z. Bern, L. J. Dixon, and D. A. Kosower, “One loop corrections to two quark three gluon amplitudes,” Nucl. Phys. **B437**, 259–304 (1995), arXiv:hep-ph/9409393 [hep-ph].
- [123] H. Ita and K. Ozeren, “Colour Decompositions of Multi-quark One-loop QCD Amplitudes,” JHEP **02**, 118 (2012), arXiv:1111.4193 [hep-ph].
- [124] F. Febres Cordero, P. Hofmann, and H. Ita, “ $W^+W^- + 3$ -jet production at the Large Hadron Collider in next-to-leading-order QCD,” Phys. Rev. **D95**, 034006 (2017), arXiv:1512.07591 [hep-ph].
- [125] K. Melnikov and M. Schulze, “NLO QCD corrections to top quark pair production in association with one hard jet at hadron colliders,” Nucl. Phys. **B840**, 129–159 (2010), arXiv:1004.3284 [hep-ph].
- [126] H. Ita, “Susy Theories and QCD: Numerical Approaches,” J. Phys. **A44**, 454005 (2011), arXiv:1109.6527 [hep-th].

- [127] R. K. Ellis, Z. Kunszt, K. Melnikov, and G. Zanderighi, “One-loop calculations in quantum field theory: from Feynman diagrams to unitarity cuts,” *Phys. Rept.* **518**, 141–250 (2012), arXiv:1105.4319 [hep-ph].
- [128] G. ’t Hooft and M. J. G. Veltman, “Regularization and Renormalization of Gauge Fields,” *Nucl. Phys.* **B44**, 189–213 (1972).
- [129] R. J. Eden, P. V. Landshoff, D. I. Olive, and J. C. Polkinghorne, *The analytic S-matrix* (Cambridge Univ. Press, Cambridge, 1966).
- [130] D. B. Melrose, “Reduction of Feynman diagrams,” *Nuovo Cim.* **40**, 181–213 (1965).
- [131] G. Passarino and M. J. G. Veltman, “One Loop Corrections for e+ e- Annihilation Into mu+ mu- in the Weinberg Model,” *Nucl. Phys.* **B160**, 151–207 (1979).
- [132] W. L. van Neerven and J. A. M. Vermaseren, “LARGE LOOP INTEGRALS,” *Phys. Lett.* **137B**, 241–244 (1984).
- [133] Z. Bern, L. J. Dixon, and D. A. Kosower, “Dimensionally regulated one loop integrals,” *Phys. Lett.* **B302**, 299–308 (1993), [Erratum: *Phys. Lett.* B318, 649 (1993)], arXiv:hep-ph/9212308 [hep-ph].
- [134] R. K. Ellis and G. Zanderighi, “Scalar one-loop integrals for QCD,” *JHEP* **02**, 002 (2008), arXiv:0712.1851 [hep-ph].
- [135] S. D. Badger, “Direct Extraction Of One Loop Rational Terms,” *JHEP* **01**, 049 (2009), arXiv:0806.4600 [hep-ph].
- [136] W. B. Kilgore, “One-loop Integral Coefficients from Generalized Unitarity,” (2007), arXiv:0711.5015 [hep-ph].
- [137] S. D. Badger, “Generalised Unitarity At One-Loop With Massive Fermions,” *Proceedings, 9th DESY Workshop on Elementary Particle Theory: Loops and Legs in Quantum Field Theory: Sondershausen, Germany, 20-25 April 2008*, *Nucl. Phys. Proc. Suppl.* **183**, 220–225 (2008), arXiv:0807.1245 [hep-ph].
- [138] R. Britto, F. Cachazo, and B. Feng, “New recursion relations for tree amplitudes of gluons,” *Nucl. Phys.* **B715**, 499–522 (2005), arXiv:hep-th/0412308 [hep-th].
- [139] R. Britto, F. Cachazo, B. Feng, and E. Witten, “Direct proof of tree-level recursion relation in Yang-Mills theory,” *Phys. Rev. Lett.* **94**, 181602 (2005), arXiv:hep-th/0501052 [hep-th].
- [140] T. Hahn and M. Perez-Victoria, “Automatized one loop calculations in four-dimensions and D-dimensions,” *Comput. Phys. Commun.* **118**, 153–165 (1999), arXiv:hep-ph/9807565 [hep-ph].
- [141] G. Cullen, M. Koch-Janusz, and T. Reiter, “Spinney: A Form Library for Helicity Spinors,” *Comput. Phys. Commun.* **182**, 2368–2387 (2011), arXiv:1008.0803 [hep-ph].

- [142] A. De Freitas and Z. Bern, “Two-loop helicity amplitudes for quark-quark scattering in QCD and gluino-gluino scattering in supersymmetric Yang-Mills theory,” *JHEP* **09**, 039 (2004), arXiv:hep-ph/0409007 [hep-ph].
- [143] S. Badger, H. Frellesvig, and Y. Zhang, “A Two-Loop Five-Gluon Helicity Amplitude in QCD,” *JHEP* **12**, 045 (2013), arXiv:1310.1051 [hep-ph].
- [144] C. Cheung and D. O’Connell, “Amplitudes and Spinor-Helicity in Six Dimensions,” *JHEP* **0907**, 075 (2009), arXiv:0902.0981 [hep-th].
- [145] M. J. G. Veltman, “GAMMATRICA,” *Nucl. Phys.* **B319**, 253–270 (1989).
- [146] C. Gnendiger *et al.*, “To d , or not to d : recent developments and comparisons of regularization schemes,” *Eur. Phys. J.* **C77**, 471 (2017), arXiv:1705.01827 [hep-ph].
- [147] A. Signer and D. Stockinger, “Using Dimensional Reduction for Hadronic Collisions,” *Nucl. Phys.* **B808**, 88–120 (2009), arXiv:0807.4424 [hep-ph].
- [148] J. C. Collins, *Renormalization*, Cambridge Monographs on Mathematical Physics, Vol. 26 (Cambridge University Press, Cambridge, 1986).
- [149] P. Breitenlohner and D. Maison, “Dimensional Renormalization and the Action Principle,” *Commun. Math. Phys.* **52**, 11–38 (1977).
- [150] S. A. Larin, “The Renormalization of the axial anomaly in dimensional regularization,” *Phys. Lett.* **B303**, 113–118 (1993), arXiv:hep-ph/9302240 [hep-ph].
- [151] G. Leibbrandt, “Introduction to Noncovariant Gauges,” *Rev. Mod. Phys.* **59**, 1067 (1987).
- [152] G. ’t Hooft, “Renormalizable Lagrangians for Massive Yang-Mills Fields,” *Nucl. Phys.* **B35**, 167–188 (1971).
- [153] R. Brun and F. Rademakers, “ROOT: An object oriented data analysis framework,” *New computing techniques in physics research V. Proceedings, 5th International Workshop, AIHENP ’96, Lausanne, Switzerland, September 2-6, 1996*, *Nucl. Instrum. Meth.* **A389**, 81–86 (1997).
- [154] J. C. Collins, F. Wilczek, and A. Zee, “Low-Energy Manifestations of Heavy Particles: Application to the Neutral Current,” *Phys. Rev.* **D18**, 242 (1978).
- [155] S. D. Ellis, R. Kleiss, and W. J. Stirling, “W’s, Z’s and Jets,” *Phys. Lett.* **154B**, 435–440 (1985).
- [156] F. A. Berends, W. T. Giele, H. Kuijf, R. Kleiss, and W. J. Stirling, “Multi - Jet Production in W , Z Events at $p\bar{p}$ Colliders,” *Phys. Lett.* **B224**, 237–242 (1989).
- [157] F. A. Berends, H. Kuijf, B. Tausk, and W. T. Giele, “On the production of a W and jets at hadron colliders,” *Nucl. Phys.* **B357**, 32–64 (1991).
- [158] E. Abouzaid and H. J. Frisch, “The Ratio of $W + N$ jets to $Z^0/\gamma^* + N$ jets versus N as a test precision test of the standard model,” *Phys. Rev.* **D68**, 033014 (2003), arXiv:hep-ph/0303088 [hep-ph].

- [159] J. M. Campbell, R. K. Ellis, and C. Williams, “MCFM, from v.7.0,” (2015), <http://mcfm.fnal.gov>.
- [160] C. Oleari and L. Reina, “ $W^\pm b\bar{b}$ production in POWHEG,” *JHEP* **1108**, 061 (2011), arXiv:1105.4488 [hep-ph].
- [161] J. M. Campbell, R. K. Ellis, F. Maltoni, and S. Willenbrock, “Production of a W boson and two jets with one b^- quark tag,” *Phys.Rev.* **D75**, 054015 (2007), arXiv:hep-ph/0611348 [hep-ph].
- [162] J. M. Campbell, R. K. Ellis, F. Febres Cordero, F. Maltoni, L. Reina, D. Wackerlo, and S. Willenbrock, “Associated Production of a W Boson and One b Jet,” *Phys. Rev.* **D79**, 034023 (2009), arXiv:0809.3003 [hep-ph].
- [163] J. Campbell, F. Caola, F. Febres Cordero, L. Reina, and D. Wackerlo, “NLO QCD predictions for $W + 1$ jet and $W + 2$ jet production with at least one b jet at the 7 TeV LHC,” *Phys.Rev.* **D86**, 034021 (2012), arXiv:1107.3714 [hep-ph].
- [164] T. Aaltonen *et al.* (CDF), “First Measurement of the b -jet Cross Section in Events with a W Boson in p anti- p Collisions at $s^{**}(1/2) = 1.96$ -TeV,” *Phys. Rev. Lett.* **104**, 131801 (2010), arXiv:0909.1505 [hep-ex].
- [165] V. M. Abazov *et al.* (D0), “Measurement of the $p\bar{p} \rightarrow W + b + X$ production cross section at $\sqrt{s} = 1.96$ TeV,” *Phys. Lett.* **B718**, 1314–1320 (2013), arXiv:1210.0627 [hep-ex].
- [166] F. J. Tackmann, J. R. Walsh, and S. Zuberi, “Resummation Properties of Jet Vetoos at the LHC,” *Phys. Rev.* **D86**, 053011 (2012), arXiv:1206.4312 [hep-ph].
- [167] S. Catani, S. Dittmaier, M. H. Seymour, and Z. Trocsanyi, “The Dipole formalism for next-to-leading order QCD calculations with massive partons,” *Nucl. Phys.* **B627**, 189–265 (2002), arXiv:hep-ph/0201036 [hep-ph].
- [168] T. Gleisberg and S. Höche, “Comix, a new matrix element generator,” *JHEP* **12**, 039 (2008), arXiv:0808.3674 [hep-ph].
- [169] A. Banfi, G. P. Salam, and G. Zanderighi, “Infrared safe definition of jet flavor,” *Eur. Phys. J.* **C47**, 113–124 (2006), arXiv:hep-ph/0601139 [hep-ph].
- [170] S. Höche, P. Maierhöfer, N. Moretti, S. Pozzorini, and F. Siegert, “Next-to-leading order QCD predictions for top-quark pair production with up to three jets,” *Eur. Phys. J.* **C77**, 145 (2017), arXiv:1607.06934 [hep-ph].
- [171] S. Dulat, T.-J. Hou, J. Gao, M. Guzzi, J. Huston, P. Nadolsky, J. Pumplin, C. Schmidt, D. Stump, and C. P. Yuan, “New parton distribution functions from a global analysis of quantum chromodynamics,” *Phys. Rev.* **D93**, 033006 (2016), arXiv:1506.07443 [hep-ph].
- [172] A. Buckley, J. Ferrando, S. Lloyd, K. Nordström, B. Page, M. Rüfenacht, M. Schönerr, and G. Watt, “LHAPDF6: parton density access in the LHC precision era,” *Eur. Phys. J.* **C75**, 132 (2015), arXiv:1412.7420 [hep-ph].

- [173] A. Denner, S. Dittmaier, M. Roth, and D. Wackeroth, “Electroweak radiative corrections to $e^+ e^- \rightarrow W W \rightarrow 4$ fermions in double pole approximation: The RACOONWW approach,” *Nucl. Phys.* **B587**, 67–117 (2000), arXiv:hep-ph/0006307 [hep-ph].
- [174] J. M. Campbell and R. Keith Ellis, “Top-quark loop corrections in $Z + \text{jet}$ and $Z + 2$ jet production,” *JHEP* **01**, 020 (2017), arXiv:1610.02189 [hep-ph].
- [175] X. S. L. Y. Hida and D. H. Bailey, “Quad-Double Arithmetic: Algorithms, Implementation, and Application,” report LBNL-46996 <http://crd.lbl.gov/~dhbailey/mpdist>.
- [176] S. Catani, S. Dittmaier, and Z. Trocsanyi, “One loop singular behavior of QCD and SUSY QCD amplitudes with massive partons,” *Phys. Lett.* **B500**, 149–160 (2001), arXiv:hep-ph/0011222 [hep-ph].
- [177] S. Actis, A. Denner, L. Hofer, J.-N. Lang, A. Scharf, and S. Uccirati, “RECOLA: REcursive Computation of One-Loop Amplitudes,” *Comput. Phys. Commun.* **214**, 140–173 (2017), arXiv:1605.01090 [hep-ph].
- [178] F. Caccioli, P. Maierhöfer, and S. Pozzorini, “Scattering Amplitudes with Open Loops,” *Phys. Rev. Lett.* **108**, 111601 (2012), arXiv:1111.5206 [hep-ph].
- [179] A. Denner, S. Dittmaier, and L. Hofer, “Collier: a fortran-based Complex One-Loop Library in Extended Regularizations,” *Comput. Phys. Commun.* **212**, 220–238 (2017), arXiv:1604.06792 [hep-ph].
- [180] A. D. Martin, W. J. Stirling, R. S. Thorne, and G. Watt, “Parton distributions for the LHC,” *Eur. Phys. J.* **C63**, 189–285 (2009), arXiv:0901.0002 [hep-ph].
- [181] L. Wolfenstein, “Parametrization of the Kobayashi-Maskawa Matrix,” *Phys. Rev. Lett.* **51**, 1945 (1983).
- [182] M. Cacciari and G. P. Salam, “Dispelling the N^3 myth for the k_t jet-finder,” *Phys. Lett.* **B641**, 57–61 (2006), arXiv:hep-ph/0512210 [hep-ph].
- [183] M. Cacciari, G. P. Salam, and G. Soyez, “FastJet User Manual,” *Eur. Phys. J.* **C72**, 1896 (2012), arXiv:1111.6097 [hep-ph].
- [184] F. Maltoni, G. Ridolfi, and M. Ubiali, “ b -initiated processes at the LHC: a reappraisal,” *JHEP* **07**, 022 (2012), [Erratum: JHEP04,095(2013)], arXiv:1203.6393 [hep-ph].
- [185] C.-H. Kom and W. J. Stirling, “Charge asymmetry in $W + \text{jets}$ production at the LHC,” *Eur. Phys. J.* **C69**, 67–73 (2010), arXiv:1004.3404 [hep-ph].
- [186] C. F. Berger, Z. Bern, L. J. Dixon, F. Febres Cordero, D. Forde, T. Gleisberg, H. Ita, D. A. Kosower, and D. Maître, “Precise Predictions for $W + 3$ Jet Production at Hadron Colliders,” *Phys. Rev. Lett.* **102**, 222001 (2009), arXiv:0902.2760 [hep-ph].
- [187] M. L. Mangano *et al.*, “Physics at a 100 TeV pp collider: Standard Model processes,” *CERN Yellow Report*, 1–254 (2017), arXiv:1607.01831 [hep-ph].

- [188] G. Aad *et al.* (ATLAS, CMS), “Measurements of the Higgs boson production and decay rates and constraints on its couplings from a combined ATLAS and CMS analysis of the LHC pp collision data at $\sqrt{s} = 7$ and 8 TeV,” *JHEP* **08**, 045 (2016), arXiv:1606.02266 [hep-ex].
- [189] A. Denner and M. Pellen, “Off-shell production of top-antitop pairs in the lepton+jets channel at NLO QCD,” (2017), arXiv:1711.10359 [hep-ph].
- [190] S. Höche, F. Krauss, M. Schönherr, and F. Siegert, “QCD matrix elements + parton showers: The NLO case,” *JHEP* **04**, 027 (2013), arXiv:1207.5030 [hep-ph].
- [191] R. Frederix and S. Frixione, “Merging meets matching in MC@NLO,” *JHEP* **12**, 061 (2012), arXiv:1209.6215 [hep-ph].
- [192] J. Butterworth *et al.*, “PDF4LHC recommendations for LHC Run II,” *J. Phys.* **G43**, 023001 (2016), arXiv:1510.03865 [hep-ph].
- [193] S. Catani and B. R. Webber, “Infrared safe but infinite: Soft gluon divergences inside the physical region,” *JHEP* **10**, 005 (1997), arXiv:hep-ph/9710333 [hep-ph].
- [194] S. Chatrchyan *et al.* (CMS), “Measurement of the Polarization of W Bosons with Large Transverse Momenta in W+Jets Events at the LHC,” *Phys. Rev. Lett.* **107**, 021802 (2011), arXiv:1104.3829 [hep-ex].
- [195] J. M. Lindert *et al.*, “Precise predictions for V+ jets dark matter backgrounds,” *Eur. Phys. J.* **C77**, 829 (2017), arXiv:1705.04664 [hep-ph].
- [196] A. Denner, L. Hofer, A. Scharf, and S. Uccirati, “Electroweak corrections to lepton pair production in association with two hard jets at the LHC,” *JHEP* **01**, 094 (2015), arXiv:1411.0916 [hep-ph].
- [197] S. Kallweit, J. M. Lindert, P. Maierhöfer, S. Pozzorini, and M. Schönherr, “NLO electroweak automation and precise predictions for W+multijet production at the LHC,” *JHEP* **04**, 012 (2015), arXiv:1412.5157 [hep-ph].
- [198] S. Kallweit, J. M. Lindert, P. Maierhöfer, S. Pozzorini, and M. Schönherr, “NLO QCD+EW predictions for V + jets including off-shell vector-boson decays and multijet merging,” *JHEP* **04**, 021 (2016), arXiv:1511.08692 [hep-ph].
- [199] S. Höche, F. Krauss, M. Schönherr, and F. Siegert, “W+ n-Jet predictions at the Large Hadron Collider at next-to-leading order matched with a parton shower,” *Phys. Rev. Lett.* **110**, 052001 (2013), arXiv:1201.5882 [hep-ph].
- [200] L. Lönnblad and S. Prestel, “Merging Multi-leg NLO Matrix Elements with Parton Showers,” *JHEP* **03**, 166 (2013), arXiv:1211.7278 [hep-ph].
- [201] D. Maître, “Private implementation of the MINLO method,” (2017).
- [202] S. Catani and M. H. Seymour, “A General algorithm for calculating jet cross-sections in NLO QCD,” *Nucl. Phys.* **B485**, 291–419 (1997), [Erratum: Nucl. Phys.B510,503(1998)], arXiv:hep-ph/9605323 [hep-ph].

- [203] N. Greiner, S. Höche, G. Luisoni, M. Schönherr, and J.-C. Winter, “Full mass dependence in Higgs boson production in association with jets at the LHC and FCC,” *JHEP* **01**, 091 (2017), arXiv:1608.01195 [hep-ph].
- [204] S. Alekhin, J. Blumlein, and S. Moch, “Parton Distribution Functions and Benchmark Cross Sections at NNLO,” *Phys. Rev.* **D86**, 054009 (2012), arXiv:1202.2281 [hep-ph].
- [205] L. A. Harland-Lang, A. D. Martin, P. Motylinski, and R. S. Thorne, “Parton distributions in the LHC era: MMHT 2014 PDFs,” *Eur. Phys. J.* **C75**, 204 (2015), arXiv:1412.3989 [hep-ph].
- [206] R. D. Ball *et al.* (NNPDF), “Parton distributions from high-precision collider data,” *Eur. Phys. J.* **C77**, 663 (2017), arXiv:1706.00428 [hep-ph].
- [207] S. Catani, Y. L. Dokshitzer, M. Olsson, G. Turnock, and B. R. Webber, “New clustering algorithm for multi - jet cross-sections in e+ e- annihilation,” *Phys. Lett.* **B269**, 432–438 (1991).
- [208] S. Catani, B. R. Webber, and G. Marchesini, “QCD coherent branching and semi-inclusive processes at large x,” *Nucl. Phys.* **B349**, 635–654 (1991).
- [209] C. W. Bauer and B. O. Lange, “Scale setting and resummation of logarithms in $p_T \rightarrow V + \text{jets}$,” (2009), arXiv:0905.4739 [hep-ph].
- [210] F. Krauss, A. Schalicke, S. Schumann, and G. Soff, “Simulating $W/Z + \text{jets}$ production at the Tevatron,” *Phys. Rev.* **D70**, 114009 (2004), arXiv:hep-ph/0409106 [hep-ph].
- [211] D. Britzger, K. Rabbertz, F. Stober, and M. Wobisch (fastNLO), “New features in version 2 of the fastNLO project,” in *Proceedings, 20th International Workshop on Deep-Inelastic Scattering and Related Subjects (DIS 2012): Bonn, Germany, March 26-30, 2012* (2012) pp. 217–221, arXiv:1208.3641 [hep-ph].
- [212] L. J. Dixon, “Calculating scattering amplitudes efficiently,” in *QCD and beyond. Proceedings, Theoretical Advanced Study Institute in Elementary Particle Physics, TASI-95, Boulder, USA, June 4-30, 1995* (1996) pp. 539–584, arXiv:hep-ph/9601359 [hep-ph].
- [213] S. Dittmaier, “Weyl-van der Waerden formalism for helicity amplitudes of massive particles,” *Phys. Rev.* **D59**, 016007 (1998), arXiv:hep-ph/9805445 [hep-ph].

Acknowledgments

First and foremost I would like to thank my supervisor Harald Ita, for his scientific guidance and his supportive attitude. Your advice and help has been invaluable! I would also like to express my gratitude to my second supervisor Fernando Febres Cordero, for the good collaboration and his outstanding commitment. I really enjoyed working with you!

I would like to thank my collaborators Stefan Höche and Daniel Maître, for the things I have learnt from them.

I would like to thank my colleague and office mate Vasily Sotnikov, for all the discussions and good collaboration on many aspects of this work. We have been a good team! To all the current and former members of the 8th (and 7th) floor for supporting me in one or another way but also for the good times shared: Kicker tournaments, Christmas parties and the “Betriebsausflug” come to my mind. A special thanks goes to Samuel Abreu for reading the manuscript of this thesis, to Matthijs van der Wild for forming the winning team of the kicker tournament ’17 and to Jerry Dormans for tolerating our long discussions in the office but also for the fun in “office 809”. To the members of the \hbar -racing team for the shared memories on snow and beyond: Lukas Altenkamp, Michele Boggia, Michael Kordovan.

I would like to thank Hannah Arnold, Giulia Gonella and Gernot Knippen for the shared time as student representatives of the “Graduiertenkolleg 2044”. From organizing BBQs to increasing the “educational value” of the seminar series: I think we provided some innovative impulses!

Finally, I would like to thank Stefanie for all the things one cannot express in words!